ROMANIAN ACADEMY
INSTITUTE OF GEODYNAMICS
"SABBA S. ŞTEFĂNESCU"

PHD THESIS

EXPLORING THE MAGNETISM OF IMPACT CRATERS ON EARTH, MARS AND MOON

Supervisor:
Dr. Crişan DEMETRESCU
Corresponding Member of
the Romanian Academy

Prof. dr. Mioara MANDEA
Centre National d'Études
Spatiales, France

Author:
eng. Anca Margareta ISAC

BUCHAREST, 2013

Acknowledgements

First I would like to thank my supervisors, prof. Mioara Mandea and dr. Crisan Demetrescu, who actually defined and gave dimensions to the thesis. Especially prof. Mioara Mandea never lost interest in my work, being always able to see the big picture. Their efforts helped me come out with this thesis today.

Many thanks go to my professors from Faculty of Geology and Geophysics, University of Bucharest for reading my thesis and being so supportive. I also thank those interested in my research and who take time to serve in my thesis committee. I have to thank all people at Geological Institute of Romania who helped me during my thesis. I owe thanks to GFZ Helmholtz Centre Potsdam for funding my participation at the ESA's Second Swarm International Science Meeting and to the wonderful people I met and studied with. They made GFZ such a wonderful place to work.

My heartfelt thanks to Michael Purucker. He provided me the opportunity to study and experience a drop of PhD-life at Geodynamics Branch of NASA's Goddard Space Flight Center. He was always there with immense patience and scientific resources and made my stay in America as well productive as enjoyable. Another person without whom I could not have completed my thesis is Benoit Langlais, who was available to explain a lot in the simplest way and to help me with ESD models.

I would like to extend my greatest appreciation to several people. First to Andrei Soare, not only for introducing me to this interesting area of research, but for his constructive criticism. Then, to Hans-Joachim Linthe who shared me scientific information regarding the observatory practice and motivated me to work harder towards my goal. Gabriela Cucu has been available whenever I need her and offered me guidance in Fortran programming. Thank all native and non-native English speakers who comprehensively revised my thesis. A special thank goes to all collaborators and coauthors who always have had time to talk about the research and helped me with ideas.

I have been privileged to discuss with many leading voices in the field of geomagnetism, planetary magnetism or impact cratering at Institute of Geodynamics of Romanian Academy, NASA Goddard Space Flight Center, GFZ Helmholtz Centre Potsdam, University of Nantes, or at several international conferences during my PhD studies. I thank them collectively to be sure I would not leave someone out.

Last but not the least I would like to thank my mother and close friends. They have offered me, silently, confidence and tried to keep my moral high every time I felt a bit low during this period. I dedicate this thesis to them.

Contents

Aims and outline of the thesis

The last decades of satellite missions dedicated to measuring planetary magnetic fields have increased considerably the available data. Due to the highest quality, a better description and understanding of magnetic fields of terrestrial bodies were rapidly improved and new magnetic field maps and models were developed. Based on these achievements, the thesis focuses on two objectives:

- The main one is a new direction of studying the magnetic lithosphere of terrestrial bodies. This axis of research is based on the use of the newest global accurate magnetic models to characterize impact craters structures. For the first time, the largest impact craters on the Earth, Mars and Moon are identified first by their quasi-circular features from the most recent and detailed topographic maps and then, after finding their specific magnetic patterns, from available global magnetic maps. The demagnetization effects due to the impact shock wave and excavation processes are evaluated by means of a forward modeling approach, using Equivalent Source Dipoles method and by reducing the thickness of the pre-magnetized lithosphere due to the impact shock wave and excavation processes. The interest in this topic has been motivated by the new topographic and magnetic models derived for these three bodies and by some of visiting fellowships at Helmholtz Center Potsdam, German Research Center for Geosciences (GFZ) and at NASA Goddard Space Flight Center, Planetary Geodynamics Lab, Maryland, USA.

- The measured field originates from several different sources. In the case of the Earth, the most complex planet regarding the magnetic field, the sources are: the core, the crust, the ionosphere and the magnetosphere. In particular, the crustal field that contains information about impact effects can be isolated by deriving crustal field models from raw data, after the external and the main field with its temporal and spatial evolution have been removed. Thus, the second objective is focusing on some temporal characteristics the Earth's magnetic field, with a special interest to the core magnetic field and its secular variation. In order to explain the possible rapid evolution of the main magnetic field and to detect singular events such as jerks

in the geomagnetic field time series, long-time series of data and spectral analysis methods are used. This axis of research is intrinsically related to the involvement of the author on running the Surlari National Geomagnetic Observatory.

The thesis is divided in two parts:

In Part I, *State-of-art of planetary magnetic fields knowledge*, a short history of geomagnetism and a brief presentation of planetary magnetism represent the very first chapter, *A short history of geomagnetism and planetary magnetism.*

In Chapter 2, *Planetary magnetic fields of terrestrial planets*, the sources of the geomagnetic field were introduced firstly, as the more complex when considering Earth-like planets. Thereafter, different possibilities and platforms to measure the magnetic fields were presented. An overview of the most used instruments, ground based observations and satellite missions is given.

The thesis has been focused on the Earth, Mars and the Moon lithospheric magnetic fields. For this reason, magnetic measurements and magnetic fields observations acquired around them were summarized. The mathematical basis to describe the temporal and spatial evolution of the magnetic field is presented, too. A brief description of the inverse problem, useful to apply one technique or another is firstly summarized. Thereafter, the geomagnetic field description using Spherical Harmonic Analysis and then different other techniques such as Equivalent Source Dipoles and two of the most used methods to analyze long time-series of data, mainly those describing the core field variations: the Short Time Fourier Transform and Discreet Wavelet Transform were introduced.

Section 2.4, *Contributions in spectral techniques applied to geomagnetic time-series*, is dedicated to spectral techniques applied to detect short-term variations. Here, a part of the research is devoted to time-analysis of long time-series in order to explain the possible rapid evolution of the main magnetic field. Two methods of spectral analysis, Short Time Fourier Transform and Discrete Wavelets Transform, are applied first to a synthetic signal and then to long series of data provided by Surlari observatory, to detect singular events such as jerks in the geomagnetic field time series. The wavelet analysis is also applied to monthly value series of secular variation generated by Gufm1 model at few hundreds points uniformly distributed over the Earth's surface.

Part II, *Contributions in understanding spatial variations of Magnetic Fields of terrestrial planets* starts with Chapter 1, *Magnetic and topographic maps and models utilized in the thesis.* The latest global maps and models of the geomagnetic field and internal (crustal) fields of Mars and Moon, which are used in the thesis, are presented. Different approaches for some of the most recent models and their resolutions are underlined here.

In Chapter 2, *Small scale magnetic fields: impact craters signature*, the crater forming process and the main morphologic characteristics of impact craters as well as the occurred post-impact modifications are shortly discussed first. The stages of the different crater types formation, as a function of increasing crater size and the gravitational forces exerted, are presented. The key structural elements, such as rim diameter, crater depth and their ratio, are summarized. These morphometric features are considered in modeling the (de)magnetization over the selected large impact craters as an additional support for circular features seen in global maps or models. The geological criteria of impact craters refer only to economic deposits associated with. The different impact related processes can produce world-class to relatively localized occurrences, with examples given for each. Then, the background information, from previous studies, on the geophysical signature observed especially over known Earth's craters were summarized. The analysis of satellite and other remote sensing data or many modern geophysical survey methods provide an invaluable initial identification of the crater, even they do not provide a diagnostic evidence as geology does.

In Chapter 3, *Impact craters seen by magnetic models*, the magnetic signature above large impact craters of the three bodies is examined in greater detail than has previously been done, due to the new ground-database for the Earth, and satellite data for the Earth, Mars and Moon. Their signatures are also visible in other models, as crustal thickness and topographic ones, which are specified and used too. Data description and craters selection from Earth, Mars and Moon is discussed here. Separately, the lithosphere magnetic field models and maps, at planetary scale, are presented. The developed local analyses by means of global lithosphere magnetic field models and maps put in evidence some interesting properties of the ancient magnetic fields of the planetary bodies. However, the main part of my work deals with the magnetic signature of the selected (largest) impact craters. By means of a NASA's software the topographic and magnetic features of the largest craters have been visualized and measured from the latest global maps and models, that were previously impossible. Systematic trends in the amplitude and frequency of the magnetic patterns inside and outside of about 100 complex craters belonging to the three planetary bodies were documented. A forward modeling approach was used to evaluate the demagnetization effects by reducing the thickness of the pre-magnetized lithosphere due to impact excavation process. Assuming that the impact craters are placed in a pre-impact magnetized lithosphere, which is described by Equivalent Source Dipoles (ESD), a comparison between predicted and observed magnetic signatures of these structures has been carried out and shown here.

The last part, *Conclusions*, provides a discussion of the major findings of this research. On one hand, new information about the Earth core field, via its secular variation and

geomagnetic jerks are summarized. On the other hand, the lithospheric magnetic fields and the magnetic signatures of impact craters with their patterns and differences between the three investigated bodies, which is the main direction of the research, are reviewed. The analysis of the magnetic signatures over largest craters produced by impact into different terrestrial planets, and the results of the impact (de)magnetization models onto Earth, Mars and Moon, are a novelty for our community. Finally, some thoughts about the vast new horizon to explore are given.

Part I

State-of-the-art of planetary magnetic fields knowledge

Chapter 1

A short history of geomagnetism and planetary magnetism

Observing and investigating the causes of the Earth's magnetic field is one of the oldest subject of scientific research. According to the ancient literature, magnetism with its practical use has been known for thousands of years. Although it is under discussion at what exact time and on which continent compasses were used first, it can be assumed that Asian, European and Arabic mariners benefited from the magnetic influence on magnetized needles orienting themselves, more or less, in a North-South direction. These compasses can be considered as the earliest magnetic field instruments. The earliest written evidence of the compass navigation is found in the book of the Chinese scientist Shen Kua, dating to 1088. The use of the mariner's compass in Europe is mentioned by Alexander Neckam, around 1190. The first scientific report, describing the Earth's magnetic field, goes back to Peter Peregrinus of Maricourt, who studied the behavior of magnetized rocks in the thirteenth century. He incorrectly attributed the Earth's magnetism to the action of *celestial poles*, but he distinguished the two different poles of a magnetic needle. In his "Epistola de magnete", written in 1269, Petrus Peregrinus gave the first detailed description of the compass construction and of some experiments performed on a sphere of lodestone. He discovered the dipolar nature of a magnet and that the magnetic field is strongest at the poles, where its vector is directed in the vertical plane (Smith, 1992).

Three centuries later, Wiliam Gilbert, physicist and royal personal physician of Queen Elizabeth I, experimented with a magnetized sphere which he called *terrela*, little Earth. From his systematic researches, he concluded properly that the Earth itself generates the forces that orient compasses. Gilbert published his results in his first book (Gilbert, 1600): *De Magnete, Magneticisque Corporibus, et de Magno Magnete Tellure*, a book with great success in Europe as reflected by the big number of copies compiled in the

following years. This can be considered the beginning of the science of geomagnetism.

Measurements performed by Henry Gellibrand in London, in 1634, revealed that the declination is a function of position, undertaking slow temporal changing. In 1830, almost two centuries later, Gauss, Humbold and Weber set up the first globally synchronized magnetic measurements network (50 at that time, including 15 outside of Europe). They named the network the *Göttinger Magnetischer Verein* (Göttingen magnetic union), soon after the installation of the first observatory in Göttingen. They also fixed the magnetic observation procedure, the data collection and processing routine. Gauss made possible, for the first time, to measure the field absolute intensity, thanks to his developments in instrumentation. Early after, he introduced the mathematical theory for separating the inner and outer sources of the Earth's magnetic field by the use of technique *Spherical Harmonic Expansions* (Gauss, 1839). His merits for geomagnetism can hardly be overestimated. His method has been the standard tool for analyzing the geomagnetic field until today. A few years later, the basic equations of electromagnetism were compiled by James Clerk Maxwell, allowing for a comprehensive study of the field. Until the middle of the 20^{th} century, a correct description of the Earth's magnetic field had mostly been limited by the sparse of data distribution. The International Geophysical Year ($1957 - 1958$) and even more, the subsequent World Magnetic Survey, initiated the installation of new observatories, urged the launch of satellites for magnetic surveys and gave impetus to field modeling and interpretation.

Since then, the understanding of the magnetic field has developed greatly, thanks to continuous ground field measurements in the last 200 years and satellite missions around the planetary bodies of our Solar System, in the few past decades. At this time, the improved field description is due to the refinements in instrumentation both on the Earth and in space. The invention of the vectorial fluxgate and the scalar proton magnetometer allows for accurate measurements. Enhanced computer capability permits the processing of the constantly growing quantity of available data. The derivation of the recent field models from the satellite data is nowadays possible thanks to sophisticated digital data processing. Measurements of the geomagnetic field are exploited now to answer some fundamental questions about the physical processes in the Earth's deep interior, about the lithosphere, the near Earth's environment or solar-terrestrial interactions.

Planetary magnetism (Stevenson, 2003) is also a recent study, born of the space age and a new era of discovery that began in the $1960s$ with the launch of spacecraft to other bodies. We learn about planetary magnetic fields by the direct detection of the field from a flyby or from a orbiter spacecraft. In little more than four decades, space probes have discovered that most of the Sun's planets and some of their satellites have main magnetic fields. Now, the Sun and stars were known to possess magnetic fields, but one could only

speculate on whether and how the planets and satellites in our solar system gained their intrinsic magnetic field.

Terrestrial planets (Mercury, Venus, Earth, Mars) and satellites Moon and Io consist, primarily, of materials that condense at high temperatures: oxides and silicates of iron and magnesium, together with metallic iron. The high density and lower melting point of iron alloys relative to silicates, generally lead us to expect that these bodies form metallic iron-rich cores. Note that the satellites, like Moon or Io, are sufficiently large (a radius roughly bigger than 1000 km) to be subject of the same planetary processes, at least for questions pertaining magnetic field. Terrestrial planets, like Mercury and Earth, have a dipolar magnetic field that are produced by a dynamo action in their metallic iron-rich conducting core (Russell, 1993). These cores are, generally, at least partially liquid, even after 4.5 Gy of cooling. Among them, Earth has a dynamic global magnetic field, time varying on all time-scales, from years to billions of years (Roberts and Glatzmaier, 2000). Mars had had an ancient dynamo, probably in the period prior to 4.0 Gy, (Acuña et al., 2001; Connerney et al., 2004). There are patches of magnetization that most likely formed long ago before their interior core dynamo of liquid material disappeared (Stevenson, 2001).

The Moon may be telling, basically, the same story but is doubting that the small lunar core, even at least partially liquid, could have supported a dynamo. Alternative explanations for the patches of strong crustal magnetization invoke plasma clouds generated by major impacts and compression of conducting plasma at the antipode. It is not known if the pre-impact field was a dynamo-global field. Mercury differs from both the Moon and Mars because of its extraordinarily large core and thin rocky mantle. It is likely to have a liquid outer core and some models predict that this core could continue to convect and perhaps sustain a dynamo. The internal field (about 1% of the Earth's main field) is just sufficient to keep the day-side magnetopause above the planet's surface under nominal solar wind conditions. New insides from the polar-orbiting MESSENGER, launched in 2004, have become available at the end of 2011. Venus is likely to have a liquid outer core, with or without an inner core, but has no dynamo at present and no measurable internal magnetic field. Its proximity to Earth has invited a large number of missions, particularly in the early decades of space exploration, but only weak magnetic fields associated with the solar wind interaction have been detected.

The gas giants Jupiter and Saturn which have hydrogen as their major constituent may have a very similar dynamo generation out to levels where hydrogen is only a semi-conductor, perhaps 80% to 85% of the planet radius (Bagenal et al., 2004). They may possess *Earth-like* central cores but it is still difficult to understand their magnetic fields. For example, the Jovian magnetic field is not generated by an internal dynamo but by a

synchrotron source of radio waves.

Ice giants Uranus and Neptune contain a hydrogen-rich envelope but their composition is rich in H_2O, CH_4 and NH_3 throughout much of the volume, extending out to perhaps 80% of their radii. Although it seems likely that high-pressure water can provide the desired conductivity for a dynamo, it is marginal and the observed field strength is small (Stanley and Bloxam, 2004). Large icy satellites and solid icy planets, Triton and Pluto, might possibly have water-ammonia oceans and might therefore be capable of small induction signals. Of the major satellites, only Ganymede is known to produce a magnetic field and has a clear signature of a permanent dipole. Neither the dynamic satellite of Jupiter, Io, nor the big satellite of Saturn, Titan, have self-generated fields. This can be a consequence of the general decline of the mantle convective vigor when the core became stably stratified and a possible early dynamo ceased to operate. Europa, with a relative small water-rich layer, mostly liquid, has a clear signature of an induction field and no evidence of a permanent dipole.

For Earth, Jupiter, Saturn, also Mercury, probably Ganymede, the field is predominantly dipolar. The tilt of the dipole, relative to the rotation axis, is of order of 10° for Jupiter and Earth and near-zero for Saturn. Uranus and Neptune represent a different class of dynamos with a magnetic field about equally dipole and quadrupole and with a tilt of the dipole of 40°-60°.

Still the observations are sparse in both space and time, they are sufficient to describe diverse group of planetary magnetic fields and provide clues to the future development of the planetary magnetic field exploration. Present-day efforts are focused mainly on the development of global, near-surface maps and models of the magnetic field that integrates satellite coverage, in order to extend the techniques to the other far away planets and moons of our solar system.

Chapter 2

Planetary magnetic fields of terrestrial planets and their description

2.1 Sources of planetary magnetic fields

Studies of the planetary magnetism have been for long concentrated on explaining the processes responsible for magnetic fields of celestial bodies. The field strength and the dipole dominated structure are deemed typical for planetary dynamos. The space missions have taught us that the magnetic fields in our solar system are very diverse and every new mission seems to bring more surprises and inside details. These missions have also revealed that only the intrinsic magnetic field shields a planet from adverse effects of the solar wind and cosmic radiation, playing an essential role in preventing the dissipation of the atmosphere (Friis-Christensen et al., 2009). Nowadays, we are able to better understand how the magnetic shielding works, how it may change its spatiality, and over time, and how the background dynamo process operates (Mandea, 2005). The Earth's magnetic field (also named the geomagnetic field) is usually defined as the magnetic field produced by all sources within and outside the solid Earth, from *Core-Mantle Boundary* up to the so-called *magnetopause*, within which the Earth's magnetic field remains confined. Beyond this boundary only the *Interplanetary Magnetic Field* (IMF) exists, due to the Sun activity, and transported by a plasma known as the *solar wind*.

According to the correct scientific magnetic definition, the field intensity is abbreviated with $\vec{H}$ and $\vec{B}$ describes the magnetic flux intensity or magnetic induction. In free-space, without any magnetization (M), the two are related by:

$$\vec{B} = \mu_0 \vec{H} \tag{2.1}$$

where $\mu_0 = 4 \cdot 10^{-7} VsA^{-1}m^{-1}$ is the vacuum permeability. It is common in geophysics to deal with and analyze the magnetic field $\vec{B}$, largely for pragmatic reasons (see *Treatise on Geophysics, 5.08.1.6, Magnetic Quantities, Units, and Conversions, p.282*). B, H and M have the same dimensions, although their units have different names ($\vec{B} = \mu_0(\vec{H}+\vec{M})$). In International System of Unity(SI), $\vec{B}$ and $\vec{H}$, both usually called *magnetic field*, differ numerically only by a constant factor. Another reason was to prevent confusion with the horizontal field intensity $\vec{H}$. The same abbreviation is used in this thesis, too.

It is well known that when, either a surface observatory or a satellite, takes a geomagnetic field measurement, it represents the superposition of many sources. Their contributions defined like:

$$\vec{B}(r,t) = \vec{B}_c(r,t) + \vec{B}_l(r) + \vec{B}_e(r,t) \tag{2.2}$$

are discussed in the following.

Also, the diversity of the three planetary magnetic fields (Earth, Mars, Moon) is clearly shown in Figure 1, which indicates the sources contributions in magnetic fields for these three analyzed bodies. As the interest has been focused on the Earth's core field and these three lithospheric magnetic fields, they have been introduced with some more details, in the following.

By far the greatest contribution is, generally, from the approximately dipolar field generated from the dynamo action within the fluid, iron-rich core of the Earth, known as the *core field* ($\vec{B}_c$), and also sometimes named the *main field*. Although depending upon the altitude and location of the reading, it may have sizable contributions from the static *lithospheric field* ($\vec{B}_l$), being generated largely from rocks and remanent magnetism within the Earth's crust. Small signals can also be observed from the electrical currents generated by the flow of the oceans (Kuvshinov and Olsen, 2005). Another significant contribution is that of external field sources ($\vec{B}_e$), which originate in the *ionosphere and magnetosphere*. These variable sources include the daily Solar quiet (Sq) variations, the ring current variations, the contributions from the Disturbance storm time (Dst) deviations, and from other atmospheric current systems such as the Field-Aligned Currents (FAC), the Auroral Electro-Jet (AEJ) and Equatorial Electro-Jet (EEJ) (Langel et al., 1993). It must also include the currents induced into the Earth from these external fields (Olsen, 1999).

The knowledge of the sources of magnetic field for planetary bodies, and their contribution of the magnetic field of each of them, is very crucial to understand every single one and connections between them. Taking into account the subject of this thesis a more detailed description of components known as the internal field (the *core field* and the *lithospheric field*) is given, while *external sources* are shortly described.

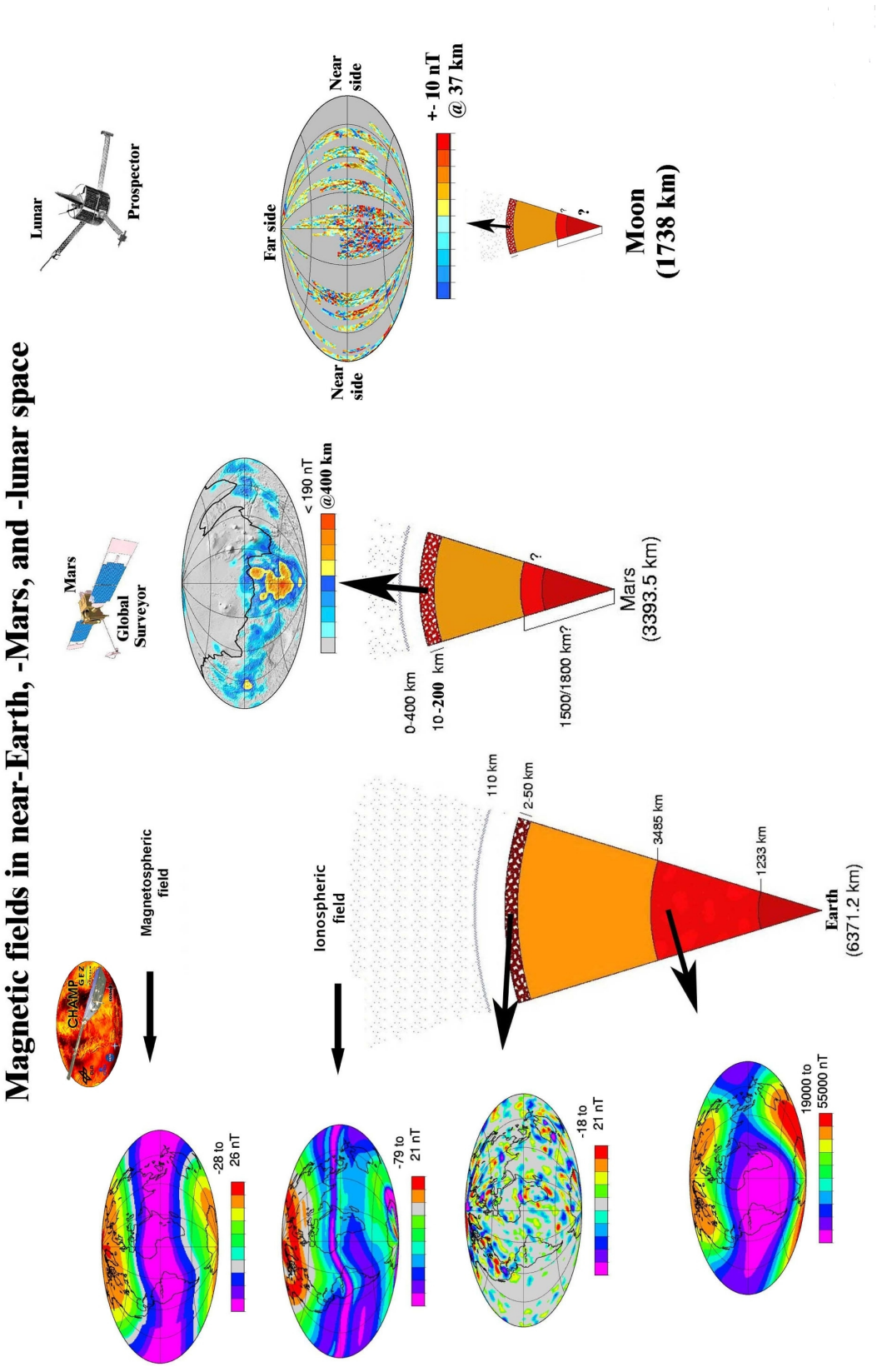

Figure 1: Comparison of the internal structures and magnetic field models for Earth, Mars and Moon *(Purucker, 2007).*

2.1.1 External sources

The main part of the Earth's magnetic field is created by processes and material in the Earth's interior. However, to this main internal contribution, external sources have to be added, produced by the magnetospheric and ionospheric currents. The space itself (from some 100 km to far away in the space) is filled with ionized gas, a plasma of positively charged ions and negatively charged electrons. The plasma motion produces significant current flows, implying magnetic field disturbances, often of the same magnitude as the field generated inside the Earth, at the same altitude. Under some specific conditions, these external current systems can be large enough, generating significant magnetic variations at the Earth's surface. The magnetospheric and ionospheric fields both result from Sun-Earth interactions. Their time variation range between seconds and decades, with daily, seasonal, semi-annual and annual periodicities. Other variations follow the solar cycle of 11 and 22 years. The external magnetic fields are characterized by rapid time variations, difficult to monitor or to predict. A description of magnetospheric and ionospheric fields is given in the following.

The *magnetosphere* is a region carved out of the solar wind plasma flow by the interaction with the geomagnetic field. The kinetic pressure distorts the outer part of the terrestrial dipolar field. A general cometary shape with compression of the geomagnetic field lines ($\sim$ 10 Earth's radii during low activity) in the Sun-ward direction and a long stretched out magnetotail in the anti-Sun-ward direction ($\sim$ 100's of Earth radii), which reaches far beyond lunar orbit, is created. Its shape is highly dynamic as it responds to changes in the solar wind density and field direction. The distortion of the internal dipole field into the typical shape of the magnetosphere is accompanied by electrical currents. Among them, the ring current lies on dipolar field lines between $\sim 4-6$ Earth's radii and it consists of energetic electrons and ions which move along the field lines and oscillate back and forth between the two hemispheres. The compression of the internal magnetic field on the day-side is associated with the magnetopause current, and with the tail and cross-tail neutral sheet currents which are connected and form a Θ-like current system (if it is seen from along the Earth-Sun line), of the night-side magnetosphere. In addition to the currents that flow across the magnetic field lines, Field-Aligned Currents (FAC) flow along magnetic field lines and connect the magnetospheric currents to those flowing in the polar ionosphere. The FAC are mainly carried by electrons in a process called reconnection and are essential for the exchange of energy and momentum between these regions.

The *ionosphere* is an ionized region of the upper atmosphere which extends to altitudes of about 1000 km and, at low and mid-latitudes, gradually merges into the plasmasphere, a torus-shaped volume inside the ring current. It contains of a cool but dense plasma of

ionospheric origin, which co-rotates with the Earth. A number of current systems exist in the conducting layers of the Earth's ionosphere, mostly at altitudes of $100 - 150$ km. Notable are the Auroral Electro-Jets (AEJ) inside the auroral oval, the daily Solar quiet variation (Sq) current in the dayside mid-latitude ionosphere, and the Equatorial Electro-Jet (EEJ) near the magnetic equator (Lanzerotti et al., 1993). At high latitudes, plasma sheet electrons can precipitate along magnetic field lines down to ionospheric altitudes, where they collide with and ionize neutral atmosphere particles. The photons emitted by this process create the polar light, the aurora.

To understanding the external field variations is crucial in all studies focused on spatial and/or temporal characterization of the internal fields. Indeed, when modeling the internal fields sources, the effects of external fields can be minimized by considering data at magnetically quiet times, but this is frequently impractical, especially at higher magnetic latitudes. Moreover, for many magnetic surveys it is important to run a continuously recording base station to monitor and correct for external variations. The base station is located at a site where the spatial field gradients are low (not on a magnetic anomaly), ideally in roughly the center of the survey area. The knowledge of external sources has been crucial in studying short-term geomagnetic field variations (see *Part I, Section 2.4*).

2.1.2 Internal sources

The research work has been focused on the internal planetary magnetic fields. On one side, the internal geomagnetic field with its wide temporal and spatial variations and, on another side, the planetary magnetic fields of terrestrial planets, have been the quintessence of the thesis. For this reason, this internal part of planetary magnetic fields was presented in more detail. A special view is given to the main part of the geomagnetic field, beside the comparison of its lithospheric part with that of Mars and Moon.

In our solar system, the planetary bodies can conveniently be classified by their primary composition. Terrestrial planets such as Earth and its Moon, Mars, Venus and Mercury (included in this category) are mainly composed of rock-silicates and oxides, with some metallic iron. Gas giants, as Jupiter or Saturn, have rock cores as much as 10 times the mass of the Earth, however their main constituents are hydrogen and helium.

Three mechanisms can be considered at the origin for the internal magnetic field of a terrestrial body:
– an active dynamo
– crustal remanence
– magnetic induction

Exploration of the solar system with spacecraft reveals that all three can operate, depending of the internal conditions and rotational parameters of a given planet or satellite.

A comparison of magnetic fields of the terrestrial planets with that of the Earth, together with new measurements provided by spacecraft, can provide a better understanding of the origin and evolution of the planetary magnetic fields.

Core field

A convective region, with sufficiently large electrical conductivity, is necessary for maintaining an active dynamo. In the terrestrial planets, only the metallic core has the possibility of providing *dynamo generation*. These cores are mainly composed of iron, but contain small but significant amounts of light elements such as Si, O, H or S. The melting temperature of iron is considerably lower than that of silicate rocks (which is a primary reason why cores form to begin with). Inclusion of light elements (especially sulfur) lowers the melting temperature, so it is possible that the cores of not-too-small planets can remain largely molten for 4.6 Gy since their formation, even with the secular cooling of the silicate mantle overlying them. The molten state only cannot guarantee, however, that convection in the core is vigorous enough to sustain a dynamo. In the Mars and the Moon, the liquid part, if still exists, is perhaps too small to generate a significant dynamo.

As the core magnetic field is a predominant characteristic for the Earth, a few significant of its features are indicated in the following. It originates from the outer liquid core between 2900 and 5200 km depth, is driven by a self excited dynamo process and is called the *core field* or *main field*, $\vec{B}_c(r,t)$. The conducting iron convects from the inner core up to the *Core-Mantle Boundary* (CMB) and it is deviated by the Earth's rotation (Coriolis forces). It features a mostly dipolar, axial and centered dominant structure, tilted by about 11° from the Earth's rotation axis. It typically represents more than 98% of the total magnetic field.

The absolute values of the core field measured at the Earth's surface, range from about $20,000\ nT$, at the magnetic equator, to $70,000\ nT$ at the magnetic pole. It is time variable, on different time scales, from monthly to decadal, centennial to 50 My for major events, as excursions or reversals times (Campbell, 1997). The dipole field has a dipole moment of about $7.746 \times 10^{24}\ nTm^3$, which is decreasing highly, at least last centuries. In reality, a multipole expansion is necessary to describe in details the core field (see *Part I, Section 2.3* for details). Long term change of the core magnetic field, for the temporal scales covering the range of decades to centuries, is called *secular variation*, defined as the first derivative of a given component time series (see *Part I, Section 2.4*). Measurements of the two field directions, declination and inclination, date back further than full vector observations. Frequent measurements were taken particularly from shipboard for navigational purposes from the late 16^{th} century on. Individual time series of declination

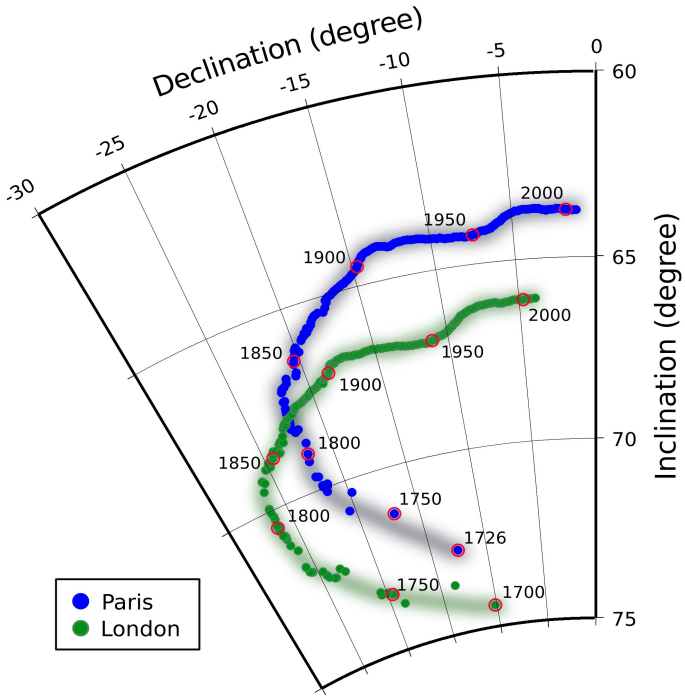

Figure 2: Temporal evolution of the angles D, I (declination and inclination) characterizing Paris and London. Points plotted on a zenithal equidistant projection *(Mandea and Thèbault, 2007)*.

and sometimes inclination have been compiled by Malin and Bullard (1981), Cafarella et al. (1992), Barraclough (1995), Alexandrescu et al. (1996), Soare et al. (1998), for London, Rome, Edinburgh, Paris and Romania, respectively. Recently, a new curve has been compiled for Munich (Korte et al., 2009). An example stands for the longest ones, Paris and London series, shown in Figure 2, as a Bauer diagram.

The abrupt changes in the second derivative time series, are usually called *geomagnetic jerks*. Courtillot et al. (1978) defined the "geomagnetic jerk" or "impulse" as a sudden change in the slope of secular variation, i.e. a discontinuity of the second time derivative (secular acceleration) of the geomagnetic field components. Nowadays, it is almost accepted they are internal in origin and it is produced by the fluid flow at the top of the outer core. Some attempts to explain their physical origin have been done. One of them, found in Bloxham (2002), explains their origin by a combination of a steady flow and a simple time-varying, axisymmetric, equatorially symmetric, toroidal zonal flow, consistent with torsional oscillations in the Earth's core. Usually, geomagnetic jerks are particularly visible in the eastward component (Y), which is supposed to be the least affected by the external fields.

The historical measurements of the magnetic field in Romania (Atanasiu, 1968; Atana-

siu et al., 1976; Constantinescu, 1979; Soare et al., 1998) and more recent ones give a picture of its distribution and time evolution over our national territory as well as characteristics of the secular variation of the geomagnetic field (Anghel and Demetrescu, 1980; Anghel et al., 1980; Demetrescu et al., 1985). Demetrescu et al. (2011) showed (using a more detailed model to describe secular variation, and based on repetition station measurements) that the secular variation has a lateral distribution reflecting peculiarities of the crust/rocks in Romania. Later, Dobrica et al. (2013), proposed a complex model of the secular variation and the lateral evolution of the main field, using data from the European network of geomagnetic observatories.

Recently, the secular variation has been determined from satellite measurements alone, together with the characteristic geomagnetic jerks over the last decade (Mandea et al., 2000; Olsen and Mandea, 2008). A study on the geomagnetic jerk represents a part of this work, it is summarized in *Part I, Section 2.4*, and the title of corresponding papers are included in the appendix.

Lithospheric field

In order to obtain a clear description of crustal anomalies, it is crucial to find adequate methods to remove the non-crustal fields. The most important is, as we have shown, the $\vec{B}_c(r,t)$, which has large amplitude and varies slowly, both temporally and spatially. External fields $\vec{B}_e(r,t)$ have much smaller amplitudes, and, as shown previously, are characterized by rapid temporal variations. Time-varying external fields also induce sub-surface magnetic fields throughout the crust and mantle, with amplitudes generally smaller compared to those of typical crustal anomalies. The magnetic field of the lithosphere $\vec{B}_l(r)$ is often referred as magnetic field anomalies. A large interest comes from the diversity of magnetic field anomalies, mainly whose characterizing the terrestrial planets.

Rocks of the upper lithosphere of the Earth and other planets such as Mars and Moon may produce a magnetic field, whatever it is induced by an internal or external source, or remanent (Runcorn, 1975). This is why the rock magnetism became an important topic for both, fundamental and applied sciences (Raymond and Labreque, 1987). Actually, at a small scale, everything is magnetic due to the interactions of orbiting electrons with an external magnetic field. These interactions may produce a very small magnetic field in case of diamagnetic materials or, for atoms possessing an atomic magnetic moment, may produce an induced magnetization. This induced magnetization is aligned parallel to the applied magnetic field and is inversely proportional to temperature. Considering the paramagnetic structures, it returns to zero if the applied magnetic field is removed. Ferromagnetic effect, the most important one, also concerns atoms with magnetic moment, but, in this case, adjacent atomic magnetic moments strongly interact, allowing

the material to retain a magnetic field even in the absence of an external magnetic field (Dunlop and Özdemir, 1997).

Ferromagnetic materials are mainly iron, cobalt and nickel, but relatively rare in nature in their native form. Magnetic minerals are much more interesting and of major importance to an understanding of crustal magnetism are: iron alloys, mainly the Fe-Ti spinel group (magnetite and titanomagnetite), titanohematites, some iron sulfides (monoclinic pyrrhotite) and oxyhydroxides (goethite). These minerals can possess remanent (permanent) or induced (in response to an inducing field) magnetizations. Induced magnetization is, to first order, proportional to and parallel to the direction of the present field, and varies spatially (Clark, 1997). Magnetic remanence, on the other hand, while also correlated with titanomagnetite content, is strongly dependent on the grain size, shape, and micro-structure of the magnetic minerals. Such minerals are capable of bearing both remanent and induced magnetization. The relative importance of the induced $\vec{M}_i$ to the remanent $\vec{M}_r$ contribution is given by the *Koenigsberger ratio* (Q) . The proportionality of induced magnetization with the inducing magnetic field, assumed to be the main field, is expressed through χ, the magnetic susceptibility, which mainly depends on the magnetic mineralogy. The relation between the remanent and the original (i.e. the one that gave the minerals their remanence) depends of several factors, including the Curie Temperature. This is the temperature at which magnetic minerals loose their remanent magnetization. The Curie temperature of magnetite and hematite, the most commonly found terrestrial magnetic minerals, is 580°C and 670°C, respectively. On the other hand, remanent magnetization arises from permanent alignment of magnetic moments in ferromagnetic material from rocks, either at the time of formation (when an igneous rock cools or a sedimentary rock compacts) or when the last major modification (metamorphic heating and cooling, chemical alteration) took place. It is proportional with the ambient field at that time. Consequently, the total magnetization, $\vec{M}$, usually points in a direction that is different from both, the current and the ancient field.

The known planets present very different lithospheric magnetic fields in amplitude, lengthscale and in their magnetic signature, remanent or induced. Large impacts, associated with destructive effects, as well as those associated with volcanoes or subduction zones can both magnetize and demagnetize rocks, through thermal, pressure or fracturing/brecciation processes. For these reasons, impacts have been recognized as a major modifying tool of a planet, their magnetic signature depending on whether they were formed while a core dynamo was active or not. The pre-impact magnetization (if any) can be modified through mainly three processes. First, due to a great excavation area, material is removed and spread away around the crater (Croft, 1985). Second, the shock wave associated with the impact generates high pressures, which may demagnetize ma-

terial, depending on the mineral magnetic coercivity. Such high pressures are also associated with local (re)magnetization processes (Gattacceca et al., 2008). At last, thermal effects are also possible, which demagnetize (and possibly remagnetize in the presence of a magnetic field) those minerals which have a Curie temperature lower than the high temperatures associated with impacts. New minerals can form and acquire a magnetic remanence. Finally, impacts can cause plasmas, which may generate transient and very intense magnetic fields (Crawford and Schultz, 1999).

Earth's lithospheric magnetic field. The Earth's outer core is surrounded by the solid mantle with temperatures between $100°C$ at the upper boundary and about $3500°C$ at the CMB, clearly above the Curie temperature of the mantle material. Hence, no remanent magnetism can persist at this depths. Contrary, the very outer layer of the Earth, known as lithosphere, is rather cool, has thickness of $5-20\ km$ below the oceans and $30-50\ km$ underneath the continents and is characterized by temperatures allowing magnetic field to remain in the material. The total magnetization is $\vec{M} = \vec{M}_i + \vec{M}_r$. When $Q \gg 1$, such as for ocean basalts, $\vec{M}$ is essentially the same as $\vec{M}_r$. The importance of remanent magnetization in oceanic rocks is connected with the identification of "magnetic strips" on the ocean floor and their interpretation in terms of new crust being generated at mid-ocean ridges in an alternating normal to reversed polarity main field. In contrast, for $Q \ll 1$, meaning a material containing coarse magnetite grains, typically has high susceptibility and weak remanent magnetization, and $\vec{M}$ is close to $\vec{M}_i$. This situation is characteristic over continents, especially in cratonic shield area. However, this approximation can be locally wrong, for example in continental volcanic areas where hydrometamorphic processes might change the magnetic properties of the rocks.

The lithospheric magnetic field (magnetization carried by rocks in the crust and upper mantle with temperatures below the Curie point) has mostly small spatial wavelengths, but can reach anomalies of several thousand nT. Prominent examples are the Bangui anomaly in Central Africa, the Beattie anomaly in South Africa or the Kursk anomaly in Russia, where the huge enhancement is due to a large iron ore, up to $200,000\ nT$ near Kursk (Jankowski and Sucksdorff, 1996), but it decreases very fast as the distance to the source increases.

Mars' lithospheric magnetic field. Mars, today, reveals an astonishing feature (dichotomy) with an evidence of strong crustal magnetizations in the southern hemisphere. Very strong magnetic anomalies reaching $\pm 1500\ nT$ at $200\ km$ altitude were observed there in a rather wide area. Moreover, the anomalies appear as zones of alternating polarity. They are elongated in the East-West direction, reminiscent of the

anomalies associated with sea-floor spreading on the Earth. However, they are quite different: the anomaly bands are much wider (typically 200 km) and their remanence intensity much higher (assuming the same layer thickness of $20-30$ km) than the typical oceanic anomalies on the Earth. At 400 km altitude, Mars crustal fields are estimated to range between ± 200 nT.

Mars, currently, has no global magnetic field of internal origin, but must have had one in the past, in the planet's early history, when the crust acquired intense magnetization (thermoremanent magnetization) by cooling in the presence of the Earth-like magnetic field (Acuña et al., 1999). The absence of magnetic field above the largest recognized impact structures has been interpreted as the proof that the core dynamo had already stopped at the time when these impacts took place. The demagnetization signatures of giant basins, associated with subsequent volcanism, smaller impacts or hydrothermal chemical alteration (implying chemical remanent magnetization) inside or near the basins, have modified the crustal magnetization of Mars, to produce the current status.

Moon's lithospheric magnetic field. As Mars, Moon has no core-generated magnetic field but a possible frozen lunar core. This hypothesis is consistent with recent lunar sample and meteoritic work implying that dynamos within planetesimals were common in the early solar system (Garrick-Bethell et al., 2009; Weiss et al., 2009). The lunar remanent magnetic field of lithospheric origin is very weak, reaching only 10 nT at 37 km altitude. The distribution is heterogeneous and the most intense anomalies are located at the antipodes of the largest impact basins. This suggests that the magnetic anomalies are linked to impact process, in which ejecta would deposit at the antipodes in the presence of an impact-amplified magnetic field. The observed linear features reveal a series of eruptions and lava solidifications on the surface. This would mean that an inducing field had to be present during the period of these basalts emplacement, which is about 3.5 Gy. How the crust of Mars and Moon acquired their magnetic imprint, is a matter of great interest, with implication in crustal formation and thermal evolution of them.

2.2 Measuring magnetic fields

The thesis takes advantage from scientific activities linked to measuring the geomagnetic field and to improving these measurements to international standards, at the Surlari observatory. The author's efforts, on national and international scales, are somehow summarized here, as a provider of reliable, high-accuracy, high-resolution magnetic data, which is crucial in understanding magnetic fields, and their spatial and/or temporal

variations.

Indeed, magnetic observations are the prerequisites to describe the magnetic field of a terrestrial body and to understand the processes generating it. Relative to other planets, the amount of data available for studying the Earth's magnetic field is very large. For these kind of studies, the data available, can be provided by observatories, repeat stations, marine and aeromagnetic surveys and satellites. For Mars and Moon we deal with data obtained only from satellites, observing their magnetic field from low orbits. Magnetic measurements from any platform give the sum of all contributions from the sources, internal and external, of the planet observed. A straightforward separation of individual sources is impossible. Data quality, documentation and availability become key requirements for a better description of all magnetic field contributions and their temporal variations. Magnetic fields measured from the spacecraft are various, different in nature, comparing with those associated with magnetic data provided by observatories (Turner et al., 2007). For example, vector magnetometers on board of spacecraft have a temperature drift, and thus, depend of the position of the satellite with respect to the Sun.

2.2.1 Earth's magnetic field observation

As it was already noted in *Chapter 1*, measuring the Earth's magnetic field components has started since the 16^{th} century, first only the declination, thereafter inclination and finally the full field vector. It is one of the oldest observable Earth's properties. In the last century, it has become more systematic and kept improving, due to common standards and global data availability. Geomagnetic measurements are performed in many ways and at various platforms. A network of ground-based geomagnetic observatories was set up since the early 19^{th} century. *Geomagnetic observatories* provide the best quality data but at low spatial resolution. To increase the density regionally, *repeat stations* are conducted by many nations as well as *marine and aeromagnetic surveys*, mainly dedicated to map in detail the lithospheric magnetic field. Finally, *satellites* offer a uniform and global coverage with abundant data sets. They all open a new era of magnetic modeling above planetary bodies' surface since the last decade, as an important complement to the consistency and accuracy of the data, obtained from satellite carrying instruments. In this chapter, all types of magnetic measurements platforms and most modern used instruments are presented. An overview of their distribution and data output, underlining the accuracy of each kind of data and their associated errors is given using ideas and texts from two co-authored papers Mandea and **Isac, A.** (2011) and Reda et al. (2011). These available magnetic vector and scalar data sets are the basis for different models which are developed for different purposes: some of them are based on both satellite and ground

data, some are based only on observatory data (as for some of the Earth's magnetic field models), some others are based only on satellite data (such as those for Mars and Moon).

Ground measurements

Magnetic observatories. A geomagnetic observatory is a place where the geomagnetic field has to be monitored accurately and continuously over a long time. Changes in the magnetic properties of the observatory area and the neighborhood are not favorable and acceptable. For that reason, the choice of the site is of great importance, far away from artificial magnetic signals, as well as from magnetic irregularities caused by local geological structures. The comprehensive information about how to organize, run a magnetic observatory and make magnetic measurements are given by (Jankowski and Sucksdorff, 1996). The World Data Centers (WDC), inaugurated with the International Geophysical Year in 1957−1958, are still the prime repositories for most national magnetic records. Now, besides archiving and distributing geomagnetic records, individual centers perform a great number of other services, such as producing indices or converting the geomagnetic data to application formats for an easy digestion and collating related solar-terrestrial phenomena. An overview of the most common indices used in geomagnetism can be found in Campbell (1997) and Langel and Hinze (1998). An important service, provided by INTERMAGNET (INTERnational MAGnetic NETwork), is the distribution of the preliminary data in near-real time via its website. Today, about 176 observatories produce 1 *minute* data but only 128 are $IMO's$ (Love, 2008), in the frame of the global network of digital magnetic observatories [1]. Surlari is one of the 14 European observatories transmitting its data in near-real time, since *March* 2009. This Quick-Look geomagnetic field data are only for monitoring and forecasting purposes, because they are not visually checked or corrected for artificial noises (Linthe et al., 2012). Although the number of observatories participating in INTERMAGNET programme is increasing continuously in the last decades, their geographical distribution is far from an optimal one. There are vast areas without observatories but, some national efforts have been done in order to install new low costs observatories in remote locations, as in oceanic islands or Antarctica. Dramatic efforts have been done by GFZ German Research Centre for Geosciences Potsdam, involved in installing or up-grading a large number of magnetic observatories over the last years. Examples are the observatories from Azores, St. Helena islands or Namibia (in order to fill these gaps) and Surlari, Panaghyuriste, Hayderabad or Vassouras and Trelew – inside of the South Atlantic anomaly (in order to update these old and reliable observatories to present INTERMAGNET standards).

[1] www.intermagnet.org

Repeat station measurements. A repeat station is a place where accurate measurements of the geomagnetic field components are made at regular time intervals, of order of two to five years. The site are marked by means of a non-magnetic pillar or a buried tile observations and located in a remote place where man-made contamination is negligible. Most countries have established and measured periodically their own repeat network. The goal is to describe how the magnetic field varies over national territory. On a global scale, the *IAGA Working Group V-MOD* sets standards for magnetic repeat station surveys and maintain a catalog of submitted measurements to World Data Centers (Newitt et al., 2009).

Details of measurements procedures and instrumentation are given by Newitt et al. (1996) and Korepanov et al. (2007). There are significant gaps over the Earth's surface such as large parts of South America, Africa and Asia (Korte et al., 2007). Even in Europe, where an European body dealing with magnetic network of repeat stations has had a central role over the last decade, some national repeat station networks are no longer active. One of the main objectives of *MagNetE* was the preparation of an European magnetic declination map at epoch 2006 [2]. This map is obtained from measurements done in Europe, in 369 repeat stations and 41 geomagnetic observatories, between $2006-2007$, in more than 20 European countries (Duma, 2010). Surlari observatory and Romania, respectively, belong to this constellation.

Marine and airborne surveys. Over oceanic area, representing about 70% of the Earth's whole surface, magnetic measurements can be obtained, however, in a different way from the ground-based ones. These observations, made either as magnetic measurements along ship tracks or from underwater autonomous vehicles, are the only way to study the magnetic signals over oceans and seas, at local or regional scale. These signals are connected with the remanent magnetization carried by the newly formed crust at mid-oceanic ridges. Airborne magnetic surveys have been commonly used for a detailed mapping of the lithospheric magnetic field in view of mineral exploration or for studying regional crustal structures. Usually, they provide only scalar measurements. Nowadays, high-level vector data are collected. Many kinds of magnetometers are used, as well as for observatories, and indicated by Hamoudi et al. (2011). They can be mounted on board fixed-aircrafts, on the boom of helicopters, or on balloons. The processing of such surveys is rather complicated, due to the difficulties of the accurate orientation of the sensor on a moving platform and due to the lack of a nearby observatory monitoring the external field variations. Additionally, data are owned by private companies and often not available. The released data are mainly owned by governmental agencies.

[2] $http://ccgm.free.fr/MagNetEurope\_UK\_b.html$

Instrumentation and Data quality. Generally, a geomagnetic observatory procedure involves absolute measurements that are sufficient in number to monitor instrumental drift of vector magnetometers, which give variation measurements of the three field components, in arbitrary units. Measurements obtained by scalar magnetometers and flux-gate theodolites are considered *absolute measurements*, while they depend only on the knowledge of a physical constant and on the accuracy by which the constant is measured.

A *scalar measurement* of the strength of the magnetic field is obtained commonly by a proton magnetometer. In a proton precession magnetometer the universal physical constant is the gyromagnetic ratio of the proton (42.58 MHz/T) and the basic unit is time (inverse of frequency). The measurements achieved with such an instruments have a great accuracy (in excess of 10 *ppm*). Another *absolute measurement* of the direction of the geomagnetic field, by measuring the angle I (inclination) and the angle D (declination) is made with a fluxgate theodolite (DI-Flux) which consists of a non-magnetic theodolite and a single-axis fluxgate sensor, mounted on top of a telescope and requires manual operation. In a land-based observatory, such absolute measurements are typically made once/twice a week and are used to monitor the drift of the fluxgate variometers (Reda et al., 2011). They are crucial to determine the level of variation of variometers (the base-lines).

A *vector measurement* is made with a triaxial fluxgate magnetometer and operates with minimal manual intervention. These instruments require temperature-controlled environments and installation on extremely stable platforms if they are not suspended and therefore compensate for platform tilt. Even with these precautions they can still be subject of drift arising from sources both within the instrument: the temperature effects and the stability of the instrument mounting also. These measurements are not absolute, they are referred to as variation measurements, the instruments are known as variometers and they have to be calibrated against standard instruments. One of the most widely used variometers is the FGE fluxgate manufactured by the Danish Technical University, Denmark. In order to improve long-term stability sensors have compensation coils wound on quartz tubes, resulting in a sensor drift of only a few nT per year.

Automatic observatories that reach the standards for geomagnetic observatories, as demanded by INTERMAGNET (St-Louis, 2008) would be a major breakthrough for geomagnetic measurements and a true global coverage, especially in remote areas. Currently, several attempts have been made to operate absolute vector field instruments automatically: a DI-theodolite automatisation (Van Loo and Rasson, 2006; Rasson et al., 2009) or a proton vector magnetometer (Auster et al., 2006), for discrete absolute measurements. Efforts have been done to develop a Geomagnetic AUtomated SyStem (GAUSS) instru-

ment based on rotating a three component fluxgate magnetometer about well-known axes (Auster et al., 2007), and now mounted in Niemegk magnetic observatory, Germany. The new system aims to be a reliable working automated absolute geomagnetic instrument worldwide in the near future.

The highest quality is ensured for data produced by observatories. They have to demonstrate the compliance of their data with the standards set up by the INTERMAGNET, in order to be accepted. Once in the network, the definitive data are reviewed carefully by a committee of experts before being published on the organization web site. The collected data are classified into three categories: *reported data* which are row data provided by variometers, *adjusted data* that have been preliminary cleaned (i.e. spikes and jumps have been removed) and *definitive data*, the adjusted data to which baseline values have been added. An INTERMAGNET member observatory has to meet the following requirements: 1 nT resolution, a 5 s sampling rate, thermal stability 0.25 $nT/°C$, long term stability 5 $nT/year$, accuracy ± 10 nT for 95% of reported data and ± 5 nT for definitive data, for field values measured with a vector magnetometer. Finally, the weekly determinations of the baseline values by absolute measurements have to include the determination of all systematic errors and have to be performed manually. In this case, the accuracy must be better than 1 nT for magnetic components and better than $0.1'$ for angular elements (Newitt et al., 1996). Thus, the quality of the measurement results depends strongly on the experience and accuracy of the observer and on regular absolute measurements. Recently, INTERMAGNET has embarked on the definition and the distribution of two new data products: 1 Hz data and quasi-definitive data. The need of 1 Hz data emerged in the early $2000's$ from the geomagnetic community to study rapid external variations such as Sudden Impulses (SI) or Storm Sudden Commencements (SSC) (McPherron, 1991; Mc Pherron et al., 2009). It is expected that the 1 Hz data to be useful for modeling ionospheric or magnetospheric magnetic fields, from a combination of ground and low-Earth orbiting satellite data, as in the case of forthcoming Swarm mission. Ideally, the quality and the accuracy of repeat station data should be comparable with those obtained at geomagnetic observatories. However, the errors, due to the measurement operation themselves, temperature changes, imperfect reduction or crustal or external magnetic fields contamination, contribute to consider as a more realistic total error of about 5 nT in the components and about $0.5 - 1'$ in inclination and declination. Regarding the quality of data of marine and airborne surveys, it is strongly influenced by the errors associated with: the ship or aircraft position and its magnetic noise, external and core field estimations, time precision, etc. For example, most of the old marine data were corrected for external field variations only recently (Sabaka et al., 2004). With the significant improvements in aeromagnetic and marine survey instrumentation (Luis and

Miranda, 2008) and high precision GPSs (less than 1 m), the total error of the recent marine and aeromagnetic data is less 1 nT.

Satellite measurements

Geomagnetic measurements, on board of artificial satellites, have become the needed solution to get a uniformly and globally data distribution. Magnetic satellite measurements are more complex and different in several aspects from the magnetic measurements obtained on ground. A low-orbit satellite moves with a velocity of about 8 kms^{-1} and, for this reason, it is difficult to decide if magnetic field variations are due to a temporal or to a spatial change. Moreover, the satellite orbits span different altitudes, which have different advantages and disadvantages. For example, for a good resolution of small-scale features of the crustal field, a lower altitude is preferred. In this case, the atmospheric drag is higher causing a satellite to lose the altitude faster. This shortens the mission lifetime dramatically. The effect of ionospheric currents should also be considered. It is preferable to orbit at an altitude which has a minimum of currents and this also favors a not too low altitude. In plus, the altitude of the spacecraft works as a spatially low-pass-filter, for an similar area on the Earth. As a consequence, the effect of local magnetic heterogeneities is reduced. One of another advantage is that satellites are generally launched in a near-polar orbit (to map the entire planet, excepting a small polar gap) and take observations with the same magnetometers to provide data with uniform quality. A good coverage requires sampling the field in all longitudes. The coverage is limited by orbital period compared to the rotation period of the planet. If the satellite completes an integer number of orbits in 24 hours, it would have the same surface of the Earth tracked day by day. This repeat track state can not be avoided totally as the orbital period of satellites is changing with time. Their period, from time to time, might be in near resonance with Earth's rotation period, keeping the satellite temporarily into a near repeated track state. A good coverage also means sampling the field at different local times. If only one local time is sampled, contributions from ionospheric currents, which are highly local-time dependent, appear constant. This makes it difficult to isolate the ionospheric contribution from other contributions.

The magnetic satellites are equipped with a $4 - 8$ meters-long boom carrying the magnetic field instruments, to avoid the contamination of measurements by magnetic noise from the spacecraft fields. The strength of the magnetic field in space is recorded with scalar magnetometers. Such absolute instrument is the known proton precession magnetometer, in particular the Overhauser instrument, which measures the magnetic field intensity with an accuracy better than 0.5 nT. It is mounted on the top of the boom. At a distance of few meters from satellite body is mounted the fluxgate vector

magnetometer. It samples the magnetic field at $16 - 100\ Hz$ with a resolution of $0.1\ nT$ and it is calibrated in-orbit, using the field intensity measured by the proton precession magnetometer. The severest problem, in satellite magnetic measurements of the vector field, is the determination of the absolute orientation. Their orientation in space, so their attitude, are determined accurately by star imagers. The method to determine the attitude requires models of the star constellation and models of the ambient magnetic field. First ones can be found in astronomical catalogs, and the second ones have to be estimated. This is an additional calibration step, called *data alignment* (Acuña, 2002). One can say that the controlling factor of the accuracy of data is not the magnetometer error, but error in the orientation. Errors in the angle of $1'$ and $1''$ correspond to $0.03\%(15\ nT)$ and $15\ ppm(0.25\ nT)$, respectively. Instrumental accuracy of this level is easily reached by most magnetometers (Mandea and **Isac, A.**, 2011). In order to get good quality data, it is important to know the exact time and location of each measurement. For this reason the GPS systems offer a precise determination of time (with a timing error of $5\ ms$) and position (with an accuracy better than a couple of meters). The contribution of position, orientation and timing errors to the overall magnetic error budget is below $1\ nT$. Thus there are many other parameters to consider when designing a satellite mission dedicated to measure the magnetic field. How the parameters are optimized depends of the main objectives of the mission itself.

Magnetic missions. The earlier satellites have measured only total field intensity, which was not ideal for the purpose of the main-field analysis because of the non-uniqueness problem, called Backus effect (Khokhlov et al., 1999). The first in-space measurements were taken by *Sputnik* 3 satellite in 1958 (Dolginov et al., 1962). In 1964, *Cosmos* 26 and *Cosmos* 49 were of much poorer quality. Next, I concentrate on satellite missions measuring high-precision data that have been used for modeling the geomagnetic field. The data of most of these satellites are available [3].

The U.S. *Polar Orbiting Geophysical Observatories* (POGO) were the first satellites which globally measured the Earth's magnetic field between $1965 - 1971$. The POGO series consists of six satellites but, only three of them flew at sufficient low altitudes $(410 - 1510\ km)$ to be of interest in modeling the geomagnetic field. They were equipped with optically pumped rubidium vapor absolute magnetometers. Intrinsic measurement errors of all three satellites is believe to be less $1\ nT$, but due to position uncertainty, results an effective magnetic error up to $7\ nT$ (Cain, 2007).

The U.S. *MAGSAT* (Oct 1979 to June 1980) made the first precise and globally distributed vector measurements of the magnetic field. Despite its short duration, the

[3] www.space.dtu.dk/English/Research/Scientific_data_Magnetic.aspx

mission was successful and next magnetic satellites were equipped as well with vector and scalar magnetometers, with a good internal consistency between these measurements. The satellite was in near-polar orbit (97°) and the mean orbit altitude decreased from about 450 km to about 350 km at the end of the mission. The satellite carried a *Cesium* 133 vapor optically pumped scalar magnetometer and a triaxial fluxgate magnetometer measuring the field at 16 Hz with a resolution of 0.5 nT. Altitude errors have limited vector data accuracy to 4 nT (Purucker, 2007).

Some 20 years after MAGSAT, in 1999, the Danish *Ørsted* satellite was launched. It is still flying in a gravity gradient stabilized configuration between $650 - 860$ km, at an average altitude of 760 km, in a near-polar orbit (96.5°), (Olsen et al., 2005). The absolute magnetometer of Overhauser type measured the total field with a sampling rate of 1 Hz and an accuracy of 0.5 nT. The attitude was determined by a star camera placed next to it. The vector magnetometer, a fluxgate, measured the field with a resolution of 0.1 nT. Currently, only the scalar magnetometer provided magnetic measurements. The accuracy of the vector data was limited by the star imager accuracy. However, the total accuracy is believed to be better than 2 nT for two of the three vector components. Unfortunately, the availability of high-accuracy vector data was limited until 2005, due to thermal problems or due to the blinding of the instrument by the Sun, Moon or Earth (Neubert et al., 2001; Olsen, 2007). Even the reduction of errors for the Ørsted satellite are due to the huge improvements in the orientation techniques (use of star sensor, etc.), considering the high satellite orbit, the smaller structures of the geomagnetic field were hardly solved.

The German *CHAllenging Minisatellite Payload* (CHAMP) satellite was launched on July 15, 2000 onto almost-circular, near-polar orbit (87.3°) with an initial altitude of 454 km, which has decreased to about 350 km by the end of 2006 (Maus et al., 2005a). After 10 years of measurements, it entered in the Earth's atmosphere on 19^{th} September, 2010. Instrumentation was very similar to that of Ørsted and the specific instruments for measuring the magnetic field are situated on the 4 m boom, far from the satellite body and its magnetic disturbances (Mandea and Purucker, 2005; Mandea and **Isac, A.**, 2011). The two fluxgate sensors are placed halfway down the boom, (close to two star cameras, in order to have precise sensor attitude) and sample with 50 Hz at an accuracy better than 0.5 nT, when attitude is measured by both star imager heads (which happens for more than 60% of time). Otherwise, an accuracy better than 2 nT, as for Ørsted is achieved (Maus et al., 2007). The scalar magnetometer, placed at the top of the boom, samples the field at 1 Hz with an accuracy similar to that of Ørsted (< 0.5 nT). Data are available at the official CHAMP web site [4].

[4] http://www.gfz-potsdam.de/pb1/op/champ/

The Argentinian satellite *SAC-C* was launched in November 2000. It has an altitude of about 712 km, and an instrumentation similar to that of Ørsted. Due to technical problems since the launch, it is no use of vector data. Some problems also occur with the scalar magnetometer which is not isotropic (the field values measured depend on the direction of the magnetometer with respect to the ambient field). Part of this effect can be corrected, but still, the *SAC-C* data have an error of about $0.5 - 1.5$ nT, which is higher than estimated errors for Ørsted and CHAMP data.

The *Swarm* constellation mission, was selected by the European Space Agency (ESA) in 2004, to provide the best-ever survey of the geomagnetic field and its temporal evolution (Olsen et al., 2006a). Scheduled for launch in 2013, the mission comprises a constellation of three identical satellites, with two spacecrafts, flying side by side, at lower altitude (450 km initial altitude) with a separation in longitude of about about 150 km at the equator, thereby measuring the E-W gradient of the magnetic field. The third satellite is planed at higher altitude (530 km) and in a different local time. Each satellite has both scalar and vector magnetometers, and no less than three star imagers for attitude determination. Improvements in the instrumentation means that Swarm is expected to be able to measure with an accuracy three to ten times better than that of the past or present missions (Friis-Christensen et al., 2006). Additional informations about the Swarm mission can be found at ESA's websites [5] [6].

2.2.2 Mars' magnetic field observation

The exploration of planet Mars began in 1960 with the launch of two Soviet probes (*Marsnik* 1 and *Marsnik* 2) that failed shortly after launch. The first successful mission to Mars was the USA's *Mariner* 4 spacecraft, in 1965. It approached to within 4 Mars radii of the planet, but did not detect anything but a bow shock (Smith et al., 1965). Despite numerous opportunities over the next 32 years, no space probe instrumented to measure magnetic fields would pass close enough to the planet's surface to establish the presence of an intrinsic magnetic field. Estimates of a Mars dipole ranged from 0.8 to $2.55 \cdot 10^{18}$ nTm^3, equivalent to an equatorial surface field of 20 to 65 nT, but its nature and origin was highly debated (Ness, 1979). The controversy did not end until *Mars Global Surveyor* (MGS) entered on Mars orbit in September, 1997. MGS was instrumented with a magnetometer and electron reflectometer experiment. Two triaxial fluxgate magnetometers were mounted at the outer extremity of the solar array panels and an electron reflectometer was mounted on the spacecraft body. A detailed description of the instrumentation is given in Albee et al. (2001) and a discussion of the

[5] http://spacecenter.dk/projects/swarm/index.html
[6] http://www.esa.int/esaLP/LPswarm.html

MGS spacecraft, spacecraft magnetic field mitigation and early results are given in Acuña et al. (2001) and Connerney et al. (2005). The MGS mission was designed to recover a subset of the science objectives of the Mars Observer Mission (MOM), which ended in August 1993, with an unsuccessful orbit insertion maneuver. To save fuel, MGS was designed to achieve its high inclination for a circular mapping orbit at 400 km altitude by aerobraking in the Mars atmosphere. As a result of a spacecraft anomaly experienced early in the mission, MGS used many more drag passes than was originally intended to slow the spacecraft. This unanticipated development allowed a far greater sampling of the magnetic field well below the nominal 400 km mapping phase altitude. The mapping orbits (MO) observations began in March 1999 and continued until November 2006 at which time, the spacecraft was lost after a series of errors, that left its battery depleted and the spacecraft unable to maintain attitude.

2.2.3 Moon's magnetic field observation

Magnetic fields of near-lunar space and of the lunar surface were firstly measured in the $1970's$ during the initial US-Soviet exploration of the Moon. Early measurements, with instruments on board of *Apollo* 15, showed that the Moon has no global, core-generated magnetic field. Magnetometers were carried on both US and Soviet landed vehicles too, and measured fields show values of up to several hundred nT and more. The polar-orbiting LP, *Lunar Prospector* (Binder, 1998) provided the first global mapping of the lunar magnetic field. The spacecraft flows at low altitude ($11 - 66$ km, 30 km average altitude) in 1998 and 1999. Both electron reflectometer (Mitchell et al., 2008) and triaxial fluxgate magnetometer (Hood and Zakharian, 2001) provided magnetic data used for mapping. The electron reflectometer (ER) employs a remote sensing approach, to place bounds on the magnitude of the magnetic field at the surface, while the magnetometer measures the direction and strength of the vector magnetic field, at the satellite altitude. The low-noise (6 pT rms) fluxgate magnetometers were mounted on a 2.5 m boom of the spin-stabilized Lunar Prospector spacecraft (nominal spin rate 12 rpm), in order to minimize spacecraft influences. The triaxial fluxgate magnetometer were similar in design to the instrument used on Mars Global Surveyor. It measured the magnetic field amplitude and direction, at spacecraft altitude, with a spatial resolution of about 100 km when ambient plasma wind disturbances were minimal. The ER measured field strengths as small as 0.1 nT with a spatial accuracy of about 3 km at the lunar surface. Lunar Prospector was followed in 2007 by the Japanese SELENE/Kaguya satellite, which mapped the magnetic fields, at an altitude of 100 km, for a year and eight months, utilizing a triaxial fluxgate magnetometer, LMAG (Matsushima et al., 2010; Takahashi et al., 2009). The results will be available to scientists in 2013.

When measuring Mars and Moon magnetic fields from satellite there are numerous potential errors, as well as when, generally, a magnetic field is measured from the near-space of a planet. These errors, the same when magnetic field is observed around Earth, include instruments errors, position, time and attitude errors, digitization and transmission errors, and errors due to the spacecraft fields. The absolute instrument error is determined on Earth before launch. For a high-quality instrument, the error must be time independent end provide uncorrelated measurements. Once in space, especially vector instruments have a slight temperature dependence which can cause a serial correlation of errors. Also errors in position or time could create large correlated errors. However, with the GPS accuracy, they can be considered negligible. Attitude errors are not negligible. Occasionally, star imagers are not able to determine the attitude if they are blinded by stars or by the Sun. They can cause error correlation between different vector components of a single measurement. This problem was solved having two or three star imagers, pointing in different directions. Errors from spacecraft were reduced as better as new non-magnetic technology was developed. Bottom of the line, the total accuracy of satellite measurements for Earth, Mars and Moon are comparable with the accuracy of the ground measurements or aeromagnetic surveys, detailed above.

The interest in measuring the magnetic fields, mainly for the Earth, and the author's participation in some international efforts to define and explain the measuring techniques and data quality are reflected in two reviewed publications, their titles being included in the appendix of this thesis.

2.3 Magnetic field variations: mathematical basis

Modeling the magnetic field means describing its shape and its time evolution with different techniques and with different mathematical tools. The magnetic field is measured on a discrete basis. Depending of the available data and processing methods, these models can be global or regional, static or time dependent. Of course, one obvious possibility is to bin and average measurements on regular grids, but a more powerful technique consists in building a continuous description of the field on the surface of a sphere. Exploiting the potential theory, magnetic measurements at the surface of the Earth or at the altitude of orbiting satellites for Earth, Mars and Moon, can be used to separate internal and external magnetic field contributions, with respect to measurement positions.

One of the most used technique to describe the spatial variations, the size and the shape of a planetary magnetic field, relies on spherical harmonics analysis. For magnetic field temporal behavior the B-splines are generally used in time-dependent models. A review of technique development can be also found in Langel (1987) and Merrill et al.

(1996).

For applying one technique or another, the main task is to perform an inverse problem and, for this reason, a brief description is useful at this stage. Thereafter, the mostly used global techniques are described, with a resume of the used techniques to describe spatial and temporal variation of the geomagnetic field.

2.3.1 Spatial variations: modeling global magnetic field

The inverse problem

To obtain the model parameters, an *inverse problem* needs to be solved. The standard techniques and nomenclature of linear inverse problem is presented. The starting place of any inverse problem is a description of a given data, derived from measurements. The data can be assembled in a data vector d of length N as $\mathbf{d}^T = (d_1, d_2, ...d_N)$. A model can be described by a set of P parameters assembled in a model vector of length P as $\mathbf{m}^T = (m_1, m_2, ...m_P)$. The basic assumption is that the data depend on model parameters, $\mathbf{d}^T = A(m)$, and considering a linear relationship, that dependency may be written in the matrix form as $\mathbf{d}^T = \mathbf{Am}$, where $\mathbf{A}$ is a $N \times P$ matrix of coefficients that are independent of data and model.

In the case of modeling magnetic fields with spherical harmonics for example, $\mathbf{A}$ contains P base functions evaluated at N data positions. $\mathbf{m}$ then comprises the Gauss coefficients and $\mathbf{d}$ the data to be described, e.g. the vertical component of the Earth's magnetic field at those N locations. If all P lines are included, the conditions equations are

$$d_i = \sum_{j=1}^{P} A_{ij} m_j \tag{2.3}$$

Usually, one has more data available than parameters to be resolved, which means $N > P$. In this case, the above equation cannot be satisfied for every i (assumed that the data are defective). The inverse problem has no exact solution and it is *overdetermined*. Hence, model parameters are sought such that equation $\mathbf{d}^T = \mathbf{Am}$ is solved approximately. The *least squares* method minimizes the sum of the squares of the errors and thus finds the "best" approximate solution. The misfit between data and model prediction is

$$e_i = d_i - \sum_{j=1}^{P} A_{ij} m_j \tag{2.4}$$

from where we gain an expression for the sum of squares of these misfits as

$$E^2 = \sum_{i=1}^{N} e_i^2 = \sum_{i=1}^{N} \left(d_i - \sum_{j=1}^{P} A_{ij} m_j \right)^2 \tag{2.5}$$

The goal is to obtain the parameter set where E^2 is minimal, so $\partial E^2 / \partial m_k = 0$ is imposed and the equation 2.5 become

$$2 \sum_{i=1}^{N} [d_i - \sum_{j=1}^{P} A_{ij} m_j](-A_{ik}) = 0 \tag{2.6}$$

or

$$\sum_{i=1}^{N} \sum_{j=1}^{P} A_{ij} A_{ik} m_j = \sum_{i=1}^{D} A_{ik} d_i \tag{2.7}$$

Expressed in matrix notation, this equation is written:

$$A^T A m = A^T d \tag{2.8}$$

Data can be affected by different error sources (see *Part I, Section 2.2*) and these errors sources can even be correlated. The *covariance matrix* $\mathbf{C}$ is introduced to account for this correlation. Generally, it is defined for two random variables by

$$\mathbf{C}(X, Y) = \varepsilon[(x - \varepsilon(x))(y - \varepsilon(y))] \tag{2.9}$$

where $\varepsilon(x)$ is the expected value of the variable x. For uncorrelated data, the covariance matrix is diagonal. In practice, it is not always easy to define what is the expected value $\varepsilon(x)$ but if it is chosen properly, the covariance matrix divides each row and datum by its variance:

$$E^2 = (\mathbf{d} - \mathbf{Am})^T \mathbf{C}^{-1} (\mathbf{d} - \mathbf{Am}) \tag{2.10}$$

Inverse problems are usually *ill-posed*: small deviations in the data can lead to considerable changes in the parameters. The error amplification must be mitigated by appropriate measures in the solution process: inverse problems can be regularized by introducing additional summands on the left-hand side of equation 2.10.

Spherical harmonics analysis

Spherical Harmonics (SH) form the natural basis to describe a potential field on a spherical surface because they are the same functions of the Laplacian in spherical geometry. They form the smallest set of functions that can describe all possible potential fields up to a given wavelength. If a magnetic field is described in term of spherical harmonics, the separation of the field due to inner sources (internal dynamo or magnetized rocks), from those due to external sources (far magnetospheric field for satellite measurements or ionospheric and magnetospheric field for ground measurements) can be separated. In planetary magnetism, the Schmidt semi-normalized spherical harmonics are commonly used.

To describe the magnetic field of the Earth, Maxwell's equations offer a good starting point. In the following, the Earth is chosen as a typical and complex planetary field, in order to describe the way the SH approach is applied. So, for the Earth's case, the two Maxwell's equations relating to the magnetic field can be written:

$$\nabla \times \vec{H} = \vec{J} + \frac{\partial \vec{D}}{\partial t} \tag{2.11}$$

$$\nabla \cdot \vec{B} = 0 \tag{2.12}$$

where $\vec{H}$ is the magnetic field, $\vec{B}$ is the magnetic induction, $\vec{J}$ is the current density, and $\partial\vec{D}/\partial t$ is the electric displacement current density. Considering the steady state, the magnetic field is generated by currents and all magnetic fields are source free. In a region that does not contain sources of magnetic field (from the Earth's surface up to about 50 km), it is reasonable to assume that $\vec{J} = 0$ so the field is curl-free, $\partial\vec{D}/\partial t = 0$. It is known that $\vec{B} = \mu_0\vec{H}$ above the Earth's surface (where the magnetic permeability in free-space, $\mu_0 = 4\pi \times 10^{-7} H \cdot m^{-1}$). However, in the following, the standard agreed notation for the magnetic field $\vec{B}$ is used. It can be written $\nabla \times \vec{B} = 0$, meaning that the vector field is conservative in the region of interest, and the magnetic field $\vec{B}$ can be expressed as $\vec{B} = -\vec{\nabla}V$, where V is a scalar potential. Generally, it follows that $\nabla \cdot \vec{B} = 0$, where V has to satisfy Laplace's equation:

$$\nabla^2 V = 0 \tag{2.13}$$

Thus the Earth's magnetic field can be described as the negative gradient of a scalar potential that satisfies the Laplace equation in current-free regions outside the Earth. To solve this differential equation, it is convenient to work in geocentric spherical coordinates (r, θ, ϕ), where r is the radial distance of a point from the center, θ is the geocentric colatitude or polar angle measured from the North pole and ϕ is the longitude or azimuthal

angle, measured from the Greenwich meridian. Laplace's equation in this system of coordinates takes the form:

$$\frac{1}{r}\frac{\partial^2}{\partial r^2}(rV) + \frac{1}{r^2 \sin\theta}\frac{\partial}{\partial\theta}\left(\sin\theta\frac{\partial V}{\partial\theta}\right) + \frac{1}{r^2\sin^2\theta}\frac{\partial^2 V}{\partial\phi^2} = 0 \tag{2.14}$$

Equation 2.14 has, as solution, a product of three expressions (the first is to be only a function of r, the second, only a function of θ and the third, only a function of ϕ) and can be solved by separation of variables, considering the potential $V(r,\theta,\phi)$ as the product of a radial and angular contributions. A completely general solution is provided by spherical harmonics and can be written as:

$$\begin{aligned} V(r,\theta,\phi) &= a\sum_{n=1}^{\infty}\sum_{m=0}^{n}[(A_{n,m}\cos m\phi + B_{n,m}\sin m\phi)\left(\frac{a}{r}\right)^{n+1} \\ &+ (C_{n,m}\cos m\phi + D_{n,m}\sin m\phi)\left(\frac{r}{a}\right)^{n}]P_{n,m}(\cos\theta) \end{aligned} \tag{2.15}$$

where $A_{n,m}$, $B_{n,m}$, $C_{n,m}$, $D_{n,m}$ are called spherical harmonic coefficients, and $P_{n,m}(\cos\theta)$ are the associated Legendre polynomials. In geomagnetism the partially normalized Schmidt functions $P_n^m(\cos\theta)$ are used. In the Schmidt normalization of the Legendre functions, the tesseral and sectorial harmonics are normalized to have the same *rms* values over the spherical surface as the zonal harmonics of the same degree, whereas no normalization is applied to the zonal harmonics (Stacey, 1992). The $P_n^m(\cos\theta)$ are functions of colatitude only. They are quasi-sinusoidal oscillations having $n-m+1$ nodes. The surface harmonics, $P_n^m(\cos\theta)\sin m\phi$ and $P_n^m(\cos\theta)\cos m\phi$, or SHs, divide the surface of the sphere into regions defined by the intersections of latitudinal zones and longitudinal sectors identified by the degree n and order m. SH is equal to 0 along m great circles passing through the poles, and along $n-m$ circles of equal latitude. Degree n and order m are thus a measure of wavelength. Some of the base functions show special characteristics and they are named individually:
(1) when $m=0$, the surface harmonics are described by the Legendre polynomials and they are referred to as *zonal harmonics*; they have vanishing m and they are independent of longitude ϕ;
(2) when $n=m$, there are no zero crossing in latitude and the surface harmonics are referred to as *sectorial harmonics*;
(3) when $0<m<n$, the surface is divided in $2m(n-m+1)$ regions, the functions vary with both latitude and longitude and the surface harmonics are referred to as *tesseral harmonics*. Some examples are given in Figure 3.

Application of spherical harmonics to the Earth's magnetic field involves writing the

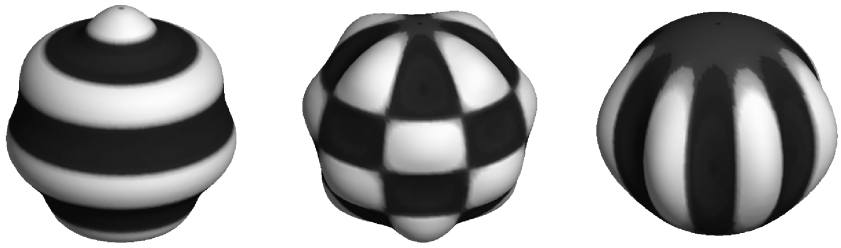

Figure 3: Zonal harmonics, for $n = 7$ and $m = 0$ (left), tesseral harmonics, for $n = 7$ and $m = 4$ (middle), and sectorial harmonics, for $n = 7$ and $m = 7$ (right). *Figures provided by prof. M.Mandea.*

magnetic scalar potential as the sum of two contributions:

$$V = V_{int} + V_{ext} \tag{2.16}$$

where V_{int} and V_{ext} are the internal and external scalar potential, respectively. These two potentials can be represented by spherical harmonic expansions:

$$V_{int} = a \sum_{n=1}^{N_i^{max}} \left(\frac{a}{r}\right)^{n+1} \sum_{m=0}^{n} \left(g_n^m \cos(m\phi) h_n^m \sin(m\phi)\right) P_n^m(\cos(\theta)) \tag{2.17}$$

$$V_{ext} = a \sum_{n=1}^{N_e^{max}} \left(\frac{r}{a}\right)^{n} \sum_{m=0}^{n} \left(q_n^m \cos(m\phi) s_n^m \sin(m\phi)\right) P_n^m(\cos(\theta)) \tag{2.18}$$

where the reference radius is $a = 6371.2\ km$, as the radius of the Earth. By this scaling, the Gauss coefficients have the same dimension as $\vec{B}$. Measurements of the magnetic field are used to estimate the so-called Gauss spherical harmonic coefficients (g_n^m, h_n^m) for internal sources and (q_n^m, s_n^m) for external sources, which, in principle, uniquely describe the geomagnetic field outside source regions. They are usually given in nT and n is the degree and m is the order of the individual terms. The summations in (2.17) and (2.18) are truncated at maximum degree N_i^{max} and N_e^{max}, respectively. The term for $n = 0$ corresponds to a magnetic monopole and violates equation 2.12. It is omitted in the analyses of the magnetic field. With the omitted $n = 0$, this requires $n(n+2)$ coefficients to be evaluated if only the internal contribution is considered.

Spherical harmonic analysis is an appropriate way of modeling the geomagnetic field. Considering only the part of the geomagnetic field, whose sources lie beneath the Earth's surface, equation (2.17) is used. However, this equation describes both the main field (with sources in the core) and the crustal field (with sources in the Earth's crust).

The Gauss coefficients can be interpreted in terms of "sources" at the Earth's center.

Each order of the expansion has a physical interpretation. The first term, g_1^0, is the term associated with the geocentric dipole oriented along the vertical axis, with dipole moment $g_1^0 4\pi a^3/\mu_0$. The first three Gauss coefficients (g_0^1, g_1^1, h_1^1) represent the *dipole* field, while the remaining terms represent the *non-dipole field*. The lowest degree terms correspond to the largest wavelength features of the field, as can be appreciated by considering the zonal harmonics. The first Gauss coefficient has a $\cos\theta$ dependence, so at distance r the "wavelength" of the associated magnetic feature is $2\pi r$. Generally speaking, the term g_n^m has a wavelength of $2\pi r/n$.

The relative importance of the two internal contributions is clearly illustrated by using the normalized power in spherical harmonics of the internal geomagnetic field. The spectrum of a model is constructed by plotting the contribution of each degree n of the spherical harmonic expansion to the mean square field over the Earth's surface. The power at degree n is computed from the next equation (Mauersberger, 1956; Lowes, 1966) and it is given in $(nT)^2$:

$$W_n = (n+1)\sum_{m=0}^{n}\left((g_n^m)^2 + (h_n^m)^2\right). \tag{2.19}$$

The analysis of the Gauss coefficients from so-called *power* or *Mauersberger-Lowes spectrum* reveals insights into the sources of the geomagnetic field. The power spectrum represents the energy contribution brought by every degree n term in the expansion from $n = 1$ to $n = m = N_i$. As it is clearly observable, the contribution to power decreases as the n increases. An isolated point is obtained for $n = 1$ and this correspond to the centered Earth dipole, as shown by the meaning of the $n = 1$ spherical harmonic analysis. The internal field at the Earth's surface contains clearly defined components from the core at least up to degree $N_i = 13$, beyond which they begin to become dominated by those from the crust. Long-term dynamo processes, the core field and the secular variation, dominate the field between $40,000\ km$ (SH degree 1) and $3100 - 2450\ km$ wavelengths (SH degree 13 or 16, respectively). The ambiguity, in quantifying the lithospheric field, is due to its complexity which reflects the heterogeneous distribution of magnetic minerals, and due to the overlap of ionospheric and Field Aligned currents, at medium to short wavelengths. The maximum associated wavelengths for the crustal components are of order of a few thousand kilometers.

With respect of lithospheric field characterization, it is also important to describe possibilities to link the magnetic field obtained from a predicted model to magnetization constrains. The lithospheric magnetic field $\vec{B_l}$ is linked to the rock magnetization by the relation:

$$\mathbf{B_l}(\mathbf{r}) = \int_v \mathbf{G}(\mathbf{r},\mathbf{s})\cdot\mathbf{M}(\mathbf{s})dv. \tag{2.20}$$

where $\mathbf{r}$ and $\mathbf{s}$ are two points in space, outside and inside the magnetized volume v respectively and μ_0 is the free-air magnetic permeability, as defined before. $\mathbf{G}(\mathbf{r},\mathbf{s})$ is the usual Green tensor given by:

$$\mathbf{G}(\mathbf{r},\mathbf{s}) = -\frac{\mu_0}{4\pi}\nabla_{\mathbf{r}}\nabla_{\mathbf{s}}\frac{1}{|\mathbf{r}-\mathbf{s}|} \tag{2.21}$$

The most often used techniques consist in describing the magnetization in term of spherical uniformly magnetized bodies (dipoles), sometimes uniformly magnetized cylinders, for 2-D geometry, or as a discrete sum of the Green tensors themselves (Parker and Rosenberg, 1987). Other techniques are described in Blakely (1995) or Purucker and Whaler (2007). Ideal body theory helps to establish bounds on quantities such as the magnetization strength required to explain a magnetic field distribution (Parker, 1991, 2003; Purucker et al., 2008). This approach is also used and in *Part II, Chapter 3* in order to investigate the magnetic signatures of impact craters.

Going back to equations 2.17 and 2.18, they contain two different expansions for the radial contributions. Both satisfy the radial differential equation but show different behavior. As r approaches zero, $\left(\frac{a}{r}\right)^{n+1}$ grows infinitely large and thus describes sources from inside of $r = a$. Terms in $\left(\frac{r}{a}\right)^{n}$ vanish with decreasing r and describe sources from outside of $r = a$. The field components $\vec{B} = (\vec{B}_r, \vec{B}_\theta, \vec{B}_\phi)$ are obtained as derivatives:

$$\vec{B}_r = -\frac{\partial V}{\partial r} \tag{2.22}$$

$$\vec{B}_\theta = -\frac{1}{r}\frac{\partial V}{\partial \theta} \tag{2.23}$$

$$\vec{B}_\phi = -\frac{1}{r\sin\theta}\frac{\partial V}{\partial \phi} \tag{2.24}$$

and the total (scalar intensity) is given by $B = \left({B_r}^2 + {B_\theta}^2 + B_\phi^2\right)^{\frac{1}{2}}$ and the measured components on the Earth, usually directed towards North, East and down (X,Y,Z) are related to (B_r, B_θ, B_ϕ) in spherical coordinates by $X = -B_\theta$, $Y = B_\phi$, $Z = -B_r$.

The presented description in SH is available for modeling the geomagnetic field at a given epoch, depending on the available data over the Earth. But the Gauss coefficients $g_n^m(t)$ are also time-dependent. However, to consider the temporally behavior of the magnetic field in global modeling, some mathematical tools are needed. Indeed, the temporal variations of the geomagnetic field have an extremely wide spectrum, ranging over more than 20 orders of magnitude (Langel, 1987). The new adopted approach is to model the temporal evolution with spline functions (de Boor, 2001). The problem is how to fit a smooth curve of unknown parametric form to a time series of observations,

with a specific tolerance. In the simplest case, these are straight lines joined at several *nodal points* or *knots*. All magnetic fields models, presented in the following section, use B-splines at different degrees for temporal modeling, excepting the IGRF models, for which the secular variation behavior is linear.

Equivalent Source Dipole

Even if the SH analysis is the widely used techniques, recently, some powerful mathematical tools have been developed. We can note a few of them as the Equivalent Source Dipole (Mayhew and Estes, 1983; Dyment and Arkani-Hamed, 1998), wavelet analyses (Holschneider et al., 2003; Chambodut et al., 2005) or harmonic splines (Schumaker, 1981; Shure et al., 1982; Parker and Shure, 1982; Shure et al., 1985). In the following, only one of the methods is described, the Equivalent Source Dipole, mainly used for description of the Martian and Lunar magnetic fields.

Equivalent Source Dipole (ESD) is the alternate and often used technique for global description of magnetic field around planets. This method was introduced by Mayhew and Estes (1983) for satellite magnetic field data. The observed magnetic field $\vec{B}$ is the gradient of the potential V_i due to a series of dipole sources located inside the planet. This method was primarily designed to reduce scattered measurements to a common altitude. When it is used to model the terrestrial magnetic field anomalies, one can use *a priori* information to constrain the model and to reduce the number of parameters. For instance, assuming a purely induced magnetization over the continents, aligned onto the main core field (Purucker et al., 1998). Considering the magnetic moment M, with its components m_r, m_θ, m_ϕ, of a given dipole located at (r_d, θ_d, ϕ_d), the magnetic potential observed at (r, θ, ϕ) is expressed as:

$$V = -M \cdot \nabla \frac{1}{l} \tag{2.25}$$

where l is the distance between the dipole and the observation location and ∇ is the gradient operator at r_d . This relation is valid provided that there are no sources between the dipole and the observation location. The distance l is written:

$$l = \left(r_d^2 + r^2 - 2r_d \cdot r \cos(\zeta)\right)^{\frac{1}{2}} \tag{2.26}$$

ζ being the angle between observation point and dipole location, and

$$\cos(\zeta) = \cos\theta \cos(\theta_d) + \sin\theta \sin(\theta_d) \cos(\phi - \phi_d) \tag{2.27}$$

It is esily to express the magnetic potential as:

$$V = \frac{1}{l^3}\left(m_r(rA_1 - r_d) - m_\theta r B_1 + m_\phi r C_1\right) \tag{2.28}$$

where:

$$A_1 = \cos(\zeta) = \cos\theta\cos(\theta_d) + \sin\theta\sin(\theta_d)\cos(\phi - \phi_d) \tag{2.29}$$

$$B_1 = \cos\theta\sin(\theta_d) - \sin\theta\cos(\theta_d)\cos(\phi - \phi_d) \tag{2.30}$$

$$C_1 = \sin\theta\sin(\phi - \phi_d) \tag{2.31}$$

The resulting magnetic field $\vec{B}$, with its components B_r, B_θ, B_ϕ, is written as derived from a scalar potential (Langlais et al., 2004):

$$\vec{B} = -\vec{\nabla}V = -\left(\frac{\partial}{\partial r}, \frac{\partial}{r\partial\theta}, \frac{\partial}{r\sin\theta\partial\phi}\right)V \tag{2.32}$$

If partial derivatives of A_1, B_1, C_1 are denoted, in respect to colatitude (θ) and longitude (ϕ) as A_2, B_2, C_2 and A_3, B_3, C_3 respectively, then:

$$A_2 = \frac{\partial A_1}{\partial\theta} = -\sin\theta\cos(\theta_d) + \cos\theta\sin(\theta_d)\cos(\phi - \phi_d) \tag{2.33}$$

$$B_2 = \frac{\partial B_1}{\partial\theta} = -\sin\theta\sin(\theta_d) - \cos\theta\cos(\theta_d)\cos(\phi - \phi_d) \tag{2.34}$$

$$C_2 = \frac{\partial C_1}{\partial\theta} = \cos\theta\sin(\phi - \phi_d) \tag{2.35}$$

and

$$A_3 = \frac{\partial A_1}{\sin\theta\partial\phi} = -\sin(\theta_d)\sin(\phi - \phi_d) \tag{2.36}$$

$$B_3 = \frac{\partial C_1}{\sin\theta\partial\phi} = \cos(\theta_d)\sin(\phi - \phi_d) \tag{2.37}$$

$$C_3 = \frac{\partial C_1}{\sin\theta\partial\phi} = \cos(\phi - \phi_d) \tag{2.38}$$

If $D_1 = r - r_d A_1$, $D_2 = -r_d A_2$, $D_3 = -r_d A_3$ and $F_1 = rA_1 - r_d$, $F_2 = -rB_1$, $F_3 = rC_1$, magnetic field components can be written:

$$B_r = \frac{1}{l^3}\left(m_r\left(\frac{3D_1F_1}{l^2} - A_1\right) + m_\theta\left(\frac{3D_1F_2}{l^2} + B_1\right) + m_\theta\left(\frac{3D_1F_3}{l^2} - C_1\right)\right) \tag{2.39}$$

$$B_\theta = \frac{1}{l^3}\left(m_r\left(\frac{3D_2F_1}{l^2} - A_2\right) + m_\theta\left(\frac{3D_2F_2}{l^2} + B_2\right) + m_\theta\left(\frac{3D_2F_3}{l^2} - C_2\right)\right) \tag{2.40}$$

$$B_\phi = \frac{1}{l^3}\left(m_r\left(\frac{3D_3F_1}{l^2} - A_3\right) + m_\theta\left(\frac{3D_3F_2}{l^2} + B_3\right) + m_\theta\left(\frac{3D_3F_3}{l^2} - C_3\right)\right) \tag{2.41}$$

In this way, the magnetic anomaly measured at one place is the sum of magnetic anomalies created by all dipoles. Only those with a certain range contribute significantly. Numerous tests performed by Purucker et al. (1996) show that this range can be confined to less than 1500 km distance between observation point and dipole. This method has several advantages. First, it associates with a magnetic data sets information about the magnetization distribution. If carefully used this information can be useful, but a simplistic direct interpretation may lead to erroneous conclusions. Second, as for the localized methods, the resolution, both in spatial and spectral domain, can be varied by changing the density of the dipoles or their depths. This freedom carries also difficulties because, for a given source depth, the density has to be high enough in order to avoid spurious model magnetic field behavior. As a results, the number of required dipoles is usually relatively high. For a given resolution (i.e. a given maximum spherical harmonic degree), the number of parameters is as least twice as high as the number of requested Gauss coefficients. An advantage of this approach, compared with spherical harmonic analysis, is that it can be applied either at a global scale or a local one, using the same method. The forward modeling using Equations 2.39, 2.40, 2.41 is presented as a study case in *Part II, Chapter 3*.

2.3.2 Temporal variations: spectral analysis of geomagnetic field series

A part of the thesis is consecrated to time-analyses of observatory data. Here, some methods to describe the core field variations are summarized, especially those used in geomagnetic jerks detection and characterization. An easy method, to determine the epoch when a geomagnetic jerk occurs, is to approximate secular variation time series by straight lines and to consider the intersection point of such V-lines as the date of an event. During the last two decades, more powerful methods to detect geomagnetic jerks and to estimate their location and duration have been developed. For example, the wavelet analysis have been largely applied to the monthly mean series provided by different geomagnetic observatories (Alexandrescu et al., 1995, 1996; Chambodut et al., 2005) or a statistical time series model has been used to analyze monthly means of the geomagnetic eastward component at different observatories (Nagao et al., 2003).

Different methods of analyses, to study time series of geomagnetic field components and secular variations, can be applied, all being essentially spectral analyses. Two of them, the Short Time Fourier Transform and the Discrete Wavelet Transform, derive directly as natural developments of Fourier Analyses, are mainly used and presented here.

Short Time Fourier Transform

The Fourier analysis breaks down a signal into constituent harmonics of different frequencies. For regularly sampled data, Fourier analysis is performed using the Discrete Fourier Transform (DFT). The Fast Fourier Transform (FFT) is a very efficient algorithm for computing the DFT of an input sequence x of length N. The output of DFT is a vector X with length N (Oppenheim and Schafer, 1989):

$$X(k) = \sum_{n=1}^{N} x(n) e^{-i2\pi(k-1)(n-1)/N} \tag{2.42}$$

where $k = 1, 2...N$

The amplitude of $|X|^2$ is named the spectrum power and its plot versus frequency is the "periodogram". The periodogram function which estimates the PSD (Power Spectral Density) of a signal $x_N(n)$ is:

$$\widehat{P}_{xx}(f_k) = \frac{|X_N(f_k)|^2}{f_s N} \tag{2.43}$$

where N is the length of the vector, $|X_N|$ is the DFT of the signal and f_s is the sampling frequency. The frequencies are:

$$(f_k) = \frac{k f_s}{N} \tag{2.44}$$

where: k and the range of the frequency are:
$k = 0, 1, ..., N-1$ and $0 \leq f_k < f_s$, in case of a complex-valued signal;
$k = 0, 1, ..., N/2 - 1$ and $0 \leq f_k \leq f_s/2$, in case of a real-valued signal,$(N = even)$;
$k = 0, 1, ..., (N-1)/2$ and $0 \leq f_k < f_s/2$, in case of real-valued signal and $(N = odd)$;

The Fourier transform of a signal can not indicate when particular events (such as drifts, trends, abrupt changes, etc.) appear within the time-series. The Short Time Fourier Transform (STFT) method as well as the Discrete Wavelet Transform (DWT) are essentially single-station time series analyses capable to detect particular events as the fast changes in the secular variations (SV) or secular acceleration (SA) in long time-series of the geomagnetic field components, obtained from geomagnetic observatories. The technique called "windowing the signal" (Gabor, 1946) or the Short-Time Fourier Transform (STFT) (Brockwell and Davis, 2009) can correct this deficiency by applying the Fourier transform only to small sections of the signal at successive times. The STFT provides some information about both time and frequencies, thus characterizing a particular event present in the analyzed time-series.

Wavelet analysis

Wavelet analysis represents a windowing technique with variable-sized regions, normally with long time intervals where more precise low-frequency information are needed to be obtained, and shorter time intervals where high-frequency information are needed. Wavelet analysis is capable to reveal aspects of data like trends, breakdown points, discontinuities in higher derivatives, and self-similarity. It is also used to compress or de-noise a signal without appreciable degradation.

This method is much more powerful and without any *a priori* assumption on the existence of the sudden change in the secular variation, to determine the geomagnetic jerk time occurrence. To get a more robust detection and characterization of such events, the wavelet analysis has been proposed, improved and applied by (Alexandrescu et al., 1996; Mandea-Alexandrescu et al., 1999; Chambodut and Mandea, 2005; De Michelis and Tozzi, 2005). This method identifies and extract all kinds of singularities in a signal, and, by its objectivity and efficiency, it can determine the geomagnetic jerks occurrence.

The theoretical background has been described in (Alexandrescu et al., 1995, 1996), and the reader is referred to these papers for a full description of wavelet analysis applied to singularity detection. To summarize them, one assumes that the geomagnetic element is the signal ($S(t)$) recorded in the observatories is the sum of a core field signal containing singularities, i.e. jerks, an external long-period signal and noise:

$$S\left(t\right) = \beta j_{\alpha}\left(t\right) + h_{S}\left(t\right) + n_{S}\left(t\right), \tag{2.45}$$

where βj_{α} is the jerk signal (it represents an abrupt change with a regularity α and intensity β localized at the time $t_{\circ}$):

$$j_{\alpha}\left(t\right) = \begin{cases} 0 & t \leq t_{\circ} \\ \left(t - t_{\circ}\right)^{\alpha} & t > t_{\circ} \end{cases}, \tag{2.46}$$

h_S is the S component of the "periodic" external signal and n_S the noise on the S component, considered as being isotropic.

We define the continuous wavelet transform of a signal $f\left(t\right)$ by the convolution product

$$Wf\left[t, a\right] \equiv \left[f * \psi_{a}\right]\left(t\right), \tag{2.47}$$

where the wavelets $\psi_{a}\left(t\right)$ are obtained by dilating an analyzing wavelet $\psi\left(t\right)$,

$$\psi_{a}\left(t\right) \equiv \frac{1}{a}\psi\left(\frac{t}{a}\right) \tag{2.48}$$

with a dilation $a > 0$. Equation (2.48) shows that the wavelet transform is defined in the (t, a) open half-space and that every voice of an octave (as in music), $WFF\,(t, a = Cst)$, is a filtered version of the initial signal $s\,(t)$. The used analyzing wavelet can be:

$$\psi\,(t) = \frac{d^3}{dt^3} \exp\left(-\frac{t^2}{2}\right). \tag{2.49}$$

Inserting the model (2.45) into (2.47):

$$Wf\,(t, a) = \beta W j_\alpha\,(t, a) + Wh_S\,(t, a) + Wn_S\,(t, a)\,, \tag{2.50}$$

which indicates that the wavelet transform of the signal is the superposition of the wavelet transforms of the jerk, of the harmonic components and of the noise.

The notion of "ridge function" has been defined as the absolute value of the wavelet transform, along a given line of extrema. Clearly, they are very useful to detect, without a priori information, the date for a jerk, with high accuracy (a couple of month, when monthly means series are investigated).

DWT applied to monthly series of secular variation

Similar to Fourier analysis, the Continuous Wavelet Transform (CWT) is a sum over all time of the signal multiplied by shifted and scaled versions of the original (mother) wavelet function Ψ. The wavelet decomposition consists of calculating:

$$c(a, b) = \int_{-\infty}^{+\infty} s(t)\Psi(a, b, t)dt \tag{2.51}$$

where $c(a, b)$ are a *resemblance coefficient* between the signal ($s(t)$) and the wavelet, of scale a, located at position b. Scaling a wavelet means compressing or stretching the wavelet by a scale factor a. The smaller scale factor is, the more stretched wavelet is. The shifting of a wavelet means delaying or hastening its onset. The family of $c(a, b)$ coefficients depends only by a and b indices (Kumar and Georgiu, 1994).

In the Discrete Wavelets Transform (DWT), a and b parameters are discrete, based on powers of 2 (dyadic scales and positions), where: $a = 2^j$ and $b = k2^j$, for $(j, k) \in Z^2$. It is possible, to construct a class of wavelets $\Psi(t)$ such that $\Psi_{j,k}(t)$ are orthonormal (the wavelets are orthogonal to their dilates and translates) and they form a complete orthonormal basis for all functions $s(t)$ that have finite norm. In this way, the time signal $s(t)$ of the DWT is defined:

$$s(t) = \sum_{j \in Z} \sum_{k \in Z} c(j, k)\Psi_{j,k}(t) \tag{2.52}$$

where $c(j,k) = \langle s, \Psi_{j,k} \rangle \equiv \int s(t)\Psi_{j,k}(t)dt$. If j is constant and if we sum on k, a detail function d_j can be written as:

$$d_j(t) = \sum_{k \in Z} c(j,k)\Psi_{j,k}(t) \tag{2.53}$$

and the signal can be written as the sum of all the details d_j, respectively:

$$S = \sum_{j \in Z} d_j \tag{2.54}$$

If we settle up a reference level J, there two sorts of details:
-those associated with indices $j \leq J$, corresponding to the scales $a = 2^j \leq 2^J$, which are the fine details;
-the others, which correspond to $j > J$, which are the coarser details and they are grouped into $a_j = \sum_{j>J} d_j$, and it defines an approximation of the signal S. Finally, the equality:

$$S = a_j + \sum_{j \leq J} d_j \tag{2.55}$$

shows that the signal is the sum of the signal approximation a_j and of its fine details, d_j.

These methods have been presented and used to investigate the temporal behavior of the geomagnetic field in co-authored paper by Duka et al. (2012). Few ideas, together with results obtained for Surlari time series are presented next.

2.4 Contributions in spectral techniques applied to geomagnetic time-series

The Earth's magnetic field, comparing with Mars and Moon, is the subject to temporal variation on the widest range of time scales: from second to hours (external, originate in solar activity), from months to decades (external and internal variabilities overlapped) or from centennial to reversals (the slowest internal variations, generated by the changes of the fluid flow in the core). As shown in *Part I, Section 2.1*, the Earth's magnetic field is the one, from the planetary ones considered here, to have a running dynamo, and to be characterized by specific temporal variations. Moreover, for the geomagnetic field a special consideration is given to its secular variation and acceleration. To understand these specific characteristics it is crucial to analyze long series of data, provided by geomagnetic observatories or deduced from satellite measurements and models. This has been one of important aims of the research and it is also presented here.

2.4.1 SFTF applied to Surlari's monthly series of secular variation

I have been mainly interested in Surlari observatory data, and geomagnetic field characteristics. For this reason the monthly mean series for the X, Y, Z components were built, and analyzed via different methods in order to define the secular variation behavior and finally to detect geomagnetic jerks. As in many studies, the Y component is the one to be analyzed, as being less affected by the external field contributions. As it was noticed before, secular variation can be described as a series of segments with slopes changing at jerks' time. Jerks are intermittent events and may be described also as steps in the second derivative of the main field or as impulses in its third derivative. Another feature of geomagnetic jerks is they do not occur simultaneously over the entire Earth's surface. Some events can show a global character (world wide events) while others are observed only in a sparse number of observation points (regional events). Even worldwide events are characterized by a bimodal distribution: they first occur in the northern hemisphere and then, after a few years, in the southern.

First, here are presented results of SFTF analysis applied first to a synthetic signal to test its real effectiveness on a signal which has breakdowns in the second derivative. The synthetic signal $f(t)$ was defined in the interval $[-0.5, 0.5]$ as:

$$f(t) \quad = \quad exp(-4t^2) \tag{2.56}$$

for $-0.5 \leq t < 0$, and

$$f(t) \quad = \quad exp(-t^2) \tag{2.57}$$

for $0 \leq t < 0.5$, sampled at every $\Delta t = 10^{-3}$.

In the spectrogram (with the magnitude of the SFTF function expressed in decibels) only the first difference of the signal values shows a breakdown of the signal, close to $t = 500$ (on the rescaled temporal abscissa $time = 500 + t \cdot 1000$), as it can be seen in Figure 4.

In order to detect geomagnetic jerks from real data by SFTF, it is better to study the spectrograms of the first difference of the geomagnetic field components. The same processing scheme was applied then, to the Surlari monthly series of 649 values (from 1950 to 2004). First, it had to remove the effect of the external sources. For this, firstly, monthly means of the secular variation of Y component, were computed. The values are less influenced by external fields, but are still irregular and noisy. A larger moving window ($12-months$ moving average) was selected to be applied to these monthly values

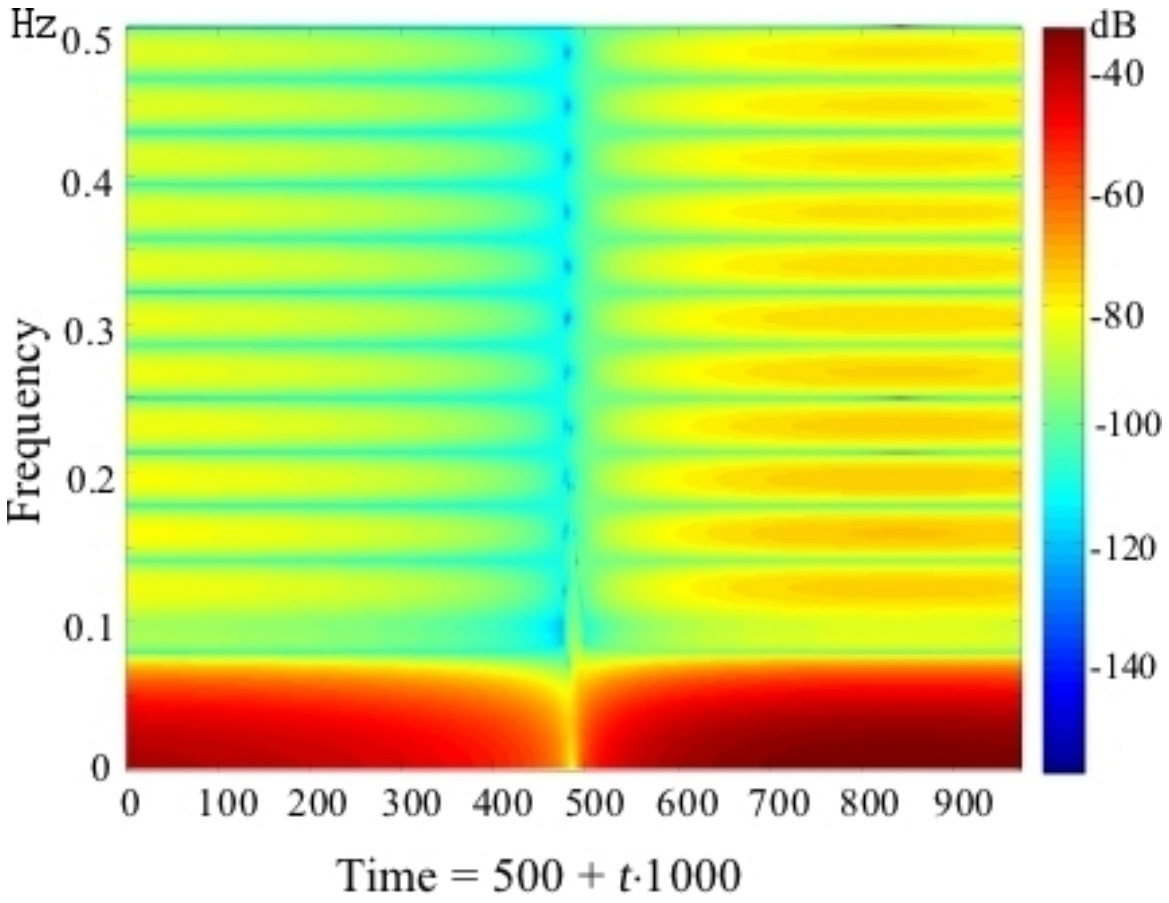

Figure 4: The spectrogram of the first difference series of the synthetic signal, sampled at every $\Delta t = 10^{-3}$. The time scale is arbitrary *(Duka et al., 2012)*.

of SV, in order to minimize the ionospheric and magnetospheric influences (Figure 5).

In order to detect particular events in the SV series, the *specgram* function of Matlab7 software (MathWorks Inc., 2004) which computed the windowed discrete time Fourier transform of a signal, using sliding windows of Gaussian-like form with a different length and different overlaps, was used. The resulted spectrogram is shown in Figure 6. It is clearly observed from analyzing this spectrogram, that geomagnetic jerks are present around 1970, 1990 and 2000, the best case being when the moving window had a $12-months$ length. For $50's$, even the monthly mean series of Y component shows a great amount of noise, due to a weaker quality of data, changes in the trend appear around 1954 and 1959.

The results of spectrogram analysis considerably depend on the length of the signal, slightly depend on the window length and overlaps and, almost do not depend on the form of window (Bohman, Chebyshev, Gaussian, Hamming, etc.).

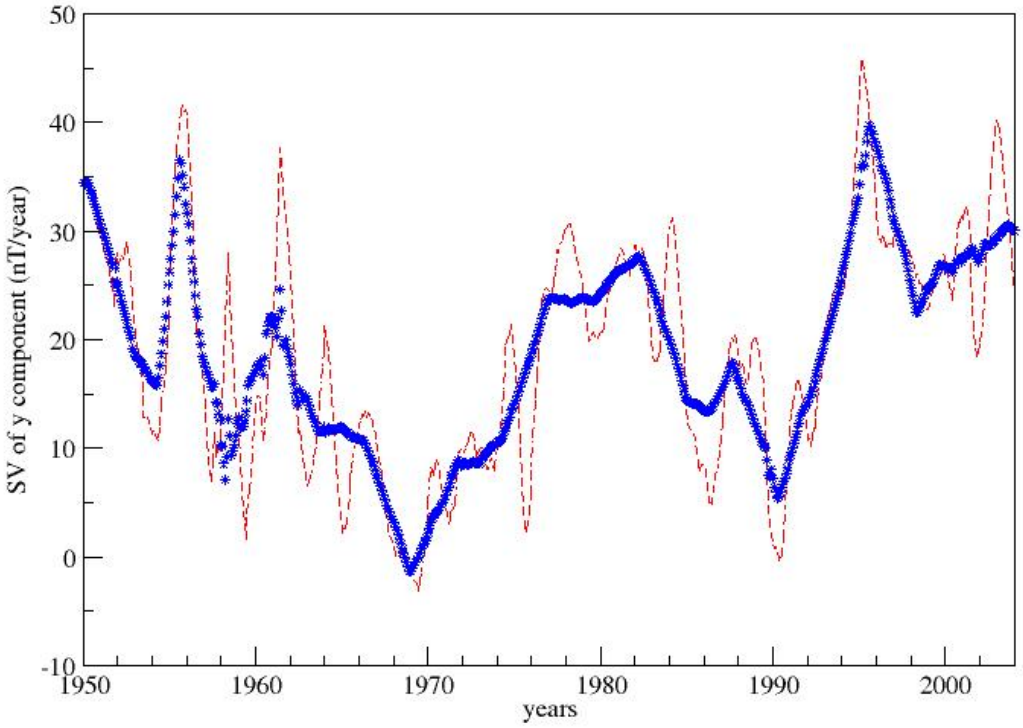

Figure 5: Secular variation (SV) time series of Surlari, calculated by $12-months$ moving average from y component (red) and its de-noised signal of the series decomposition by $Db3$ wavelets of level 5 (blue), in nT/year.

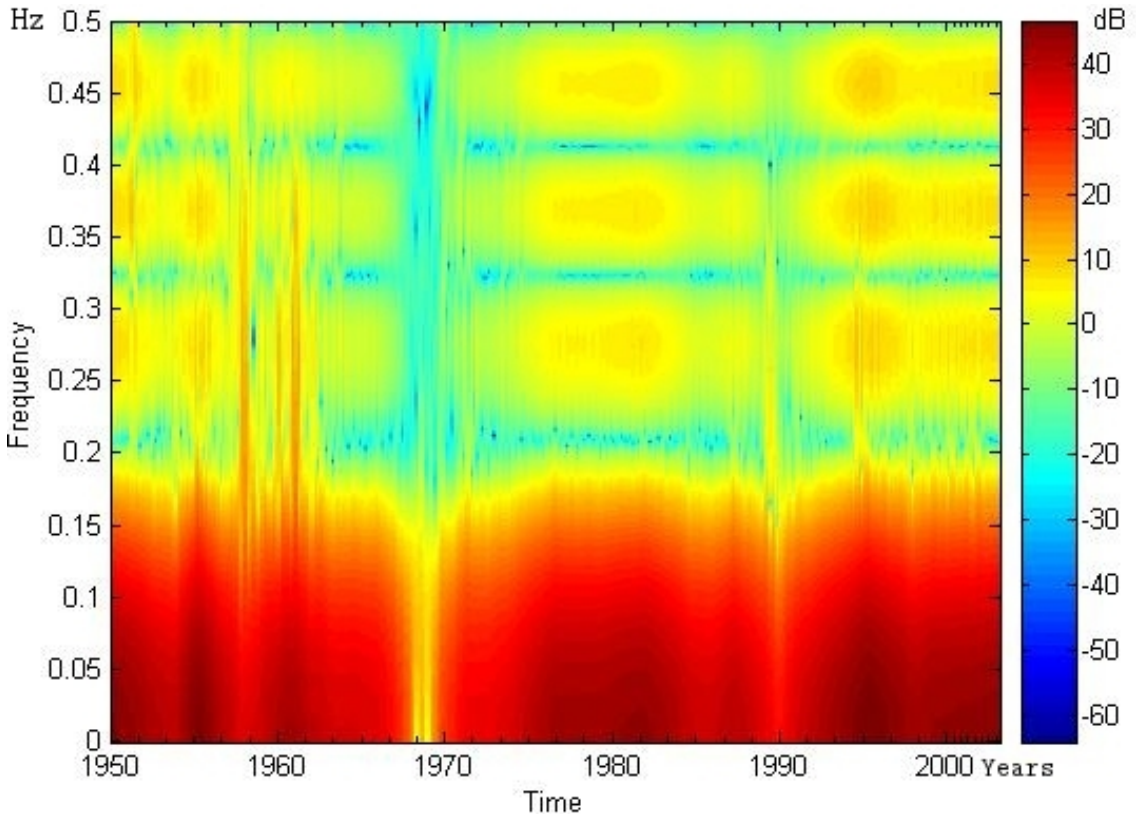

Figure 6: Spectrogram of monthly values series of the secular variation of Y component ($12 - months$ moving average) at Surlari observatory ($1950 - 2004$).

2.4.2 DWT applied to Surlari's monthly series of secular variation

To determine the second derivative breakdown of the geomagnetic field components, the wavelet transform to the monthly mean values series of Y component recorded at Surlari observatory was also applied. It was considered different kinds of wavelet shapes and level parameters among those contained in the wavelet toolbox of Matlab software [7]. The wavelets that successfully detected the change in the second order derivative of the selected signal was the Daubechies wavelet (Daubechies, 1992) of order 3 ($Db3$) at level 2 of the signal decomposition, and of the form:

$$S = a_2 + d_2 + d_1 \tag{2.58}$$

where the decomposition is stopped at $J = 2$ (to detect a *rupture* in the j^{th} derivative, it have to select a regular wavelet with at least j vanishing moments). Great anomalous values of d_1 and d_2 coefficients appear where the $time = 500$ signal (Figure 4) has the second derivative breakdown (better localized by d_1 coefficients).

The presence of noise in the data makes the identification of discontinuities more complicated. The first level of the decomposition can be used to eliminate the largest part of the noise, but the *fine details* are visible only at deeper levels in the decomposition. For this reason, first, a synthetic signal as a series of values with spikes which have different changes of slopes was created. To this synthetic signal, a noise (blue dots) generated by the *warma* function from Matlab was added, in order to provide a realistic noise in a SV signal. The warma signal was extended and increased to provide an amplitude of the noise of about 15% of the signal itself, see on the top panel of Figure 7.

Then, the synthetic composed signal is de-noised by using Daubechies wavelets of order 3 and level 4, using Matlab7 wavelet Toolbox. The received signal (s) is decomposed according to Equation 2.58, up to level 2, by using Daubechies wavelets of order 4, as it is shown in Figure 7. It is easily seen that the peaks of d_1 and d_2 coefficients correspond to the ruptures of the first derivative of the signal.

Finally, considering again Surlari observatory, with its original $12 - months$ averaged signal, it was possible to get, via the wavelet analyses, the de-noised signal of the monthly SV value series, by applying the Db3 wavelets at level 5 decomposition. The result is shown on the same Figure 5, together with the initial data. The new time-series is clearly less contaminated by external field contributions. Then, the obtained signal (Figure 8), without distortion of the signal itself, was used to apply the $Db3$ wavelet for the wavelet decomposition of level 2.

[7] http://www.mathworks.com/help/toolbox/wavelet/

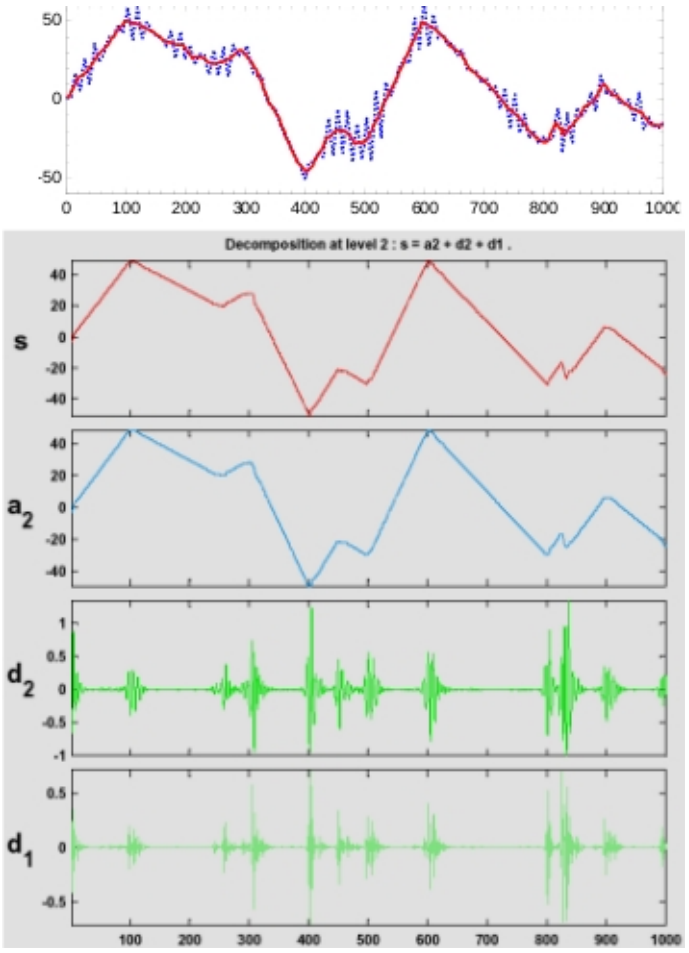

Figure 7: Synthetic composed signal: V-like shapes and blue noise (up), the decomposition of the de-noised signal (s), with its approximation (a_2) and fine details (d_1 and d_2) up to level 2, down *(Duka et al., 2012).*

The results show evidences of different kind of events, including some of the well-known geomagnetic jerks, which have been seen before, in the spectrogram, Figure 6, also. The de-noising process improved the further analysis of SV monthly means, in order to detect particular events. Considering the amplitude of detailed coefficient d_1 of the signal decomposition, as a measure of the breakdown of the second derivative of the signal, I have calculated the averaged values for each year, for the hole signal duration:

$$d_1(year(k)) = \sqrt{\frac{\sum_{i=1}^{12}(d_1(year(k), month(i))^2}{12}} \tag{2.59}$$

The d_1 values (as described before) were computed and represent them in Figure 9. The averaged d_1 coefficients get some clear maxima values. Unfortunately, those of the beginning of the series have a lower signifiance, as data are less accurate until mid-60$'s$.

Figure 8: Surlari SV de-noised signal (up) and its decomposition up to level 2 (down). The time scale is arbitrary.

Thereafter, the observed maxima are situated around dates of well-known jerks: 1970, 1980, 1990 and 2000. All dates are somehow found to be with a couple of years after the other jerk dates determined previously. The double maxima after 1970 has to be investigated in more detail taken into account the data quality of Surlari and the different behavior of SV over the globe.

2.4.3 DWT applied to long series using Gufm1 model

In addition, time series of geomagnetic field components, secular variation or secular acceleration were generated from geomagnetic field models. Such data was used instead of real data of geomagnetic observatories in order to have time series from a regular (uniform) grid of points over the Earth.

As before, the wavelet analyses was applied to the monthly value series of SV, the Y component, generated by Gufm1 model (see *Part II, Section 1.1*), at each location of the

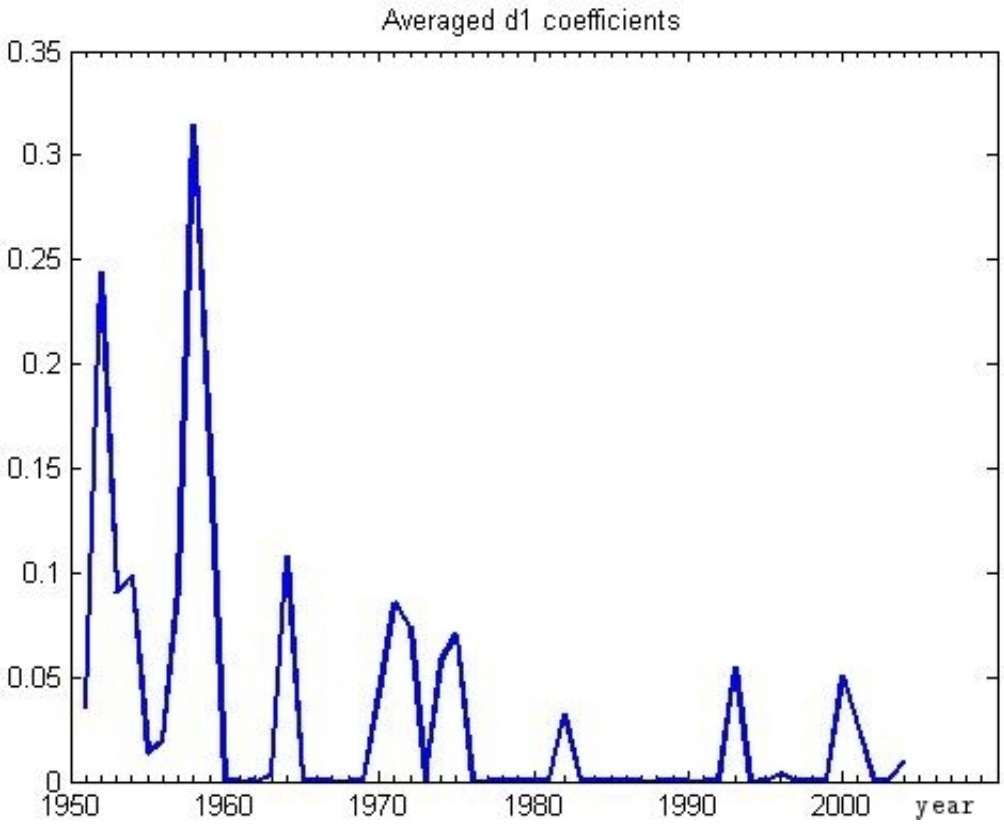

Figure 9: The averaged d_1 coefficients of the series decomposition by $Db3$ wavelets of level 2.

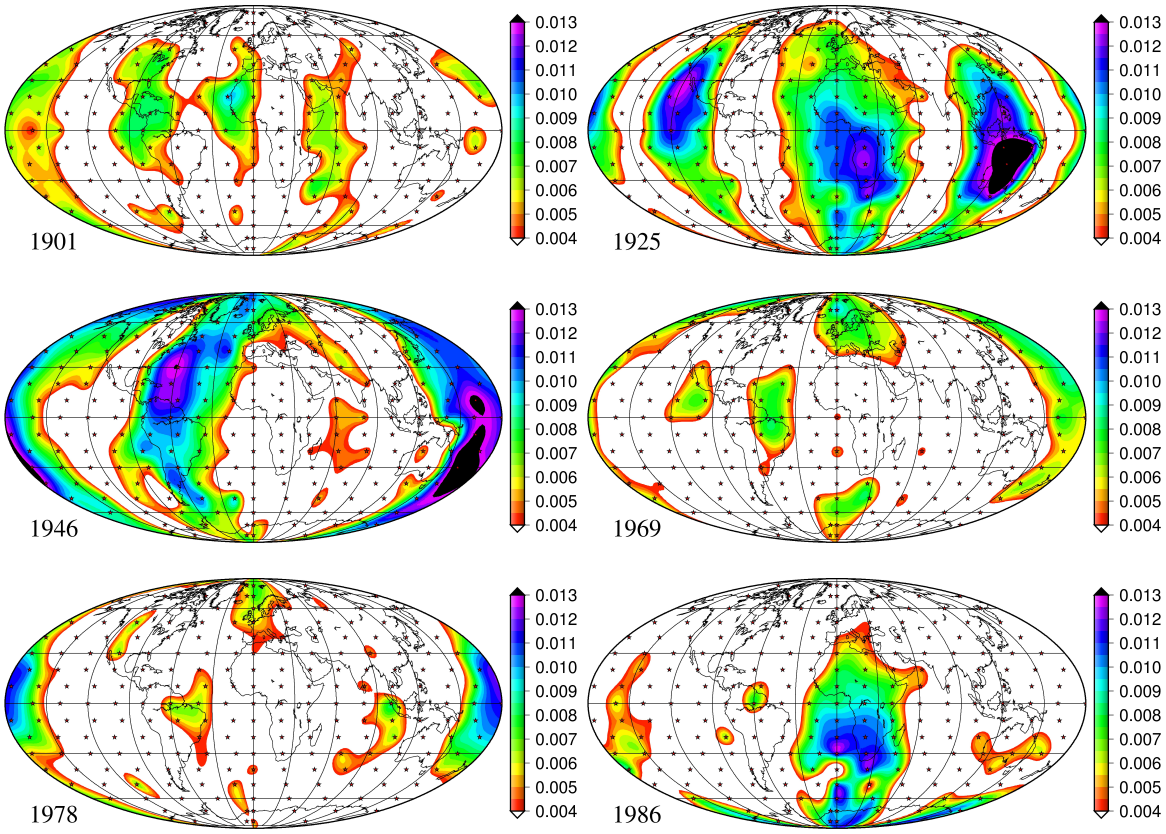

Figure 10: The d_1 coefficient behavior, for the epochs: 1901, 1925, 1947, 1969, 1978 and 1986, a selection from the movie by *Duka et al. (2012)*.

212 points uniformly distributed over the Earth' surface. From Gufm1 model, monthly values series of the secular variation for the period $1900-1990$ was generated. Each time series of all 212 points is decomposed by $Db2$ wavelets at level 2, saving the d_1 coefficients of decomposition.

Then, the squared average value of such coefficients for every year of the selected period, over the Earth, was calculated. From such plots, information about the spreading and evolution of geomagnetic field jerks (Duka et al., 2012) is given. The interested reader is referred to this paper and associated animations for a spatial and temporal description of geomagnetic jerks over the last century [8].

In Figure 10, the areas of averaged d_1 coefficients for a selection from the XX^{th} century, are presented. Actually, the deviation of d_1 coefficients from their mean value of the whole period was plotted. In such way, the white areas correspond to the regions where the d_1 values are less than the mean value, and the colored areas, correspond to regions where the values d_1 are the greatest than the average.

A specific behavior, like some kind of periodicity in longitude, can be seen in Figure

[8] http://www.solid-earth.net/3/131/2012/

10. These particular events, geomagnetic jerks, with a signature identical with strong fields of the d_1 coefficients, are not globally extended over the whole globe, in the same time. For example, starting with the 1901 event, stronger field is concentrated in four longitudinal belts, and as well as is the case in 1925, when the largest one is in the center. From 1945 until 1949, strong fields have a large spread in many longitude belts. The well known geomagnetic jerk, in 1969 is presented as a spot over Europe and only one eastern belt. The 1978 jerk is shown as local strong fields over some regions on the Earth. The 1986 jerk is represented as a large longitudinal area over the African and South pole region.

These kind of spectral analysis are generally applied to geomagnetic annual means, monthly means or hourly means provided by the network of magnetic observatories as well as to satellite data. Of course, it is better to investigate monthly mean series rather than annual means for jerk analyses, as the abrupt changes occur on very short time-scale. For this reason, the temporal resolution of annual means is not sufficient to get an accurate information on their characteristics. On the other hand, the monthly means are able only to minimize the external contributions, by averaging all hourly mean values.

Even the detection of jerks are based on spectral techniques (Mandea et al., 2010), Qamili et al. (2013) proposed in the most recent co-authored paper a new method which is not a spectral one, but a Nonlinear Forecasting Approach in the Time Domain. Considering the geomagnetic field an ergodic and chaotic system (following De Santis et al. (2011)) this method was applied to Gufm1 model long time series, too. First, all jerks detected by previous authors (with different other methods) were confirmed and added some new ones. Second, despite the limitation of few years, the geomagnetic field showed that it is chaotic and out of any reliable prediction after $6-7$ years. The time interval when the geomagnetic field is more predictable than usual was named Steady State Geomagnetic Regime (SSGR), as a counterbalance of a jerk event period, when the geomagnetic field is more chaotic.

The results for Surlari observatory show that the chosen methods are very appropriate to characterize the geomagnetic jerks. A few other results of geomagnetic jerk characteristics, obtained by applying these methods on time series of geomagnetic field of different observatories or time series of synthetic data generated by different models, represent the core of co-authored paper by Duka et al. (2012), and which title is included in the appendix of the thesis. In this paper spectral methods of analyses on different kinds of data have been applied. To synthetic data from Gufm1 model as well as to time series of geomagnetic field components recorded at geomagnetic observatories on the Earth (Niemegk, Alibag, Hermanus, etc). They are chosen to be longer than 50 years and placed as far as possible from each other.

Part II

Contributions in understanding spatial variations of magnetic fields of terrestrial planets

Chapter 1

Global magnetic and topographic maps and models utilized in the thesis

After presenting the mathematical basis of describing the spatial and temporal variations of the planetary magnetic fields, a short presentation of available models is considered to be useful considering the role of the available global models, in describing and understanding magnetic fields. This is done for the three planetary bodies, Earth, Mars and Moon, in which I am interested in. A special attention is given to the Earth's magnetic field, due to its complexity. Since the geomagnetic field changes in space and time, magnetic observations must be made continuously and models have to be generated to accurately represent the magnetic field. Magnetic models have been published since Gauss time and the degree/order of their representation continuously increase, due to the improving of the computer capability and to data availability. During the last decade of geopotential research, several satellites provided highly accuracy vector magnetic measurements with global coverage (see *Part I, Section 2.2*). Together with ground data, these data sets serve as an input for the recent field models.

1.1 Earth's magnetic field maps and models

The main difficulty, when dealing with magnetic data, arises from the contribution of the magnetic fields generated in the magnetosphere, ionosphere and by Field Aligned Currents. Of particular concern is the part generated in the ionosphere that is seen as an external source by the ground-based measurements and as an internal source by satellites. To circumvent these problems one approach is to process (sometimes referred to as filtering) the survey data and to remove, as much as possible, these undesirable contributions. This is an approach used in deriving crustal magnetic field models. An alternative method is described as a "comprehensive" approach. It consists in modeling

as accurately as possible all the main sources of the magnetic field. Even though this approach has been very efficient in providing accurate models of the core magnetic field, it has been less successful regarding the lithospheric field. These different approaches and some of the recent models are presented below, on short.

IGRF. The *International Geomagnetic Reference Field* is an internationally agreed series of global SH models of the Earth's magnetic field, dealing with the sources which are only in the Earth's core. It is provided by the International Association of Geomagnetism and Aeronomy (IAGA), Division V-MOD every five years (Mandea and Macmillan, 2000; Maus et al., 2005b). In this case, the Gauss coefficients are considered linear time dependent for these five years intervals. These models are simply truncated series: for the core field, up to degree and order 13 for the current 11^{th} generation, and for the secular variation, up to degree and order 8. Additionally, a predictive linear secular variation is given for the subsequent five years (Finlay et al., 2010). IGRF models now cover the period from 1900 to the present and record the ongoing decay of the dipole field that can be seen in historical recordings since absolute measurements were first initiated but there are not appropriate for long term studies of the field behavior. The series of Gauss coefficients, the source codes and on-line calculators can be found [1].

Gufm1. The gufm1 is a model of the magnetic field for the interval spanning $1590 - 1990$ (Jackson et al., 2000). The model early data are largely based on historical observations of the magnetic field. The greater part of the new dataset originates from unpublished observations taken by mariners engaged in merchant and naval shipping. Considerable attention is given to both correction of data for possible mis-location (originating from poor knowledge of longitude) and to proper allocation of error in the data. The variability of navigational errors, as a function of the duration of the voyages, was analyzed too. For the period before 1800, more than $83,000$ individual observations of magnetic declination were recorded at more than $64,000$ locations and taking into account. Also more than 8000 new observations are for the 17^{th} century alone. The gufm1 [2] model was built from similar data from the 20^{th} century and due to a vastly expanded historical dataset, the model contains over $365,000$ data. The model is parametrized spatially in terms of spherical harmonics and temporally in B-splines and no account is explicitly taken for external fields. It has improved the resolution of the ancient core, exploiting the vast amounts of data available in national libraries, and now represents the longest continuous model of the field available from direct observation. This model

[1] www.ngdc.noaa.gov/IAGA/vmod/IGRF-11
[2] http://jupiter.ethz.ch/ cfinlay/gufm1.html

have been used (see *Part I, Section 2.4*) to study some specific temporal characteristics of the Earth's magnetic field, such as the secular variation.

CM4. The basic idea, behind the *Comprehensive Models* series, is to co-estimate the major source fields using many different data sets. The fourth version was developed by Sabaka et al. (2004). The CM4 model relies on POGO, MAGSAT, Ørsted and CHAMP satellite data and observatory hourly means, and is continuous through the time span from 1960 to mid 2002 [3]. By including data sets from different altitudes, a separation of various source fields is facilitated. It describes the static field up to degree and order 65. The secular variation, which has to be taken into account in field models extending over several decades, is represented by cubic B-splines with $2.5-years$ knots, spacing through degree and order 13. The model accounts for field aligned currents and the ionospheric and magnetospheric fields along with their induced counterparts and all their systematic and less systematic variations. Due to the simultaneous description of most of the known field sources, the comprehensive models have extensive applications as reference models especially. In addition, due to the co-estimation of all the source fields, the CM4 allows studies where the isolation of the field from one or several specific sources is desired. The great advantage of CM4 is that it is a continuous model. The CM codes can return the local geodetic X,Y,Z components of the $\vec{B}$ field of the various contributions: core, crust, primary magnetospheric, secondary (induced) magnetospheric, primary ionospheric, secondary (induced) ionospheric, toroidal magnetic field due to in-site radial currents at satellite altitude.

GRIMM. *GFZ Reference Internal Magnetic Model* series is derived by Lesur et al. (2008) and Lesur et al. (2010), from CHAMP satellite data and observatory hourly means. It covers the years 2000 to 2010. It special characteristic is the use of full vector satellite data at high latitudes at all local times. GRIMM attempts to separate fields into the contributions generated by the ionosphere and the field aligned currents on one hand and, on the other hand, the contributions generated in the Earth's core and lithosphere [4]. This model uses order six B-splines with $0.5-years$ knots to describe the time-dependence of the core field up to degree 16. Despite the high order in the time representation, GRIMM series, as well as other comparable up-to-date global field models, fail to perfectly fit the secular variation calculated from observatory monthly means. However, the GRIMM model is able to very well describe the field components and their temporal variation at the Earth's surface.

[3] http://dtam.gsfc.nasa.gov/cm/
[4] http://www.gfz-potsdam.de

CHAOS. *CHAOS* [5] is based on the CHAMP, Ørsted and SAC-C data. The new modeling approach considers data selection comparable to the GRIMM series. It is derived by Olsen et al. (2006b), Olsen et al. (2010). The seven years of high-precision data ($1999 - 2005$) gave an opportunity to study the fine structure of secular variation, described by cubic B-splines. CHAOS describes the core and crustal fields up to about degree 40 and the reliable description of the secular variation was obtained up to degree 15. The unpredictability and chaotic nature of the Earth's magnetic field is recognized. With the new secular variation model, the characteristic timescale for the core-reorganization was estimated to be of order of 20 years for short wavelength structure (about 1400 km) at the core-mantle boundary.

POMME. *POtsdam Magnetic Model of the Earth* [6] provides the geomagnetic field in the region from the Earth's surface to an altitude of a couple of thousand kilometers. It gives the estimation of the internal, as well as the external geomagnetic field. The input data are from the CHAMP satellite. The Ørsted and SAC-C data are used only to verify the accuracy of the model. The core field secular variation is modeled up to degree 15. It is the most advanced model concerning the influence of the large-scale magnetospheric contributions in specific coordinate systems, in which the currents are best organized (Maus and Lühr, 2005).

MF. *Magnetic Field* series [7] are designed to isolate and represent the crustal (lithospheric) field only (Maus and Weidelt, 2004; Maus et al., 2005a, 2008). The purpose is to determine the crustal field with sufficient precision such that it may be used for geological and geophysical interpretation. The core field model, used in earlier MF3 model, was based on five years of Ørsted data, three years of CHAMP data and observatory measurements. Starting with MF4, the POMME (Maus et al., 2005b) field model was used. The long-wavelength parts of the crustal field, unfortunately, are also subtracted from the data. The latest, MF7 model, was produced using CHAMP measurements from 2007 to 2010 when CHAMP satellite at that time was in low-Earth orbit (LEO). It resolves the crustal magnetic field to spherical harmonic degree 133, corresponding to 333 km wavelength resolution. MF7 model is the first satellite-based magnetic model to resolve the direction of oceanic magnetic lineations, revealing the age structure of the oceanic crust.

The latest and best models of the Earth's crustal field have been derived mainly from the CHAMP satellite data set. GRIMM (Lesur et al., 2010) and CHAOS (Olsen et al.,

[5] http://www.gfz-potsdam.de/pb2/pb23/Models/CHAOS/index.html
[6] http://www.gfz-potsdam.de/pb2/pb23/
[7] http://www.gfz-potsdam.de/pb2/pb23/SatMag/model.html

2009) models, present a remarkable agreement up to SH degree 45 (Lesur et al., 2008). Other models go up to SH degree 60 or 65, but they start to be contaminated by noise. Conclusively, there is no reliable global crustal field models for high degrees of SH.

WDMAM. *World Digital Magnetic Anomaly Map* project of Korhonen et al. (2007) is an important achievements in describing the Earth's crustal field. It is due to an international scientific joint effort, supported by the International Association of Geomagnetism and Aeronomy (IAGA), as well as by the Commission for the Geological Map of the World (CGMW). Because maps of the crustal magnetic field are so useful for regional geologic understanding, and because magnetic surveys are usually acquired over small regions, there was a need to assemble the individual magnetic surveys into a combined grid, a compilation. This map is derived from a multitude of aeromagnetic surveys, acquired over continents or from ship cruises, during the past seven decades. For the first time, these data are referenced to satellite magnetic measurements and geomagnetic observatories in a comprehensive way. The resulting product is a printed magnetic anomaly map of the world at scale $1 : 50,000,000$ (Figure 11) and a digital database (which was used in this study), that includes anomaly values on a grid of $3'$ *arc* resolution (about 5 km at the equator), on the World Geodectic System 1984 ellipsoid (WGS84). The nominal observation altitude is defined as 5 km above the geoid and gives the essence of the magnetic anomalies up to spherical harmonic degree 15, capturing wavelengths between 10 and 2500 km. The B version contains model data derived from CHAMP satellite data, which were included in preexisting data compilations, and marine age data. Larger wavelengths (corresponding to > 400 km maximum resolution or spherical harmonic degrees < 100) are spurious, at a global scale in aeromagnetic compilations, and were removed, and replaced with the satellite based lithospheric model $MF5$ to degree 100, downward continued also to 5 km altitude.

Now, WDMAM is an ongoing project through a more complete spatial coverage and a better control of the long wavelengths from the following the 2012 Swarm mission[8], consisting in three satellites providing direct measurements of magnetic field gradients (Maus et al., 2006), which will improve the next version of the lithospheric magnetic anomaly map of the world. The map and the digital xyz ascii grid of the magnetic total intensity, was downloaded[9] [10], as a permanent archive. The changing core field, due to the acquisition of data at different epochs, makes the compilation more challenging. Also, due to the differences in coverage and quality, the grid is not everywhere consistent. This is observable when focusing on short-wavelengths, for example around 40 km diameter in

[8](http://www.esa.int/esaLP/LPswarm.html

[9]http://geomag.org/models/wdmam.html

[10]http://earthref.org

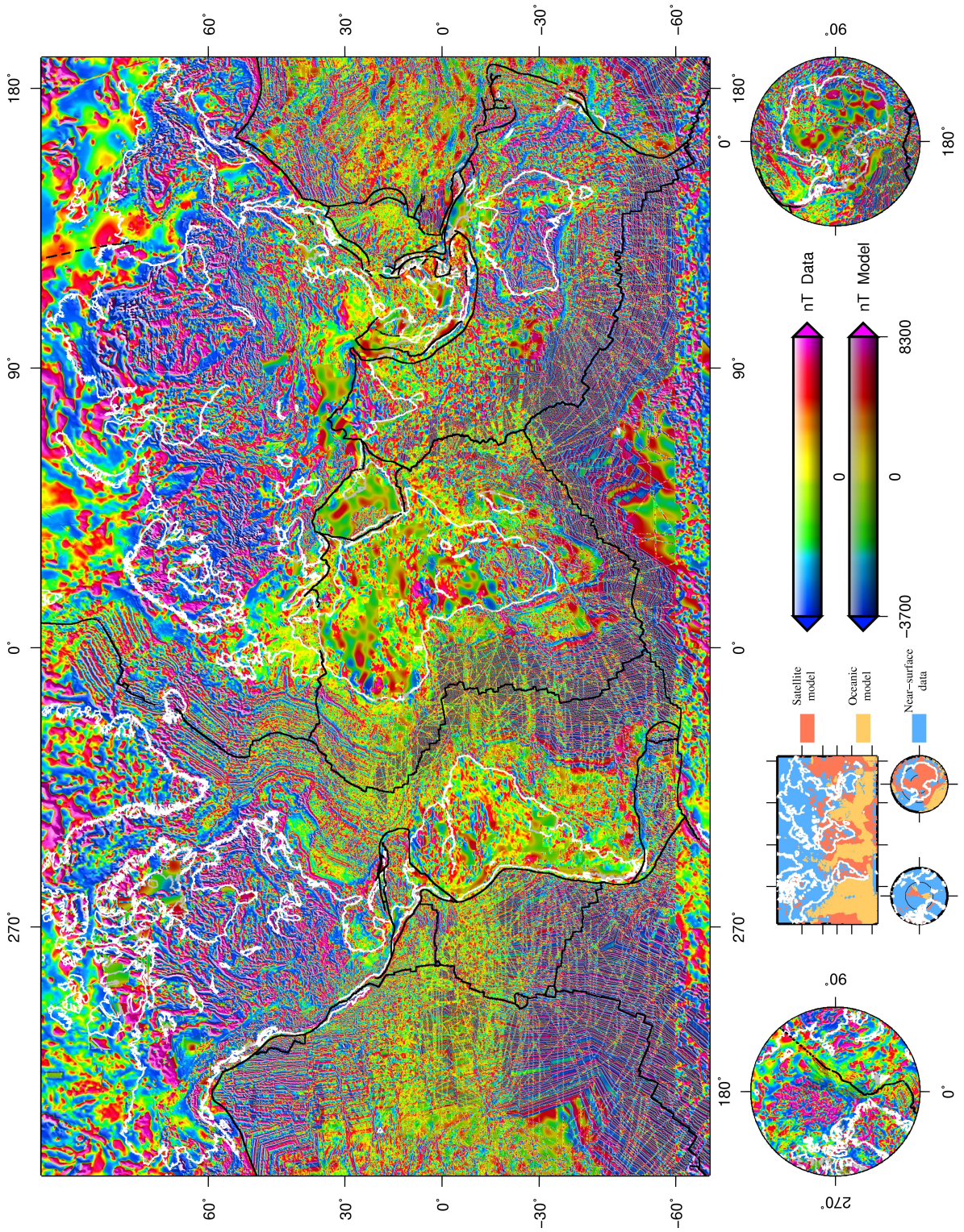

Figure 11: The first edition of the World Digital Anomaly Map (CGMW, 2007), B version, which gives the essence of the worldwide magnetic anomalies at 5 *km* altitude. Thanks to the satellite based model and to the near-surface data magnetic field model, the general shapes of the magnetic anomalies can be predicted *(Korhonen et al., 2007)*.

the case of smaller impact craters. The coverage is sparse especially over oceans but also over Africa, Asia and South America where the lack of data or data sampling, delivered by different nations, is not homogeneous. It varies from about 50 km for India, 30 km for South America or Africa, to 1 km spacing for North America or Australia. Despite the areas of various intrinsic resolutions, WDMAM gives the essence of the worldwide magnetic anomaly distribution (Hamoudi et al., 2007).

1.2 Mars' magnetic field models

The MGS vector magnetic field observations, from all phases, were compiled into different maps and models of the three components of the Mars' magnetic field. At an altitude of 400 km, the martian magnetic field varies between ± 650 nT. The first model, based on those measurements, was that of Purucker and Dyment (2000), using binned measurements of the radial field only. Later, an ESD-equivalent source dipole approach (Arkani-Hamed, 2001) used all three components to produce the first SH model (up to degree 50) of the martian magnetic field. Later models were more elaborate and used measurements of all three mission phases, to produce SH models up to degree 90 (Cain et al., 2003; Arkani-Hamed, 2004) or constant altitude maps through ESD (Langlais et al., 2004) or continuous magnetization solutions (Whaler and Purucker, 2005).

Maps of the vector components of the Mars crustal magnetic field are constructed at the mapping altitude (360 to 410 km) using selected sets of data, obtained with the Mars Global Surveyor magnetometer, during thousands of orbits around the planet, in $90's$. The models used different data sets and modeling techniques. On the Earth, spherical harmonics models are commonly employed but it is very sensitive to incomplete data coverage. In contrast, on Mars, Equivalent Source Dipoles (ESD) approach is less sensitive to geographical data distribution and, implicitly, more adequate. In addition, it gives insights on what could be the magnetization contrasts in the source region.

Equivalent Source Dipoles (ESD) model. The internal dipole model (at each point, the magnetic field is the result of the addition of the fields created by each individual dipole source) of Langlais et al. (2004), at 400 km altitude (Figure 12) was used in the first stage of this study (see *Part II, Chapter 3*). At that time, 2004, data was limited to $1997 - 2001$ time period, with no external field proxy, and an horizontal resolution of about 200 km.

New ESD - Langlais, Purucker and Mandea (LPM) model. With 2.3 million measurements over 7 years, spatial resolution of 120 km, external field proxy for Mapping

Orbit (MO) data, a new ESD improved model, at different altitudes ($200-400\ km$), was carried out. ER data (the pitch angle-dependent attenuation, of the reflected electrons, contains information, on one hand, about the crustal magnetic field, which reflect the electrons, and the atmosphere, on the other hand, which absorbs them) also was used. The new model have more input data, an improved spatial resolution, a sharper definition and better noise reduction. This model offered me more confident results for detailed studies on some craters.

Correlative spherical harmonic model. The low-noise internal magnetic field model of Lillis et al. (2010) is an evaluation of a spherical harmonic representation of the magnetic field of Mars using a correlative technique and the seven years ($1999-2006$) of mapping orbit magnetic field observations from MGS. Internal total magnetic field is evaluated at 400 km from a degree 51 spherical harmonic representation. The contribution from non-crustal sources varies geographically and ranges from 1 to 2.5 nT, comparing with 3 to 5 nT in the LPM model. The spherical harmonic solution and a 2° (110 km) grid can be downloaded [11] and the technique is described in Purucker (2008). The wavelength resolution of the data is 417 km.

Electron Reflectometry (ER) model. For detailed analysis of impact craters the electron reflection (ER) map of Lillis et al. (2008b) was used. The total field, due to crustal sources only, at 185 km altitude above the martian datum, was mapped. The Electron Reflectometer instrument was included in the MGS payload and used, in connexion with MGS' magnetometers, to measure the magnetic reflection of electrons caused by crustal fields. The map was constructed from data collected between $1999-2006$, with 3 years of additional data and a better statistical confidence than the previous ER maps. The full details of ER technique and the construction of the ER magnetic map may be found in Mitchell et al. (2007) and Lillis et al. (2008b). The increased resolution (200 km) and its sensitivity, which is greater for weak crustal fields, allows me to study the magnetic signature of a substantially large number of impact craters, than was possible with the other maps.

Mars Crustal thickness model. The model of Mars crustal structure (Neumann et al., 2004) as the radial difference between the crust-mantle density interface and the surface topography [12] is represented by spherical harmonic coefficients to degree 85, and revealed the crustal structure of Mars to 300 km wavelengths. The model incorporates the data coverage from 5 years of topography (MOLA) and gravity measurements.

[11] http://core2.gsfc.nasa.gov/research/purucker/mars2009
[12] ftp://ltpftp.gsfc.nasa.gov/grids/mars/marscrust3/

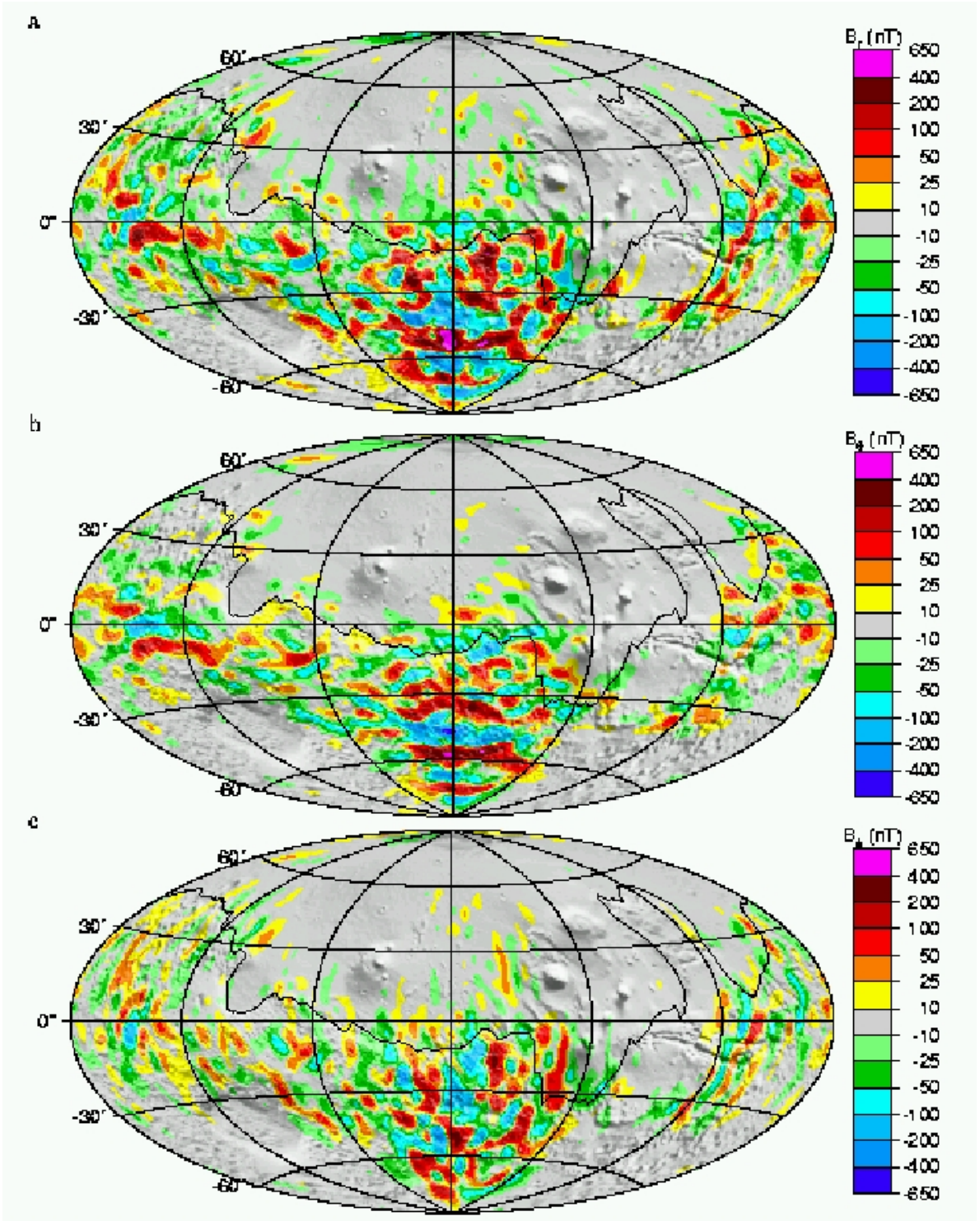

Figure 12: Predicted vectorial components of the magnetic field of Mars at an altitude of 400 *km* above the martian mean radius, based on the equivalent source dipole model (ESD) overlapped onto a martian shaded relief *(Langlais et al., 2004).*

The planet's hemispheric dichotomy correspond to a crustal thickness of 30 and 60 km in the northern and southern areas, respectively. Gravity anomalies at wavelengths of $250-300$ km are similar in spatial scale with many craters and, when they are combined with topography, they may contain information about the response of the crust to impacts. The thickness of the model varies between $5-100$ km, with the smaller values near the center of largest impact craters (especially in the northern highlands), with a chosen mean crustal thickness value of 40 km. The North Polar crustal anomalies, unrelated with visible craters, suggest ancient large impacts, obliterated by the youngest geological processes.

1.3 Moon's magnetic field models

Recent global models of the internal magnetic field of the Moon include those of Purucker (2008), Richmond and Hood (2008) which are using the vector fluxgate magnetometer of Lunar Prospector and the map of Mitchell et al. (2008) using the electron reflectometer (ER). The most detailed map of lunar magnetic field, especially in the small scale features, is that of Purucker who maps the magnetic field components to spherical degree 150, corresponding to wavelengths of 73 km (see *Part II, Chapter 3*). The map is made from radial and theta field data in the lunar wake and tail regimes, after first removing a simple model of the external magnetic field (Purucker et al., 2006). This model is based on the physics of external field in quiet times, and during times when the Moon is in the Earth's magnetic tail. An uniform external field is then determined for each orbit, based on least-square approach that utilizes the 3-dimensional vector observations. Determination of the equivalent source dipoles (Purucker et al., 1996) allows for the generation of altitude-normalized maps of B_r, B_θ and B_ϕ and B at 30 km altitude. The error levels of this map are connected with the accuracy of the Lunar Prospector magnetometer, around 0.5 nT.

Correlative model. This is a preliminary model of the internal magnetic field of the Moon, developed by Purucker (2008), using a correlative technique for the low-altitude observations of Lunar Prospector magnetometer, taken after the end of 1998, when the satellite's orbital altitude was reduced from about 100 km to $30-33$ km (Figure 13). An internal dipole model, from which a simple model of the external field was removed, was used to construct a 178 degree spherical harmonic model, at a constant altitude of 30 km above the mean lunar radius. The model details the low magnetic field regions, associated with large basins, the anomalous areas antipodal to some of the largest lunar carters, but is less reliable in the polar regions.

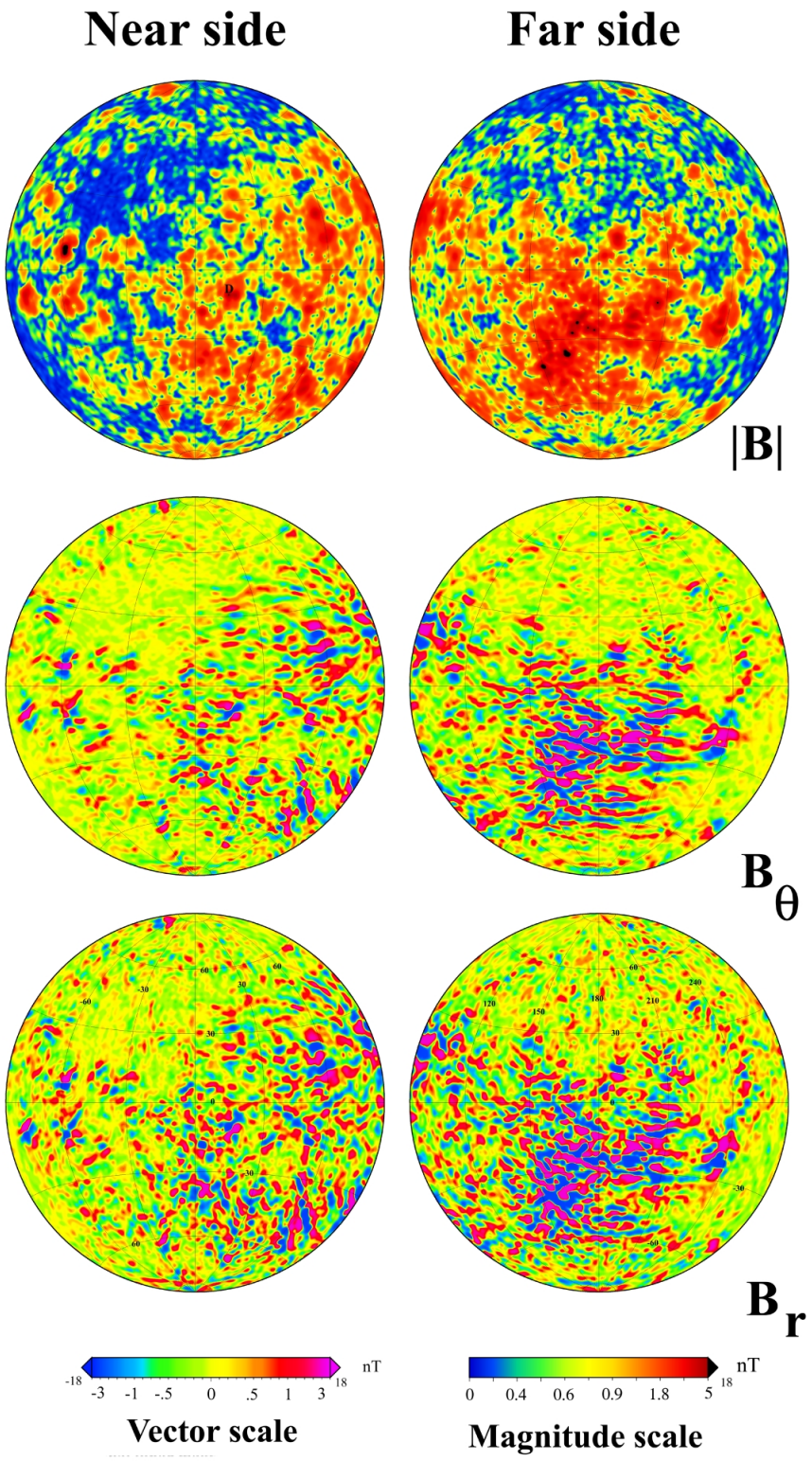

Figure 13: Global spherical harmonic model of the internal magnetic field of the Moon, at 30 *km* above the lunar mean radius. From top to bottom: scalar magnitude, theta and radial component fields. Lambert equal area projection *(Purucker, 2008)*.

Combined, sequential and coestimation, spherical harmonic model. The newest global internal magnetic field model, based on Lunar Prospector (LP) fluxgate magnetometer observations, is a global spherical harmonic model (Purucker and Nicolas, 2010), using combined sequential and coestimation approach, for modeling its interaction with the solar wind. The model is created between degrees 1 and 170, corresponding to 64 km full wavelength resolution, at 30 km mean altitude above the mean lunar radius [13]. Terms for spherical harmonic degrees up to 15 (666 km wavelength) are almost absent from the Moon's magnetic field. This map is able to increase the map resolution, at least locally, regarding smaller or ancient craters.

1.4 Global topographic maps

Next, topographic maps used in this thesis are presented. The position of craters and their rings were first established on the morphologic evidence no other than their circularity, and traces of their internal topography as not completely buried rims. Generally, a look on any circular, rimmed depression with a lower floor than the level of the terrain, in which the possible crater was excavated, was taken. The main objective, in this first stage, was to identify and analyze the magnetic signature associated with the shape of a large impact crater, determined with the help of their topographic shape.

Earth

SRTM30. The Shuttle Radar Topography Mission (SRTM) (Farr et al., 2007), on board Space Shuttle Endeavor, acquired enough data in 2000 to obtain the most complete near-global high-resolution map of the Earth's topography. SRTM30 is a 30 arc second resolution global topography grid (approximately 1 kms near the equator) and spans the globe from $60°N$ to 56° latitude, produced by NASA and NIMA and downloaded from NASA portal [14]. A new version of the data set, including bathymetry, is also available (Becker et al., 2009) and used.

Mars

MOLA map. The MOLA map is the result after an year of global mapping of Mars with Mars Orbiter Laser Altimeter (Zuber et al., 1992; Smith et al., 2001), operated on the MGS (Mars Global Surveyor) spacecraft between 1998 and 2001. The MOLA topographic grid, at 1/64° resolution in latitude (aprox. 1 km at the equator) and 1/32° resolution in

[13] $http://core2.gsfc.nasa.gov/research/purucker/moon\_2010/index.html$
[14] http://www2.jpl.nasa.gov/srtm/

longitude (aprox. 2 km at the equator), is available through the Planetary Data System [15]. MOLA reveals, as well as crustal thickness distribution map (Neumann et al., 2004), that the Mars' dichotomy boundary are not circular, and there is not an evidence that a huge single-scale impact would shape the planet in the past. Maybe another process or processes than impacts, should be invoked to explain the hemispherical difference (for example a possible ancient ocean in the northern lowlands).

Moon

ULCN map. The Unified Lunar Control Network 2005 (ULCN) it is a lunar topographic model (Archinal et al., 2005) based on a combination of Clementine mission images and the old ULCN network (derived from Earth and Apollo photographs, Mariner 10 and Galileo images of the Moon). Only in limited regions of the Moon higher density topographic data are available. Due to the irregular distribution of the data and relative accuracy, it was not used intensively.

Kaguya-SELENE map. The finest lunar global shape and the detailed topographic map, especially for the far side of the Moon (Araki et al., 2009), with a spatial resolution of lesser than 0.5°, has been derived from laser altimeter from Japanese (JAXA) lunar explorer SELENE or Kaguya, in 2008, data being available to the public from 2009 onward [16], as a NASA World Wind platform.

LOLA map. LOLA topography is an equi-rectangular map-projected Digital Elevation Model, which has been obtained by Lunar Orbiter Laser Altimeter Investigation on Lunar Reconnaissance Orbiter Mission (LRO), in 2010. LOLA was designed to measure the shape of the Moon by measuring with a higher resolution (64 $pixels/degree$) and a nominal accuracy of 10 cm, in order to produce a global geodetic grid, to which, all other observations can be precisely referenced (Chin et al., 2007; Smith et al., 2010). A wide variety of crater depths and degradation stages were observed. Topographic maps of the North and South poles were produced by Kaguya laser altimeter. LOLA provided the highest resolution of the lunar geodetic grid (10 m radial and 100 m spatial accuracy) with respect of the Moon's mass center.

All the data used in this thesis, and presented before, were downloaded from NASA Portal, by courtesy of NASA, in a frame of a joint research with Planetary Geodynamics Lab team, on magnetic signature of large impact craters, at NASA Goddard Space Flight Center, in 2010.

[15] http://pds-geosciences.wustl.edu
[16] http://worldwind.arc.nasa.gov/

Many other planetary global field models, based on different data types (from ground based to satellite) and considering several field sources are continuously derived by several teams around the world. On the Internet, some institutions provide their models together with on line calculators or source codes. Those codes are convenient for generating *synthetic data*. The GFZ German Research Center for Geosciences [17] or the National Oceanic and Atmospheric Administration NOOA [18] offer a good overview on the great number of field models together with user-friendly calculators. Several models of the crustal field have been produced in the last decade. Some of available lithosphere models or maps for Earth, Mars and Moon, together with some other physical parameters models (topographic, magnetization) are utilized in *Part II, Chapter 3*.

[17] http://www.gfz-potsdam.de/portal/gfz/Struktur/Departments/Department+2/sec23/topics/models
[18] http://geomag.org

Chapter 2

Small scale magnetic fields: impact craters signatures

Meteorite impacts, a term which is usually inferred to include impacts of asteroids and comets with planetary bodies, are the most common geological events that occur within the Solar System. Large numbers of the resulting craters are observed on most of the rocky planets and their moons, and even on the asteroids themselves. Nowadays, it is known that collisions between astronomical bodies have been an integral process in the formation of the solar system. The Earth, experienced the same bombardment as the other planetary bodies (Lillis et al., 2007). Additionally, the impacting bodies themselves may have contributed to the Earth's budget of volatiles or to frustrate the development and evolution of early life.

Catastrophic events, such as meteor impacts and associated phenomena, have not been given enough consideration when assessing the forces that have shaped our Planet. The Earth's ancient geological history contains clear signatures of such events (Mandea and Purucker, 2005). For example, 65 My ago, at the end of the Cretaceous period, a meteor impacted the Yucatan Peninsula, this event being considered as a possibility for an end of the "Age of the Dinosaurs". A large celestial body, which impacted the nowdays southern Africa region, may end the "Age of Amphibians", 256 My ago. The meteor which created the Manicouagan Crater, in Canada, may end Triassic period, 210 My ago. Most of the terrestrial impact craters that ever formed, however, have been obliterated by other terrestrial geological processes. Some examples however remain. A number of small impacts are recorded in recent history on the Earth, most recent notable events being the 1908 Tunguska fireball in Siberia. There, a small meteoroid exploded above the ground created a shock-wave that flattened over $2,000\ km^2$ of uninhabited forest. In 1947 a meteorite fall over Sikhote-Alin region of Siberia, and formed about 100 cavities up to 23 m in diameter, due to the break-up of a small iron meteorite. However, the only well-

documented first-hand account, of a large explosive impact event, was the 1994 collision of the Shoemaker-Levy 9 comet into Jupiter. Hence, most of our understanding comes from the examination of the craters preserved on the Earth, high-yield weapons testing and hydrocode modeling (computer simulation) of impact events. The recognition of impact cratering as an important planet-building and planet-modifying process on Earth has been rather slow. But scientists are now realizing that giant impacts have had a determining influence on geological and biological evolution of our planet.

To-date, approximately 192 impact craters have been clearly identified on Earth with a current average detection rate of $3-5$ impact sites per year. Now, in the last decades, using data obtained by probes orbiting Mars and Moon, including those that have delivered landers and rovers on the Red Planet, researchers estimated the number of craters 500 m wide or larger at nearly $600,000$ on Mars, and at nearly a million, on the Moon. Our planet has not been less bombarded than Moon or Mars, but here on Earth, erosion and plate tectonics have slowly erased these terrestrial scars. For this reason, the temporal distribution of impact craters seems highly irregular, on continental areas, and more than half are less 200 My old. No craters have been confirmed on deep oceanic floors, due to the recycling of them. At the same time, several possible impact structures still awaiting confirmation, but extreme climatic conditions, remoteness or vegetation and sedimentary covers, have limited further investigations.

The geologic processes, associated with meteorite impacts, are vastly different from those commonly observed on the Earth, except possibly earthquakes. Unlike normal terrestrial processes which progress slowly over thousands and millions of years, crater-forming impacts are destructive events where a massive amount of energy is released almost instantaneously due to their cosmic hypervelocity, which is around 200 kms^{-1}. The shock-waves that result from an impact at this velocity propagate through the target at a rate greater than the speed of sound through rock (about $5-8$ kms^{-1}), generating shock pressures in excess of 100 GPa at the point of impact. No other surface geological process is capable of producing pressures of this magnitude. The kinetic energy (bigger than 10^7 J/g) stored within a meteorite or comet traveling at cosmic velocities is comparable with the nuclear energy from U^{239} fission of 10^{10} J/g, after Mark (1987).

2.1 Impact cratering and morphological features of impact craters

Observations of terrestrial and extraterrestrial craters provide complementary data sets to study craters and the cratering process. The differences, between these data sets,

complicate the comparisons, significantly. On one hand, features discernible in the types of data that can be acquired for terrestrial craters, where observations are made in situ and to a limited extent in three dimensions, are often impossible to detect or measure at comparable craters on other planets, where the only available data are acquired from orbit. On the other hand, terrestrial craters are subject to rapid erosion, tectonic modification, and burial leaving few fresh examples, whereas craters on other planets are typically less modified and provide much information on crater morphology and structure, especially regarding relationships between geometric aspects of craters as a function of crater size and target parameters. It is therefore difficult to accurately compare a pristine extraterrestrial crater with the eroded terrestrial crater, particularly if the original size or nature of the eroded crater is uncertain. Terms like "crater size" and "crater diameter" in reference to impact structures that have complicated morphologies, especially large or eroded ones which exhibit multiple concentric features, can be a problem, leading to ambiguity in establishing which feature is the best measure of crater size. This still inconsistent use of terminology leads to considerable controversy within the impact community. A large proportion of terrestrial impact structures is so highly degraded they are no longer clearly recognizable as craters. Beside this, buried structures, formed in active sedimentary basins, account for about one third of all known terrestrial impact craters (Grieve and Masaitis, 1994). To provide a consistent measure of the degree of erosion of an impact crater, a numeric system in seven steps was developed by scientists from the Geological Survey of Canada, which is widely used by the impact community (Grieve and Pilkington, 1996).

Mars has a lower mass than Earth, and so it has a lower ability to attract objects; however, Mars is closer to the asteroid belt than Earth, and has a better chance of being hit by objects from that region. Still, Mars has less craters on its surface than the Moon. One major reason is the fact that Mars has a thin (low-pressure) atmosphere that prevent the smallest meteors from space to reach the surface. The large number of craters indicates that the surface of Mars is ancient, and has probably remained unchanged for billions of year. During the Noachian epoch, the oldest period of the geologic history of Mars (between $4.5-3.5\ Gy$ ago), many of the largest craters on Mars were formed. They have various amounts of weather. Some are worn down by wind and possibly water, while others look freshly formed.

With no atmosphere, everything reaches the surface of the Moon. Without water, tectonic plates or erosion, the Moon is full of "scars", the most dramatic features being impact craters. A large number of them are believed to be formed $4.1-3.8\ Gy$ ago, in the Late Heavy Bombardment (LHB) period, and by interference, on Mars and Earth, too.

2.1.1 Crater forming process

The model for crater formation, after French (1998), divides the process into three main stages of crater development: *contact and compression*, describing the generation of the shock-wave during the initial stages of impact, *excavation* of the transient cavity, and *modification* of the transient cavity to produce the final crater form. These stages are discussed separately below for convenience, but they occur simultaneously with one stage beginning before the previous stage ends and they generally form an overall continuous process of crater formation.

Contact and Compression This stage begins as soon as the projectile makes contact with the target, and involves the transfer of kinetic energy of the projectile into the target rocks. At the contact a shock-wave is produced. This shock-wave is transmitted both outward from the point of impact into the target rock as well as back into the projectile itself. The target rock is heated, melted and vaporised, flowing hydrodynamically (Grieve, 1991). The energy of the shock front has been found experimentally by French (1998) to decay as power function of the distance from the point of impact. Shock pressures of greater than 50 GPa are sufficient to melt the target, while pressures between 5 and 50 GPa may produce distinctive shock metamorphic features within the rock. At lower energy levels (< 1 GPa), the velocity of the shock waves drops to the speed of sound and they are converted into seismic waves. This part of the process takes less than seconds. During not more than a second the projectile penetrates $1-2$ times its diameter into the target before being destroyed.

Excavation The product of crater excavation is a simple bowl-shaped cavity: the transient crater. The result is a large scale movement of material (Melosh, 1989). During this stage, the cavity of the impact crater is opened up by the interaction of the rapidly expanding shock-front within the target rocks. The process of outwards expansion of the transient cavity also raise the rim of the crater above the ground surface. Eventually, a point is reached where the shock waves can no longer transport material and the transient cavity stops to expand. For the second, before the effects of gravity and rock mechanics can exert themselves, the size of the transient cavity is at its maximum. This point marks the end of the *excavation* stage, and the beginning of the crater *modification* stage. Excavation of the transient cavity can be complete within a matter of seconds for small craters and in less than 2 minutes for the largest of terrestrial impact events. Evidence, from numerical calculations and laboratory experiments, suggests that the idealized shape of the transient cavity is not hemispherical, but a paraboloid of revolution with a depth to diameter ratio of between 1/3 and 1/4 (Melosh, 1989). This shape was used to model

the deficit of magnetization of impact craters from the Earth, Moon and Mars in the last part of the thesis.

Modification This last stage it is known as the *collapse* or *modification* stage. In essence, it is the gravity-driven modification of the unstable cavity formed during *excavation*, into a stable form, that the different crater types (*simple, central-peak or peak-ring*) are produced. The bowl-shaped depression of the smallest, *simple crater* type looks superficially like the transient cavity from which it was produced. The transient cavities formed by larger impacts are deeper and have higher raised rims. The downwards forces exerted by the cavity walls are sufficient to produce a central uplift of the rocks beneath the crater floor and a *central-peak crater*. Finally, the upper walls of the transient cavity collapse inwards along a series of roughly concentric normal faults, creating the terraced terrain that forms the outer margin of the final collapse structure (Melosh and Ivanov, 1999). For some of larger impacts, rebound of the crater floor may produce an central-peak that overshoots the point where it is gravitationally stable. The subsequent collapse of this uplift is interpreted as the mechanism for producing complex craters of the *peak-ring crater* type (Melosh, 1989). This stage of crater modification is predicted to be complete within tens of seconds, for a small crater, to minutes for a large one. Recent modeling studies of the impact that created the 170 *km* diameter Chicxulub crater suggests the main features of the structure were formed within about ten minutes of the time of impact (Stöffler et al., 2003). For simple craters, the collapse process is well understood and intuitive. For larger and morphologically more complex structures, collapse is still not well understood (Melosh and Ivanov, 1999). Their distinguishing features are described in the following.

2.1.2 Impact crater morphology and morphometry

The population of impact craters within our Solar System is morphologically diverse. The impact craters, that shape the surface of nearly every planet and satellite in the Solar System, may be divided into two distinct morphological classifications: *simple craters* and *complex craters* (Dence, 1965).

Simple craters. As the name suggests, they are circular, bowl-shaped depressions with raised rims, a form that most people associate with the word "crater". In cross-section a simple crater exhibits an approximately parabolic profile with a raised rim. Theoretically, there is no lower limit to the size of simple craters (Melosh, 1989). In reality, the minimum simple crater size is a function of the ability of the atmosphere (if it exists) to absorb small meteors. The upper limit to the size of a simple crater

is the point where the crater's morphology becomes "complex". This simple-to-complex transition, occurs at different crater diameters on different planetary bodies. Both gravity and target characteristics are involved. On the Moon and on the Mars, craters begin to exhibit complex characteristics at diameters of 15 *to* 25 *km* and of 4 *to* 10 *km* respectively due to inverse relationship between gravity and crater diameter. On Earth, the transition occurs at much lower diameters for simple craters form in sediments – at sizes smaller than 2 *km* – than in crystalline rocks where the diameter is approximately 6 *km* (Grieve and Head, 1981). The density difference in the projectiles is also an important constraint. Iron meteorites penetrate more deeply, whereas comet heads or carbonaceous chondrites explode at shallow depths.

Complex craters. In contrast, complex craters are larges craters with complicated features. They exhibit central peaks or an internal ring of mountains, terraced rim walls and flat floors. The central area of the *complex crater* contains rocks from great depth which have been structurally uplifted by gravitational collapse of the transient crater. At crater diameters just above the transition from *simple crater* to *complex crater*, complex craters exhibit central peak. At larger crater sizes the central peak is replaced by an internal mountainous ring. This ring of peaks is often referred to as the peak-ring. There is also evidence that, above a certain crater diameter, the size of the internal ring grows proportionally with the crater itself and the crater diameter to peak-ring diameter ratio is about 2. At the largest crater sizes, an additional concentric "ring" is formed, external to the main rim of the crater. This type of complex crater is known as a *multi-ring basin*. The "basin" terminology was defined by Hartmann and Kuiper (1962), who were the first to discover the multi-ring basin on the Moon, Orientale and to separate such features from impact craters. Since then, the name *multi-ring basin* has survived, but their definition has been modified. It is plotted here a lunar topographic map showing the Orientale basin (Figure 14), the largest young impact basin on the Moon. This young basin formed from a projectile that impacted the Moon about 3.8 *Gy* ago, ejecting millions of cubic kilometers of material around.

Until recently, peak-ring craters were classified as a sub-set of multi-ring basins. Now, the classification scheme of Melosh (1989) is adopted: peak-ring craters are considered to be the largest type of complex crater. The definition of a multi-ring basin is any large circular impact structure, that possesses at least two concentric scarps, one of which may be the original crater rim.

Craters on the Mars and Moon, with diameters larger than about 15 *km*, have more complex forms, including shallow, relatively flat floors, central uplifts, and terraces on the inner wall of the crater rim. In craters with diameters between about 20 and 175 *km*, the

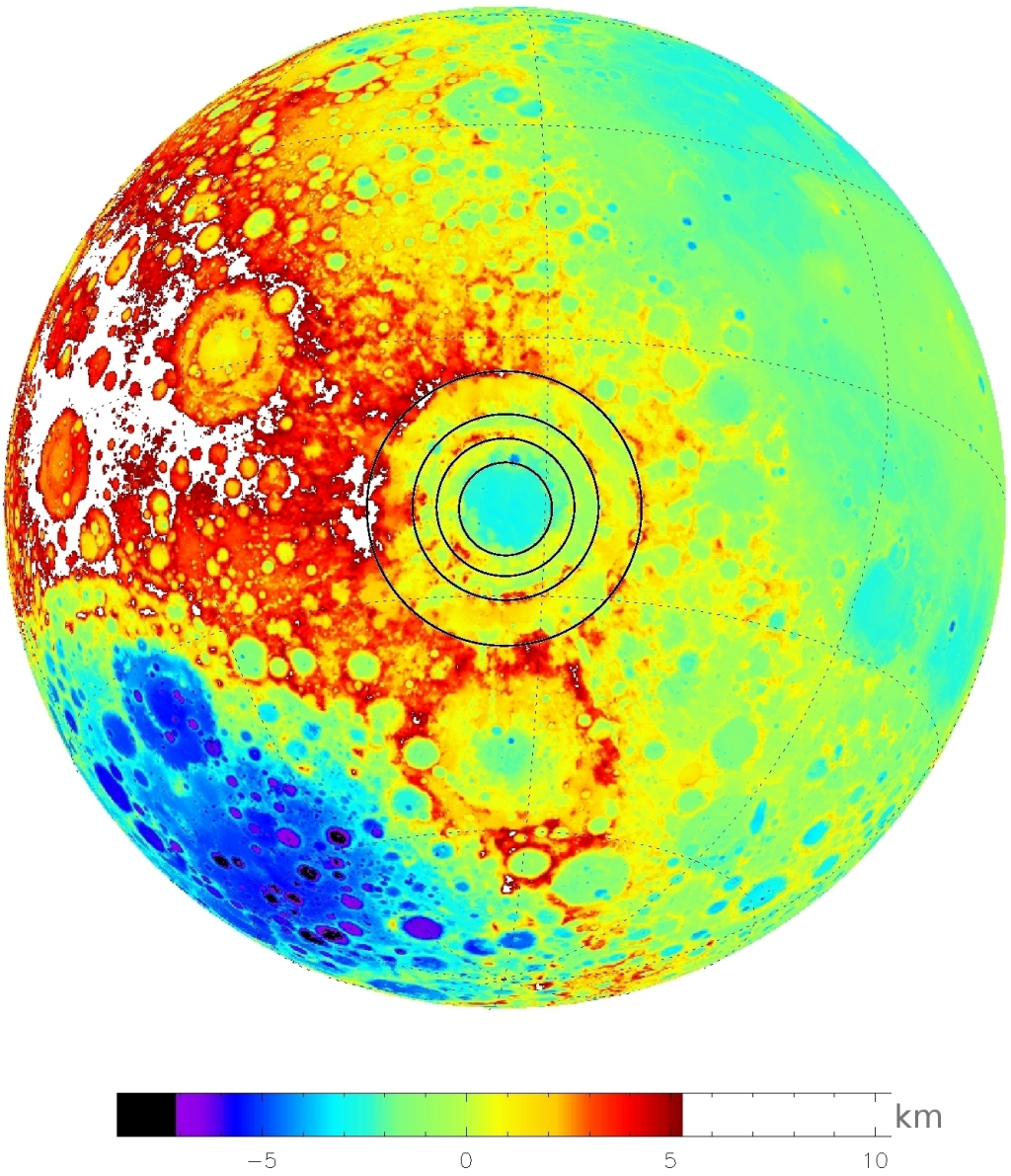

Figure 14: GRIDVIEW display of Orientale multi-ring basin system showing its relief from LOLA map. The left side of the image extends onto the dark side of the Moon, impossible to be seen from the Earth.

central uplift is typically a single peak or small group of peaks. Craters with diameters larger than about 175 km can have complex, ring-shaped uplifts. When impact structures exceed $300-400$ km in diameter, they are termed impact basins rather than craters. More than 40 such basins are known on the Moon, as well as more than 12 on the Mars, and they have an important control on the regional geology of these planets.

There are no unequivocal terrestrial multi-ring basins but three large craters on the Earth are considered as potential candidates: Vredefort in South Africa, Sudbury in Canada and Chicxulub in Mexico. Of these, only Chicxulub has not been extensively eroded or tectonically deformed. However, although the Chicxulub crater is thought to be almost pristine, it is buried under over a kilometer of Tertiary sediments. In 1996, the Chicxulub Seismic Experiment acquired a series of marine seismic deep-reflection profiles and onshore-offshore wide angle profiles across the Chicxulub impact structure. The data collected have been instrumental in furthering current understanding of large impact craters. The central findings from the Chicxulub Seismic Experiment were the identification of three distinct ring types (crater rim, peak ring and outer ring), and the presence of what appear to be massive terraced slump blocks beneath the crater. The presence of these three types of ring suggests that the Chicxulub impact structure is analogous to the multi-ring basins observed on other planets.

Early observations of craters consisted in estimating their diameters and heights. Thereafter, it was possible to estimate rim diameter, and the height of the rim above the crater floor and its height above the surrounding plains, (Baldwin, 1949, 1963). More complex crater forms were discovered: multi-ring impact basins (Hartmann and Kuiper, 1962) and peak-rings (Hartmann and Wood, 1971), as well terrestrial impact craters, in various states of degradation (Shoemaker, 1998, 1963; Beals et al., 1963; Dence, 1972). For this reason, it became more difficult to relate diameters measured from various features to the rim diameters of smaller craters. In larger craters, the diameters of peak-rings were measured from topographic high to topographic high (Hartmann and Kuiper, 1962).

Early detailed studies of the morphometry and shape of lunar impact craters showed that the ratio of key structural elements, such as rim diameter and crater depth, is consistent regardless of the size of the structure (Hartmann and Wood, 1971; Pike, 1974). The definitions of these features found in simple and complex impact craters are summarized in Figure 15.

It can easily be seen, that for a fresh simple crater, the rim-to-rim diameter, D, is obvious. Due to the increased amounts of erosion, it is only possible to measure an apparent diameter, the bigger peak-ring diameter. Rim-to-floor depth, often quoted for craters, is the sum of the rim height with respect of the original ground surface h_r and d_a. A schematic cross sections of a fresh central-peak crater are represented on the left

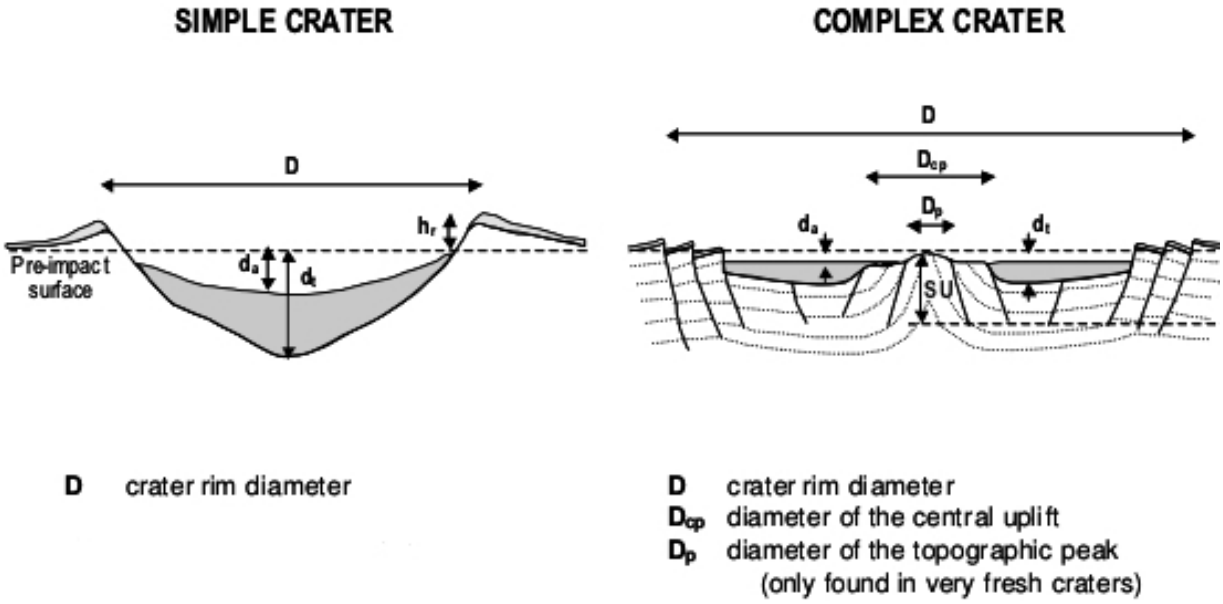

Figure 15: Schematic cross sections through a simple (left) and complex (right) impact structures. *Modified after Melosh (1989).*

of the Figure 15. Simple craters have final depth to diameter ratios of approximately 1/5 to 1/3, regardless of gravity. Complex craters form after a specific transition diameter which is reached by the transient crater.

The relationships, between morphometric features on the Earth, have been established from field measurements of a relatively small number of proven terrestrial impact craters. For Earth, as was seen before, this transitional diameter is about $2-6\ km$ for simple to complex morphologies and is dependent on target rock properties (Pilkington and Grieve, 1992; Grieve and Pilkington, 1996). Although, transient craters which go on to become complex craters have depth to diameter ratios of 1/4 to 1/3, similar to simple craters. From these studies, some general "rules-of-thumb" for the geometry of terrestrial impact structure have been proposed. For simple impact craters, the depth to the true crater floor d_t is approximately 1/3 of the rim diameter D, and the apparent depth d_a is about 1/6 of D (Grieve and Pilkington, 1996). The depth to diameter ratio of complex craters is much smaller, with the apparent depth usually less than 1/20 of the rim diameter after Rondot (1994) and decreasing as craters increase in size. For complex craters, the relationship between the size of the central peak and the rim diameter, can be more easily measured as these features are usually preserved, even in moderately eroded structures. However, there is some inconsistency in the literature about the definition of the diameter of the central uplift D_{cp}, ranging from the diameter of the central topographic peak D_p (Pike, 1985), to the "maximum extent of evidence for uplift in the true crater floor"

after Therriault et al. (1997). The diameter of the central uplift is defined here as the diameter of the top surface of this uplifted area, as shown in Figure 15 and is estimated to be between about 1/4 of D after Pike (1985) and 1/3 of D after Therriault et al. (1997). There is also an evidence that, above a certain crater diameter, the size of the internal ring grows proportionally with the crater itself. For peak-ring craters with a distinct two-ring structure, the diameter of the inner ring is 1/2 of D (Wood and Head, 1976). The same ratio is found for peak-ring craters on the Moon, Mars and other rocky worlds (Hartmann and Wood, 1971; Pike, 1985; Melosh, 1989). Surprisingly, a recent comparison shown in Therriault et al. (1997) shows a 1/3 ratio for structures up to 100 km in diameter, which should include many structures larger than the 40 km transition from central-peak to peak-ring craters. The amount of vertical movement, of the central uplift of complex craters, SU, is estimated to be about 1/10 of D after Grieve and Pilkington (1996). More precisely, central-peaks craters on Earth demonstrate stratigraphic uplift comparable to transient crater depth. While the mechanics leading to central uplift formation is still controversial, it is likely that the uplift is primarily a result of gravitational collapse of the transient crater and possible a hydrodynamic-type process. A summary of the morphometry of simple and complex impact craters is illustrated in Table 1.

Simple craters		
Apparent depth	$d_a = 0.13D^{1.06}$	Grieve and Pilkington, 1996
True depth	$d_t = 0.28D^{1.02}$	Grieve and Pilkington, 1996
Complex craters		
Apparent depth	$d_a = 0.27D^{0.16}$	Grieve, 1987
-*sedimentary target*	$d_a = 0.12D^{0.30}$	Grieve and Pilkington, 1996
-*crystalline target*	$d_a = 0.15D^{0.43}$	Grieve and Pilkington, 1996
Central-peak diameter	$D_p \approx 0.15D$	Rondot, 1994
-*topographic high*	$D_{cp} = 0.199D^{1.058}$	Pike, 1985
-*central uplift*	$D_{cp} = 0.31D^{1.02}$	Therriault et al., 1997
Peak-ring diameter	$D_{pr} = 0.464D^{1.017}$	Pike, 1985
Uplift height	$SU = 0.06D^{1.1}$	Melosh, 1989
	$SU = 0.086D^{1.03}$	Grieve and Pilkington, 1996

Table 1: Morphometric relationships of simple and complex craters. The various parameters definition are illustrated in Figure 15 or given in text. Unfortunately, the number of terrestrial craters used to define each relationship varied between 2 and 45.

2.2 Some geological aspects of an impact crater

From a more commercial point of view, impact craters on Earth have been linked to economic deposits of various materials and, in some cases, these deposits are world class. Furthermore, few of the world's largest economic resources are directly related to impact craters:the Sudbury Mining Camp in Canada, the Gulf of Mexico oil fields and the vast gold fields of the Witwatersrand Basin in South Africa. While materials in the vicinity of impact craters have been exploited for many decades, only recently an inventory has been made on the revenues generated by this exploitation (Grieve and Masaitis, 1994). Of the 179 known terrestrial impact craters, over a quarter is been associated with economic deposits while currently 31 (18%) are being actively exploited or exploited in the past. The current estimated annual revenues from these deposits is estimated at over 12 billion dollars. This estimate is based largely on North American deposits (annual revenues of 5 billion) and the gold and uranium ores of the Vredefort structure in South Africa (annual revenues of 7 billion), and does not include revenues generated from the extraction of building materials (e.g. cement and lime products at Ries, Germany of about 70 million per year) or from the generation of hydroelectric power (e.g. 4000 GWh/y from the reservoir at Manicouagan, Quebec, about 200 million per year). Deposits of materials formed in or around impact craters are divided among three categories (Grieve, 2004):

Progenetic deposits are those which originated by endogenic geological processes. In this case, the impact has the effect of redistributing the deposit allowing it to be more easily retrieved. Examples include the gold and uranium deposits of the Vredefort structure in South Africa (7 billion dollars per year). The Vredefort dome of 70 km diameter represents the central uplift of a deeply weathered large impact crater. Estimates of the size of Vredefort crater using geophysics (Henkel and Reimold, 1998) and morphometric analysis (Therriault et al., 1997) give diameters between $250-350$ km, roughly the same size of the present day extent of the Witwatersrand Basin, one of the world's most important mineral fields, representing more than a third of the total production of gold and more than $136,000$ tones of uranium associated with the gold ore.

Syngenetic deposits are those which originate during or shortly after an impact event. These types of deposits are, generally, attributed to the direct deposition of energy into the target rocks causing melting of the crust and/or phase transitions of mineral species. The Cu-Ni deposits at Sudbury, Ontario, are of the first type – created by impact melting of the Archaean rocks from the lower crust that already had elevated concentrations of nickel and copper (2 billion dollars over the last five years). As a phase transition, diamonds may derive from the melt sheets created by impact into graphite or coal-bearing target rocks. Perhaps, the most famous impact diamond resource is Popigai structure.

Name	Type	Commodity	Resource
Vredefort	progenetic	gold,uranium	48 ktAu, 136 ktU recovered
Carswell	progen(epi)	uranium	1.76 Mt(0.66%U)
Charlevoix	progenetic	ilmenite	Ti ore mined for a century
Slate Island	progenetic	gold	vein gold, up to 14 g/t over cm's
Sudbury	syngen(epi)	Ni/Cu/PGE	1650Mt(1.2%Ni, 1.05%Cu, 4g/tPGE
Popigai	syngenetic	diamond	diamondiferous tagamites
Kara	syngenetic	diamond	-
Chicxulub	epi(hydroc)	oil & gas	30,000 $Mbbl$ oil, 15,000 bcf gas
Tookonooka	epi(hydroc)	oil	assoc. with Tintaburra oil filed?
Siljan	epi(hydroth)	led/zinc	300kt(3%Pb, 1.5%Zn, 70ppmAg)
Saint Martin	epi(sediment)	gypsum	since 1901 mined a 10m thick layer
Manicouagan	epi(water)	hydroelectric	5stations, 4,500MW
Puchez-Katunki	epi(water)	hydroelectric	-
Manson	epi(water)	hydroelectric	soft drinking water

Table 2: Summary of economic resources associated with largest impact structures. Resource values are calculated assuming 100% recovery *(Grieve and Masaitis, 1994).*

The Popigai tagamite is 500 m thick and may be traced over $10-15$ km length. The industrial diamonds found here are only resistant to fracturing and not gem-quality stone and use in many cutting applications.

Epigenetic deposits are formed after the impact and are, generally, attributed to hydrothermal alteration, formation of enclosed basins with isolated sedimentation, or the flow of fluids into structural traps associated with the crater. Hydrocarbon accumulations associated with craters are of this type. Almost half the impact craters in petroleum producing basins of North America is related to hydrocarbon resources with high economic value (11 out of 26 known structures). Post-K/T tectonics within the Gulf of Mexico, directly linked to the Chicxulub impact event (Grajales-Nishimura et al., 2000), deformed the breccia formation to create the structural traps for oilfields, such as Cantarell. For three large Russian structures: Popigai, Kara and Puchez-Katunki were identified dominant minerals like clays, zeolite and calcite indicating that hydrothermal systems, with temperatures in the range of $50°-350°$C, were active for several thousand years after the impact event. The up to 30% zeolite deposits (Grieve and Masaitis, 1994) from Puchez-Katunki have not been exploited yet. Very large impact craters, such as Sudbury, which can maintain hydrothermal activity for millions years, can produce their own exhalative systems in the overlying sedimentary rocks, allowing the trapping of later, metal-rich hydrothermal fluids to form Zn-Cu-Pb deposits (Ames et al., 2000).

Hildebrand and Pilkington (2002) discovered similar carbonate mounds which they named crater floor exhalative or "crafex" deposits, at present day depth of 1.1 km above the Chicxulub structure, Mexico. They have not yet been tested for any potential metal

association. Deformation of the target rocks by impact may also affect the local hydrogeology increasing their ability to store ground water, as in the case of Manicouagan. Due to the high permeability of shattered rock, it is important for powering several hydroelectric stations, providing a very profitable and renewable resource.

A summary, of the known resources associated with the largest terrestrial impact craters and the resource-forming processes, is presented in Table 2. Meteorite impact craters should be considered valid targets for the exploration of exploitable natural resources on Earth or on extraterrestrial bodies in the future. Now, impact craters can also form tourist centers, like around the Ries crater in Germany, or Meteor Crater in USA, or recently built center dedicated to Sudbury impact crater and its associated mining industry by the city of Sudbury, Ontario.

2.3 Geophysical signatures of impact craters – previous studies

The processes, resulting from hypervelocity impact that cause the structural and mineralogical changes in the target, also affect the petrophysical properties (density, magnetic susceptibility, acoustic velocity) of the target rocks. These changes can be mapped using the appropriate geophysical technique. Unlike geological mapping, most geophysical techniques can detect property contrasts beneath the surface and so they can be used to provide constraints on the internal geometry of the crater, which can only be otherwise determined through drilling. Geophysics has also been instrumental in the discovery or, after that, subsequent investigation of the significant number of terrestrial impact structures that have been completely buried by post-impact sedimentation. However, the geophysical signatures associated with impact structures are not consistent, even for structures of roughly the same shape and dimension. Target stratigraphy and the level of erosion are also important factors in determining the observed geophysical response. As it is possible to develop geophysical anomalies, similar to those commonly associated with impact craters by normal terrestrial processes, geophysics is still not considered a diagnostic tool for the identification of impact craters. While a good argument can be made from coincident anomalies in geophysical data, confirmation of the impact origin of candidate structures can only be made by the identification of shock metamorphic features and meteorite fragments.

The expected geophysical responses over impact structures as described by previous workers are summarized below. It should be noted that with the exception of the seismic technique, the geophysical characteristics of impact structures given in Grieve and Pilk-

ington (1996), French (1998) or Melosh (1989) are considered to be the classical texts describing the geological processes resulting from hypervelocity impact. They have focused on the geophysical signatures of craters, formed in crystalline targets rocks, or targets with a thin layer of sedimentary rock over a crystalline basement. There are only a few case studies in the literature describing the potential field responses of impact craters formed in dominantly sedimentary target rocks and the geophysical characteristics of this group of structures are not well documented. For this reason, together with the huge amount of satellite data sets, an important part of the work has been dedicated to study the magnetic signature of impact craters (see *Part II, Chapter 3*).

2.3.1 Magnetic signature of impact craters

Impact craters, commonly, exhibit some strong geophysical signatures (Pilkington and Grieve, 1992). Among them, airborne magnetics is the cheapest and, hence, the most widely available, of all the geophysical mapping techniques. Consequently, magnetics is potentially one of the most powerful tools for the identification of new structures potentially of impact origin, particularly those that are buried by up to a few hundred meters of post-impact sediment. However, the magnetic signatures, associated with impact craters, show a much greater variability than either gravity or seismic responses.

Based, primarily, on studies of craters formed in crystalline rocks, the papers on the geophysical signatures of impact craters (Pilkington and Grieve, 1992; Grieve and Pilkington, 1996) suggested the main effect of extraterrestrial impact is to reduce the magnetic susceptibility of the target rock, resulting in an overall magnetic low. It has recently shown that magnetic data can be useful for determining morphometric parameters of the impact craters. Pilkington and Hildebrand (2003) showed that the estimate of the transient cavity diameter will correlate with the extent of the subdued magnetic response in the target lithologies. They also suggested that the central magnetic high can be used to give an estimate of the extent of the thick melt layer or the diameter of the uplifted magnetic basement rocks. However, due to the highly variable nature of the observed magnetic responses over known craters and considerable scatter in these data, the interpretation of these morphometric features is likely to be more subjective and should be treated with caution than from either the seismic or gravity techniques. The relatively intense magnetic anomalies occurring within the crater can be attributed mainly to:
– uplifted magnetic lithologies, often basement;
– magnetized impact melt rocks or breccia;
– shock remanent magnetization or demagnetization;
– some combination of the above.

The magnetic signature of impact craters can be complex but, generally, two types of features are often apparent (Pilkington and Hildebrand, 2003). Short-wavelength, relatively intense magnetic anomalies, that occur near the center of the structure, are the first of these types of features. Impact craters also disrupt the pre-existing magnetic signature and that disruption is the second feature that can sometimes be recognized (Spray et al., 2004). Magnetic signatures at impact craters can originate from impact breccias, as in the Ries crater, impact melt rocks, as at Sudbury, and/or impact-induced thermal overprint of stratigraphically uplifted material, as at Vredefort dome (Pilkington and Hildebrand, 2003)) above which, a negative anomaly appears. This can be seen in Figure 16, too, where the magnetic map of ΔT over the Vredefort impact crater, at 5 km above the geoid was drawn by means of GMT software from the Magnetic Anomaly Map of the World (WDMAM). The negative magnetic anomaly in the center of the Vredefort structure was interpreted by Henkel and Reimold (2002) as a shock induced remanent magnetization of magnetite ($Q = 3 - 4$) generated at the time of impact. Generally, the largest impact structures are characterized by broad magnetic lows (Grieve and Pilkington, 1996; Dunlop, 2005).

High-amplitude aerial or ground magnetic anomalies may be found over the centre of larger impact structures with diameters larger than 10 km (Pilkington and Grieve, 1992). These anomalies are described as "high-frequency" indicating a shallow magnetic source and usually have magnitudes < 1000 nT, such as those observed over Chicxulub (Figure 61) and Ries (Pilkington et al., 1994).

Case studies on the magnetic responses over 15 Australian impact structures, categorized into three groups based on their stratigraphy and with significant differences between the magnetic signature of structures formed in different rock types, were carried out by Hawke (2004). A possible impact origin for the oldest circular structure and its magnetic anomaly: Bangui, Central Africa was carried out by Girdler et al. (1992). There have been very few detailed studies of the magnetic field response over impact structures formed in purely sedimentary targets. However, a ship-borne magnetic survey over the Mjølnir structure in the Barents Sea (Tsikalas et al., 1998) showed magnetic anomalies of 100 nT coinciding with the crater moat of the structure, not with the central uplift, as expected. These anomalies were attributed to weakly magnetized melt dispersed throughout the allochthonous breccia layer or injected into the shattered rocks of the crater floor.

The concentric magnetic trends have been used by many scientists to predict the transitory diameter of impact structures and this has led controversy over the size estimates of some of structures. An example of this includes the debate on the dimension of the Acraman impact structure (Hawke, 2003). The mechanism for producing these magnetic

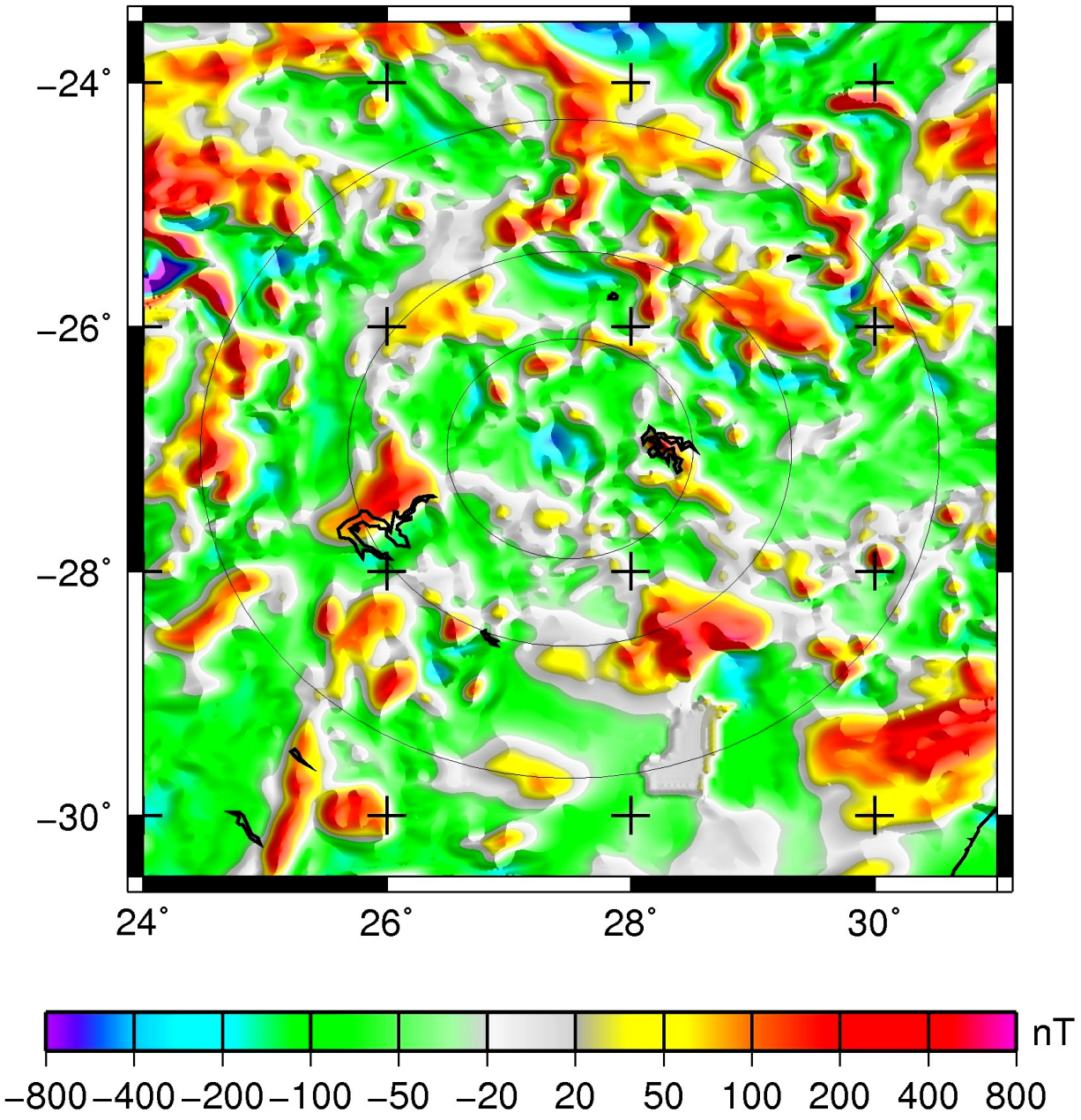

Figure 16: Magnetic map (ΔT), over the Vredefort impact crater, at 5 km above the geoid. The light black circles represent the main rim and additional rings interior to this.

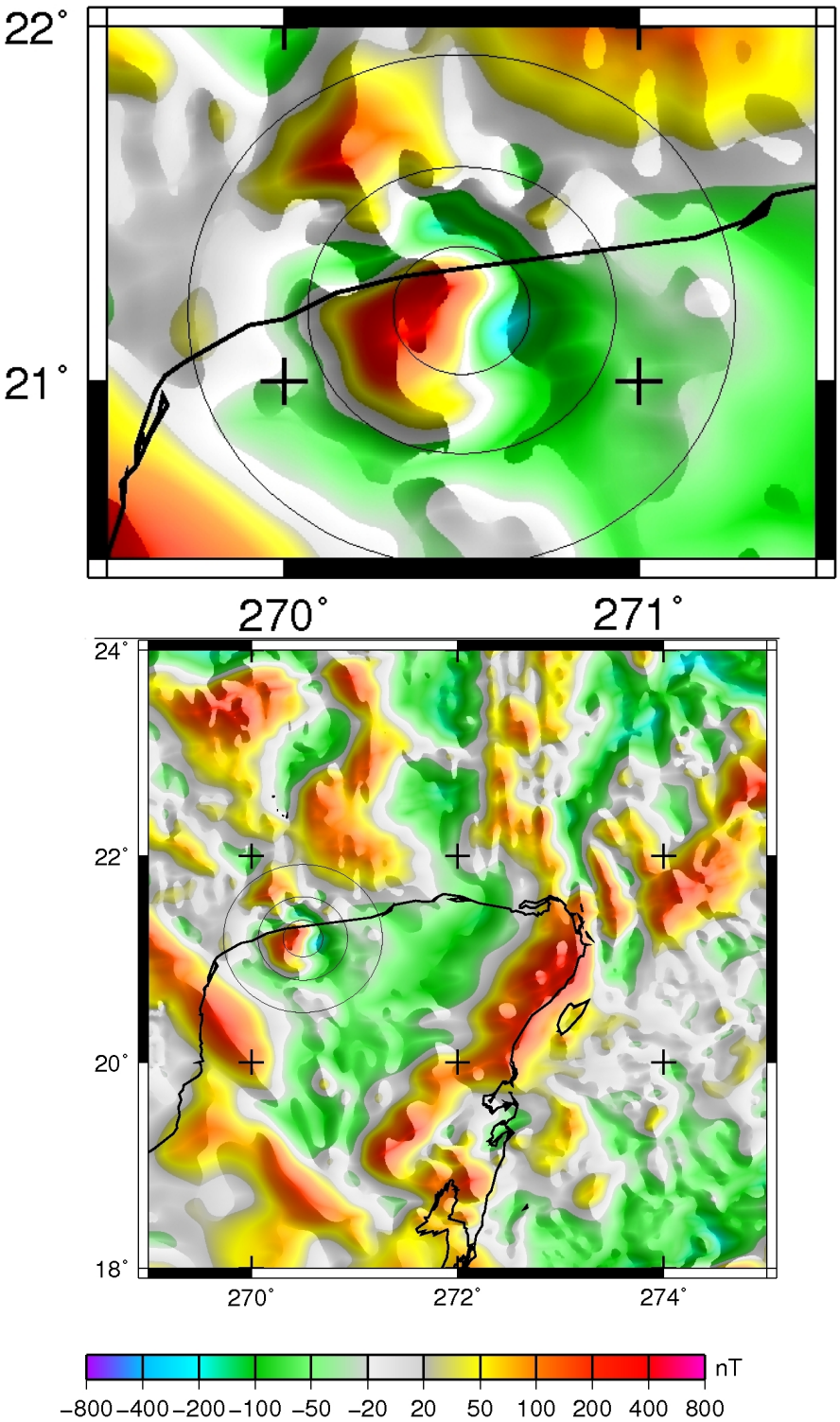

Figure 17: Magnetic map (ΔT) over the Chicxulub impact crater (with a detail on the top), at 5 *km* above the geoid. Coastline showed as solid black line. The light black circles represent the main rim and additional rings interior to this.

lows is still not entirely clear. Experimental studies have shown that shock pressures of 1 GPa are sufficient to remove magnetic remanence and pressures in excess of 10 GPa can reduce magnetic susceptibility (Pilkington and Grieve, 1992). In previous studies, these shock pressures were restricted to an area smaller than the transient cavity. Weakly magnetic post-impact crater fill and allochthonous breccia can also contribute to the subdued magnetic response. Modeling studies of the Canadian impact craters exhibiting reduced magnetic field responses has shown that these effects alone are insufficient to account for the amplitude of the observed anomalies over these structures (Scott et al., 1997). These authors suggest that the magnetic properties of the rocks have also been attenuated beneath the transient cavity by low pressure shock waves, too . The oxidation of magnetic minerals in the target rocks fractured by the impact event may also be a contributing factor to the magnetic responses over impact craters, particularly of deeply eroded structures. The variability of the magnetic signature of Earth's craters are provided by the works of Cowan and Cooper (2005). Numerical modeling also, using 2 D hydrocodes, can predict the distribution of pressure and temperature from which inferences can be made about the final magnetization distribution (Ugalde et al., 2005). While very useful, this numerical model does not take into account later hydrothermal processes, which can change or alter the magnetization distribution, and can be often be a source of ore deposits (Clark, 1997). Ideal body theory developed by Parker (1991), Parker (2003) and Purucker et al. (2008) establishes bounds on quantities such as the minimum magnetization strength required to explain a magnetic field distribution.

To date, there has been a little work to systematically determine the petrophysical property variations that occur within different target rock types as a result of hypervelocity impact on Earth and practically impossible on Mars and Moon. Studies of shocked rocks and minerals from Earth's craters began with Meteor crater, Ries and older structures formed in Precambrian crystalline rocks of the Canadian Shield (Beals et al., 1963; Dence, 1972). Hood et al. (2003) and Lillis et al. (2009) studied impact phenomena and shock effects of basin-forming impacts on Mars.

The remanent magnetization in the ALH84001 martian meteorite (Weiss et al., 2002; Weiss et al., 2009) indicates that a strong global field should have existed in the planet history which have impressed the Noachian crust, more than 4 Gy before. Current knowledge of impact demagnetization of the martian crust was summarized by Louzada et al. (2011). Hood and Zakharian (2001) correlated for the first time the shock pressure with magnetic field intensities over impact basins of Mars. The absence of central magnetic anomalies over the youngest impact basins of Mars and Moon has been used to date the cessation of their dynamos at about 4 Gy ago (Acuña et al., 1999; Arkani-Hamed, 2001, 2004; Lillis et al., 2007, 2008a; Frey, 2008; Hood et al., 2011; Purucker et al., 2012).

Earlier works of Halekas et al. (2002) and Richmond and Hood (2008) have shown that many lunar impact craters are demagnetized because there were no internal magnetic field at the time of impact.

As these characteristics are the ones on which this study is focusing, they are analyzed in more details in *Part II, Chapter 3*.

2.3.2 Other geophysical signatures

Gravity signature. Most craters are characterized by a gravity low whose diameter increases with increasing crater size. Larger craters may also have a central gravity high (Manicouagan, Chicxulub and Vredefort) that is most likely caused by structural uplift of denser rocks. The characteristic density changes of the target rocks and the resulting gravity responses were summarized in papers by Pilkington and Grieve (1992) and Grieve and Pilkington (1996). In these papers, authors suggest that a negative gravity anomaly is the most common geophysical signature coinciding with impact craters. The gravity field over the Chicxulub crater is typical of the negative gravity response expected over a large impact crater, as can be seen in Figure 18. The data is displayed here in perspective view, where highs in the gravity field appear as positive topographic features. The crater was first identified from the presence of the 170 km diameter circular gravity low, which closely correlates with the location of the crater rim defined by reflection seismic profiles (Hildebrand et al., 1991). While it may be a somewhat convenient analogy, the gravity anomalies do not strictly reflect the topography of the structure. Rather they map the distribution of low density material within the crater.

A large component of the 30 $mGal$ negative anomaly is due to crater-fill, including allochthonous breccia and impact melt, as well as the overlying post-impact sediment (Pilkington et al., 1994; Ebbing et al., 2001; Sharpton et al., 1992). Fracturing and brecciation of the target rock to produce autochthonous breccia increases porosity, thus lowering the overall density of the rock, which also contributes to the negative anomaly. Modeling studies of the gravity field over Chicxulub (Ebbing et al., 2001) suggest that the density of the allochthonous breccia is 10% lower than the undisturbed target rock, with in-situ brecciation lowering the density by 5%. The central gravity high is related to the uplift of dense material beneath the central cavity of the peak-ring crater.

Gravity may be a useful tool for determining the morphometry of an impact structure, particularly the diameter of the crater rim, identified by the extent of the gravity low and the central uplift from the presence of a central gravity high. Modeling of gravity data can also be used to estimate the depth extent of deformation and amount of structural uplift that has occurred (Plescia, 2003), although such estimates are only reliable if they are constrained by density measurements of the target rocks and impact generated

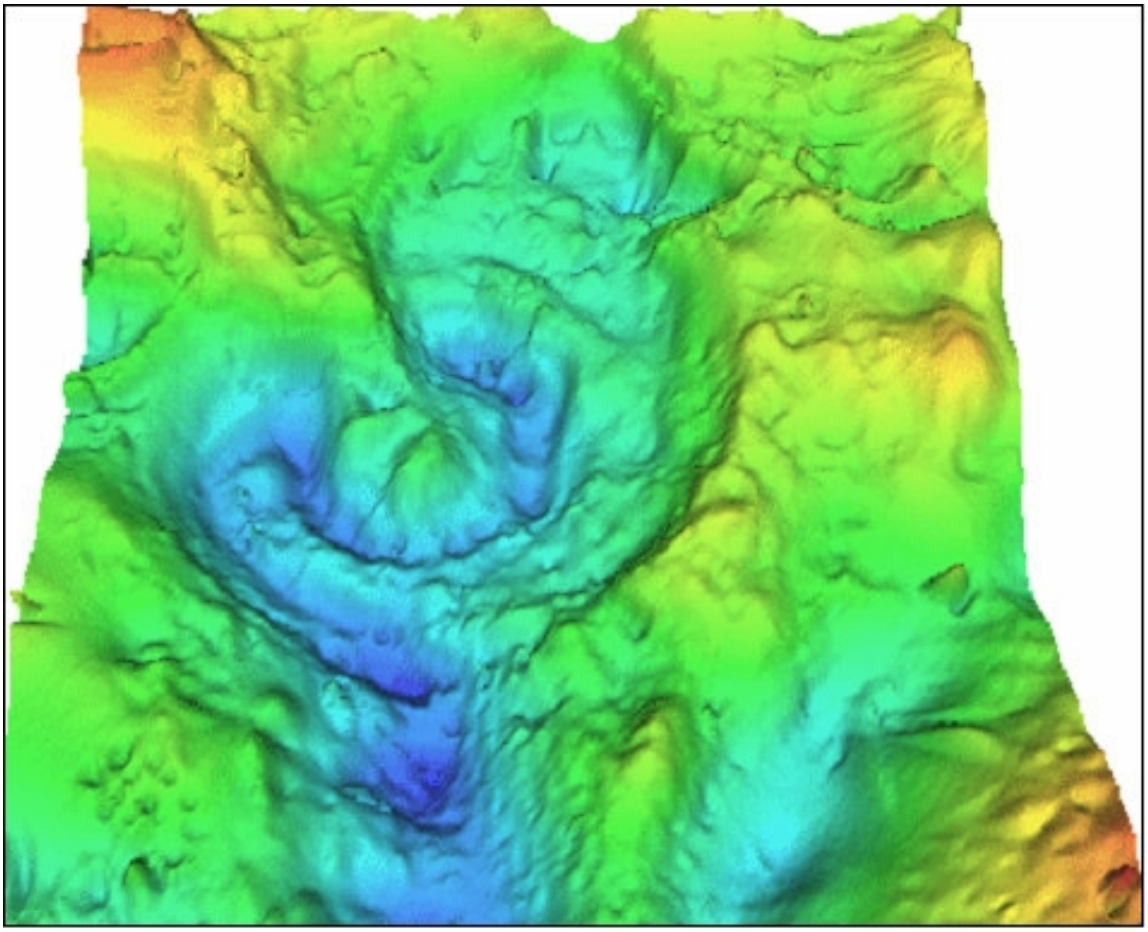

Figure 18: Oblique three-dimensional view of the Bouguer gravity anomaly of combined land and shipborne gravity survey over the 170 km diameter Chicxulub crater (viewed from the South). The rim of the crater closely correlates with the semicircular concentric gravity low pattern. The central gravity peak (green) is due to uplifted basement. *Courtesy by the Lunar and Planetary Institute.*

lithologies. There is, in fact, an order of magnitude of variability in the maximum negative anomaly observed for structures of similar size. There are two main reasons given for this high degree of variability. The first is related to the lithology of the target rocks. A greater increase in porosity would be expected to result from impact into crystalline target rocks, which are generally denser and have a lower porosity than a sedimentary target. Typical density contrasts between fractured and undisturbed target rocks range between $0.15 - 2.5\ g/cm^3$ (Pilkington and Grieve, 1992). Secondly, erosion will act to reduce the negative gravity response by removing the low-density impact generated lithologies, particularly the allochthonous breccia layer. Anyway, the main effect of erosion is to reduce the amplitude of the gravity anomaly without changing its general shape. Positive gravity anomaly coincident with the central part of the structure are also observed over the Montagnais (Pilkington et al., 1995) and Mjølnir (Tsikalas et al., 1998) structures. All of these structures have been formed in sedimentary target rocks, which may have been poorly consolidated and contained a high volatile content at the time of impact. It is plausible that the impact had little effect in reducing the density of the sedimentary target rocks and the resulting gravity anomaly is primarily due to the uplift of denser consolidated sediments or crystalline basement.

Seismic signatures. Beyond gravity and magnetic signatures, a crater can also be seen by other geophysical methods, the more considered being the seismic investigations. Seismic reflection and refraction surveys largely map changes in sonic velocity with depth. One of the primary effects of meteorite impact is brecciation and fracturing, which can reduce the speed of sound in the rock by up to 50%, after Pilkington and Grieve (1992). Seismic reflection is most appropriately used in sedimentary basins. Consequently, most data is acquired for petroleum exploration and detailed coverage is largely restricted to Phanerozoic sedimentary basins. Most of the main structural features of an impact crater can be imaged by a seismic reflection survey, including the raised crater rim and the central uplift, ring depression and faults forming the terraces of complex structures (Tsikalas et al., 1999). The amount of structural uplift SU can often be directly measured from reflection seismic data and a marked transition between incoherent and coherent reflectors is often considered a reasonable estimate of the dimension of the transient cavity (Grieve and Pilkington, 1996). Refraction is a simpler form of the seismic technique, where the travel times of seismic signals are analyzed as a function of distance away from the source. This technique lacks the detail of seismic reflection surveys and simply aims to map the sharp contacts in the velocity structure of the Earth.

Seismic reflection and refraction data sets, across impact craters, provide structural and lithological information, which is particularly useful when the crater is buried. How-

ever, the acquisition of seismic data is expensive, and the data sets that are currently available for impact structures are variable in quality. The best seismic images of a crater to date have been obtained from three dimensional tomographic refraction data across the Chicxulub crater (Morgan et al., 2002). Sub vertical faults are particularly good located by seismic reflection data within the target rocks but, there are some ambiguities in relating these to geological mapping of faults at surface.

Electrical signatures. The electrical geophysical methods, including the resistivity, electromagnetic (EM) and magnetotelleuric (MT) techniques are, all, used to map the ability of the ground to conduct electricity. The main change in the electrical properties of the target rocks due to impact will probably be an increase in conductivity due to the fracturing of the rock, due to increasing porosity and, more importantly, permeability, allowing a current to be carried by ions in pore fluids. High conductivity would be expected for allochthonous breccia and post-impact sedimentary fill deposits, while low porosity melt might be expected to have a lower conductivity. Simple resistivity mapping experiments (Henkel and Pesonen, 1992), vertical electrical soundings or frequency domain (EM) method, have also been used as mapping tools to identify zones of very resistive crystalline target rocks or, of low resistivity, associated with fractured crystalline target rocks and post-impact crater fill. Electrical sounding survey using the MT technique at Chicxulub, conducted by Unsworth et al. (2002), detected conductive features attributed to saline water in fractured target rocks to depths of 5 to 10 km. This technique had not sufficient resolution to be able to map structural elements of the crater with a better degree of accuracy. Despite recent advances in the acquisition and processing of EM and resistivity data, only a few structures have been surveyed using these techniques. The greater cost of these surveys in comparison to the potential field methods, and the inability of the few deep sounding surveys, that have been trialled to adequately resolve the internal structure of the crater were the reasons.

Ground penetrating radar signatures. Ground penetrating radar (GPR), the high-frequency electromagnetic technique, is analogous to seismic reflection, except that it maps horizons with different dielectric properties rather than acoustic impedance. While this technique, like seismic, can deliver high-resolution images of the subsurface, it has a limited depth of investigation from about 10 m in many cases, up to about 30 m in ideal conditions. GPR was used to investigate the cause of a circular ring of sinkholes, that it is formed at a radial distance of $70 - 90$ km from the center of the Chicxulub structure (Schmidt and Williams, 1995), which approximately defines the position of the crater rim.

Although estimates of crater diameter that are obtained from geophysical data alone may be accurate, they should always be interpreted with a degree of caution. Individual anomalies are strongly dependent on the geophysical properties of the target rocks, on how these properties change with depth, and on the extent of erosion, burial and post-impact deformation. Furthermore, there is an inherent non-uniqueness in modeling geophysical data, and multiple models can reproduce the observations equally well. But despite of different types of crater structures which can be produced by an impact event, the process is repeatable: similar sized impacts will generally produce structures of similar shape and dimension, with a predictable type of crater form, function of the event magnitude and the surface gravity of the target body. There are also similarities in the changes produced in the physical properties of the target rock due to the impact, resulting in characteristic geophysical signatures over many impact structures. Their magnetic fingerprints represent my work in modeling the magnetic effects of large impacts, in the second part of my thesis. The analyze of magnetic signature patterns of impact craters from Earth, Mars and Moon, seen in global maps and models would be a challenge.

Chapter 3

Impact craters seen by magnetic maps and models

The lithospheric field is the magnetic contribution that remains after subtraction of the core plus the external fields from the measured signal. From this point of view, the lithospheric field is defined as an *anomaly* with respect to dominant internal and external contribution. This definition shows how difficult is to ascertain the geophysical origin of the anomalies, since the accuracy with which the data are corrected, for core and external fields, has a profound effect on them. This lack of clarity can be illustrated in the spectral domain which shows a different behavior from a planet to another and underline the complexity and uniqueness of the geomagnetic field.

Figure 19 shows the magnetic energy spectra built for the Earth, Moon and Mars. The Earth shows a break in the slope of the power spectrum which clearly appears between degrees (n) 13 and 16. Again, let us note that this change of slope, in the geomagnetic power spectrum, represents transition from core-dominated processes to lithospheric-dominated processes. The dominance of the internal, static magnetic field, of lithospheric origin on Mars and Moon and no contribution from a present core-source magnetic field are illustrated too. The difference in magnitude in the power spectra spans almost twelve orders of magnitude between the three bodies. This illustrates the large disparity which exists in the remanence carriers that host the magnetic field (Garrick-Bethell et al., 2009). However, it is intriguing that the shape of the lunar and martian power spectra is not very different, suggesting that, despite the fact the remanence carriers may differ, the source depths on the two bodies may be very similar.

The lunar and martian spectra may also serve as a model for the Earth's unknown low degree crustal power spectra, due to the fact their spectra show only the signature of the lithospheric field which is remanent in origin (Voorhies et al., 2002). Inside Moon and Mars, the liquid part, if still exists, is perhaps too small to generate a significant

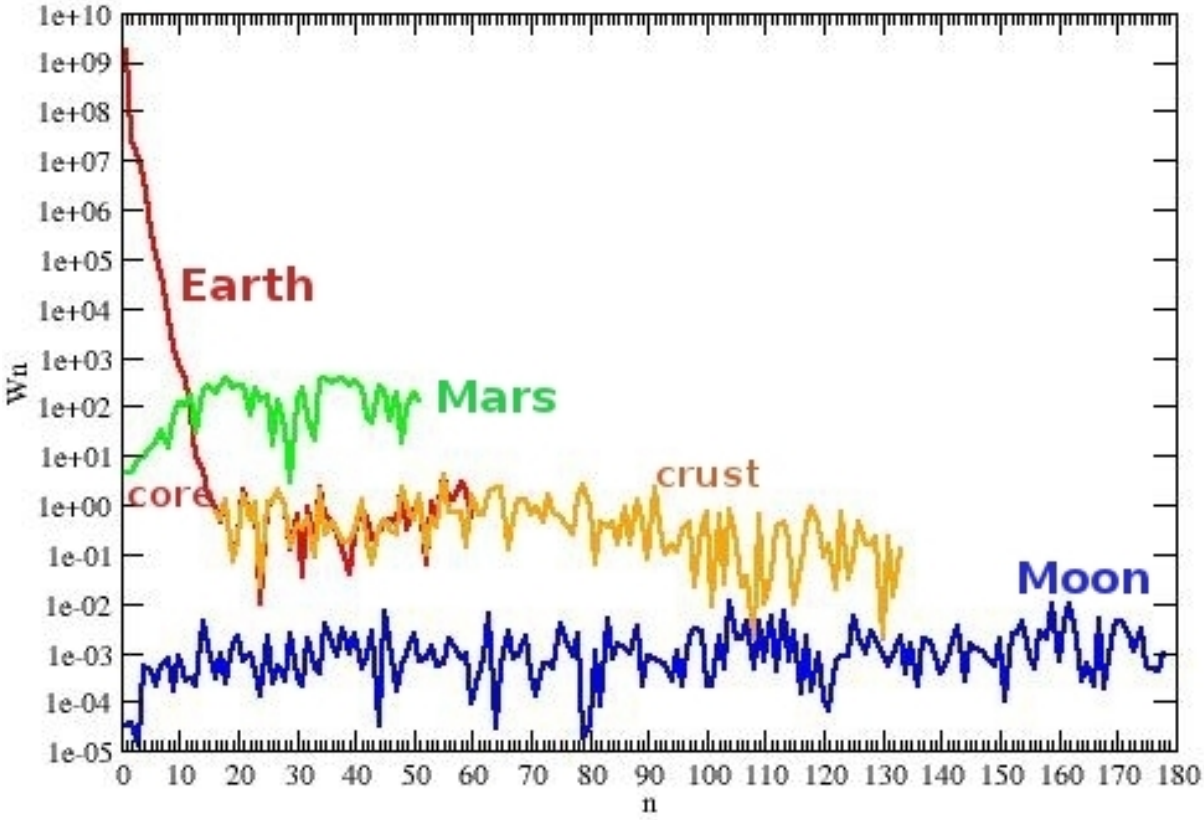

Figure 19: Lowes-Mauersberger power spectra at the Mars' (*Lillis et al., 2010*) and Moon's surface (*Purucker, 2008*), compared with recent determinations of the power spectra of the magnetic field of the Earth using POMME 6.0 and MF7 models (*Maus, 2010, 2010a*). W_n is the mean square amplitude of the magnetic field in nT^2 produced by harmonics of degree n. All the global models used satellite data: MGS, LP, CHAMP and Ørsted, CHAMP only, respectively.

dynamo. Moreover, the temperature gradient within the mantle might not be as large as in the Earth. Also, the volatile content of the upper mantle might be low, inhibiting the formation of an asthenosphere, which lubricates the mantle and makes plate tectonics possible on Earth. Fortunately, the very low surface temperature does not prohibit a crustal remanence field to remain, and so, an evidence of dynamo action in Mars' or Moon's past may exist.

It is known that the mode of dynamo operation has also changed with time. Existence of magnetic anomalies on the Moon and Mars indicates that such smaller bodies may have had self-sustaining dynamos early in their histories. Now the observational constraints, such as the crustal field hiding the short-wavelength part of the main field, are well understood. These ambiguities in defining and quantifying the lithospheric field are due to its complex nature, which reflects the heterogenous distribution of magnetic minerals in the subsurface. At the Earth's surface as for the Moon and Mars, the power spectrum of the lithospheric field is almost flat, which means that all spatial scales are equal energetic. Therefore, a large number of good quality observations, covering different spatial ranges and altitudes are needed to depict accurately these sources, from local scale to the larger scales of tectonic units. Impact craters are one of these features, which stamp their magnetic signature in the lithosphere.

After presenting, separately, the lithosphere magnetic field models and maps at planetary scale, the main characteristics of impact craters (see *Part II, Chapter 2*) were indicated. Their signatures are also visible in other models, such as topographic ones, which were specified. In the followings, the magnetic signature above large impact craters of the three bodies, was examined in greater detail, than it has previously been done, due to the new ground-database for the Earth, and satellite data for the Earth, Moon and Mars. The local analyses revealed some interesting properties of the ancient magnetic field of the planetary bodies (Purucker et al., 2002), which brought new and important constraints on their formation and evolution. However, next, the main part of the work deals with the magnetic characterization of impact craters.

3.1 How are craters seen in the newest global maps and models?

Many terrestrial impact structures have been found using remote sensing techniques, satellite imagery and airborne geophysics, but only ground analysis may be conclusive for recognizing shock geological features. Due to last decade satellite missions, the magnetic field signatures of many thousands impact craters, on Mars and Moon, offer a

unique opportunity to study the magnetic properties of the crust, impact shock demagnetization, and the processes of basin formation. Fortunately, the evidence of this heavy bombardment from the past results from the Moon's observations, where the lack of geological and atmospheric processes have prevented erosion of millions impact craters on its surface. Magnetic models and maps, presented earlier, represent a framework for determining the effects of impact shock, such as the demagnetization radius and the width of the demagnetization gradient zone.

3.1.1 Earth

In order to investigate the magnetic signature of the impact craters, the data grid from World Digital Manetic Anomaly Map (WDMAM-B) have been considered, starting from the largest ones, to map the confirmed impact structures [1]. From this, for each Earth's crater the total (ΔT) magnetic anomaly map, centered on the crater and extended over at least two radii have been plotted. The next figures were produced using the Generic Mapping Tools (GMT) package of Wessel and Smith (1991) [2], which is an open source database of tools for manipulating geographic and Cartesian data sets, and producing PostScript File illustrations under GNU General Public License. From all the investigated impact craters the first 30 large structures with diameters bigger than 30 km were selected. Few of them, with distinctive magnetic signature are presented.

The central anomalies may possess a positive or negative magnetic response, the latter indicating that remanence must be the dominant source of magnetization. The increase in magnetization, as a result of meteorite impact, is usually attributed to two main effects. Following Grieve and Pilkington (1996), new magnetic minerals may be generated at high shock pressures of $> 30\ GPa$, in particular by the decomposition of biotite and amphibole to magnetite, and through post-impact hydrothermal processes. The target rocks may acquire a remanent magnetization as a result of high shock, during the formation of new magnetic minerals by chemical processes or by thermal resetting (resulting from heating and cooling the rocks through the Curie point). Central magnetic anomalies may also be the result of the structural uplift of the magnetic basement beneath non-magnetic target rocks (Figure 20) as has also been interpreted at Chicxulub by Ortiz-Aleman et al. (2001). This interesting and deeply investigated crater, the Chicxulub structure, a 170 km crater, 65 My old, is not visible at the surface. Only field work, drilling, and geophysical data could identify it. The magnetic signature consists of a relative circular magnetic low, suggesting a multi-ring impact structure, but not well identified in the global map, except the circularity of the pattern, and a central magnetic peak (50 km diameter) of

[1] www.unb.ca/passc/ImpactDatabase/
[2] http://gmt.soest.hawaii.edu/

about 400 nT (Isac et al., 2011).

Impact melt and melt-breccia, heated over the Curie point, will often carry a high magnetic remanence. High remanent magnetization intensities and huger Køenigsberg ratio ($Q > 50$) have been found in samples at many impact places. These remanently magnetized units are interpreted to be the cause of magnetic anomalies associated with the impact structures. The carriers for remanent magnetism are the normal magnetic minerals of magnetite, hematite and pyrrhotite. Remanently magnetized melt is likely to be the main source of the central magnetic anomalies observed over many terrestrial structures. For example, the Vredefort impact structure, a 300 km diameter, 2020 My old and severely eroded, which is currently the oldest and largest impact crater. The positive anomalies of about $50 - 100$ nT may suggests the circularity of a multiring structure, with a central magnetic low. Negative magnetic anomalies in the center of the Vredefort structure (Figure 21) are interpreted to be due to shock-induced remanent magnetization of magnetite ($Q = 3 - 4$), generated at the time of impact (Henkel and Reimold, 2002). Vredefort might be the best analogue for the giant impact basins on Mars and Moon. Remanent magnetization set at the time of impact allows for the use of paleomagnetic dating techniques to constrain the age of the impact structure, as demonstrated for the Acraman crater and associated ejecta deposits (Schmidt and Williams, 1996).

The Bangui magnetic anomaly (Figure 22), one of the most intense crustal magnetic anomaly detected from space surveys, is circular in shape, with a diameter of about 800 km and amplitudes between -800 and $+800$ nT and a central low. It appears as an isolated and distinct signature, coincident with a comparable gravimetric low. This large feature, located in African Central Republic, was proposed by Girdler et al. (1992) as a result of a very old (early Precambrian) and large impact, but until now, unconfirmed.

The Popigai is one of the very large impact structure, with diameter of about 100 km which may have induced environmental perturbations or even significant climate changes, associated with general late Eocene cooling process. In the total magnetic field anomaly map, Popigai crater (Figure 23) is associated with a quasi-circular magnetic low of -800 nT. Here, the impact transformed instantaneously the graphite into diamonds near the center of the crater, due to the shock pressure.

The disruption of the pre-existing magnetic signature can sometimes be recognized for some terrestrial craters too, usually for smaller craters, under 50 km, like in the case of Clearwater W and Clearwater craters, seen in Figure 24.

The coherence scale (the size of the region characterized of coherent magnetization), following Lillis et al. (2010), is very important to the interpretation of the magnetic signature over impact craters. A typical example comes from the Vredefort impact crater, where aerial measurements of the magnetic field are lower than over surrounding regions,

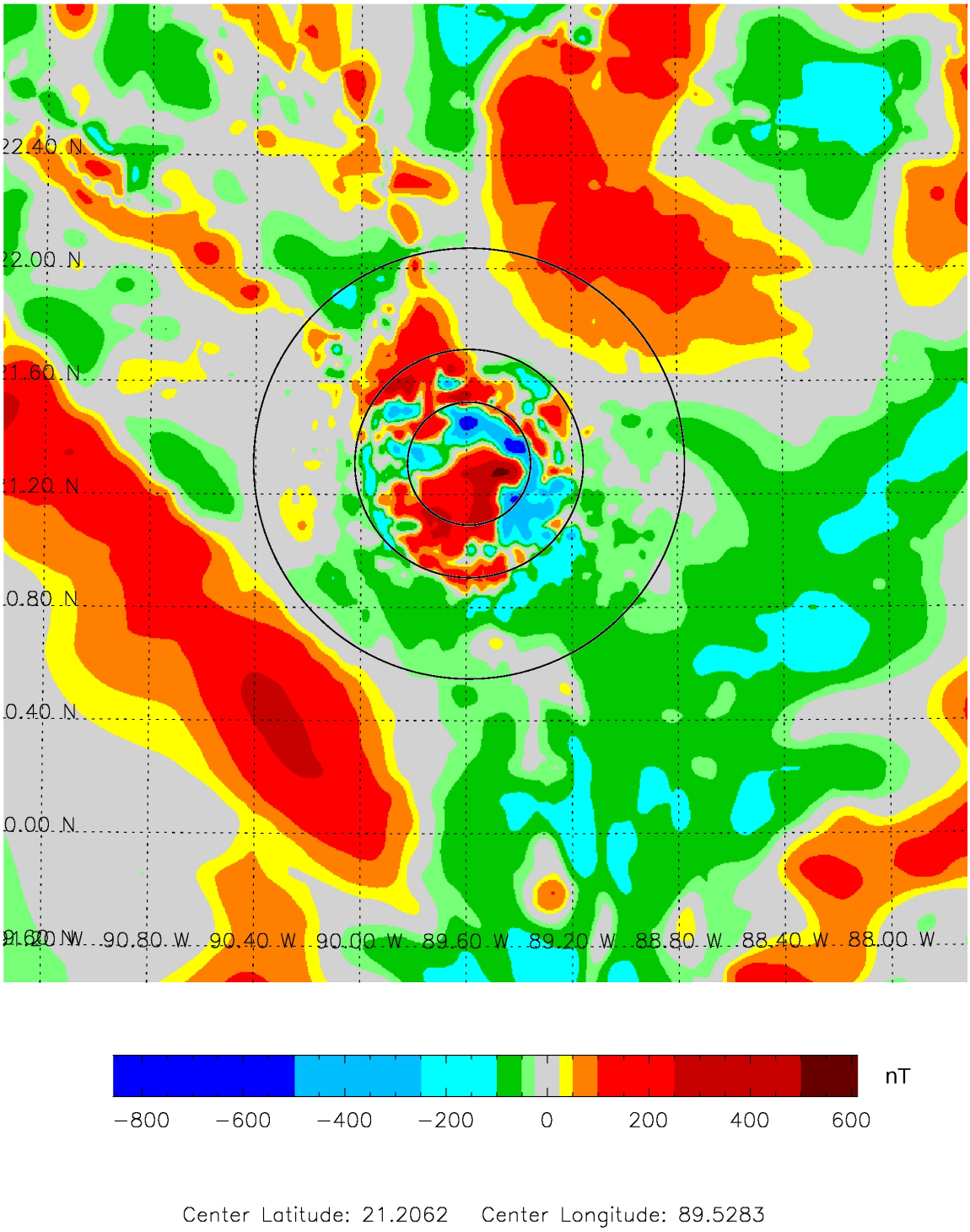

Figure 20: Short-wavelength and relatively intense magnetic anomalies ΔT near the center of the 170 km Chicxulub structure. The magnetic signature was mapped from 1 km grid of upgraded compilation NAMAG 2002. The circular features were identified from SRTM, a 30″ of arc resolution global topography grid. GRIDVIEW was used for graphics.

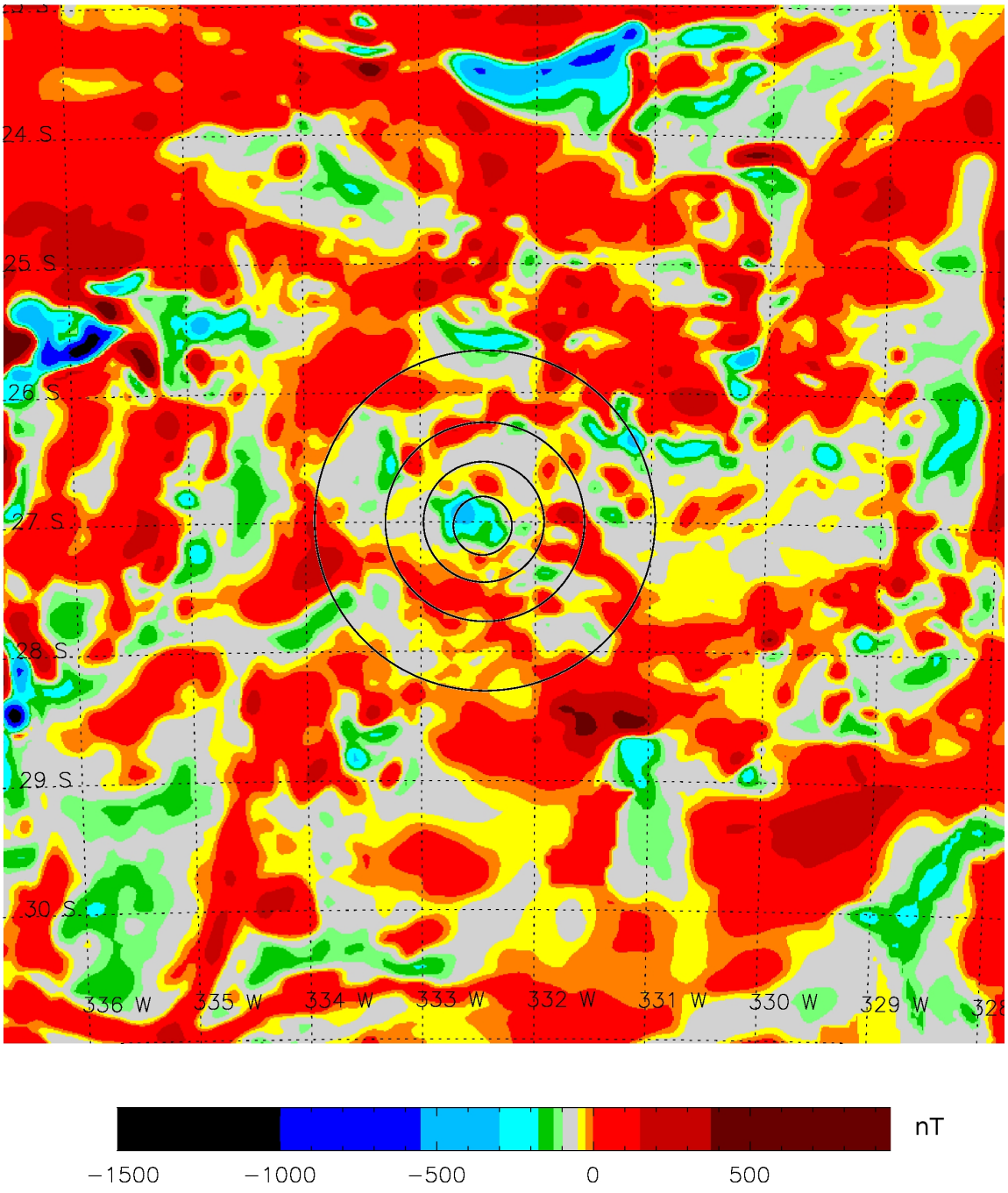

Figure 21: Short-wavelengths and relatively low intensity magnetic anomalies ΔT near the center of the 300 km Vredefort dome structure. The magnetic signature was mapped from 5 km grid of WDMAM (Korhonen et al., 2007). The circular features were identified from SRTM global topography grid. GRIDVIEW was used for graphics.

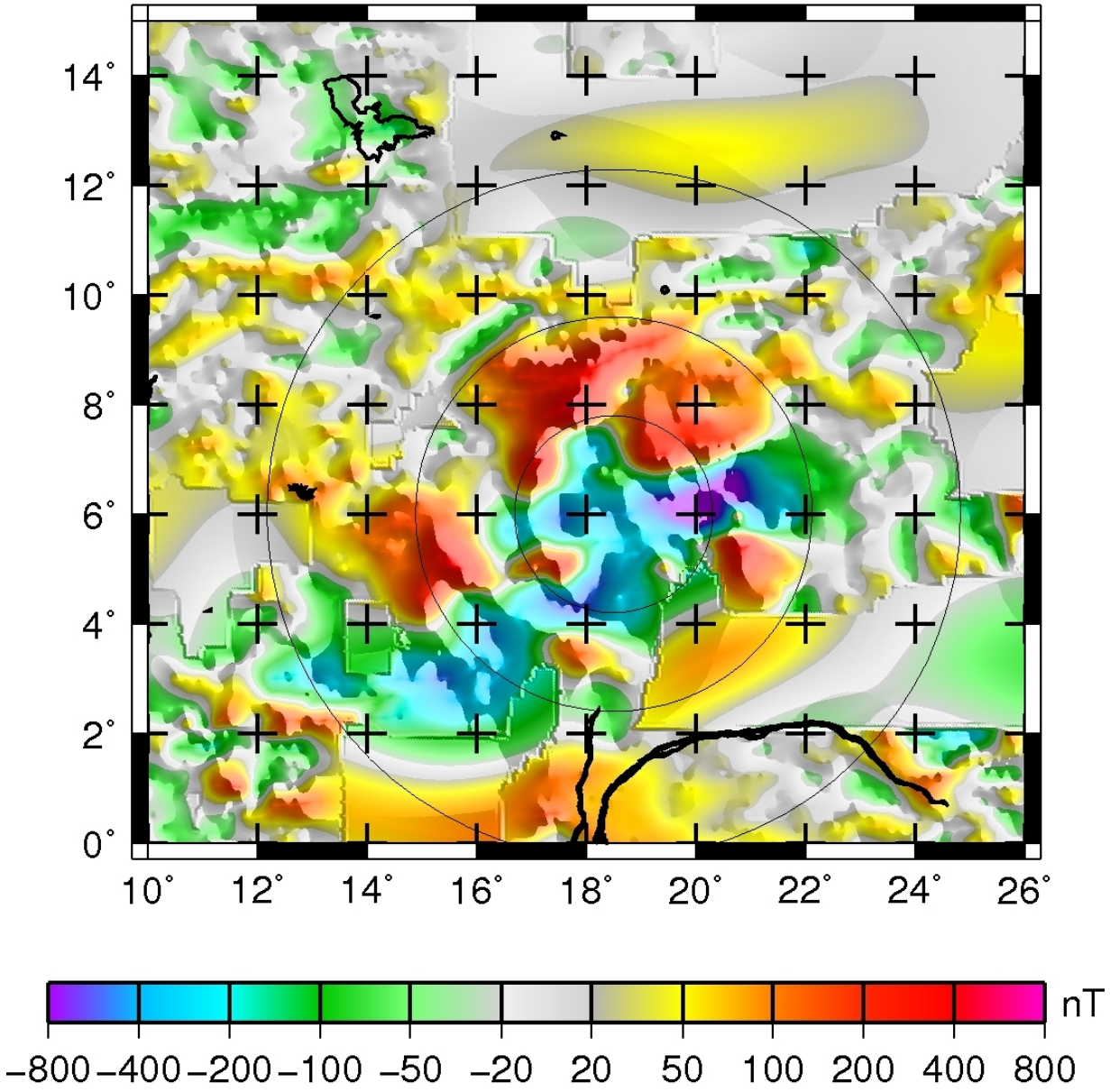

Figure 22: Magnetic map (ΔT), over the Bangui structure, at 5 km above the geoid. The light black circles represent the main rim and additional rings interior to this. GMT was used for graphics.

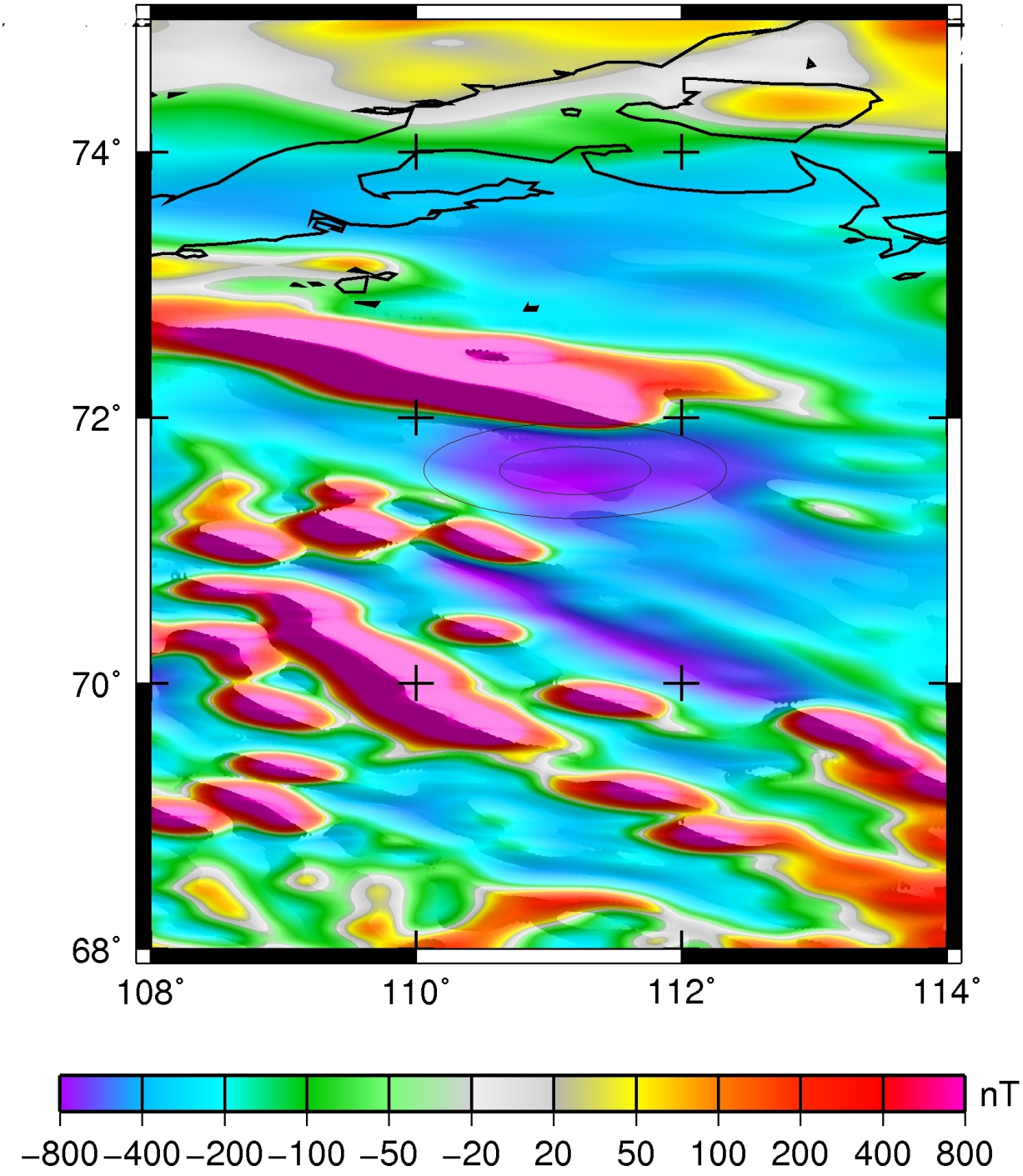

Figure 23: Magnetic map (ΔT), over the Popigai impact crater, at 5 km above the geoid. The light black circles represent the main rim and additional rings interior to this. GMT was used for graphics.

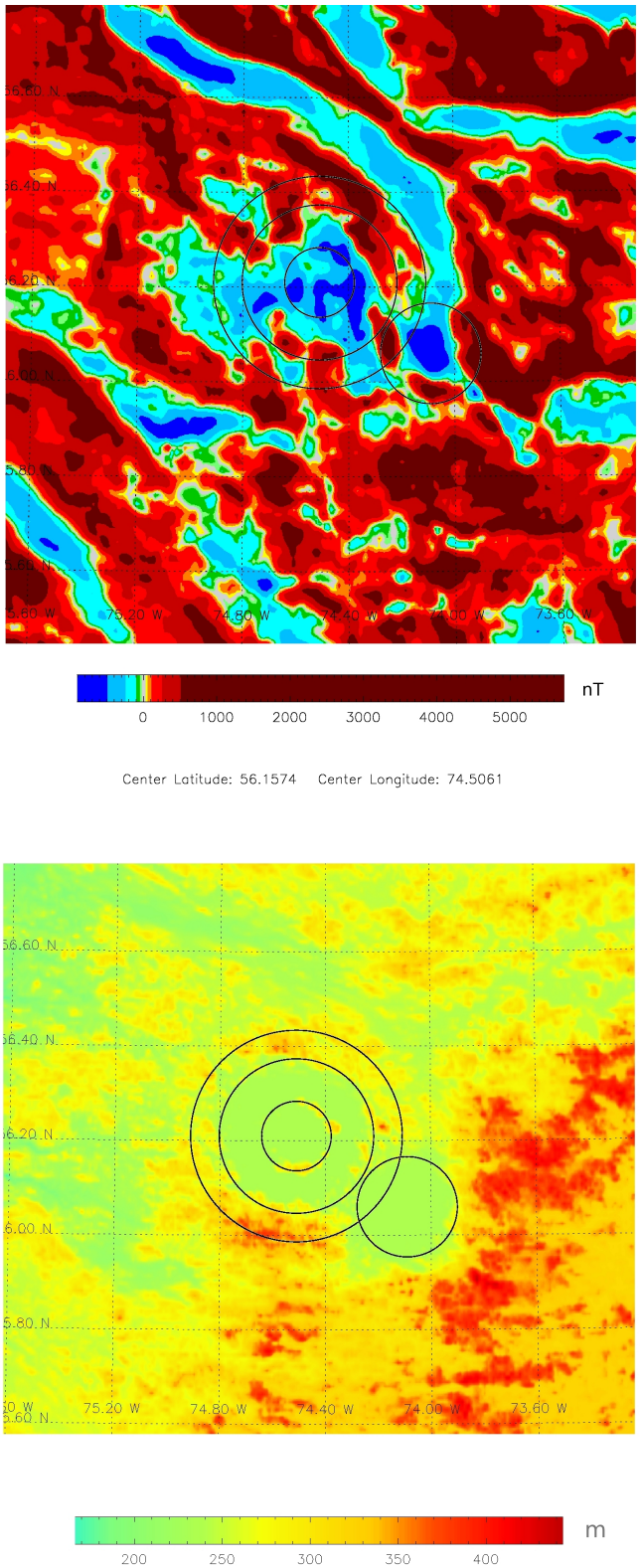

Figure 24: Low magnetic anomalies ΔT above the 50 km and 23 km Clearwater structure (top). The magnetic signature was mapped from 1 km grid of upgraded compilation NAMAG 2002. For the topographic map SRTM global topography was used (bottom). GRIDVIEW was used for graphics.

even the rocks in this crater possess much higher magnetic intensities than the same type of lithology found elsewhere on Earth. Carporzen et al. (2005) argued that intense, randomly oriented magnetization observed in surface samples at Vredefort were the product of impact-generated magnetic fields. Moreover, the magnetite grains contributing to the magnetic remanence crystallized during impact, directly relates the randomization and intensification to the impact event. The strong and randomly oriented magnetization vectors cancel out when they summed over the whole crater. Seen from high altitudes, as for martian craters, the magnetic field appears much lower than that of neighboring areas, implying that magnetic anomalies of meteorite craters cannot be used as evidence for the absence of the planet's internally generated magnetic field at the time of impact. On the Moon, the resulting impact melts, might record during cooling any ambient planetary magnetic field, as well as magnetic fields generated by impact plasmas. These impact-generated magnetic fields represent an alternative to the dynamo hypothesis for lunar magnetism.

3.1.2 Mars

Here, on the magnetic anomaly map of Langlais et al. (2004) the locations of the circular crater rims with diameters larger than 200 km, selected from MOLA grid were superimposed. Three of the largest craters, Argyre, Isidis and Hellas were selected here. They do not show any strong magnetization but a magnetic low in the scalar component of $5-10$ nT (Figures 25, 26 and 27). The lack of magnetic anomalies suggests that impacts demagnetized the crust by shock or by thermal and shock effects to a distance of at least 1.5 radii. The Hellas basin, with a transient diameter of approximately 2000 km, and the Argyre basin, with a tranzient diameter of 1300 km, might explain the relative weakness of the southern highland anomalies (Isac et al., 2010).

Again, to the interpretation of the magnetic signature, the coherence scale is of critical importance. In the case of Earth's craters, the high-frequency and relatively intense magnetic features, seen in the interior of impact basins, often result in broad magnetic lows when upward-continued, because adjacent coherently magnetized regions cancel out. But the reality is more complex and it depends not only to the altitude and the density of observations. Generally, magnetic surveys of the martian and lunar surface have revealed significantly lower magnetic field intensities over the gigantic impact craters than over surrounding regions. But there, reduced fields are commonly attributed to pressure demagnetization, caused by shock waves generated during meteorite impact, in the absence of a significant ambient magnetic field, as can be seen for the 1370 km martian crater Isidis in Figure 28 or, for the smaller, of 380 km diameter, Coulomb-Sarton lunar crater, in Figure 29.

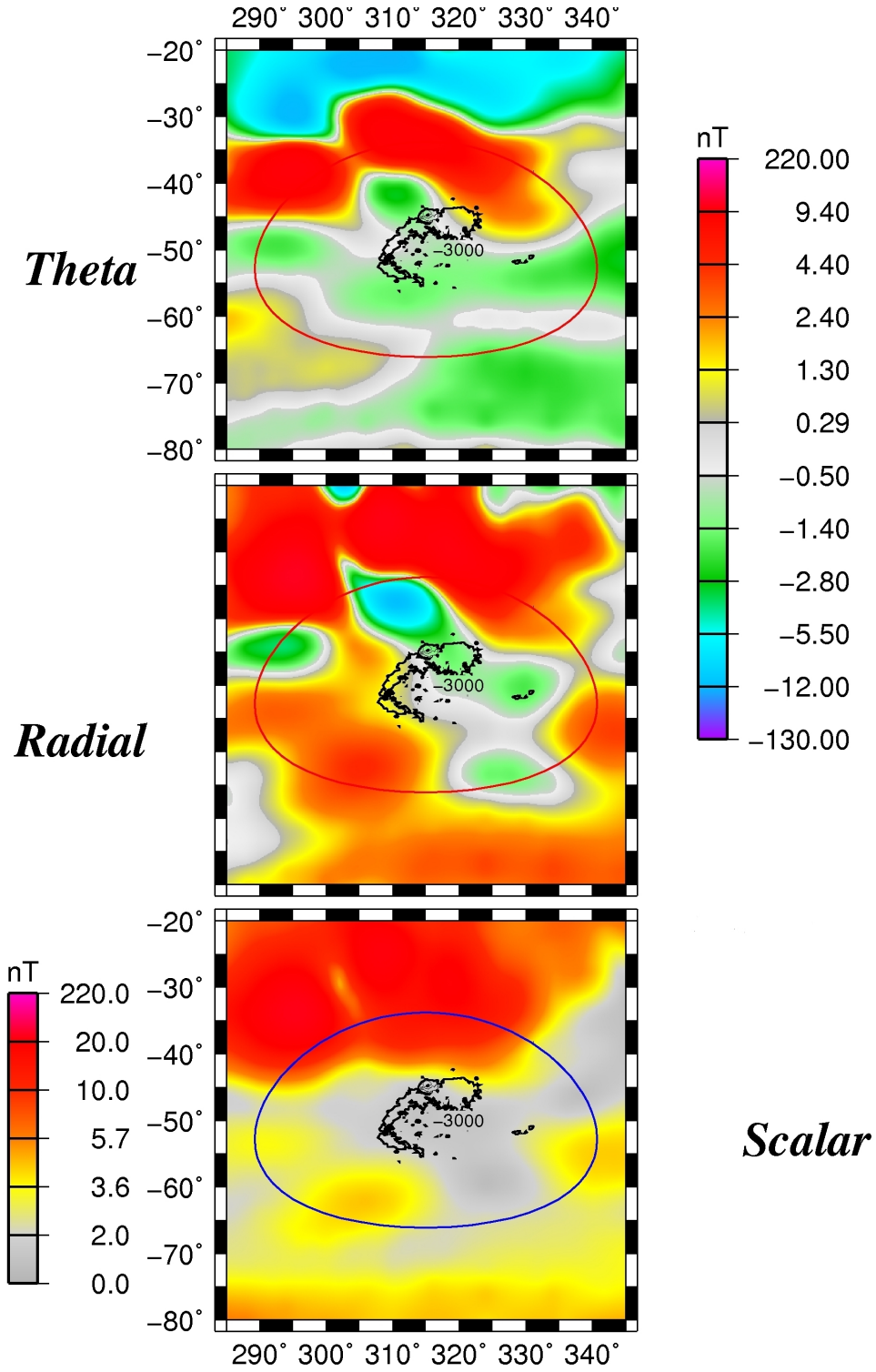

Figure 25: Magnetic maps for Argyre crater. Theta, radial and scalar Mars Global Surveyor magnetic data, ESD model at 400 *km* altitude (from top to the bottom), superposed on MOLA's altimetry. The blue/red circular shape represents the main rim uplift. Azimuthal equidistant projection. GMT was used for graphics.

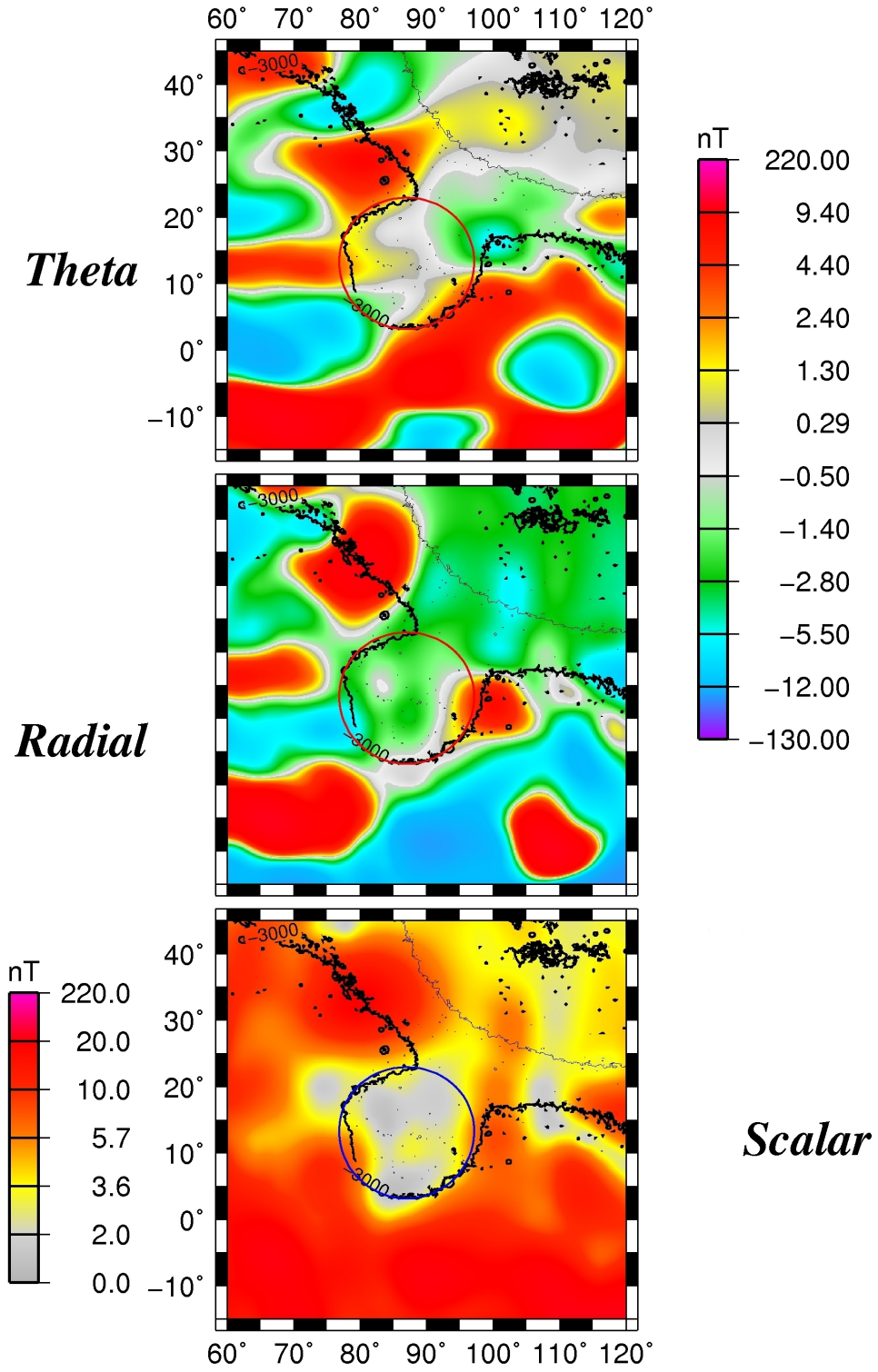

Figure 26: Magnetic maps for Isidis crater. Theta, radial and scalar magnetic data, ESD model at 400 *km* altitude (from top to the bottom), superposed on MOLA's altimetry. The blue/red circular shape represents the main rim uplift. Azimuthal equidistant projection. GMT was used for graphics.

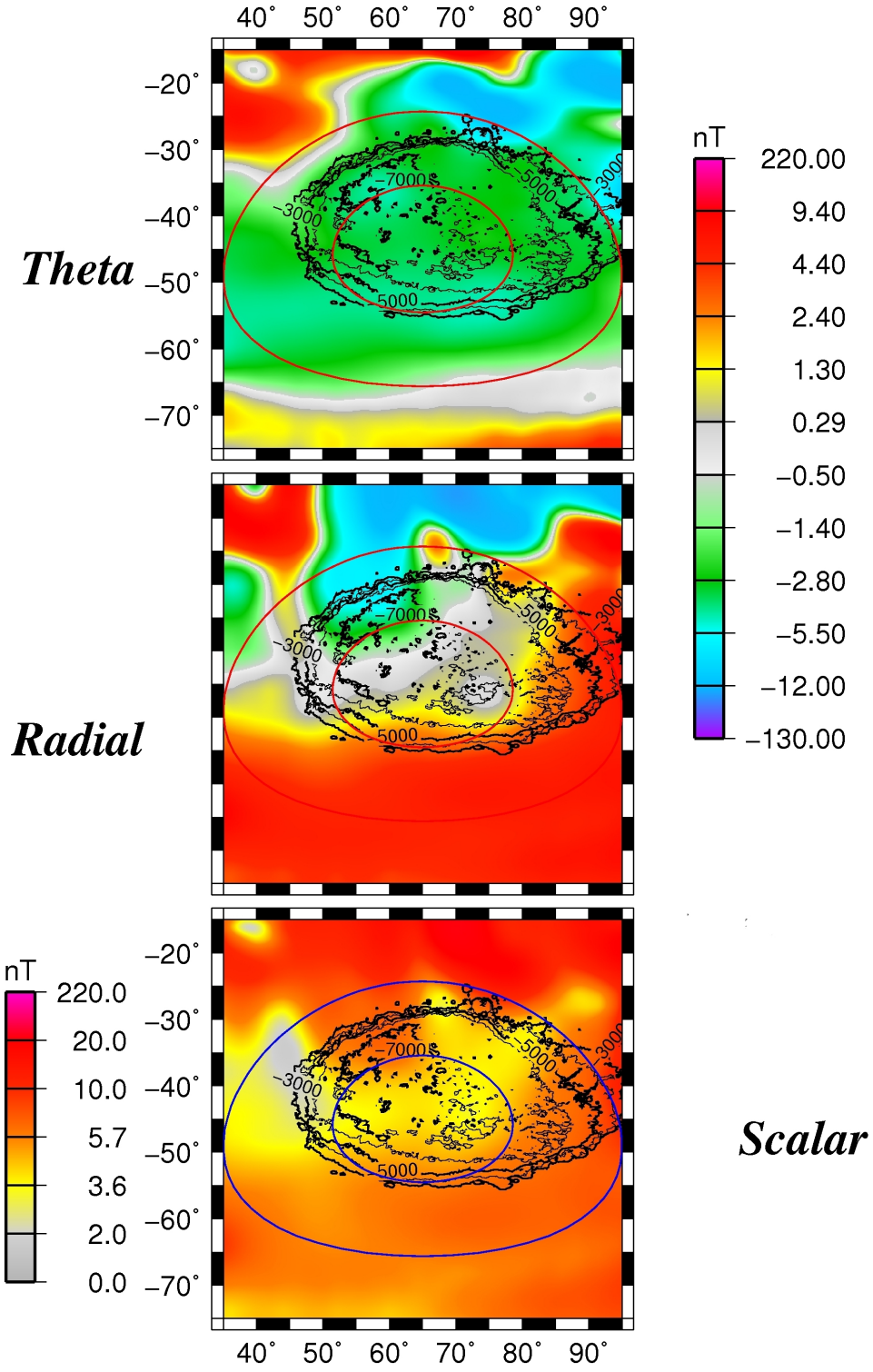

Figure 27: Magnetic maps for Hellas crater. Theta, radial and scalar magnetic data, ESD model at 400 km altitude (from top to the bottom), superposed on MOLA's altimetry. The blue/red circular shape represents the main rim uplift. Azimuthal equidistant projection. GMT was used for graphics.

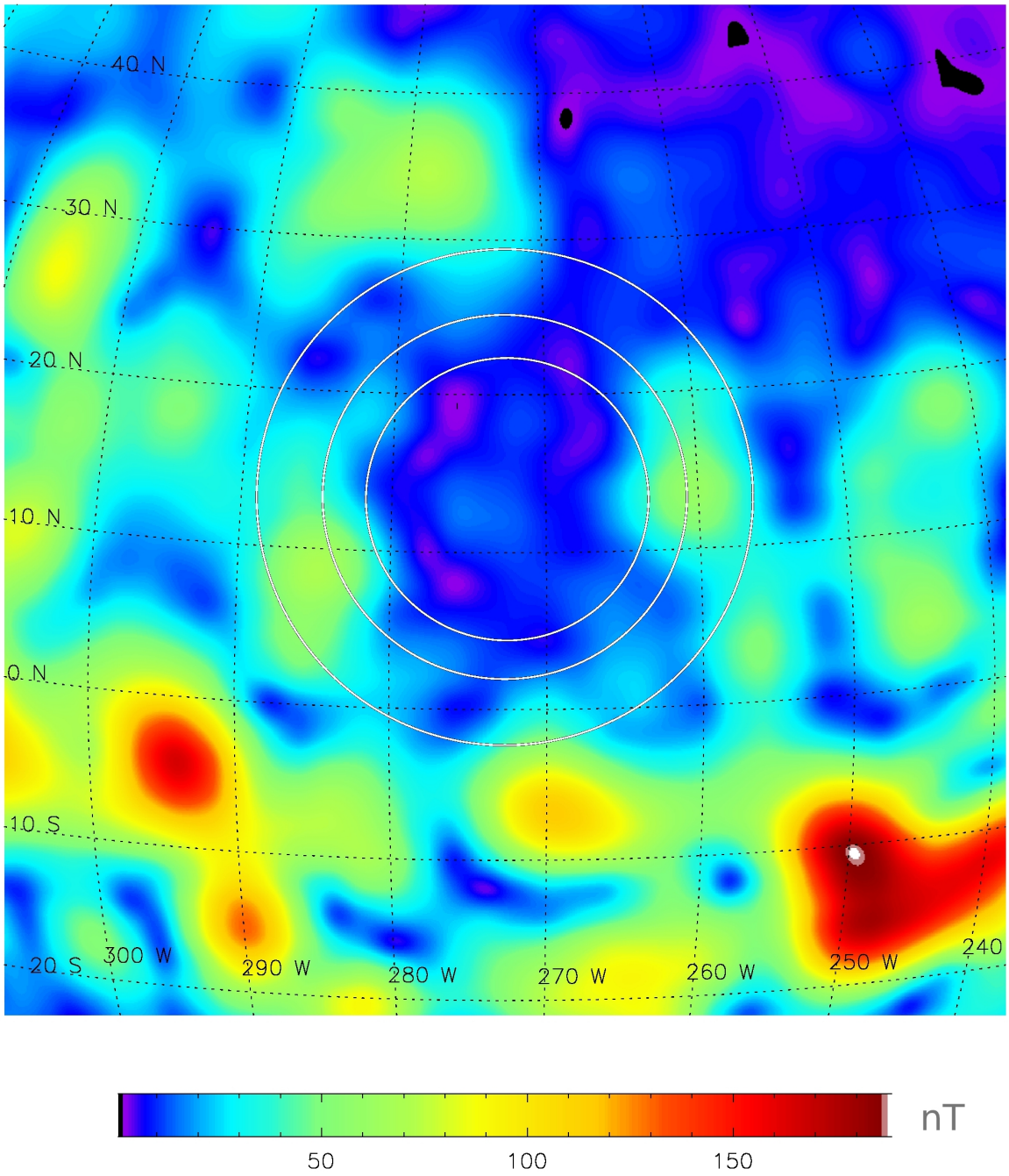

Figure 28: The magnetic field map (due to crustal sources only) of the 1370 km crater Isidis was obtained from ER map at 185 km altitude above martian datum. The circular features were identified from MOLA topographic map. GRIDVIEW was used for graphics.

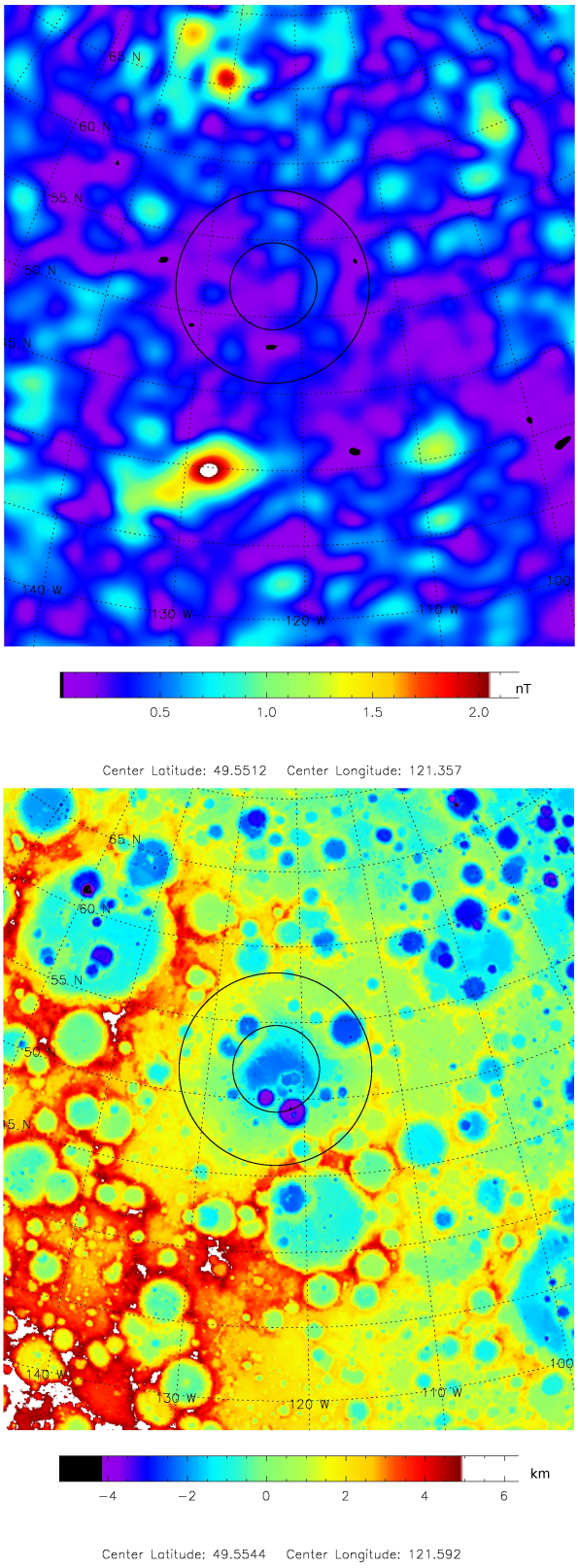

Figure 29: The magnetic field map of 380 km crater Coulomb-Sarton from Moon (top) obtained from a global magnetic model of the Lunar Prospector observations, 30 km altitude (Purucker and Nicolas, 2010). The circular features were identified from LOLA topographic map (bottom). GRIDVIEW was used for graphics.

3.1.3 Moon

In the case of the Moon, the ULCN topography data revealed about 30 quasi-circular depressions over known basins and craters larger than 300 km diameter. But many of craters have magnetic fields comparable to their surroundings or lower. Even if they have higher average fields than their surroundings, as in the case of Serenitatis or Nectaris their values do not exceed few nT. Is presented here the 700 km diameter Serenitatis crater (Figures 30 and 31) mapped using two topographic maps (ULCN and LOLA) and the latest magnetic models (coestimation and correlation models of Purucker (2008), Purucker and Nicolas (2010)). This crater lies in a region with stronger magnetic fields (about $5 - 10$ nT). In both maps a magnetic low centered on the crater is clearly seen (Isac et al., 2009). In the case of early-Nectarian craters, as Nectaris 865 km diameter, a stronger magnetic field (about 3 nT) appears in the central area, mostly seen in the scalar component of the correlative model developed by Purucker in 2008 (Figure 32). This type of positive anomalies could be a response of the crust to a large impact when an active internal dynamo was present (Isac et al., 2012).

The preliminary analysis (carried out at GFZ-Helmholtz Center Potsdam, Germany in 2009) aimed to identify a direct correlation of magnetic signal over the known large impact craters on these three bodies. The resolution of the maps used in this stage allowed me to identify around 30, 50 and 65 craters on Earth, Mars and Moon, respectively, which show more or less a magnetic signature. Their smallest diameters, of 30 km, 70 km and 150 km for Earth, Mars and Moon, respectively, lies around the maximum resolution of the available magnetic maps and models at this time. A substantial number of analyzed craters are demagnetized. To find a clear trend between the size and demagnetization effects, the tools from GMT software and available magnetic and topographic models are not resolutive enough for detailed studies. An equivalent number of craters for the three terrestrial bodies, around 30, for an easier comparison was preserved for the next stage of work. Their coordinates (determined by means of another tool, in the next section) and relationships between diameters and position are presented in Figures 35, 36 for Mars, and Figures 37, 38 for Moon, respectively. Regarding the Earth (Figures 33, 34), the spatial distribution of the impact craters is not random, as celestial mechanics requires. They are concentrated in Canada, Australia, Northern Europe and Asia (in former Soviet Union), only in old cratons. Their diameters do not exceed 300 km, the only exception being Bangui structure, not yet validated as an impact crater and only three of them have a multiring shape. Craters on Mars are (especially the larger ones, bigger than 2000 km) randomly distributed. Medium-size ones (between $500 - 2000$ km) are distributed especially in the southern and eastern hemispheres. Craters of the Moon are randomly distributed, with a lack at the North Pole. Diameters bigger than 1000 km

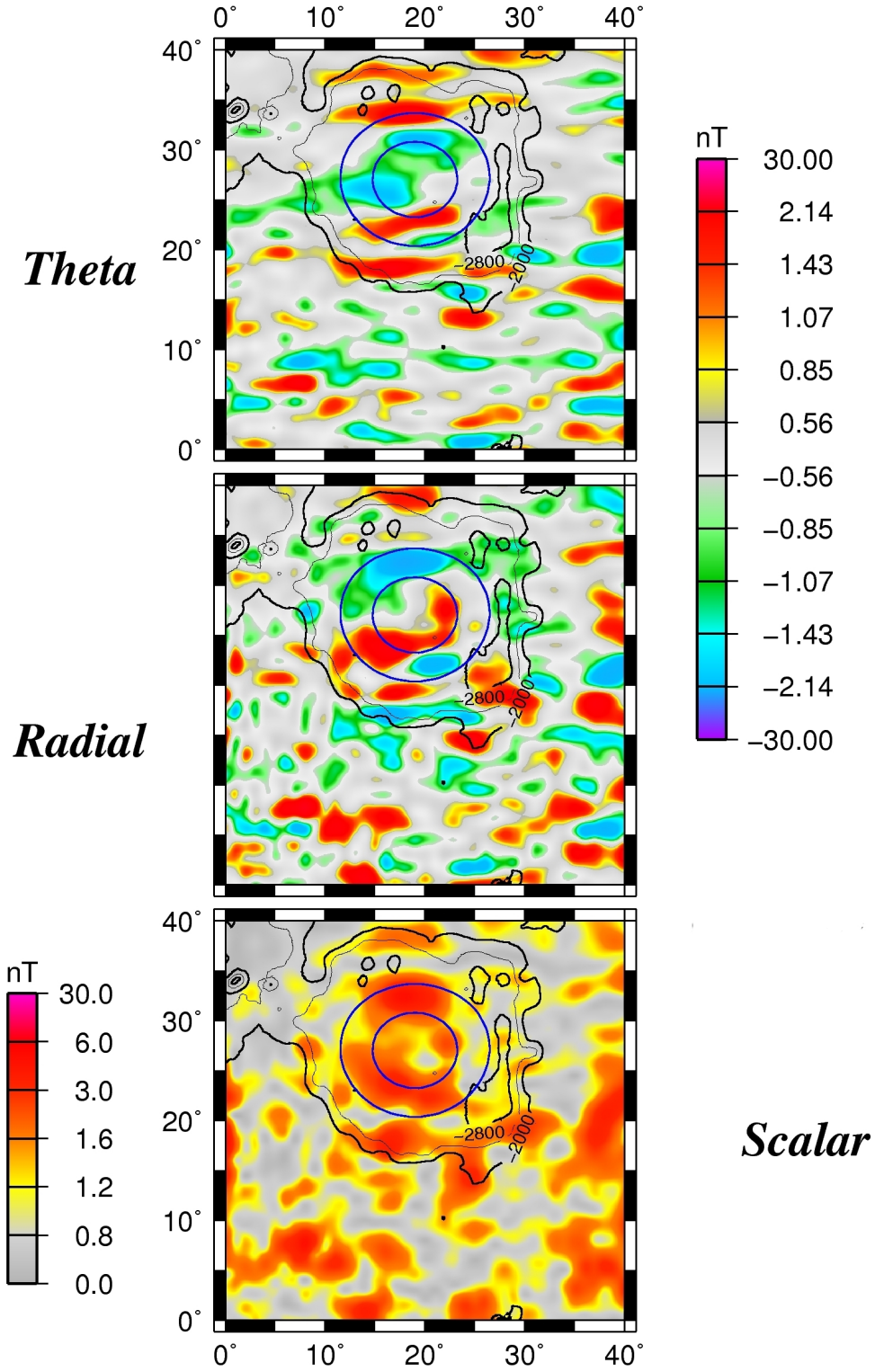

Figure 30: Magnetic anomaly map for Serenitatis lunar craters. Theta, radial and scalar magnetic data from the correlative model (from top to the bottom), at 30 km above the lunar datum, are superposed on ULCN2005 gridded topography. Blue/red circles represent the main rim and the additional rings interior to this. Azimuthal equidistant projection. GMT was used for graphics.

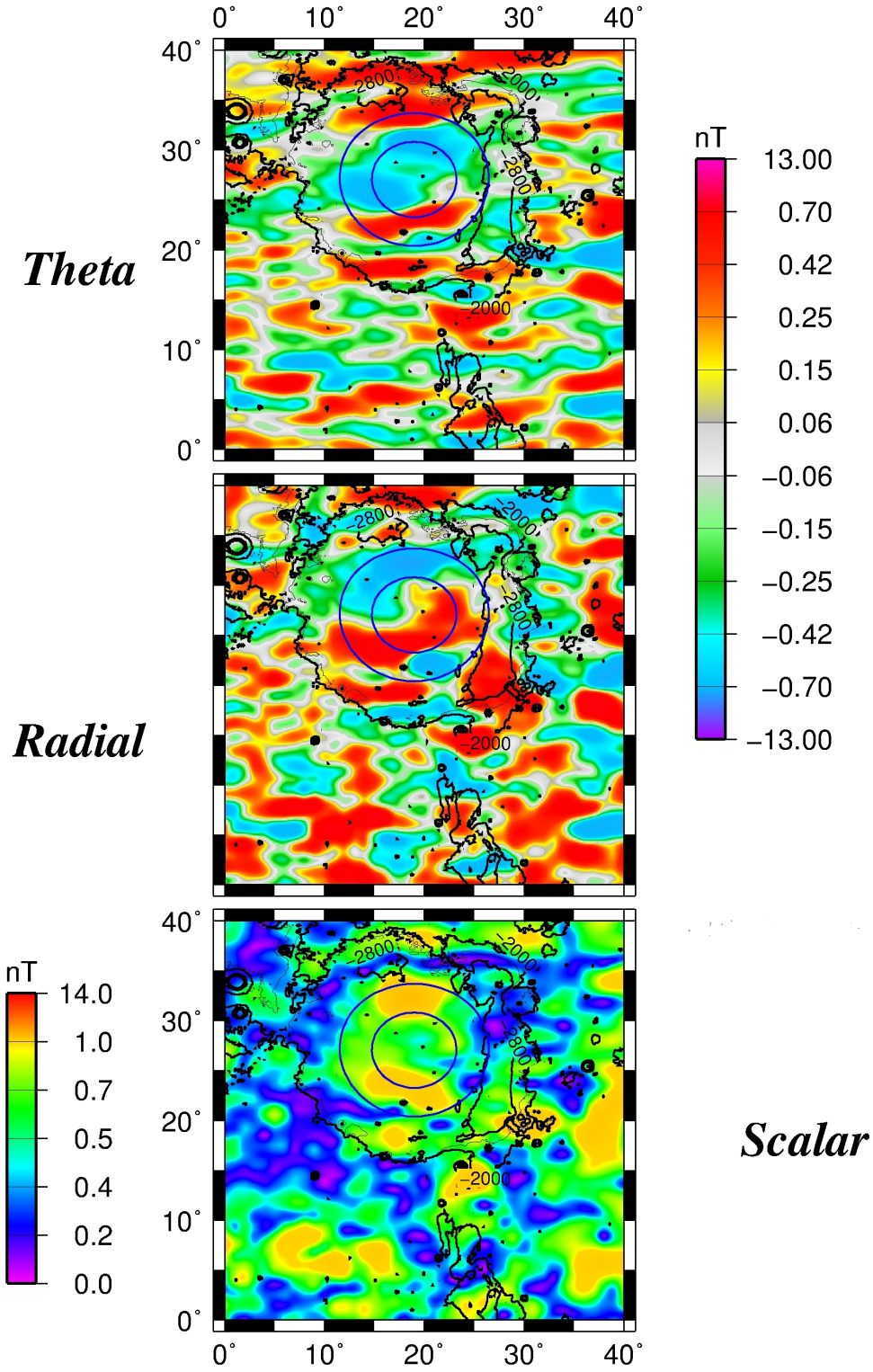

Figure 31: Magnetic map for Serenitatis lunar craters. Theta, radial and scalar magnetic data are from the combined sequential and coestimation model (from top to the bottom), at 30 km above the lunar datum, superposed on LOLA gridded topography. Blue/red circles represent the main rim and the additional rings interior to this. Azimuthal equidistant projection. GMT was used for graphics.

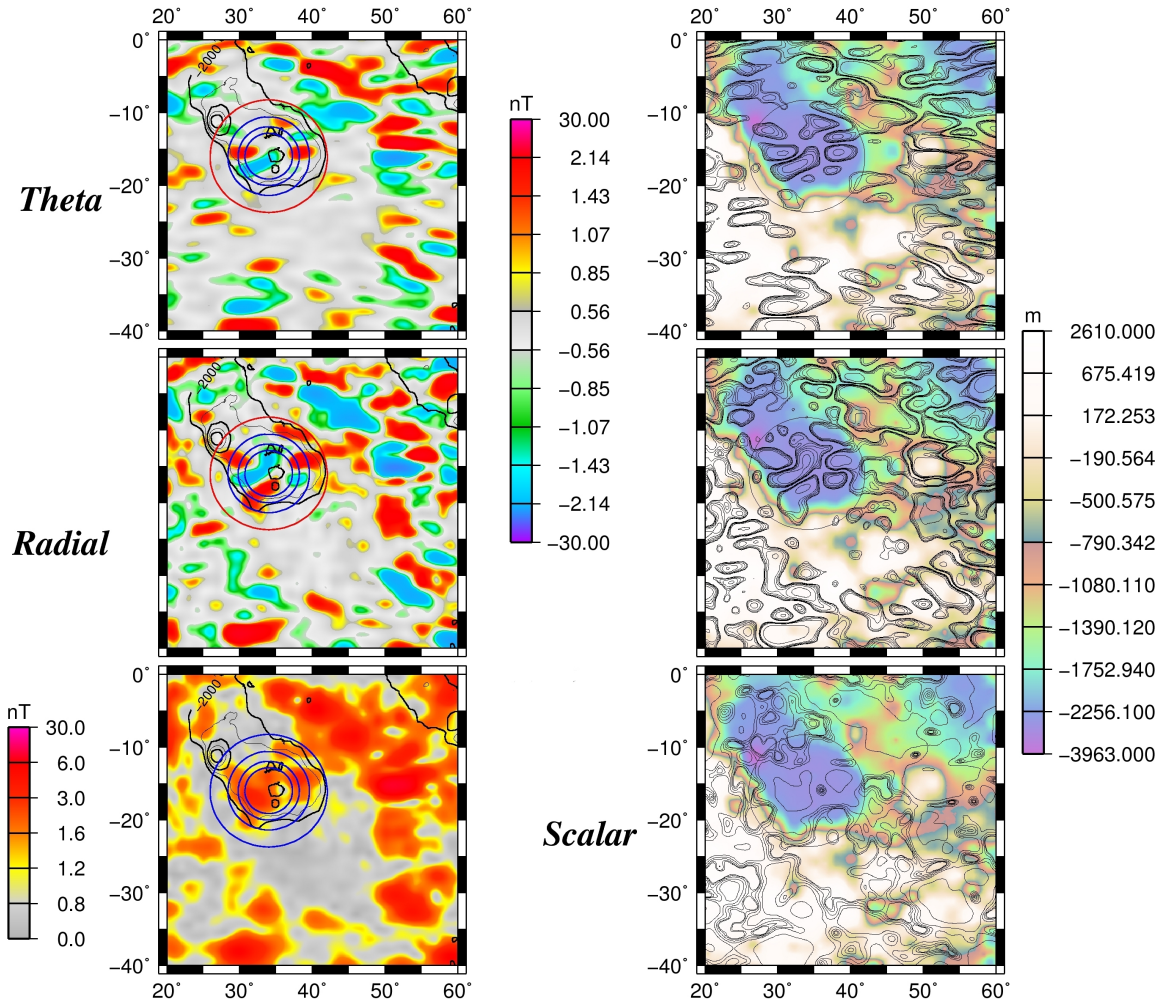

Figure 32: Magnetic and topographic ULCN 2005 maps for Nectaris crater. Theta, radial and scalar magnetic data (on the left, from top to the bottom), from correlative model of Purucker, 2008 at 30 *km* above the lunar datum, are superposed on lunar topography (black). Blue/red circles represent the main rim and the additional rings interior to this. On the colored topographic map (on the right), magnetic data are in black. Azimuthal equidistant projection. GMT was used for graphics.

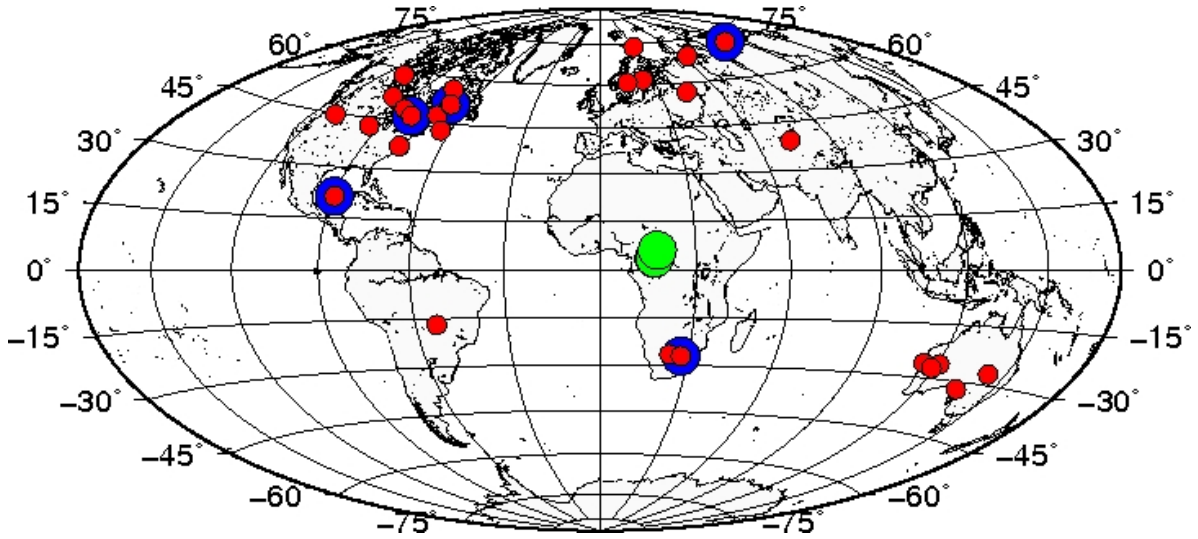

Figure 33: Illustration of the selected craters' position on the Earth. Red dots are simple craters. Blue and red dots represent multiring craters. Green dots represent craters bigger than 500 km diameter. Zenithal equal area projection (Hammer-Aitoff).

are the few, and the biggest and medium-size ones (between $350 - 1000$ km) are mostly antipodal.

3.2 Analysis of impact craters

The detailed analysis of the magnetic signature over impact craters was carried out during PhD research at NASA, Washington DC USA, in 2010. Then, magnetic and topographic features over craters were visualized and measured in a manner that were previously impossible. It was possible by means of GRIDVIEW software, an analysis tool, created by NASA Goddard Space Flight Center, Planetary Geodynamics Lab, (Roark et al., 2000; Roark and Frey, 2001), which can view, measure and make graphics of gridded data. It is based on the Interactive Data Language (IDL) programs, written for analysis of data from NASA missions, such as Mariner missions for Mars. GRIDVIEW is oriented now toward use by scientists in the analysis of one to three dimensional data sets, and as a tool to make new discoveries, especially in the gridded topographic data products of MOLA [3]. The software allowed with an interactive menu driven point and click interface, to obtain various display and measurement options, using different sets of global gridded data for Earth, Mars and Moon. Therefore, precise measurements and the most detailed magnetic maps of selected impact craters have been obtained. First, the high-precision topographic gridded data were analyzed, which easily revealed the presence of the quasi-

[3] http://denali.gsfc.nasa.gov/mola–pub/gridview

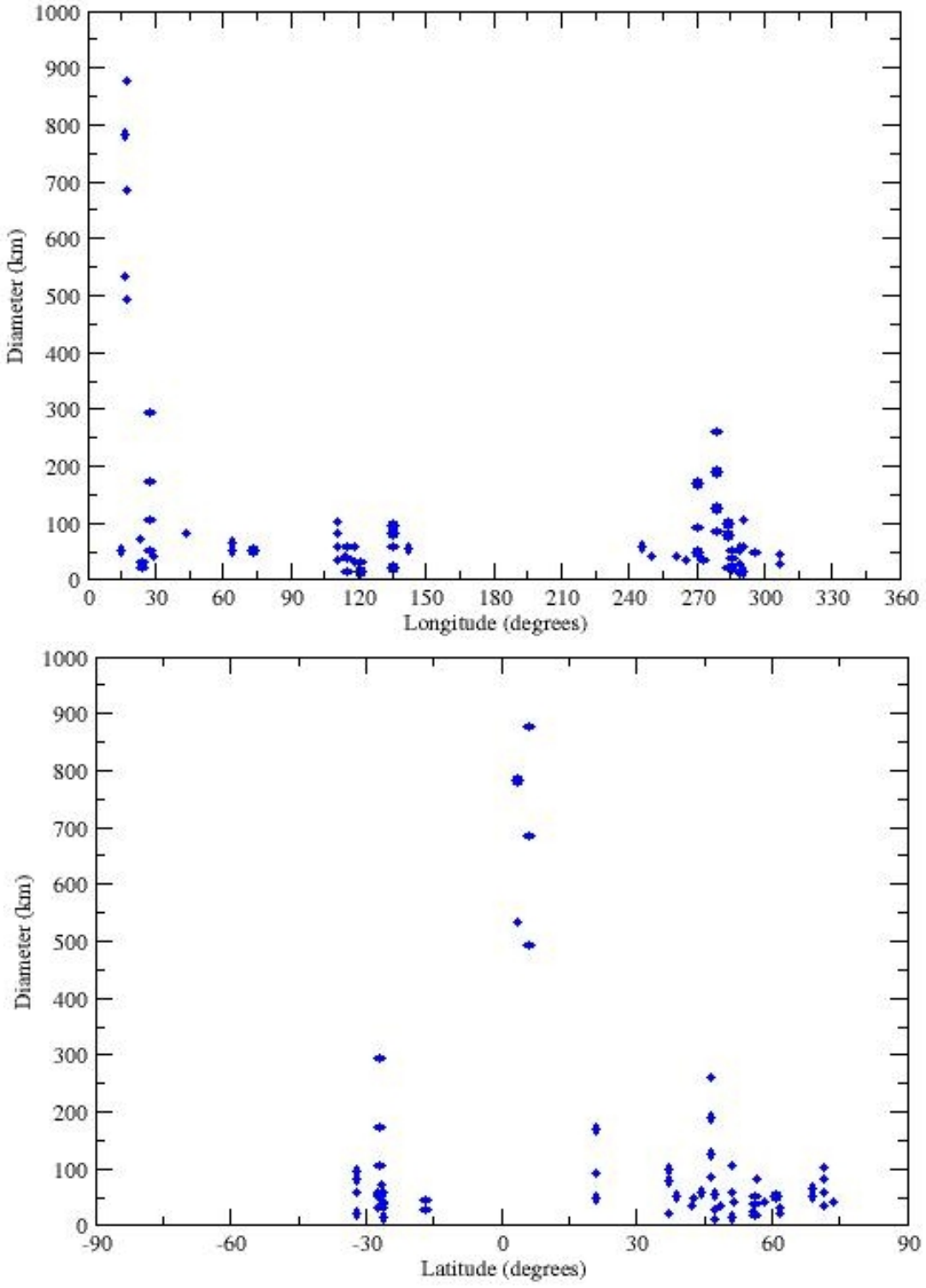

Figure 34: Diagrams showing the global distribution of Earth's different diameters-size craters versus longitude (top) and latitude (bottom).

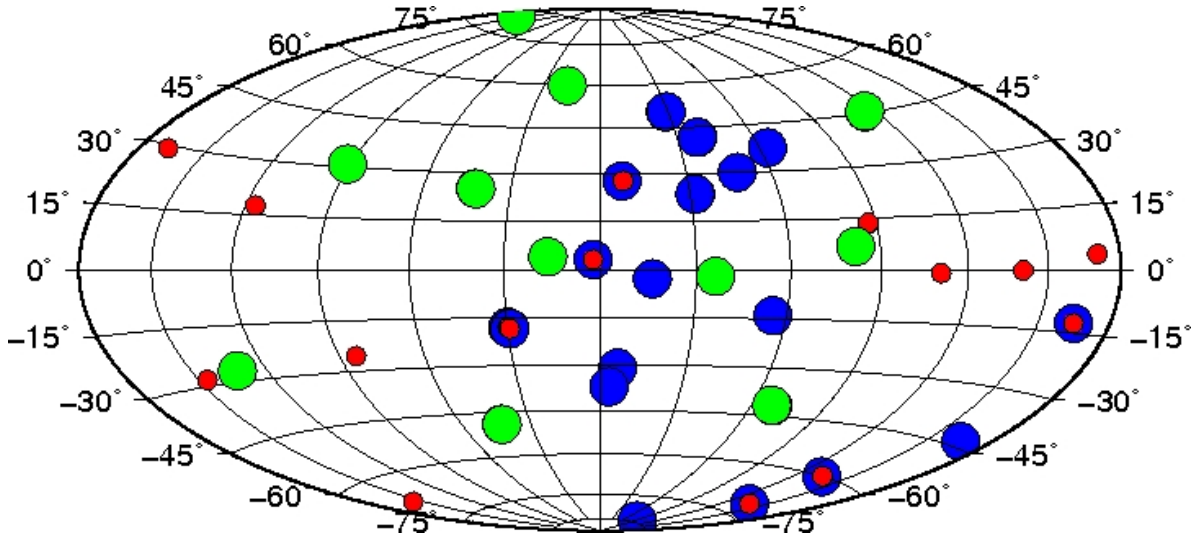

Figure 35: Illustration of the selected craters' position on the Mars. Red dots are craters smaller than 500 km diameter. Blue dots are simple craters, bigger than 500 km diameter. Blue and red dots represent multiring craters. Green dots represent basins bigger than 2000 km diameter. Zenithal equal area projection (Hammer-Aitoff).

circular depressions or set to be at least somewhat circular. Generally, circular, rimmed depression, whose floor is lower than the level of the terrain in which the crater was excavated, or crustal blocks relatively down-dropped between two circular fault systems, were tracked. The global rotation, zooming, shading, color stretching and contouring tools of the topographic images enhanced craters' appearance. After stretching the topographic image, in order to enhance appearance of quasi-circular depressions (QCD), either single or multi-ringed diameters, were drawn and measured. Then, the available magnetic gridded data from NASA library were mapped and overlapped the determined rings on them. Additionally, the software allows to document systematic trends in the amplitude and frequency of the magnetic patterns inside and outside of 37 mostly multi-ring basins on the Moon, 34 large basins on the Mars and 28 complex craters on the Earth. These basins were documented and their wide patterns and magnetic modeling/fitting parameters were noted. The results are synthesized at the end, for each of the three bodies.

3.2.1 Earth

The largest crater impacts from Earth (diameters > 30 km) were identified by their quasi-circular features from the most recent and detailed topographic map, $SRTM30$, and superposed on their magnetic maps, after. In order to investigate the magnetic signature, the total field component ΔT data grid from the same World Magnetic Anomaly Map-

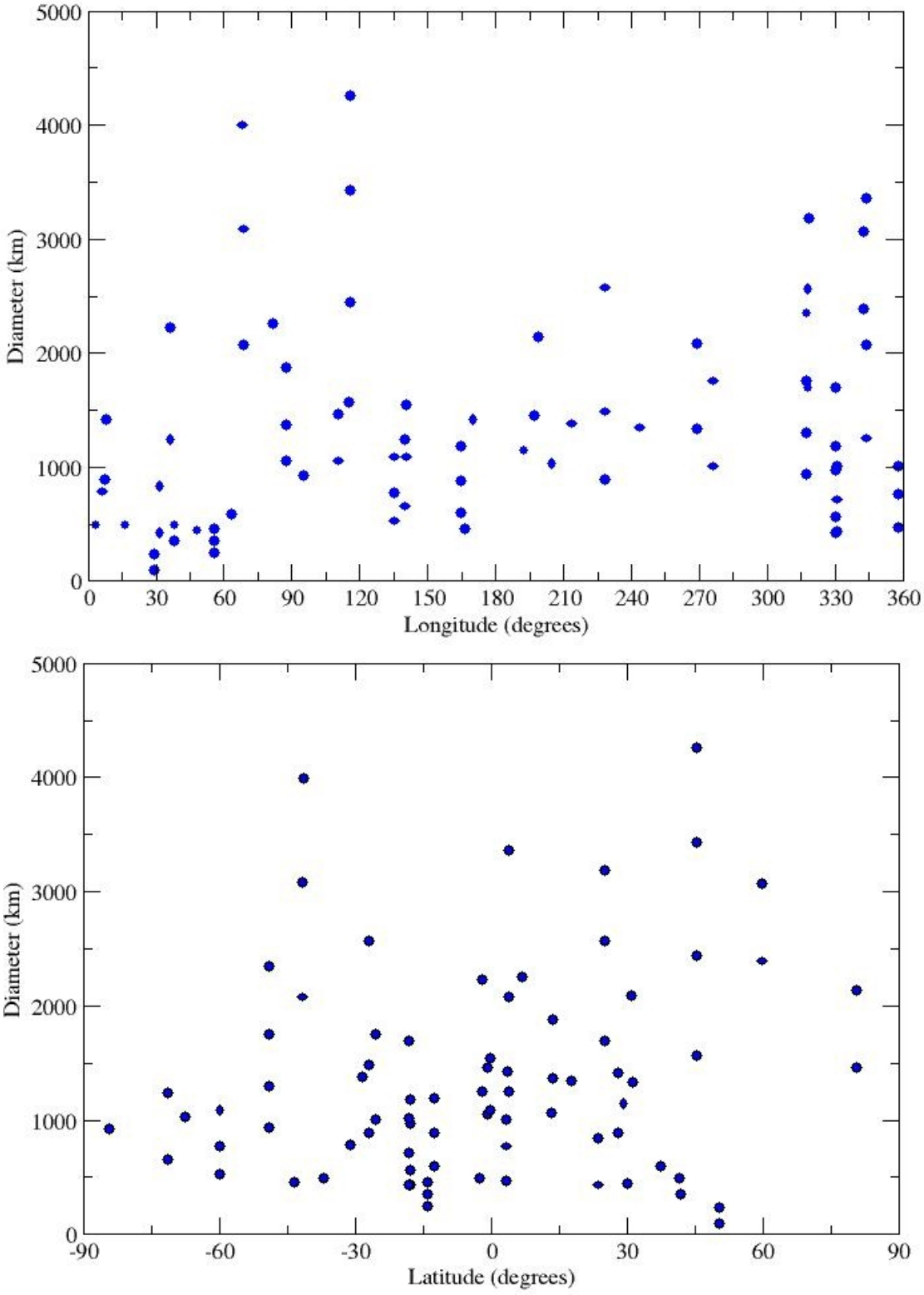

Figure 36: Diagrams showing the global distribution of Mars' different diameters-size craters versus longitude (top) and latitude (bottom).

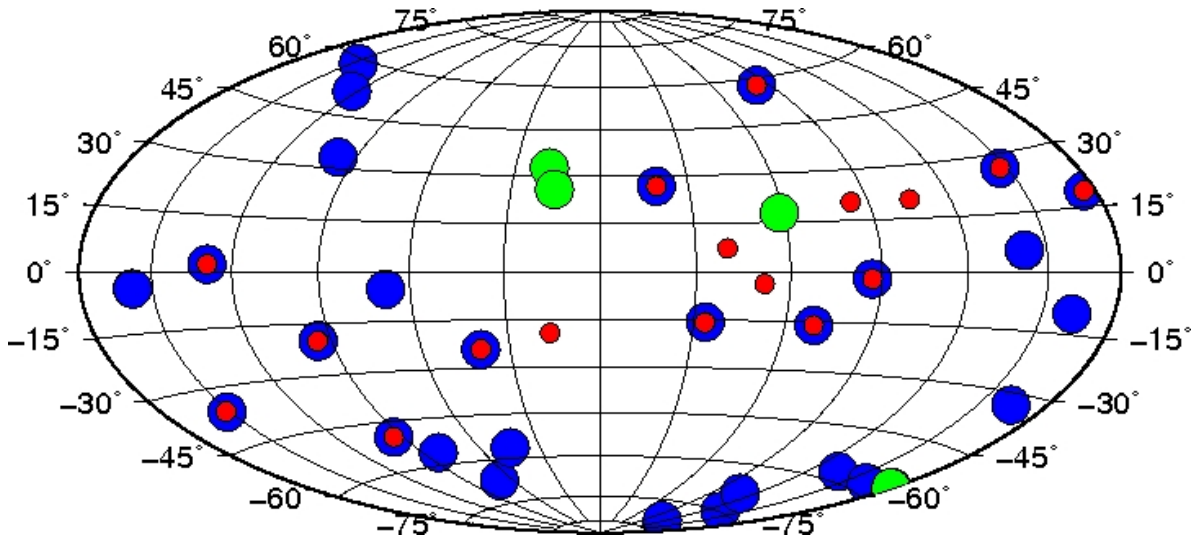

Figure 37: Illustration of the selected craters' position on the Moon. Red dots are craters smaller than 350 km diameter. Blue dots are simple craters, bigger than 350 km diameter. Blue and red dots represent multiring craters. Green dots represent basins bigger than 1000 km diameter. Zenithal equal area projection (Hammer-Aitoff).

WDMAM 2007B, mainly, were computed. For North America, it was used the 1 km grid of upgraded North American Magnetic Anomaly compilation (North American magnetic Anomaly Group, NAMAG, 2002 [4]). The North American anomaly magnetic map includes the individual grids from Canada, the U.S., Mexico, and the Arctic area at 1 km above the terrain. It represents a significant upgrade but still not able to accurately represent anomalies over 150 km wavelengths, particularly in the U.S. and Canada. For Australia, a 1 km grid resulted from a completely new compilation of total crustal magnetic intensity grid data (Purucker, 2007) [5] was used. For South America, various data sets which have been re-processed and re-leveled to generate a unified 1 km grid or $15'$ of arc grid of total magnetic intensity data [6], at 4 km altitude, were used.

The magnetic signature of Chicxulub (Figure 20) the only large crater in the terrestrial record with a preserved topographic peak ring, and Vredefort (Figure 21) are distinctive. Beside the above ones, a large variety of magnetic signatures are encountered in the other terrestrial impact structures, dependent on target rocks, the rocks homogeneities, impact magnetizations and subsequent geological evolution of the area. Few of them are obvious impact craters, strongly visible in images, consisting in concentric zones, in contrast with the weaker amplitude anomalies from the surrounding. The central area is sometime characterized by a single, high amplitude anomaly, as in Figure 20, and numerous, short

[4] www.pubs.usgs.gov/sm/mag_map
[5] Geoscience Australia, www.ga.gov.au
[6] GETECH, www.getech.com

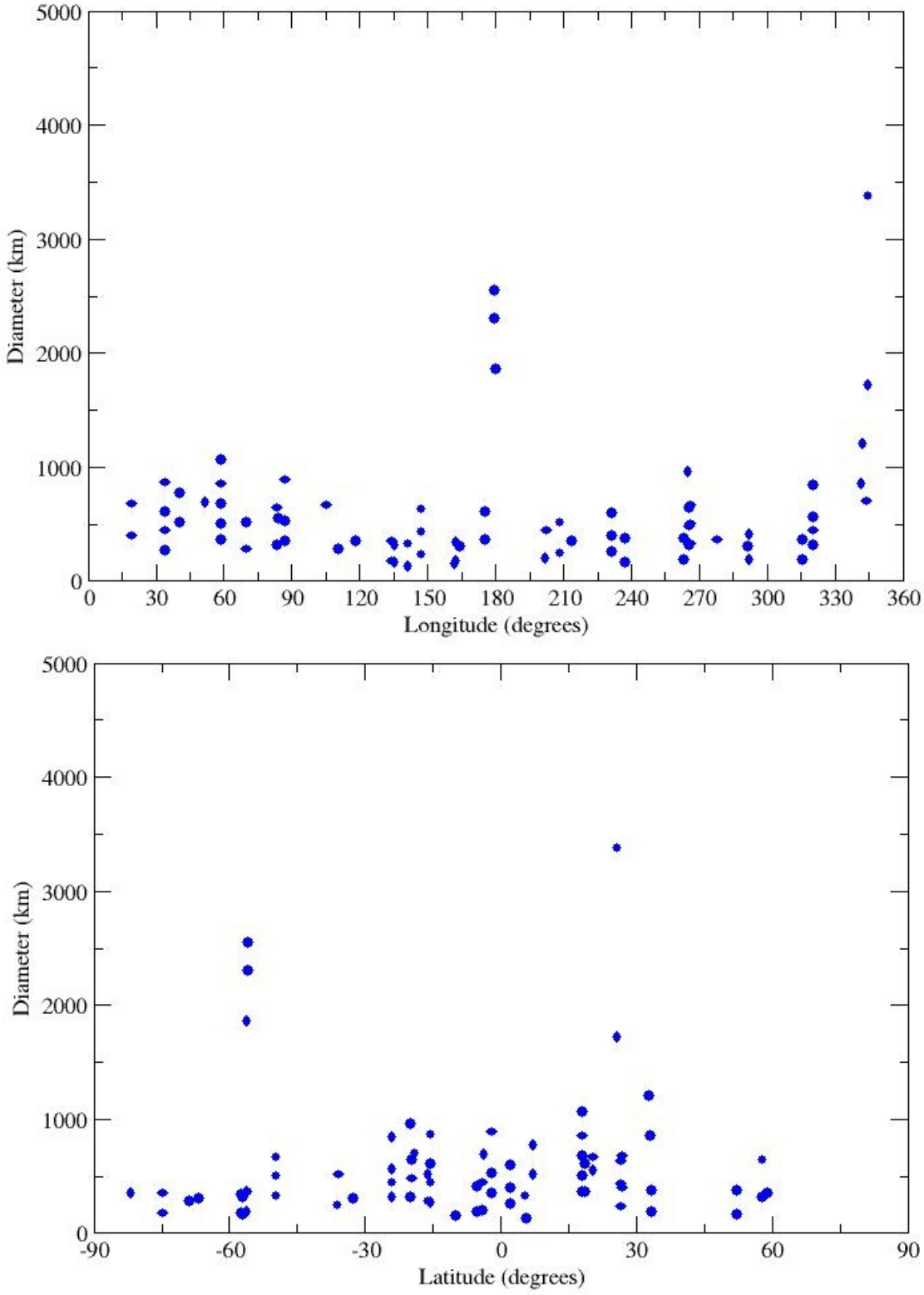

Figure 38: Diagrams showing the global distribution of Moon's different diameters-size craters versus longitude (top) and latitude (bottom).

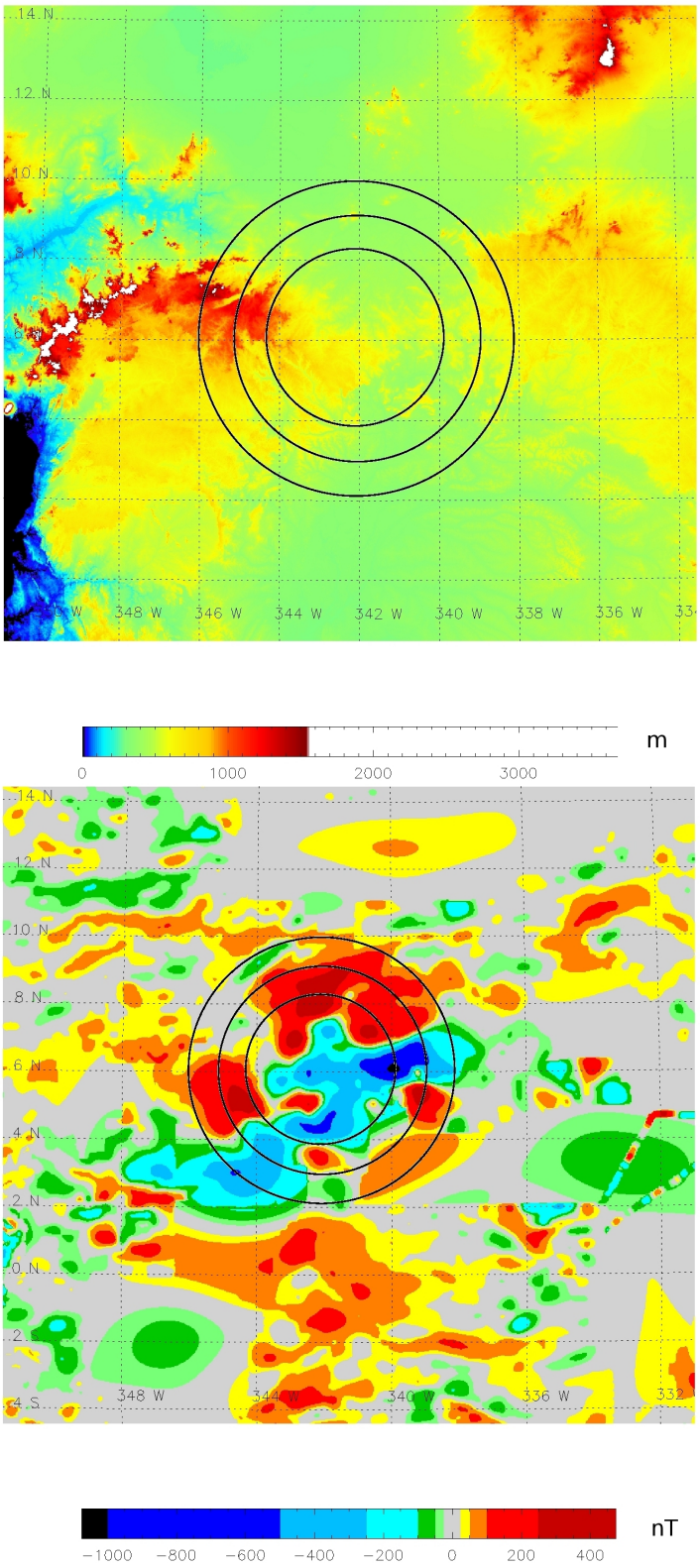

Figure 39: The improved magnetic map (ΔT) from WDMAM, over the 875 km diameter Bangui structure, at 5 km above the geoid (bottom), using GRIDVIEW tools. The black circles represent the selected rings from SRTM30 global topography map (top).

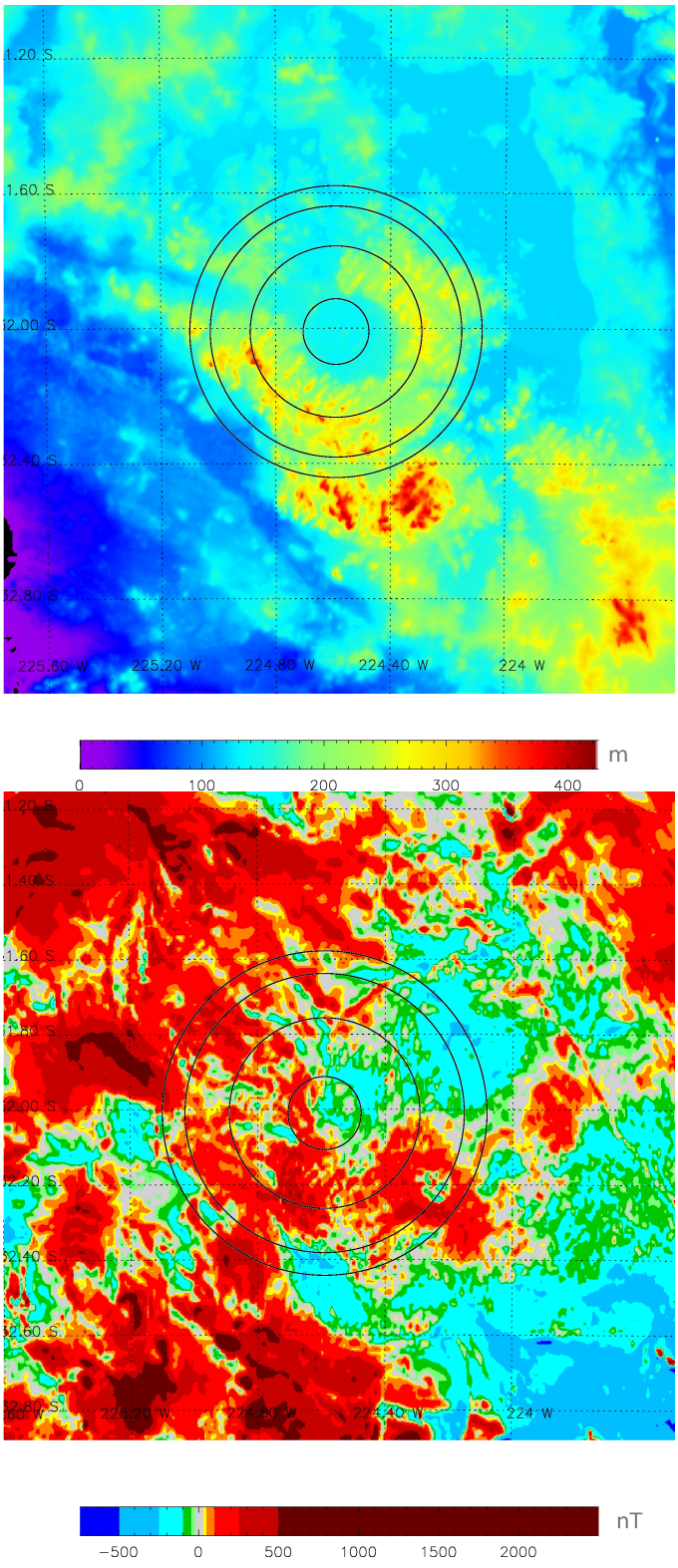

Figure 40: Magnetic map (ΔT) from 1 km grid new compilation of Geoscience Australia, 2007, over the 96 km diameter, Acraman impact crater, at 4 km altitude (bottom), using GRIDVIEW tools. The black circles represent the selected rings from SRTM30 global topography map (top).

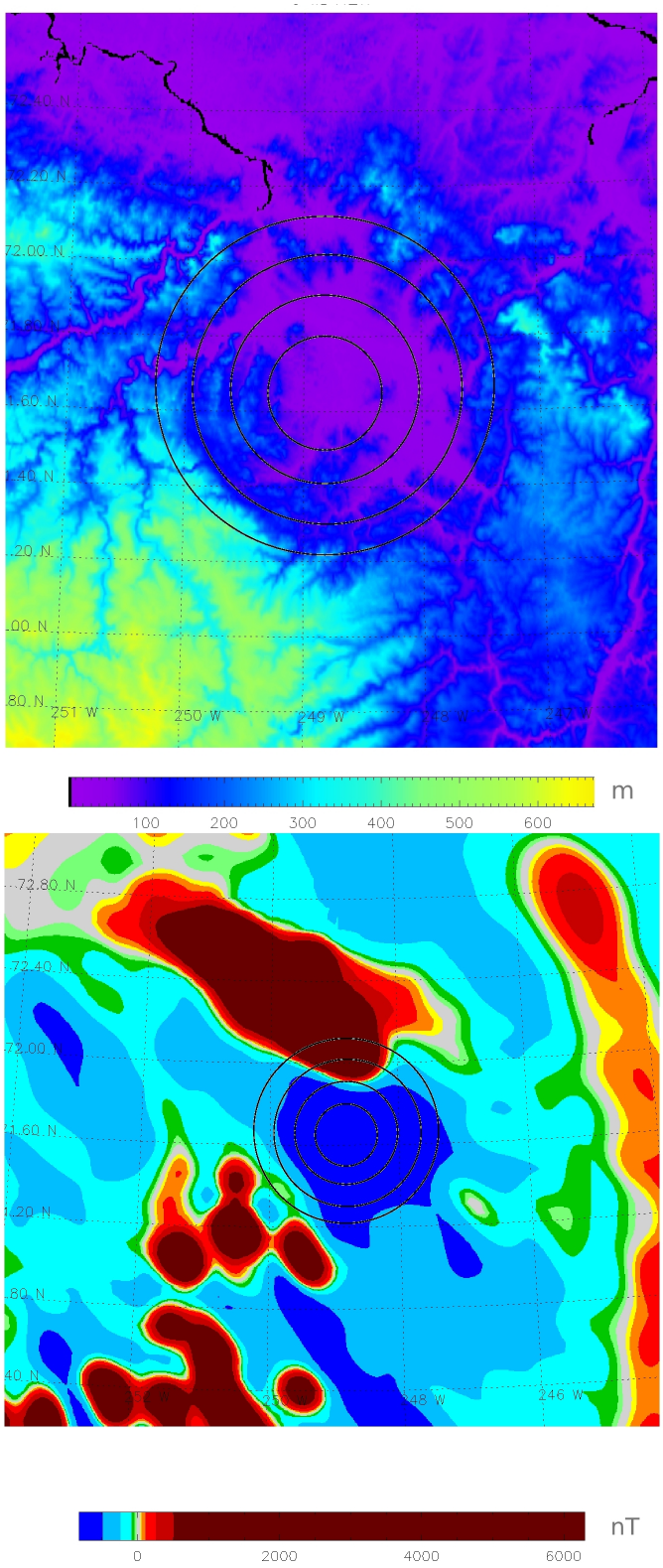

Figure 41: The improved magnetic map (ΔT) from WDMAM, over the 80 km diameter Popigai structure, at 5 km above the geoid (bottom), using GRIDVIEW tools. The black circles represent the selected rings from SRTM30 global topography map (top).

wavelengths, intermediate amplitude, dipolar anomalies, in the middle area. Generally, a magnetic low is encountered in the center of the crater, as for Acraman crater (Figure 40) possible due to a reduction of magnetization during the impact, or a magnetic low over the entire area as for Popigai structure (Figure 41) the circular shape of the crater being defined only from topographic view.

Some of them, have no corresponding visible structural feature on the surface, and might be surface representation of completely buried impact craters with their topographic feature obliterated, as the case of Bangui (Figure 39) still under debate about its origin. The relationship between magnetic anomaly and circular topography, clearly show that the anomaly continues and opens southwestward, through the Atlantic Ocean. Bangui is the subject of many interpretation and different models. One of them invoke a decompression melting triggered by a large impact and a large scale volcanism, but with no evidence in Bangui basin (Girdler et al., 1992). Others explain it as an emplacement of basalts in the lower crust, connected with the Pan-African orogeny (Hemant and Maus, 2005).

The results are presented in Tables 3 and 4. In the first, latitude and East longitude center (degrees) and diameters of all obvious rings seen in topographic map (kilometers) are determined with GRIDVIEW tools. Diameters listed are those of the largest confidently identified rings. The Age estimates (in My) are from the Earth's impact database[7] source. In the second one, only the topography is evaluated with the same GRIDVIEW software. The mean field strength (nT), in the central peak/inner ring, within each ring, and outside the crater, was evaluated by means of computation, using only three qualitative levels (1, 2, 3), in ascending order, from the center to a distance of two crater radii outwards. These levels allowed to associate labels, such as $(1-2-3)$, which describe the magnetic behavior from inside to outside the craters rims. In this case, the crater has only two rings, with a magnetic low in the center, a medium low between first and second ring, and with the most intense features seen outside the crater. Additionally, the maximum crustal anomaly intensity ($|B|$max. inside), in absolute value, at 5 km altitude, observed inside the outer rim, was computed for each crater.

The same procedure was carried out for Mars and Moon, too. First, the stronger gravity on the Earth caused less material to be ejected by the impact, resulting in a smaller transient crater and smaller scars of the old impacts. This means to deal with a lot of small craters (less 100 km diameter) rather than large craters, only 7 ranging between $100-500$ km diameter. The topo vertical evidence is poor for the smaller and older craters, even with large diameters, as presumable crater Bangui, 875 km diameter (early Precambrian) or Beaverhead, 59 km (900 My) old, Yarrabubba 56 km (200 My)

[7] www.unb.ca/passc/ImpactDatabase

old, making it difficult the selection of the rings by means of topographic maps. Some of impact structures are located on young and dynamic oceanic crust. Among them, Chicxulub multiring impact basin, 170 km, of Yucatan Peninsula and Montagnais, 46 km, offshore of Nova Scotia have a topo evidence and a magnetic signature of 500 nT with label $(3-3-2-1)$ and 50 nT with label $(1-2)$, respectively. Other three, even with large diameters, such Chesapeake Bay, offshore of the Atlantic coast of Virginia, 99 km, 400 nT and Kara in Kara Sea, 65 km, 100 nT maximum magnetic field value or Mjölnir crater from Barents Sea, 39 km and 0 nT show no magnetic signature, described by labels as $(2-2-2-2)$, $(2-2-2)$ or $(1-1)$, respectively, without any contrast, as in case of the other smaller Earth's craters.

On the Earth, the pattern of impacts which alter the magnetization of the entire depth of crust over a geographic area comparable at least to the final size of the impact crater is not mandatory. Here, first, when the crust cools immediately after the impact, the melt sheet heated above their Curie point can acquire a new thermoremanent magnetization (TRM), with a magnitude proportional to the strength of the main magnetic field and with the capability of the target rock to carry remanence. Second, in addition, the shock from the impact can add or remove net magnetization, depending on the strength and polarity of local magnetic field. Sometime, magnetization can be reduced or even erased if the minerals are shocked in an ambient field too weak to induce a sufficient shock remanent magnetization (SRM). In addition, post-impact hydrothermal activity can lead to the acquisition by crustal rocks of chemical remanent magnetization (CRM). These, and short waves component of the geomagnetic main field which overlap the long waves crustal field make the interpretation of the magnetic signature of impacts on Earth more complicate.

The magnetic signature is visible only over few and largest craters as Chicxulub, label $(3-3-2-1)$, Bangui, label $(3-3-3-2)$, Clearwater-W 50 km, label $(3-2-2-1)$, Manicouagan 103 km, label $(3-2-2-2)$, Vredefort 293 km, label $(3-2-2-2-2)$, Sudbury 260 km, label $(3-2-2-2-2)$. It is important to note (see the labels) the short-wavelength characteristics of strong crustal fields within the crater, compared with the outside impact structure. The absence of this feature on smaller craters is possibly due to more rapid decay of short wavelength than long-wavelength magnetization above the craters at WDMAM compilation altitude (5 km) than aeromagnetic altitudes of hundreds of meters. For example, Vredefort crater is characterized at 5 km altitude by moderated magnetic lows due to the fact that its inside magnetization coherence length is as small as centimeters (Carporzen et al., 2005). The main feature for smallest craters, like Carswell (39 km), Montagnais (46 km), Saint-Martin (40 km) or Shoemaker (30 km) is the disruption of the main magnetic trend, and forming of a circular low anomaly.

Name	**Latitude center**	**Longitude East center**	**Ring** 1 **diam.**	**Ring** 2 **diam.**	**Ring** 3 **diam.**	**Ring** 4 **diam.**	**Ring** 5 **diam**	**Age** (My)
Acraman	-32.1	135.41	21.61	56.43	82.66	96.11	-	590
Araquainha	-16.79	307.02	27	42.73	-	-	-	244
Bangui	6.05	17.95	492.24	683.96	875.12	-	-	early Prec.
Beaverhead	44.65	245.95	58.55	-	-	-	-	900
Carswell	58.47	250.40	38.99	-	-	-	-	115
Charlevoix	47.53	289.70	8.85	26.49	54.68	-	-	342
Chesapeake	37.3	283.92	19.45	78.64	99.47	-	-	35.5
Chicxulub	21.31	270.41	48.4	89.91	169.65	-	-	65
Clearwater-W	56.21	285.49	16.38	36.38	49.84	-	-	290
Kara	69.11	64.40	51.94	65.04	-	-	-	70
Kara-Kul	39.15	73.45	51.42	-	-	-	-	5
Keurusselka	61.8	24.17	19.5	30.75	-	-	-	1150
Manicouagan	51.38	291.27	15.1	57.9	103.03	-	-	214
Manson	42.53	265.47	34.15	-	-	-	-	73.8
Mjölnir	73.18	29.78	39.45	-	-	-	-	142
Montagnais	42.88	295.80	45.81	-	-	-	-	50
Morokweng	-26.46	23.57	71.17	-	-	-	-	145
Popigai	71.66	111.18	33.77	55.86	79.9	100.37	-	35.7
Puchez-Katunki	56.92	43.95	80.98	-	-	-	-	167
Saint-Martin	51.78	261.46	40.46	-	-	-	-	220
Shoemaker	-25.86	120.89	14.53	30.04	-	-	-	570
Siljan	60.87	15.14	51.81	-	-	-	-	377
Slate Island	272.99	311.34	33.19	-	-	-	-	450
Sudbury	46.65	278.84	84.02	125.91	190.34	259.89	-	1850
Tookonooka	-27.14	142.80	55.25	-	-	-	-	128
Vredefort	-27	27.55	50.37	103.73	171.4	293.05	-	2020
Woodleigh	-26.05	114.67	39.81	-	-	-	-	364
Yarrabubba	-27.18	118.84	30.76	55.94	-	-	-	2000

Table 3: Position and morphometry information and morphometry for Earth's craters, determined with GRIDWIEV tools.

Name	Total rings	|B|char. inner	2nd ring	3rd ring	4rd ring	5rd ring	|B|char. outside	|B|max inside	Topo evidence
Acraman	4	2	2	2	2	-	2	500	Yes
Araquainha	2	3	2	-	-	-	1	50	Yes
Bangui	3	3	3	3	-	-	2	800	Maybe
Beaverhead	1	2	-	-	-	-	2	200	Maybe
Carswell	1	1	-	-	-	-	2	200	Maybe
Charlevoix	3	2	2	2	-	-	2	300	Yes
Chesapeake	3	2	2	2	-	-	2	400	Yes
Chicxulub	3	3	3	2	-	-	1	500	Yes
Clearwater-W	3	3	2	2	-	-	1	500	Yes
Kara	2	2	2	-	-	-	2	100	Yes
Kara-Kul	1	2	-	-	-	-	1	100	Yes
Keurusselka	2	2	2	-	-	-	2	100	Yes
Manicouagan	3	3	2	2	-	-	2	0	Yes
Manson	1	2	-	-	-	-	1	0	Maybe
Mjölnir	1	1	-	-	-	-	1	0	No topo
Montagnais	1	1	-	-	-	-	2	50	Yes
Morokweng	1	-	-	-	-	-			Maybe
Popigai	4	2	2	2	2	-	2	500	Yes
Puchez-Katunki	1	1	-	-	-	-	2	400	Maybe
Saint-Martin	1	1	-	-	-	-	2	600	Maybe
Shoemaker	2	1	2	-	-	-	2	1000	Yes
Siljan	1	1	-	-	-	-	2	200	No topo
Slate Island	1	2	-	-	-	-	2	1000	Yes
Sudbury	4	3	2	2	2	-	2	2000	Yes
Tookonooka	1	2	-	-	-	-	1	50	Maybe
Vredefort	4	3	2	2	2	-	2	300	Yes
Woodleigh	1	2	-	-	-	-	2	200	Maybe
Yarrabubba	2	1	2	-	-	-	2	1000	Maybe

Table 4: Supporting criteria for Earth's craters.

They are represented by labels as $(1-2)$ for the first three and as $(1-2-2)$ for the fourth. The main mechanism for the depletion of the magnetization is in these cases the shock remanence. In the case of Yarrabubba crater (56 km), label $(1-2-2)$, which lies in the center of a large sub-circular magnetic low, beside the shock remanence, the subsequent hydrothermal alteration might have caused magnetite destruction along and around radial and concentric faults related to the impact.

However, the magnetic signatures over impact structures on Earth can be more complex than the magnetic low characteristic. They consist in a mix with high amplitudes and short wavelengths magnetic fields. The shock remanent magnetization (SRM) has the main role, and it is induced by the high pressure ($> 30-50$ GPa). For larger structures, as Manicouagan or Slate Islands, the natural remanent magnetization (NRM) can be present, if there is enough occurrence of magnetic carriers in target rocks. Generally, the melt will have a higher magnetic susceptibility than the target due to the recrystallization process. For example, biotite and amphibole could decompose to an assemblage of phases that often contain magnetite when they are exposed to high post-shock temperatures. Also, the hydrothermal alteration processes favored by the brecciation and by the heat generated by impact are not to be forgotten. A chemical remanent magnetization (CRM) in the direction of the present magnetic field is acquired, too. The circulation of the hydrothermal fluids in the presence of oxygen favors an increase of magnetization intensities.

3.2.2 Mars

For Mars, the correlative model of Purucker (Lillis et al., 2010), at 400 km altitude or the Electron Reflectometry (ER) model of Lillis et al. (2008b), at 185 km altitude were used to superpose the largest craters, bigger than 400 km, selected from Mars Orbiter Laser Altimeter (MOLA) topograhy map (Smith et al., 2001), by means of GRIDVIEW software. Some of them are looking like topographic depressions, with no corresponding visible rings on the surface but the most of large craters are obviously visible in topographic images, like Hellas (Figure 45). The first ones are completely buried impact craters and their topographic feature was compared with Crustal Thickness model (CT), as in the case of Utopia (Figure 42). By comparing maps of observed magnetic field over the largest apparently demagnetized impact craters, plotted at different altitudes, 185 km and 400 km, as can be seen in Figures 43 and 44, it is obviously that low altitude models show a detailed view of short wavelengths of the very weak, almost nonexistent crustal field. This is the case of younger impact craters, as Isidis (Figure 28), following Hellas, which seems to have not been remagnetized after the impact, due to the missing of an active core dynamo at that time.

Tables 6 and 5 offer mostly the same information obtained from GRIDVIEW and mean field calculations. For the age estimates (in Gy) were used Crater Retention Age (CRA) for impact basins diameter $> 1000\ km$ (Frey, 2008) for Age^* $N300$ column, and from Hartmann and Neukum (2001) or Lillis et al. (2008a) (in brackets), in the last column (Age). "No" represents craters of Noachian age, between $3.6 - 4.2\ Gy$. The high-precision topographic gridded data set revealed easily the presence of any depression set to be circular. These circular features were compared in this case with Barlow (1988), Frey (2006), Langlais and Quesnel (2008), Frey (2010) or with Crustal Thickness model (CT).

Mars does not possess a global dipolar magnetic field of internal origin. The remanent magnetization in the Martian meteorite $ALH84001$ shows clearly that a substantial global field must have existed early in the history of Mars and it was 10 times greater than on the Earth, at similar altitude (Weiss et al., 2002). The strongest magnetic anomalies, of hundreds of nT, are mainly located in the Noachian crust (around 4 Gy) of the southern hemisphere (Hood et al., 2005). They may be due to post-impact heating within large craters, associated with heating by magmatic intrusions and thermoremanent magnetization acquired as the feromagnetic minerals from the crust cooled below the Curie temperatures. This distribution and the shape of the magnetic anomalies are still subject of debate and it is believed to have major implications for the ancient dynamo on Mars and its crust. Any interpretation relies on the understanding of volcanism and impact cratering that surely affected the remanent magnetization during Mars' history (Thébault, 2006).

Among these two different processes, impact cratering appears to demagnetize large regions of the crustal magnetic field, especially on the smoothed lowlands which do not show significant anomalies. The younger giant impact basins ($0.17 - 2.68$ Crater Retention Age), such Hellas 3996 km diameter (4.07 Gy old), Argyre 2348 km (4.04 Gy old), Isidis 1878 km ($3.81 - 3.96\ Gy$ old) and the oldest in this group, Utopia 4260 km diameter (4.11 Gy old) show an absence of central magnetic anomalies because the crust has presumably been demagnetized by these impacts after the cessation of the Martian dynamo, at about $4.15 - 4.12\ Gy$, after the analysis of Table 5. The maximum amplitudes, inside these craters, range from 8 to 20 nT, at an altitude of 185 km. Note the absence of magnetic signatures associated with the hugest Olympus Mons volcano lavas and Tharsis Montes, as well as over impact basins Hellas and Argyre, with comparable ages. They are characterized in Table 6 with labels of type $(1-2-2-2-3)$ such Argyre, $(1-2-2-3)$ for Isidis or $(1-1-1-2-2)$ for Utopia.

The older large craters, such Ares 3369 km diameter (4.33 Gy old), Daedalia 2568 km (4.17 Gy) and Zephyria 1188 km (4.21 Gy old) are associated with moderate – to – strong

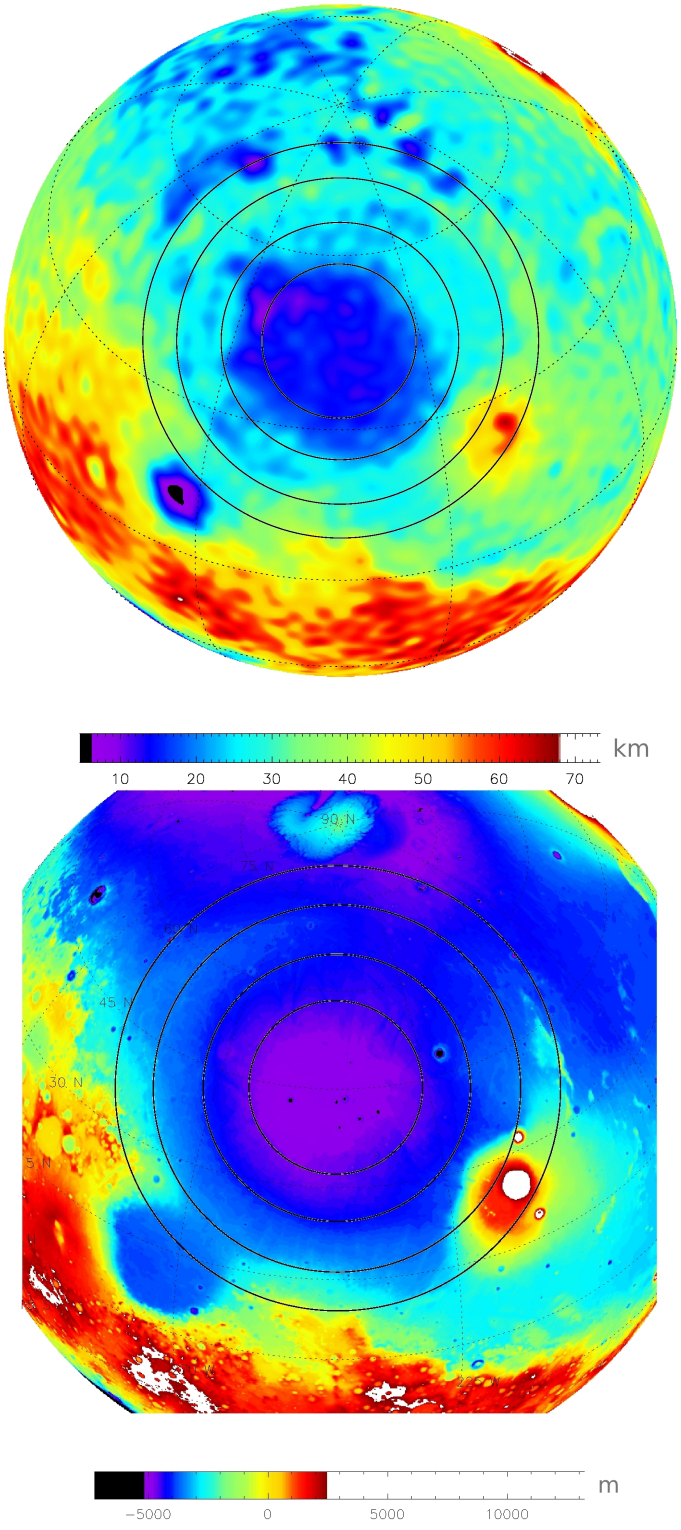

Figure 42: Crustal Thickness (CT) model of Neumann et al. (2004) (top) and MOLA altimetry map (bottom) of 4260 *km* diameter Utopia with the black circles as selected rings from CT model using GRIDVIEW tools for graphics.

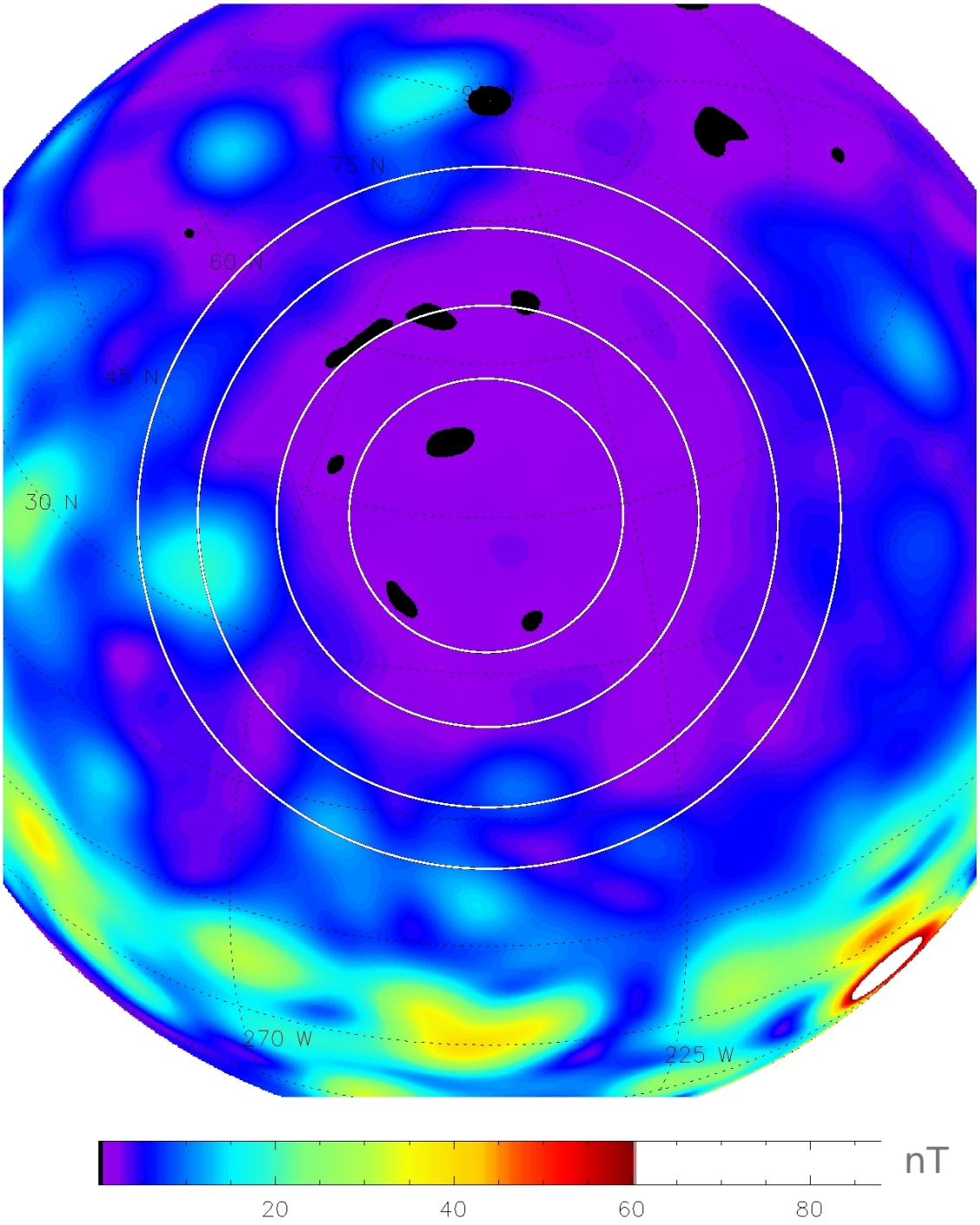

Figure 43: Crustal magnetic field map of Utopia, 4260 km diameter, from the Correlative model of Lillis et al. (2010), at 400 km altitude, using GRIDVIEW tools for graphics.

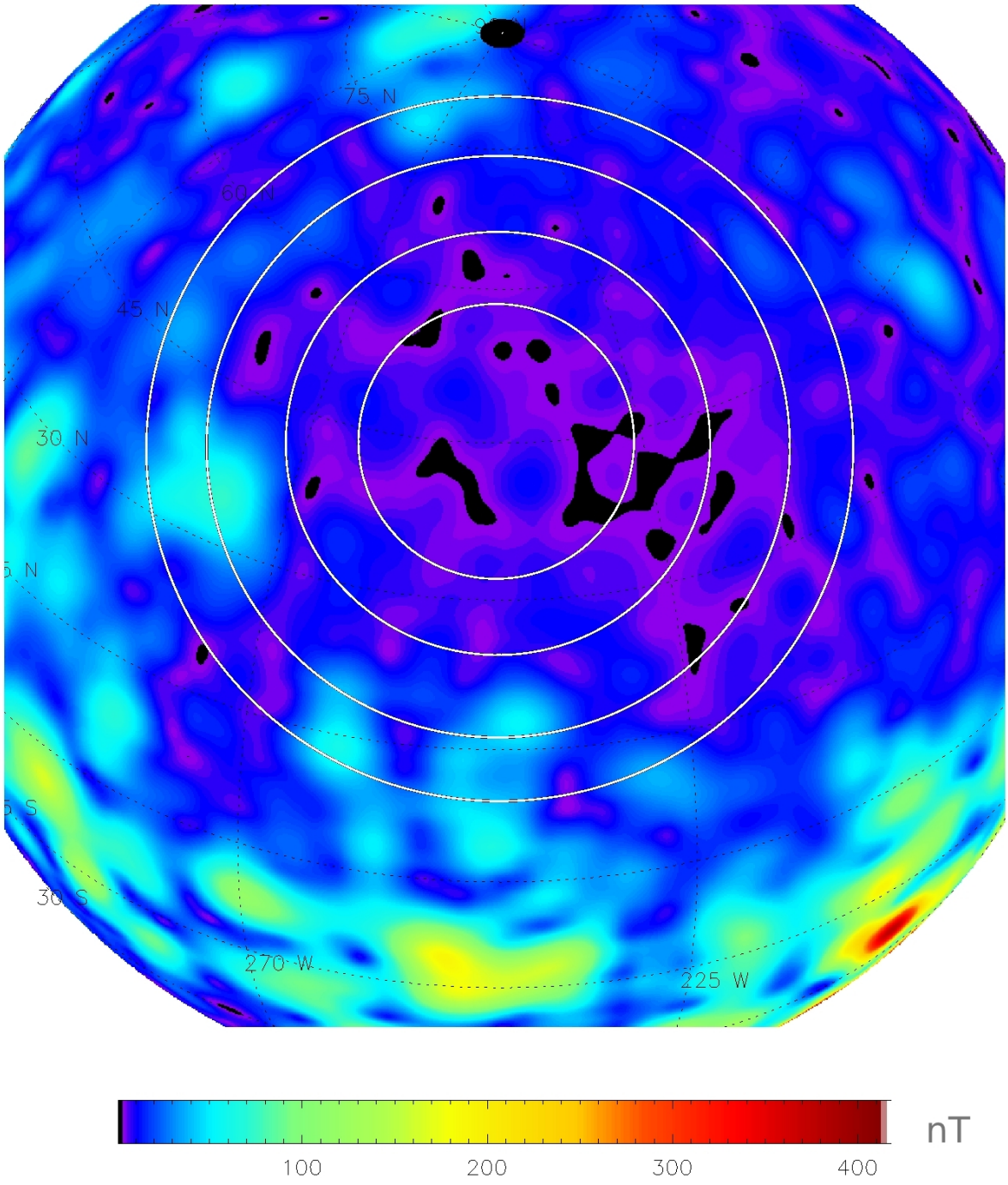

Figure 44: Crustal magnetic field map of Utopia, 4260 *km* diameter, from the ER model of Lillis et al. (2008b), at 185 *km* altitude. GRIDVIEW was used for graphics.

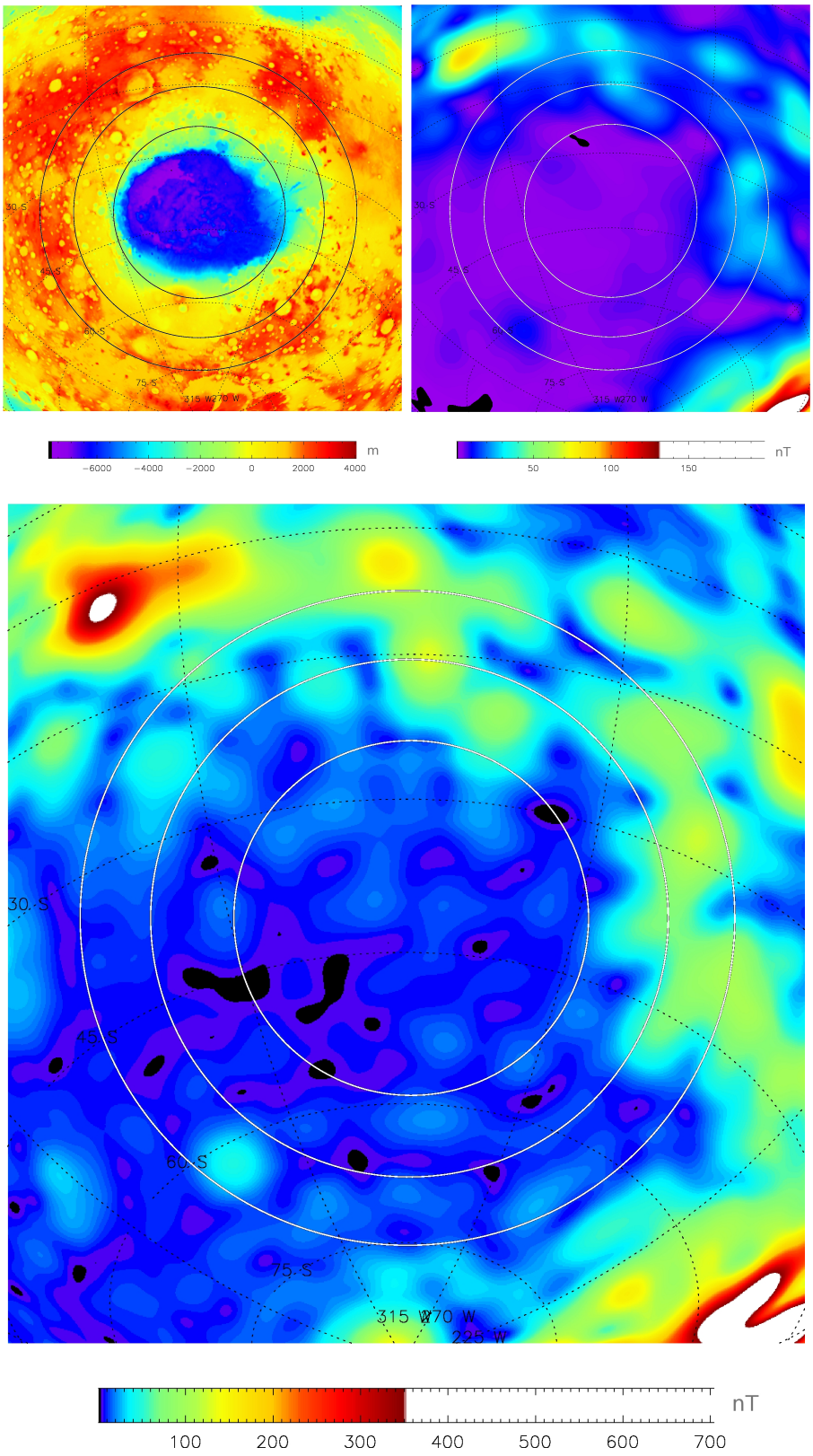

Figure 45: MOLA altimetry of Hellas, 3996 *km* diameter crater (upper left) and its crustal magnetic maps, at 400 *km* (top) and 185 *km* altitude, from Correlative (upper right) of Lillis et al. (2010) and ER model (bottom) of Lillis et al. (2008b) respectively. The black circles are drawn using GRIDVIEW tools, from MOLA map.

Name	**Latitude center**	**Longitude East center**	**Ring 1 diam.**	**Ring 2 diam.**	**Ring 3 diam.**	**Ring 4 diam.**	*Age** N(300)	**Age** (Gy)
Acidalia-Frey	59.8	342.66	2389.09	3069.92	-	-	3.21	3.21-(3.7)-No
Alba	31.11	268.86	1335.38	2086.8	-	-		
Amenthes	-0.9	110.3	1051.93	1463.79	-	-	6.68	4.21-No
Ares	4	343.75	1247.42	2075.13	3360.46	-	4.33	4.16-No
Argyre	-49	317.27	938.22	1300.49	1754.97	2348.44	1.47	4.04-(3.83)-No
Cassini	23.52	31.72	428.3	837.28	-	-		
Chryse	25	318	1693.24	2565.04	3186.96	-	3.42	4.14-No
Daedalia	-26.96	228.43	888.6	1482.76	2568.43	-	5.7	4.17-No
Hellas	-41.59	68.37	2074.05	3084.78	3996.09	-	1.78	4.07-(3.99)-No
Hematite	3.2	357.8	468.14	766.65	1006.07	-	3.37	4.14-No
Huygens	-14	55.5	250.92	356.16	462.52	-		3.92-(3.85)-No
Inside-Amazonis	29.32	192.63	1142.84	-	-	-	3.81	4.15-No
Isidis	13.48	87.42	1059.73	1370.3	1877.79	-	0.17	3.81-(3.96)-No
Ladon	-18.5	330.78	433.02	710.65	1012.75	-		
Lyot	50.45	29.12	101.06	235.55	-	-		x - 3,4
MOLA hole	30.1	48.18	442.87	-	-	-		
N-Tharsis	17.63	243.6	1341.82	-	-	-	3.51	4.14-No
Rev. N. Pole	80.56	196.9	1457.32	2141.48	-	-	2.99	4.12-No
Rev. Solis	-25.5	275.9	1003.51	1752.19	-	-	3.68	4.14-No
Schiaparelli	-2.7	16.4	488.48	-	-	-		3.92-No
Scopolus	6.75	81.65	2258.02	-	-	-	3.24	4.13-No
SE-Elysium	3.57	170.27	1421.37	-	-	-	3.24	4.13-No
Sirenum	-43.53	166.41	458.94	-	-	-		
Sirenum-CTA	-67.65	204.99	1032	-	-	-	5.57	4.19-No
S-Lyot	41.65	38.11	355.57	489.11	-	-		
S-Renaudot	37.45	63.09	592.21	-	-	-		
S-Polar	-84.25	95	924.43	-	-	-		
Unnamed-B	-59.95	135.12	523.42	776.54	1086.38	-		
Unnamed-Barlow	31	6.22	783.73	-	-	-		
Unnamed-C	-71.31	139.89	651.9	1242.31	-	-		
Unnnamed-F	-0.2	140.32	1086.87	1544.44	-	-		
Utopia	45.3	115.5	1567.59	2444.91	3432.76	4260.16	2.68	4.11-(3.8)-No
W-Le Verrier	-37.12	3.36	488.56	-	-	-		
Zephyria	-12.7	164.46	597.84	883.96	1187.82	-	6.27	4.21-(3.81)-No

Table 5: Position and morphometry information for Mars' craters, determined with GRIDWIEV tools.

Name	Total rings	|B|char. inner	2nd ring	3rd ring	4rd ring	5rd ring	|B|char. outside	|B|max inside	Topo evidence
Acidalia-Frey	2	1	2	-	-	-	2	20	Yes
Alba	2	1	1	-	-	-	2	3	Maybe
Amenthes	2	1	2	-	-	-	2	30	Maybe
Ares	3	2	2	3	-	-	2	40	Yes
Argyre	4	1	2	2	2	-	3	20	Inner ring
Cassini	2	1	1	-	-	-	2	24	Yes
Chryse	3	1	2	2	-	-	2	40	Yes
Daedalia	3	2	2	2	-	-	1	60	Maybe
Hellas	3	1	2	2	-	-	3	10	Yes
Hematite	3	1	2	2	-	-	3	22	Yes
Huygens	3	1	1	1	-	-	1	10	Yes
Inside-Amazonis	1	1	-	-	-	-	2	5	CT
Isidis	3	1	2	2	-	-	3	12	Yes
Ladon	3	1	1	1	-	-	1	12	Yes
Lyot	2	1	2	-	-	-	2	5	Yes
MOLA hole	1	1	-	-	-	-	2	10	Yes
N-Tharsis	1	1	-	-	-	-	2	5	Maybe
Rev. N Pole	2	1	2	-	-	-	2	15	Maybe
Rev. Solis	2	1	2	-	-	-	2	25	Yes
Schiaparelli	1	1	-	-	-	-	1	20	Yes
Scopolus	1	1	-	-	-	-	2	40	Yes
SE-Elysium	1	1	-	-	-	-	2	50	Yes
Sirenum	1	1	-	-	-	-	2	100	Maybe
Sirenum-CTA	1	1	-	-	-	-	2	70	CT
S-Lyot	2	2	1	-	-	-	1	14	Yes
S-Renaudot	1	1	-	-	-	-	2	10	Maybe
S-Polar	1	1	-	-	-	-	2	20	Maybe
Unnamed-B	3	2	2	2	-	-	2	50	Maybe
Unnamed-Barlow	1	2	-	-	-	-	2	7	Maybe
Unnamed-C	2	1	1	-	-	-	2	60	Maybe
Unnnamed-F	2	1	1	-	-	-	2	40	Maybe
Utopia	4	1	1	1	2	-	2	8	Yes
W-Le Verrier	1	1	-	-	-	-	2	4	Yes
Zephyria	3	1	1	2	-	-	2	70	Maybe

Table 6: Supporting criteria for Mars' craters.

crustal magnetic fields ranging between $40 - 60\ nT$, extremes of crustal field intensity counted over the studied craters. They likely formed before the dynamo ceased and they have acquired a thermoremanence in the presence of an ambient magnetic field and that remanence would have persisted to the present-day. Maybe deep and coherently magnetized bodies, associated with magma intrusions beneath the basins, could explain the crustal anomalies, analogous to those of the Sudbury crater, on Earth. In this case, labels resulted from Table 6 look like $(2-2-3-2)$ as for Ares or $(2-2-2-1)$, as for Daedalia.

Comparing with early-mid Noachian craters as Isidis, Argire or Hellas, the mid-late Noachian ones ($3.85 - 3.92\ Gy$ old) such as Huygens ($462\ km$), Ladon ($1012\ km$) or Schiaparelli ($488\ km$) show labels such as $(1-1-1-1)$, $(1-1-1-1)$ or $(1-1)$ respectively. They show no magnetic signature, with no distinction between the inner demagnetized area and surroundings (Isac et al., 2011). These characteristics confirm the turn-off of the global field at that time and a deeply demagnetized crust due to the heavy bombardment in the past. The magnetic signature over of most large impact craters on Mars reveals mainly an anomalous magnetic low with or without a random magnetic signature among the regional magnetic pattern.

3.2.3 Moon

Here, a global magnetic map by Purucker and Nicolas (2010), a spherical harmonic model corresponding to 64 km wavelength resolution from 30 km mean altitude above the lunar datum, was utilized to show the magnetic fields in and around the Moon's impact craters, with diameter size limit of 150 km. Their circular features were identified from LOLA map with the same GRIDVIEW tools.

The largest concentration of weak surface magnetic fields, less $0.3\ nT$, is located within the youngest and larger basins of the Moon, like Imbrium crater (Figure 48). This can be a result of shock demagnetization, associated with impacts. The older impact craters, like Crissium and Nectaris (Figures 46 and 47) are not so strongly demagnetized, with short scale anomalies inside inner rings of about $1.5 - 6\ nT$.

The same information, as for the Earth and Mars, are carried out in Tables 8 and 7. These circular features from the Moon, were compared with the ringed impacts database from *Lunar Sourcebook: A User's Guide to the Moon* (Heiken et al., 1991), or from Frey (2010). Due to the fact that the chronology of lunar impact basins is uncertain, the largest impact craters were reliably placed into 15 age-groups (see Age^* column), from the youngest (1) to the oldest (15), on the basis of photo-geologic observations related to degradational state and crater density (Wilhelms, 1984), numbered in the reverse order of the impact sequence, and where "I"=Imbrian, "N"=Nectarian, "pN"=pre-

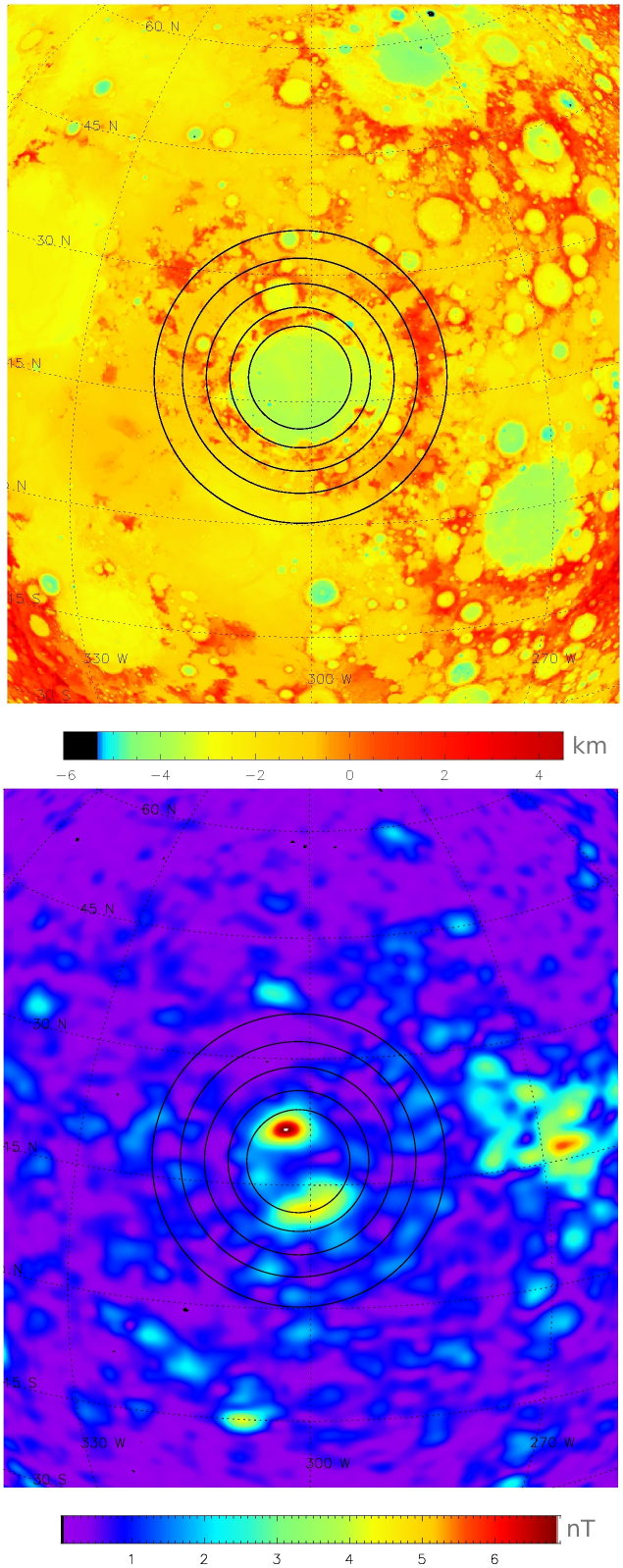

Figure 46: LOLA altimetry map of 1069 *km* diameter Crissium crater (top) with the drawn black circles, as selected rings, and the new spherical harmonic map of the internal magnetic field (Purucker and Nicolas, 2010), on the bottom. GRIDVIEW was used for graphics.

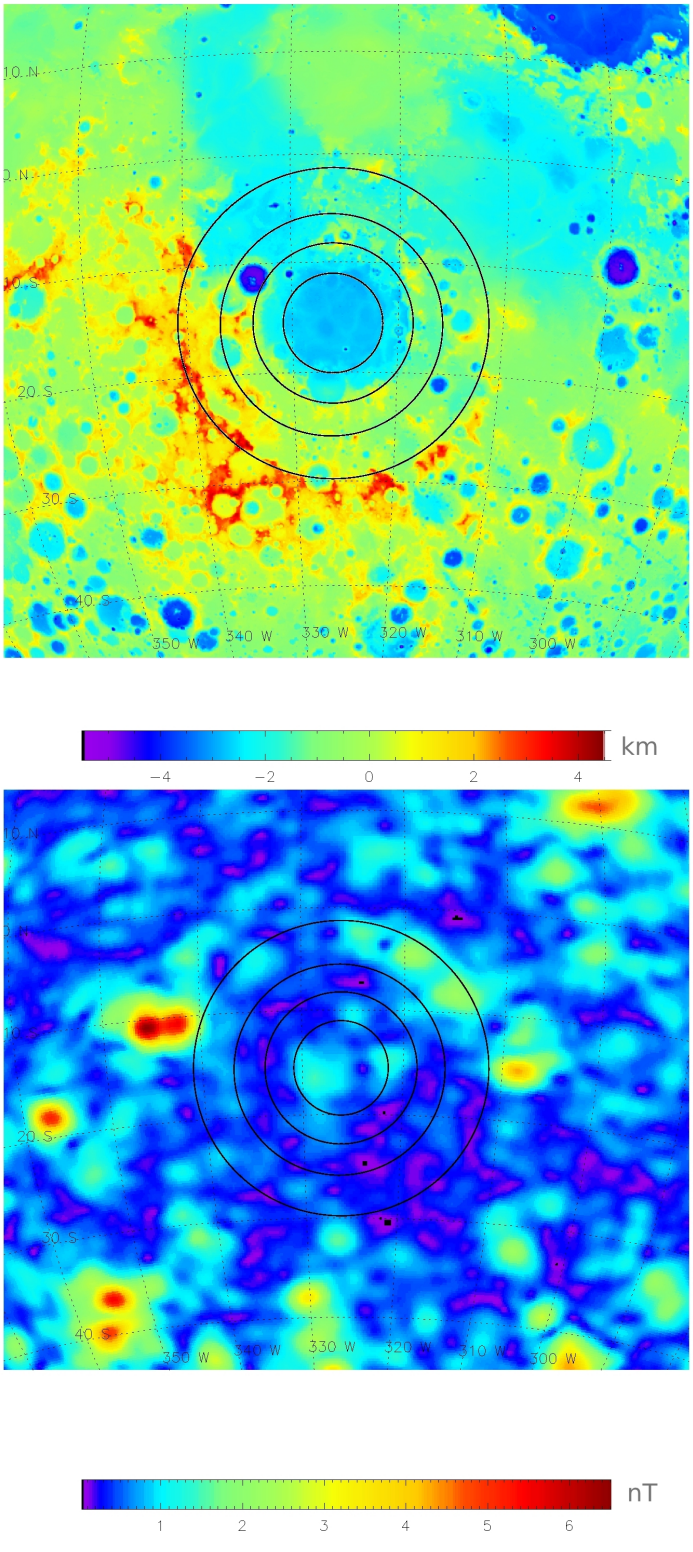

Figure 47: LOLA topographic map of 865 km diameter Nectaris crater (top) and the new spherical harmonic map of the internal magnetic field of it (Purucker and Nicolas, 2010), bottom. The black circles represent the tracked rings from LOLA map. GRIDVIEW was used for graphics.

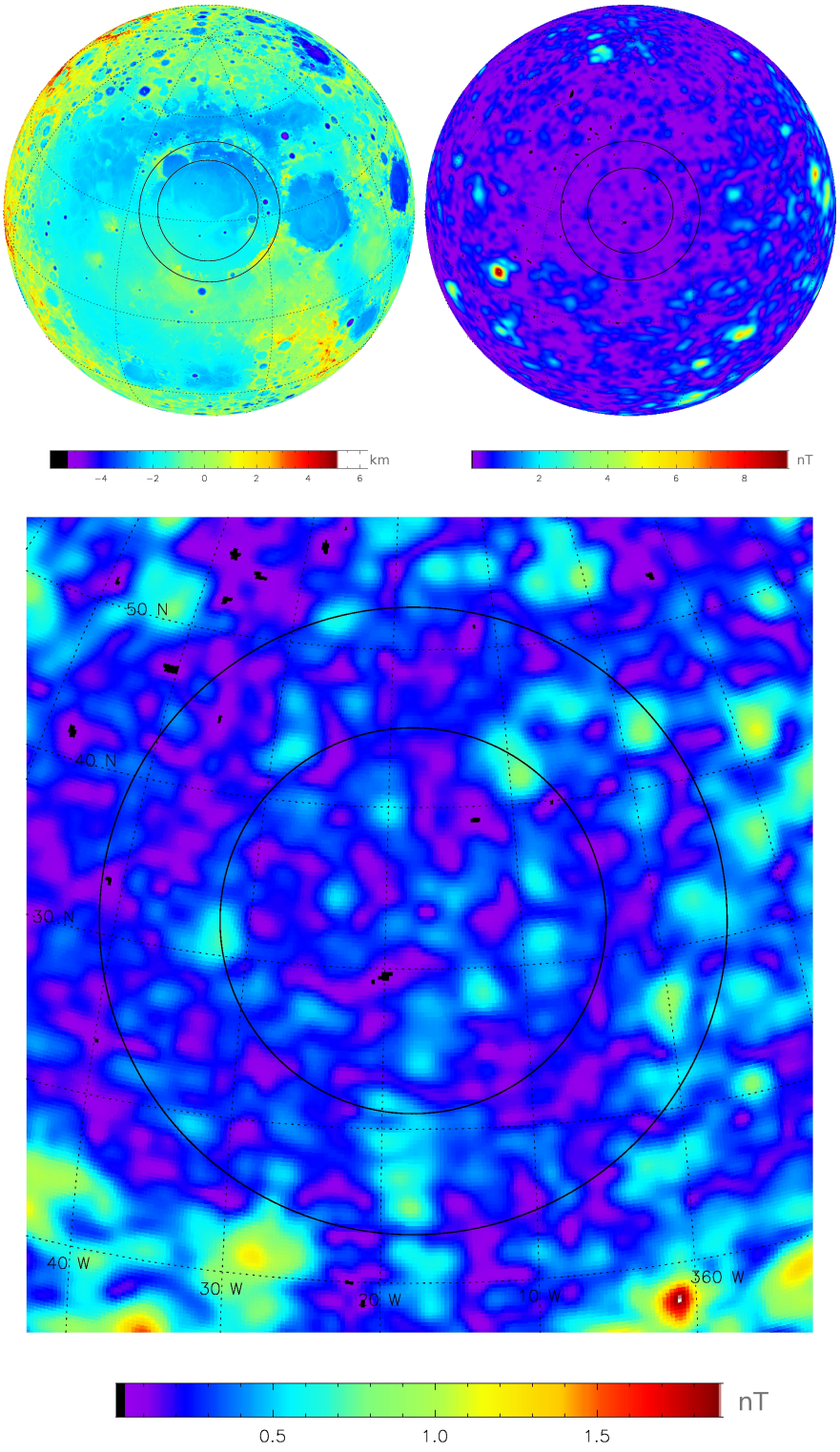

Figure 48: LOLA topographic map (upper left) of Imbrium, 1212 *km* diameter crater, previous sequential model of internal magnetic field (upper right) of Purucker (2008) and the new spherical harmonic model of Purucker and Nicolas (2010) (bottom). The black circles represent the tracked rings from LOLA map. GRIDVIEW was used for graphics.

Nectarian. *Age* column represents the latest views on the lunar stratigraphy (based on radiogenic isotope ages which have been determined on lunar samples), and the principles of absolute age dating of the basins which have been reevaluated by Stöffler and Ryder (2001), Neukum et al. (2001) and Cohen (2008). An evaluation of the specific magnetic signature often makes it difficult to clear identify it, especially when the average field in the crater is weaker (in the most studied craters), with labels as $(1-2)$ for Grimaldi, $(1-2-3)$ for Scrödinger, or $(1-1-1-2-2)$ for Orientalis. Few of them, of Nectarian age, have a stronger magnetic signature than the background fields, with labels such as $(3-3-2-2-2-2)$ for Crissium or $(3-2-2)$ for Serenitats, as examples. The maximum internal magnetic field inside the crater ranges between $0.5-6\ nT$ at 30 km altitude, with three exceptions: Procellarum Oceanus (3377 km diameter), Mare Ingenii crater (307 km diameter) and South Pole-Aitken basin (2551 km diameter). There, local high crustal magnetic fields, of $10-12\ nT$ occurred. The magnetic signature for the first two of them is associated with swirls (bright material or albedo). Their exact formation mechanism is unknown, but imply a powerful electric discharge in a conductive crust. In South Pole-Aitken (SPA), a pre-Nectarian basin, a linear trend of magnetic anomalies, in the northwestern part is defined. Purucker et al. (2012) used a forward model of a dike swarm that best fit the observations, consistent with nearside basalts eruptions in the Imbrian period. This linear magnetic anomalies can be the manifestation of magnetized dikes due to the ascent of magma and emplacement of mare basalts in the South Pole-Aitken basin.

Nevertheless, magnetic measurements indicate a correlation between meteor impact basins, their demagnetization (ranging over a few nT) and strong magnetic fields (tens up to hundreds of nT to a common altitude of 30 km) on the diametrically opposite side of the moon (Purucker and Whaler, 2007). Figure 49 shows the antipodal feature of the Moon, where the largest crustal magnetic anomalies are concentrated in the equatorial and sub-equatorial area, antipodal to the largest Imbrian (I) and late Nectarian (N) impact craters: Orientale $(1-I)$, Imbrium $(3-I)$, Crissium and Serenitatis $(4-N)$. These large impactors (in addition to the excavation of basins) sprayed ejecta over the lunar surface due to the huge shock and seismic waves. Melt ejecta can be magnetized in an external magnetic field (the solar wind plasma sheet) through shock remanent magnetization (SRM). The stronger magnetic fields observed may be a consequence of remagnetization of the melt ejecta in the presence of an external magnetic field. The impact that formed Orientale basin, 964 km diameter (white circle no.1 in Figure 49) obliterated all prior craters within the basin itself and exerted a positive magnetic anomaly (no.1 black circle) in the north-eastern part of Crissium crater (no.8 white circle). And Orientale is not the biggest lunar basin.

Name	**Latitude center**	**Longitude East center**	**Ring** 1 **diam.**	**Ring** 2 **diam.**	**Ring** 3 **diam.**	**Ring** 4 **diam.**	**Ring** 5 **diam**	*Age**	**Age** (Gy)
Amundsen	-81.76	117.88	354.21	-	-	-	-	9-pN	
Bailly	-66.92	291.19	305.26	-	-	-	-	4-N	
Balmer-Kapteyn	-16.06	69.54	280.33	519.61	-	-	-	14-pN	
Birkhoff	58.85	213.59	357.57	-	-	-	-	9-pN	
Coulomb-Sarton	52	237.1	171.26	381.02	-	-	-	11-pN	
Fecunditatis	-3.73	51.79	689.89	-	-	-	-	13-pN	
Freundlich-Sharonov	18.54	175	364.69	612.45	-	-	-	8-pN	
Grimaldi	-5.3	292.15	192.99	417.21	-	-	-	7-pN	
Hertzprung	1.96	231.07	263.45	402.51	597.63	-	-	4-N	
Orientale	-20	265.2	322.64	479.31	649.02	964.44	-	1-I	
Imbrium	33	342	859.22	1211.79	-	-	-	3-I	3,85 - 3.77
Humorum	-24.08	320.04	319.58	441.71	565.85	849.31	-	4-N	
Crisium	17.85	58.5	370.34	507.09	678.76	853.27	1069.11	4-N	3.89 - 3.84
Serenitatis	26.85	19.17	395.37	677.05	-	-	-	4-N	3.89 - 3.84
Humboldtianum	57.8	83.3	323.34	639.87	-	-	-	4-N	
Moscoviense	26.46	147.2	233.7	432.2	629.91	-	-	6-N	
Mendel-Rydberg	-49.65	265.91	325.29	500.33	665.16	-	-	6-N	
Apollo	-36.07	208.5	243.2	511.2	-	-	-	7-pN	
Ingenii	-32.79	163.97	307.89	-	-	-	-	12-pN	
Keeler-Heaveside	-10	162	157.35	-	-	-	-	11-pN	
Korolev	-4.18	202	206.04	440.75	-	-	-	6-N	
Lomonosov-Fleming	20.37	105	664.69	-	-	-	-	13-pN	
Lorentz	33.24	263.18	192.94	380.41	-	-	-	10-pN	
Marginis	20.46	84	551.36	-	-	-	-	14-pN	
Mendeleev	5.4	141.31	136.27	324.15	-	-	-	5-N	
Nectaris	-15.54	33.84	273.91	441.68	614.51	864.45	-	6-N	3,92 - 3.85
Nubium	-19.08	343.7	698.37	-	-	-	-	13-pN	
Pingre-Hausen	-55.9	277.65	361.82	-	-	-	-	14-pN	
Plank	-57.24	135.44	167.34	319.13	-	-	-	9-pN	
Poincaire	-57.54	162.57	176.51	343.85	-	-	-	12-pN	
Procellarum	25.7	344.66	1721.51	3377.02	-	-	-	15-pN	
Schiller-Zucchius	-56.15	315.27	192.31	370.12	-	-	-	9-pN	
Schrödinger	-74.87	134.04	173.56	348.19	-	-	-	2-I	
Sikorsky-Rittenhouse	-69	110.58	284.86	-	-	-	-	4-N	
Smythii	-2.09	86.9	357.17	534.16	885.19	-	-	11-pN	
SPA	-56	179.46	1859.73	2304.95	2551.36	-	-	15-pN	
Tranquillitatis	7.15	40.15	521.88	774.97	-	-	-	13-pN	

Table 7: Position and morphometry information for Moon's craters, determined with GRIDWIEV tools.

Name	Total rings	|B|char. inner	2nd ring	3rd ring	4rd ring	5rd ring	|B|char. outside	|B|max inside	Topo evidence
Amundsen	1	1	-	-	-	-	1	2	No
Bailly	1	2	-	-	-	-	1	1.5	Yes
Balmer-Kapteyn	2	2	2	-	-	-	2	1	Maybe
Birkhoff	1	2	-	-	-	-	2	0.8	Yes
Coulomb-Sarton	2	2	1	-	-	-	2	0.8	Yes
Fecunditatis	1	2	-	-	-	-	2	4	Yes
Freundlich-Sharonov	2	1	2	-	-	-	3	1	Yes
Grimaldi	2	1	2	-	-	-	2	1	Inner ring
Hertzprung	3	2	1	1	-	-	2	1	Yes
Orientale	4	1	1	1	2	-	2	3	Yes
Imbrium	2	1	1	-	-	-	2	2	Yes
Humorum	4	2	3	3	3	-	3	2	Inner ring
Crisium	5	3	3	2	2	2	2	6	Yes
Serenitatis	2	3	2	-	-	-	2	2	Yes
Humboldtianum	2	3	2	-	-	-	2	2	Yes
Moscoviense	3	3	2	2	-	-	2	2	Yes
Mendel-Rydberg	3	2	1	1	-	-	1	4	Inner ring
Apollo	2	2	1	-	-	-	1	5	Yes
Ingenii	1	3	-	-	-	-	2	12	Yes
Keeler-Heaveside	1	1	-	-	-	-	2	0.5	Yes
Korolev	2	2	2	-	-	-	2	3	Yes
Lomonosov-Fleming	1	2	-	-	-	-	2	4	Maybe
Lorentz	2	1	1	-	-	-	2	1	Yes
Marginis	1	2	-	-	-	-	2	4	No
Mendeleev	2	1	2	-	-	-	3	1	Yes
Nectaris	4	2	1	1	2	-	3	1.5	Yes
Nubium	1	1	-	-	-	-	2	1	Yes
Pingre-Hausen	1	1	-	-	-	-	3	1	No
Plank	2	1	2	-	-	-	2	4	Yes
Poincaire	2	1	1	-	-	-	2	4	Yes
Procellarum	2	1	2	-	-	-	2	10	Yes
Schiller-Zucchius	2	2	1	-	-	-	1	1	Maybe
Schrodinger	2	1	2	-	-	-	3	1	Yes
Sikorsky-Rittenhouse	1	2	-	-	-	-	2	1.5	No
Smythii	3	2	1	2	-	-	3	3	Yes
SPA	3	2	3	2	-	-	2	12	Yes
Tranquillitatis	2	2	2	-	-	-	3	4	Maybe

Table 8: Supporting criteria for Moon's craters.

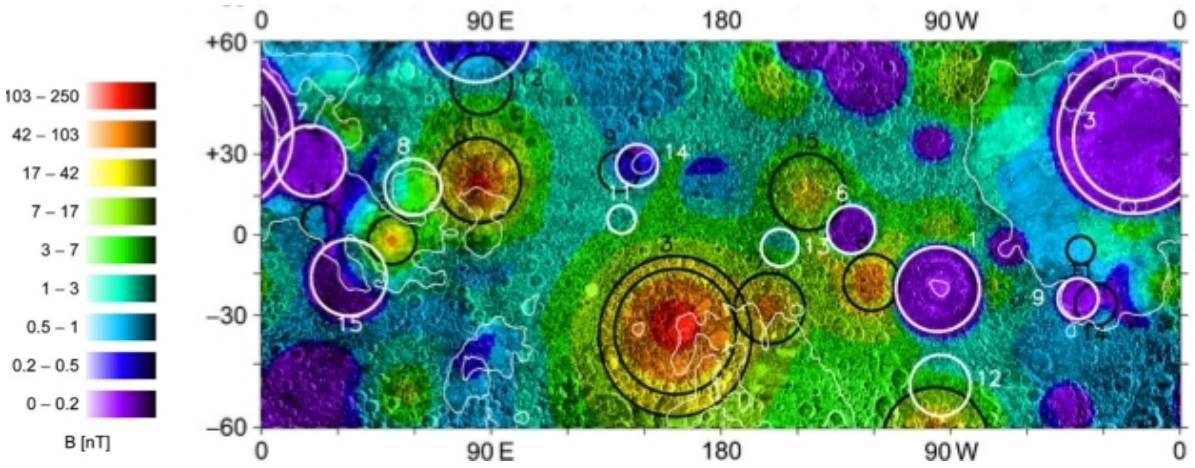

Figure 49: An empirical model based on crustal magnetic field intensity at the martian surface, showing the magnetizing and demagnetizing effects of the biggest 15 Nectarian and Imbrian impact craters. The main rims are marked with white circles and numbers, and their antipodal with black circles and numbers, respectively. *Adapted from Mitchell et al. (2008).*

Another larger impact, the Imbrium Basin, 1211 km diameter (no.3 white circles in the same Figure 49) affected an even larger fraction of the terrain, including Korolev crater, with 3 nT amplitude of the southern area, antipodal with it. Generally, all Imbrian and few Nectarian $(4 - N)$ are completely demagnetized, with no significant magnetic anomalies with labels type such $(1 - 2 - 2)$ for 417 km Grimaldi crater or $(1-1-1-2-2)$ for Orientale youngest basin. Other Nectarian basins such Moscoviense (no.14 white circle) show moderate magnetic anomalies $(2 - 4\ nT)$, associated, as in the case of Crissium or Korolev, with an antipodal impact (no.9 black circle), Humorum crater, with label $(2-3-3-3-3)$. These Nectarian-aged craters, such as Moscoviense with label $(3-2-2-2)$, Mendel-Rydberg with label $(3-2-2-2)$, Humboldtianum with label $(3-2-2)$, Crisium with label $(3-3-2-2-2-2)$, present a single main anomaly near the basin center, especially between the inner and outer rings, whith one exception, Crissium (Figure 46). Here, 6 nT anomalies are distributed in a semi-circular arc near the basin center and inside the first ring (Isac et al., 2013). These distributions, and a lack of other anomalies near the basin, might indicate that the sources of these anomalies are genetically associated with the crater-forming events, even they are located just to the west of the Orientale anomaly. This should imply shock remanent magnetization of the central uplift and thermoremanent magnetization of the impact melt rocks in a steady magnetizing field of a former dynamo (Mitchell et al., 2008).

One of the main conclusions of this detailed analysis is that impacts alter the magnetic character of the affected rocks, disrupt the pre-existing magnetic fabric and they

can be often characterized by broad magnetic lows also because the coherence length of the magnetic features is not yet well-matched to the magnetic observations. The largest crater impacts of Earth, Mars and Moon can be identified not only by their quasi-circular features from most recent and detailed topographic maps but from available global magnetic maps, too. For some large impact craters of the three bodies, a study case using a forward modeling approach was carried out and presented in the following. The aim is to underline the most important features of the magnetic signature over the impact craters at a planetary scale: the shock impact demagnetization.

3.3 Direct modeling of the magnetic field over impact craters

Forward methods begin with one or more magnetic bodies whose prominent features are selected a priori, on the basis of geological, geophysical or morphological characteristics. Magnetic fields are then predicted for these bodies at the survey location, model parameters being adjusted on the basis of the closeness of the fit to the observation or model. This process continues until a sufficiently close fit to the observations is achieved. An analytical upward continuation to the map or observation altitude is carried out, too, in order to compare with the forward model.

Procedures for calculating magnetic forward models involve simplification of complex bodies into simpler ones, either as collections of polyhedrons (Bott, 1963), rectangular prisms (Bhattacharyya, 1964) or magnetic dipoles (Dyment and Arkani-Hamed, 1998; Langlais and Thébault, 2011). This part of my work consists in a pure forward modeling approach, using the Equivalent Source Dipole (ESD) method developed by Purucker et al. (1996), see *Part I, Section 2.3* for the description of the used technique, in order to investigate the magnetic signature associated with large and demagnetized impact craters, at different maps or models altitudes for the three bodies. Impact demagnetization effects are evaluated here assuming a reduced thickness of the magnetized lithosphere. How big might be a crater to associate it a magnetic low effect in the available global maps, and how large and deep may be the zone influenced by the impact are two of important questions to offer an answer in the following.

3.3.1 Study cases based on the Equivalent Source Dipoles method

A close relationship exists between large impact craters and weak magnetic fields over them. Here, the largest multi-ring impact craters of Earth, Mars and Moon, identified from SRTM, MOLA and LOLA high-precision topographic gridded data sets, which

show a well-recognized magnetic low over them are analyzed. The forward modeling approach aims to evaluate the demagnetization effects by reducing the thickness of the pre-magnetized lithosphere due to the impact excavation process. Unlike the gravity field, which would exhibit regional low values above an uncompensated impact crater, a deficit of magnetization is theoretically not expected to produce a deficit or a low magnetic field intensity. In a simplest scenario for all three bodies, a continuous and homogeneous crust formation (the crust cooled down globally with a slow cooling rate in the presence of a dynamo) was taken into account. This scenario allows me to consider that only perturbations from the spherical shell, in this case topographic lows, as craters, are associated with magnetic fields. A slow cooling rate means a stable global magnetic field and then, following Runcorn's theorem (Runcorn, 1975), the resulting magnetization does not produce any magnetic field outside the spherical shell after the vanishing of the dynamic field. Even this assumption is geophysically simplistic, the information from the available global maps and models is not favorable to put the problem in a more realistic way.

When forming, an impact crater is first associated with an approximately hemispherical cavity. When maximum depth is reached the crater is larger than a hemisphere, and can be approximated by a paraboloid. This crater is often referred to as a transient crater, since it is later modified by gravity and collapse effects (Melosh, 1989). This transient crater defines the cavity in which the pre-impact material has been affected during the impact process. The forward modeling scheme describes the pre-impact magnetized lithosphere by Equivalent Source Dipoles and impacts are modeled as isolated holes of demagnetized area simulated by the surface of revolution of the parabola, a quadratic surface described by the equation $z = a(x^2 + y^2)$, see Figure 50. This assumed pre-impact magnetization of the lithosphere is modified through mainly two processes. First, the impact is associated with an excavation area, material being removed and spread away around the crater (Croft et al., 1979). Second, the shock wave associated with the impact generates high pressures, which may demagnetize the material, depending on its magnetic coercivity as it was shown by Cisowski and Fuller (1978). In this way only the signature of the impact demagnetization effect is computed, and the predicted intensity field of selected craters for Earth, Mars and Moon is compared with the measured or modeled field at the same altitude for each planetary body. Remagnetization processes are omitted, because only excavation consequences on the magnetic field are considered here.

To estimate the magnetic signature of craters, a few important steps of computation are used, by means of an adapted software for each planetary body. The main steps of the program written in C language are:

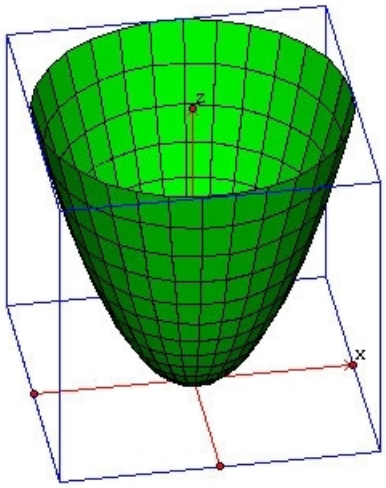

Figure 50: A paraboloid of revolution which simulates the magnetic deficit over a hole shaped by the impact and layers of 4 km thick used as dipole meshes to calculate the predicted magnetic signal over an impact crater by means of ESD method.

- A dipole mesh is created onto a equidistant grid, taking into account the planet radius and polar coordinate subdivision (Katanforoush and Shahshahhani, 2003). This initial mesh is used to shape from it the source body - the paraboloid of revolution. This grid of dipoles has to be large enough to cover up to 2 crater radii. A few spatial parameters are initialized: a mean horizontal distance between adjacent dipole sources is set to 4 km as well as the thickness of each ESD shell which is set to 4 km also, considering an appropriate value, common for all planets. Thus, the mean distance between dipoles become 0.03869° for Earth, 0.06109° for Mars and 0.14180° for Moon. For each layer an out-file (**filename**00**, filename**04**, filename**08**, filename**12**,...filename**40) is created by means of the source code **icosahedron.c**.

  For example, **icosahedron_earth.exe filename**00 0 4 10 30 160 180 will produce in out-file **filename**00 a grid of dipoles, between 160°/180° in longitude and +10°/+ 30° in latitude, with a thickness of 4 km at a depth of 0 km. For each dipole the intensity, inclination and declination are calculated. Magnetization is normalized to be 1 at the equator and 2 at the pole. It is modified for each planet and crater by multiplying each row in all out-files by the appropriate value. These values were adjusted function for each planetary body using the domain range from Figure 51.

- The entire magnetized layer is considered as a vertical superposition of several ESD layers of 4 km thickness (out-files). In each layer the demagnetized area corresponds to a section of the paraboloid and only the crater area is taken into account.

Diameter, depth-to-diameter ratio and center are defined here. The source code **create_crater_area.c** reads a dipole network and simulates the demagnetized area, at different depths, of the set paraboloid.

For example **create_crater_area.exe filename**00 **crater**00 20 170 140 10 will produce only crater area for out-file **crater**00, at 0 km depth, for a crater centered at 20° latitude, 170° longitude, 140 km diameter and 10% depth/diameter ratio. Then, all out-files (**crater**00**, crater**04**, crater**08**, crater**12**,...crater**40) are combined into a single one (**crater**).

- From the obtained equivalent source magnetization distribution, the field components are carried out (B_r, B_θ, B_ϕ) at a constant altitude of 5 km for Earth, 185 km and 400 km for Mars and 30 km for Moon (referred to a spherical value of radius 6371.2 km for Earth, $R = 3393.5$ km for Mars and 1738 km for Moon) by means of the source code **dbcomp_planet.c**.

  For the previous selected crater of Earth, the final out-file **predicted_field_earth_5km** is created with the program: **dbcomp_earth.exe -dipfile crater -outfile Predicted-field-earth_5km -alt 5 -lat_min 10 -lat_max 30 -lon_min 160 -lon_max 180 -inc 0.5**, where 0.5 is grid increment for output. The predicted total component is calculated and compared then with the measured/global modeled field at the same altitude for a specific crater. The last two source codes were recompiled whenever needed.

3.3.2 Modeling hypothesis applied to a synthetic signal

The "deficit" of the magnetic field signature above a crater is assumed to be influenced by the transient diameter of the crater, the pre-impact magnetization direction and magnitude, and the thickness of the magnetized layer.

Crater parameters. Based on experiments, numerical computations and observations, the excavation depth is estimated to be about 1/3 of the transient crater depth, or about 1/10 of the transient crater diameter (Croft et al., 1979; O'Keefe and Ahrens, 1993). For this reason, I set up the inner ring of the studied largest craters as transient crater and the depth of the approximate paraboloid of revolution, as 1/10 of the transient crater diameter, but not more than the depth of Curie isotherm. Depth-to-diameter ratio of the transient craters was set to 1/10, consistent with observed terrestrial bodies. It has been considered that the demagnetization volume with the largest depth is confined within transient crater cavity.

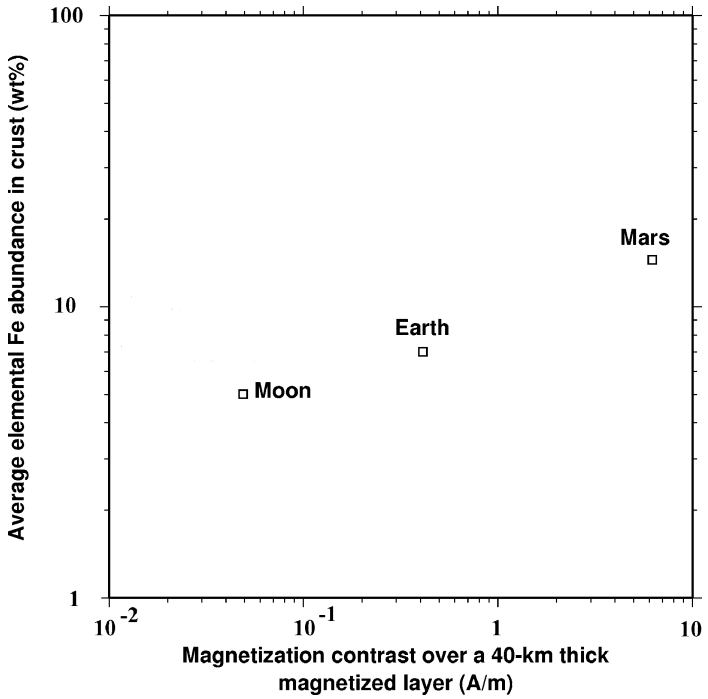

Figure 51: Minimum magnetization contrast (Am^{-1}) versus Fe content of crust (wt%) for the Earth, Mars and Moon assuming a 40 km-thick magnetized layer. *Adapted from Purucker et al. (2008).*

Magnetization: direction and magnitude. There have been several attempts to characterize the martian or lunar paleomagnetic field, in terms of magnetic pole location (Arkani-Hamed, 2001; Hood et al., 2005; Boutin and Arkani-Hamed, 2006; Langlais and Purucker, 2007; Quesnel et al., 2007; Hood et al., 2011). For simplicity of the model, I assume that the magnetization was acquired in the presence of a dipolar centered dynamo for all terrestrial planets. Magnetization intensity also increases with the depth of the magnetized layer (as the distance from the core decreases) by 3% between the surface and a depth of 40 km, considering that the magnetic minerals are located above the Curie isotherm. More importantly, the magnetization intensity varies with respect to the magnetic latitude, so that:

$$M(\lambda_{mag}) = A(1 + \sin^2(\lambda_{mag}))^{\frac{1}{2}} \tag{3.1}$$

where A is considered a constant (in Am^{-1}) and represents the magnetization at the magnetic equator. For each planet was set up an estimate of the magnetization intensity, a mean intensity value for the equator for Mars and Moon and specific mean values for well known Earth' craters. For example, an average of 1 Am^{-1} was taken into account for Mars, and 0.01 Am^{-1} for the Moon, respectively. On the Moon, magnetizations may

locally exceed $0.2Am^{-1}$ in the lunar crust only if the magnetic crust is as thick as 40 km (Purucker et al., 2008).

Inclination (angle between the horizontal and the magnetization vector) directly relies on the magnetic latitude λ_{mag}. Declination is zero everywhere the magnetic and rotation poles are collocated, the case of an axial centered dipolar paleomagnetic field, but it takes different values otherwise.

The thickness of the magnetized layer. The thickness of the pre-impact magnetized layer was also taken into account due to the fact that this parameter depends on the magnetic mineralogy, on the surface temperature and temperature gradient of the lithosphere when the magnetization was acquired. The proposed model requires a fixed thickness of an uniform magnetized layer even it is well known the variation of the Curie isotherm (above which rocks lose their magnetization). Based on available seismic refraction data, the Earth continental interior is enclosed by a 40 km contour, at least on the well surveyed areas (North and South America, Australia, and Eurasia). For less than 10% of the continental crust exceeds a crustal thickness of 50 km. A mean thickness of 45 km for Mars is consistent with its crustal structure from gravity and topography (Neumann et al., 2004) and with global density models of large impact basins (Zuber, 2001). The latest SELENE lunar gravity and topography model obtained by Kaguya mission (Araki et al., 2009) revealed a lunar crustal thickness of 45.1 km at Apollo 12 site, 49.9 km at Apollo 14 site and the thinnest crust, of 32 km at the Moscoviense. Different magnetized layer thickness were tested, up to 60 km for all three bodies and they stop around 40 km, considering this depth as the "depth of Curie isotherm" for all studied bodies following (Hamoudi et al., 1998; Fox Maule et al., 2009; Langlais and Thébault, 2011). The adopted model is consistent with how the satellites, at altitudes of few hundred kilometers, "see" the magnetized crust: as a compact thin sheet (compared with the body's radius) and without providing its variation with depth.

3.3.3 Predicted magnetic fields signal

In the following, the results associated with three varying parameters: pre-impact magnetization, the magnetized layer thickness and crater diameter are presented. Therefore, two configurations were tested, near the magnetic pole and at the magnetic equator. The magnetic field, radial component (Figures 52 and 53) and total component (Figures 54 and 55) is stronger when the crater is placed within a magnetized layer, at the magnetic pole. At 185 km altitude, the magnetic intensity above 400 km diameter crater reaches around 55 nT if it is placed near the pole. It decreases to 15 nT in both components above the magnetic equator. The shape of the anomaly also changes, from a quasi-circular a-

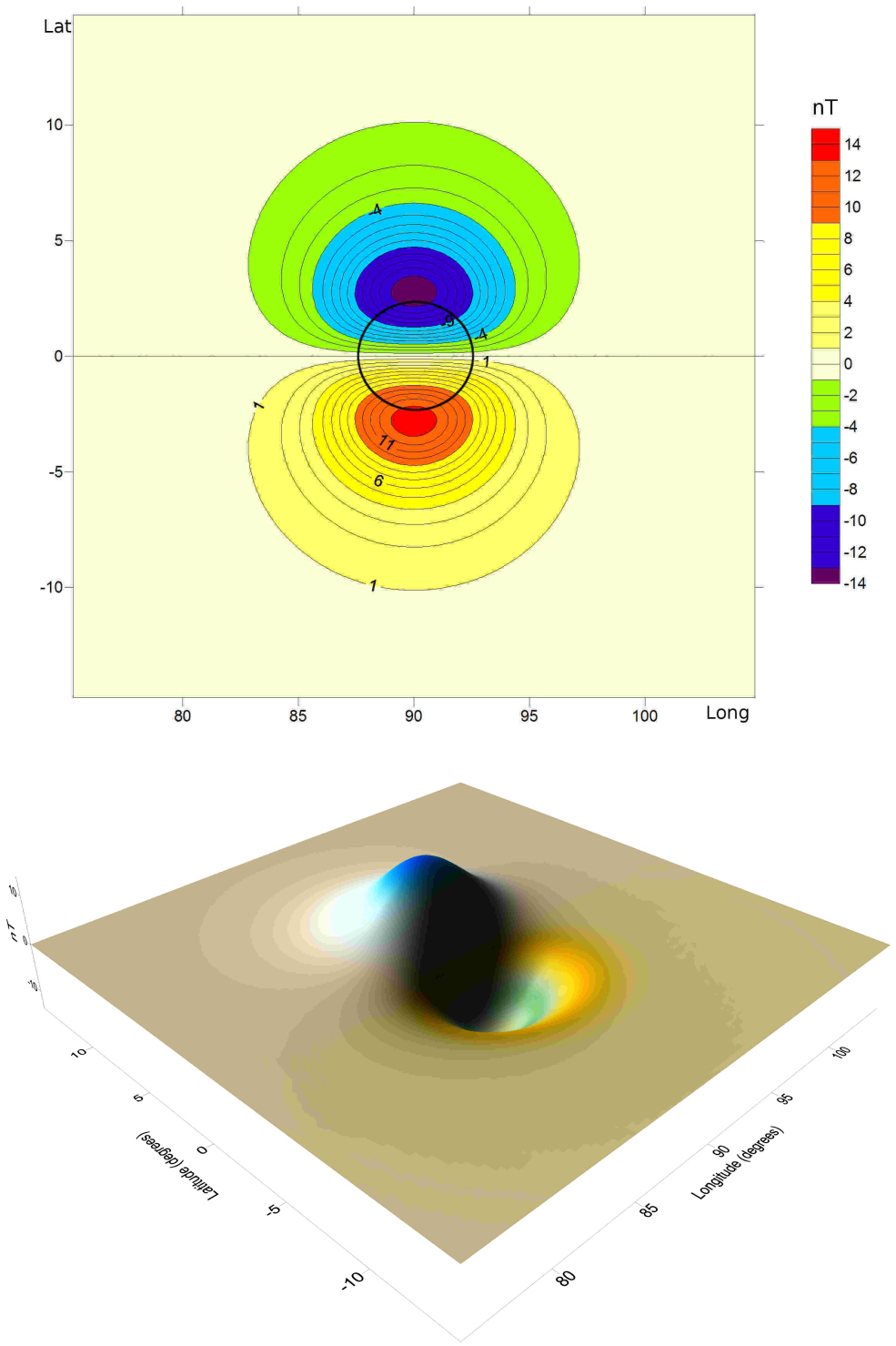

Figure 52: Contour map of the predicted radial magnetic field signature at 185 km altitude, for a 400 km wide impact crater above the equator (top) and a $3D$ view of the contour map, as a deficit (bottom). The rim is shown by the black circle.

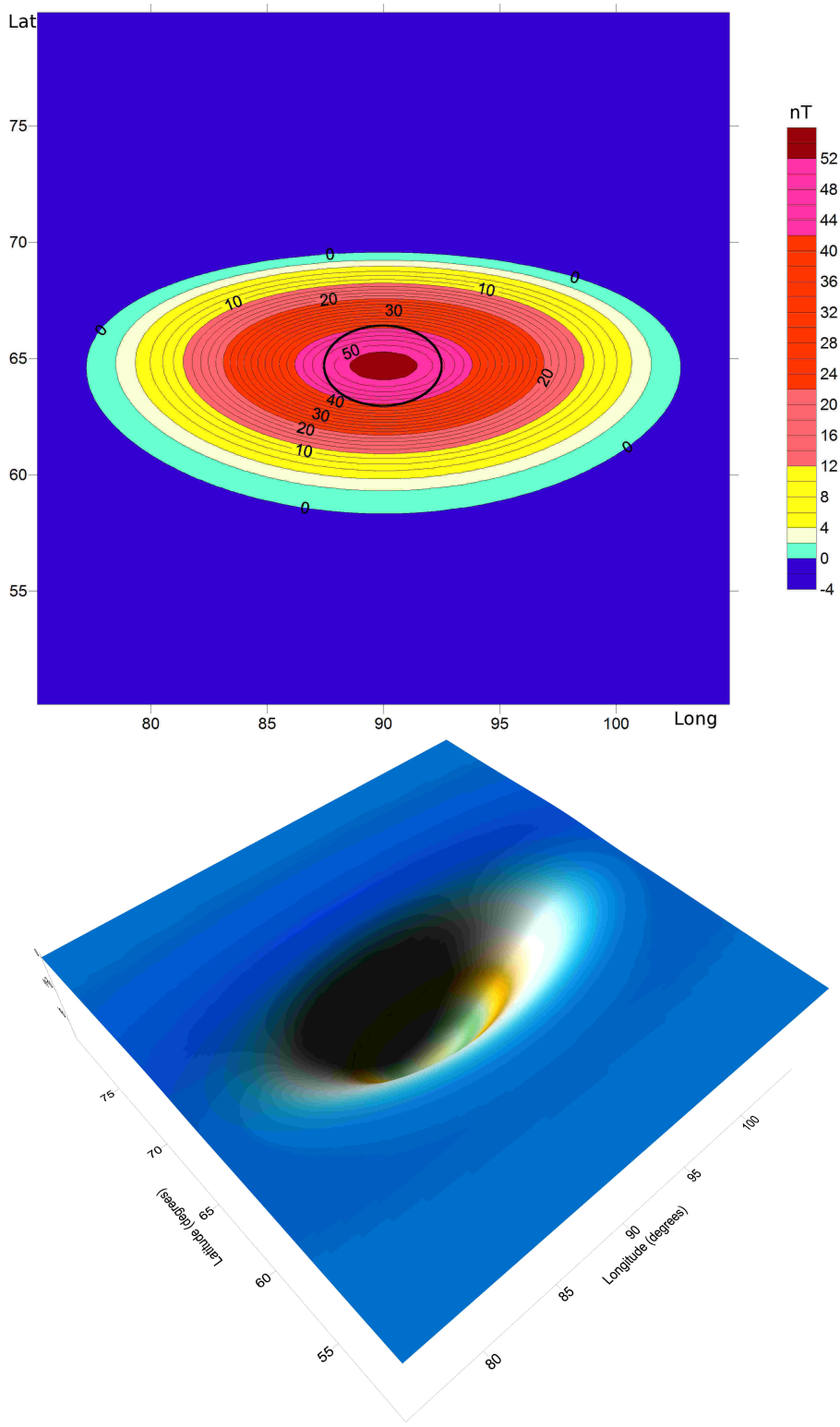

Figure 53: Contour map of the predicted radial magnetic field signature at 185 km altitude, for a 400 km wide impact crater near the North pole (top) and a $3D$ view of the contour map, as a deficit (bottom). The rim is shown by the black circle.

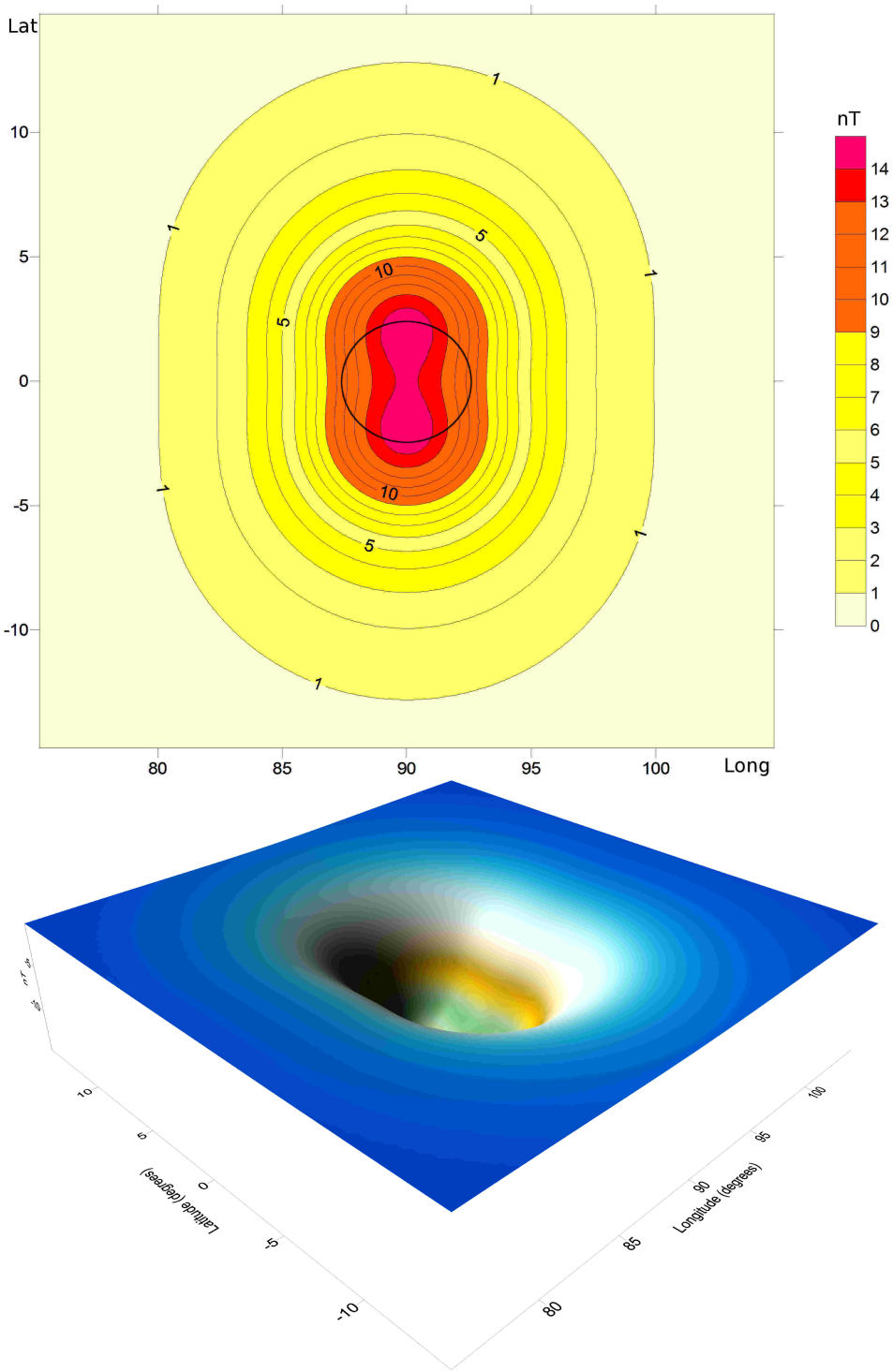

Figure 54: Contour map of the predicted total magnetic field signature at 185 km altitude, for a 400 km wide impact crater above the equator (top) and a $3D$ view of the contour map, as a deficit (bottom). The rim is shown by the black circle.

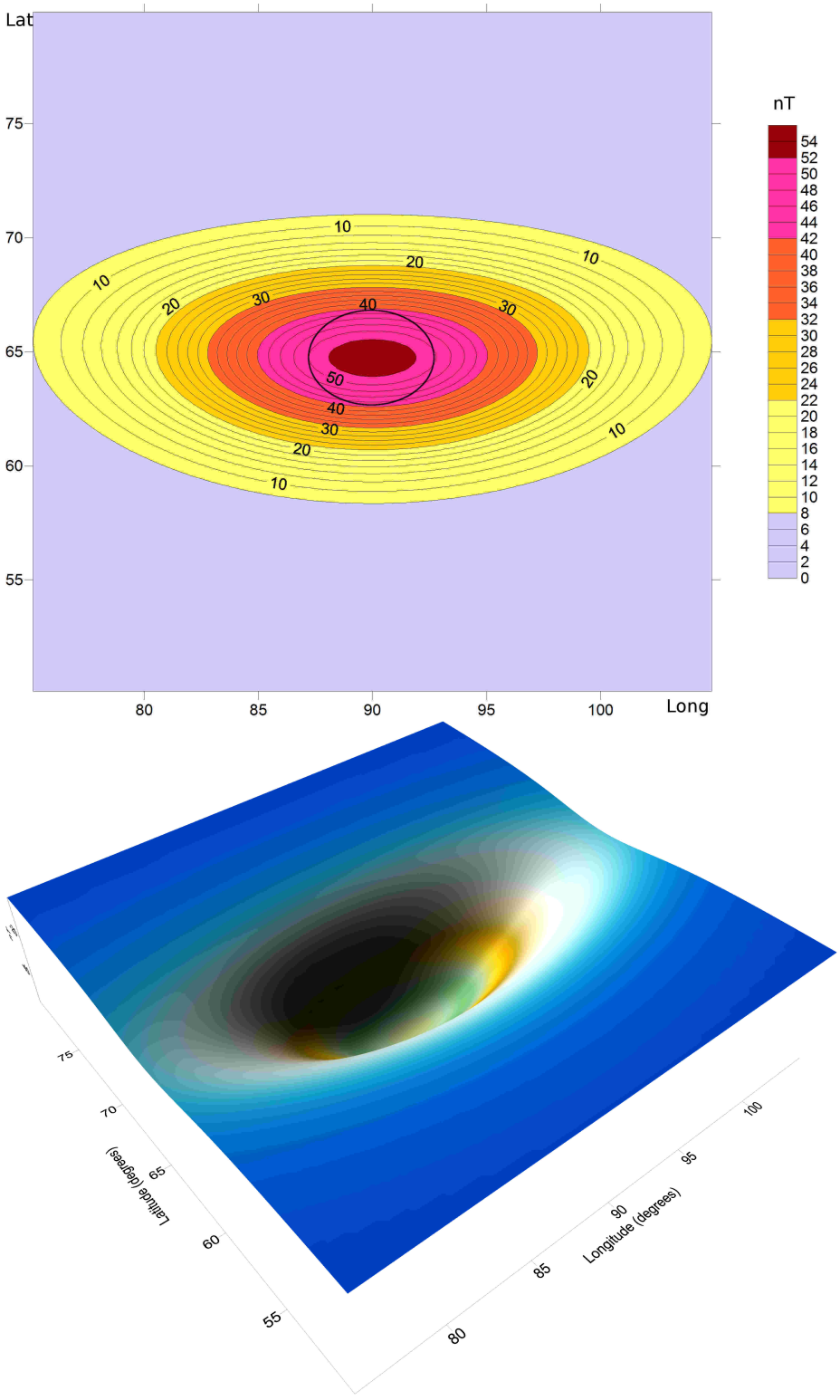

Figure 55: Contour map of the predicted total magnetic field signature at 185 km altitude, for a 400 km wide impact crater near the North pole (top) and a $3D$ view of the contour map, as a deficit (bottom). The rim is shown by the black circle.

nomaly to an anti – symmetric anomaly (Figure 52) for the radial field component computed at equator, associated with a total field anomaly, elongated on N-S direction away from the crater center (Figure 54). The zero contour for the radial anomaly represents the magnetic equator, and it is perpendicular to the elongated total field anomaly.

The influence of the magnetized layer thickness can be evaluated by means of Figures 56, 57, 58 and 59. 5 crater diameters (200, 400, 600, 800 and 1000 km) were tested, their diameters controlling the excavation depth (the excavation depth is estimated of about 1/10 of the transient crater diameter). Corresponding excavation depths range from 20 to 40 km, the maximum depth of the pre-impact magnetized layer. The field is predicted at the same 185 km altitude, for comparison. In the previous tests it was assumed that the demagnetization associated with 400 km impact crater affects the whole magnetized layer (40 km). For larger diameters, the pre-impact magnetized lithosphere is thicker than the impact-related excavation depth (60, 80, 100 km, respectively). In the case of the magnetic field signature of a 200 km diameter crater, situated near the magnetic pole and computed at 185 km altitude, results are shown in Figures 57 and 59. The maximum thickness of 40 km is equivalent to the four extreme curves, with amplitudes, in absolute value, between 55 and 85 nT for total and radial component. For crater diameters between 400-600 km, the maximum magnetic field is located above the crater center for both components. For 800 and 1000 km diameters, the center of the magnetic anomaly became more and more narrowed and more and more larger than the cratered area, the case of the largest craters and basins of Mars and Moon. For the 200 km diameter, the radial and total magnetic fields decrease to 8 nT for 20 km thick layer.

The magnetic field is smaller in amplitude (about 30 nT) when the pre-impact magnetization is horizontal (above the equator). For craters larger than 400 km two extrema are present (Figures 56 and 58), shifted with respect to the crater center, more clear for the largest diameters with constant thickness of 40 km. When the initial thickness is 20 km, as the case of 200 km crater, there is only an absolute intensity of $2 - 3$ nT for both magnetic field components, above the crater center, with a change of polarity for radial component. The thickness of the pre-impact magnetic layer affects the amplitude of the signal, but also its shape, especially for a horizontal magnetization. For a deepest magnetized layer, as the case of largest craters, the total magnetic field presents a clear central peak and two-peaks shape, symmetric with the crater center. The larger the crater is, the more pronounced this shape is, especially near-equator (Figures 58, 59).

Another important parameter which define the shape of the magnetic field is the crater diameter. Results are shown in the same Figures 56, 57, 58 and 59. Radial component (Figures 56 and 57) and total field (Figures 58 and 59) are shown along the same N-S profile centered above the crater. At 185 km altitude, the maximum radial and total

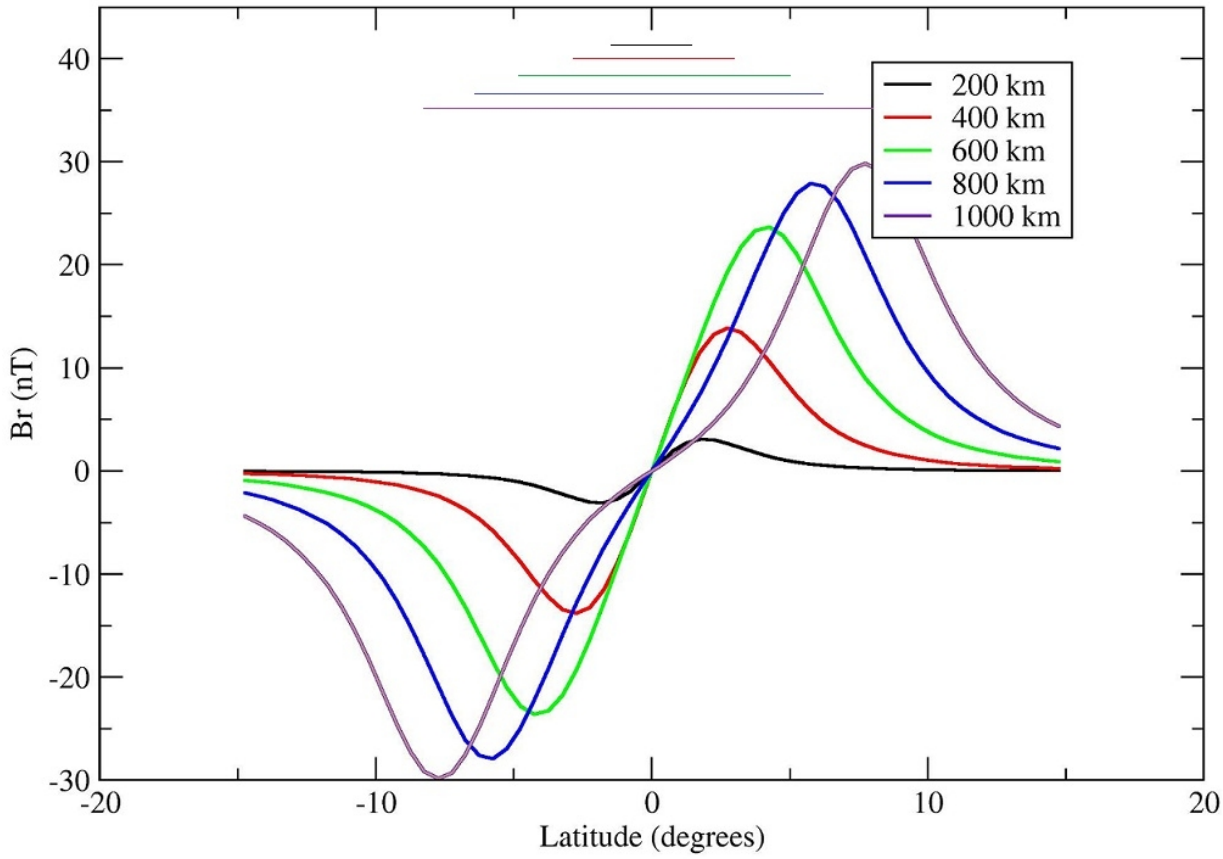

Figure 56: Predicted radial magnetic field (deficit) at 185 km altitude over an impact on a 4000 km radius planetary body along a N-S profiles centered above crater centers with increasing diameters (colored labels), localized at equator (horizontal magnetization). The extension of 200, 400, 600, 800 and 1000 km diameter craters is shown with straight colored lines.

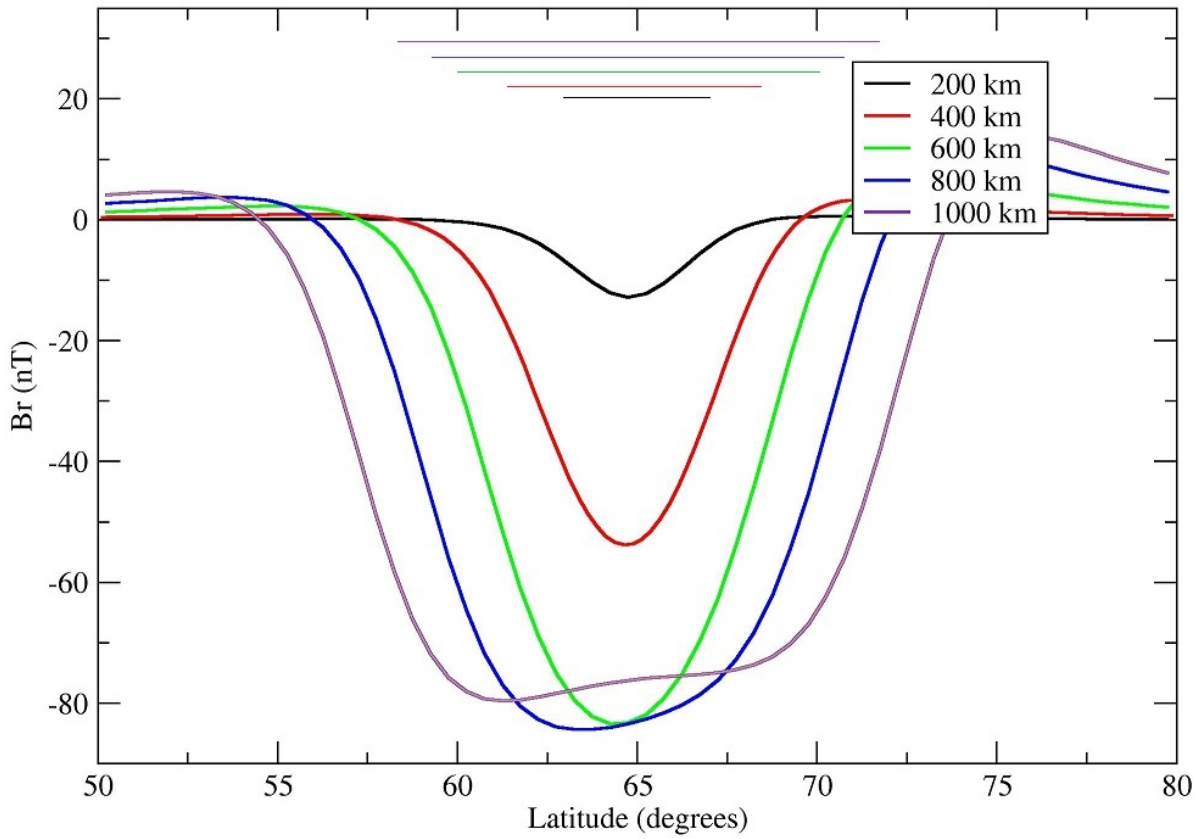

Figure 57: Predicted radial magnetic field (deficit) at 185 km altitude over an impact on a 4000 km radius planetary body along a N-S profiles centered above crater centers with increasing diameters (colored labels) localized in sub-polar areas (vertical magnetization). The extensions of 200, 400, 600, 800 and 1000 km diameter craters are shown with straight colored lines.

magnetic field, in absolute values, associated with a 1000 km diameter emplaced near the magnetic pole is around $80-85$ nT, but it decreases to 50 nT for 400 km diameter, and to $3-5$ nT for 200 km crater diameter, respectively. The radial component has a weak change in polarity, which disappear above the magnetic pole, where is zero (Figure 57). The total field reaches similar intensities, but with wider peaks. The situation is different when the magnetization is horizontal (the case of a crater situated at the equator). The radial field changes clearly its polarity at the magnetic equator while the total component is maximum above the crater, for all crater diameters, with amplitudes between $3-30$ nT in ascending order of crater diameter. Again, for craters larger than 400 km, the total field anomalies show two extrema located North and South of the crater center, but still inside the transient crater area.

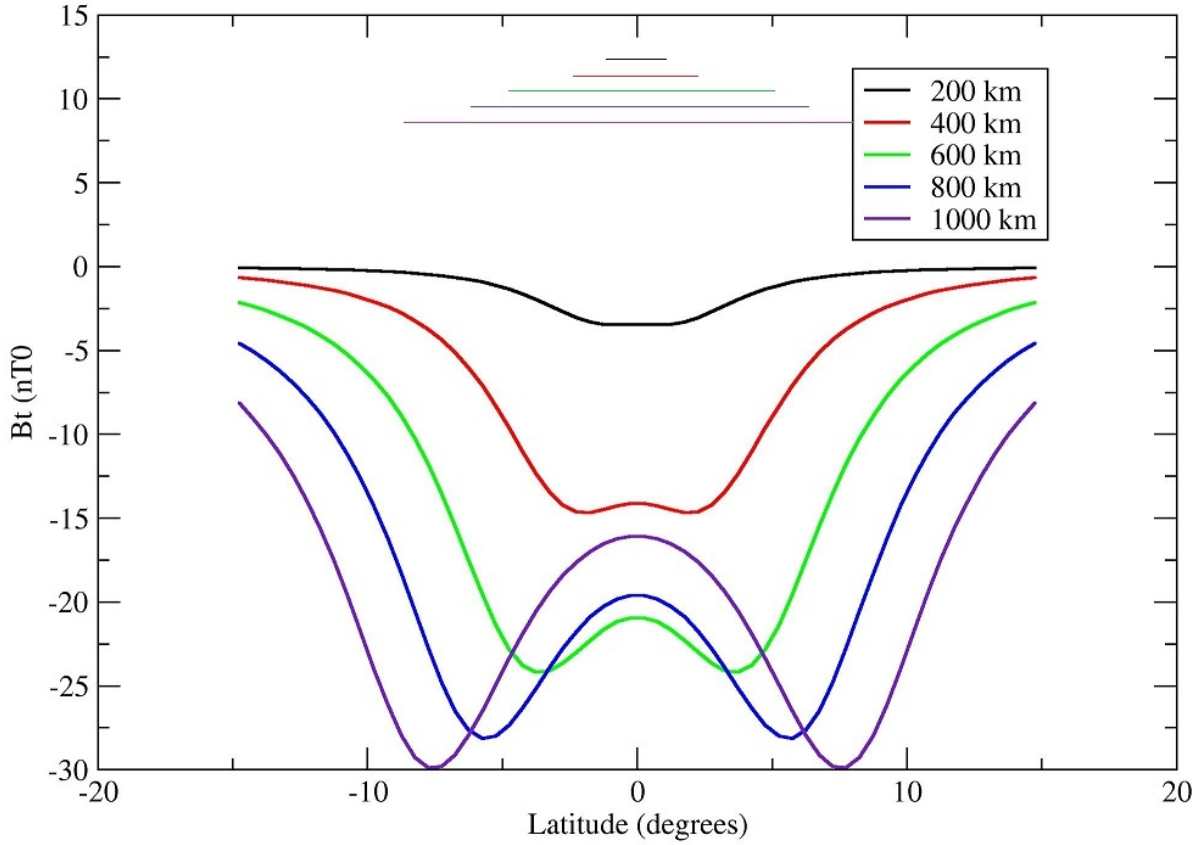

Figure 58: Predicted total magnetic field (deficit) at 185 *km* altitude over an impact on a planetary body (4000 *km* radius) along a N-S profiles centered above crater centers with increasing diameters (colored labels) localized at equator (horizontal magnetization). The extension of 200, 400, 600, 800 and 1000 *km* diameter craters is shown with straight colored lines.

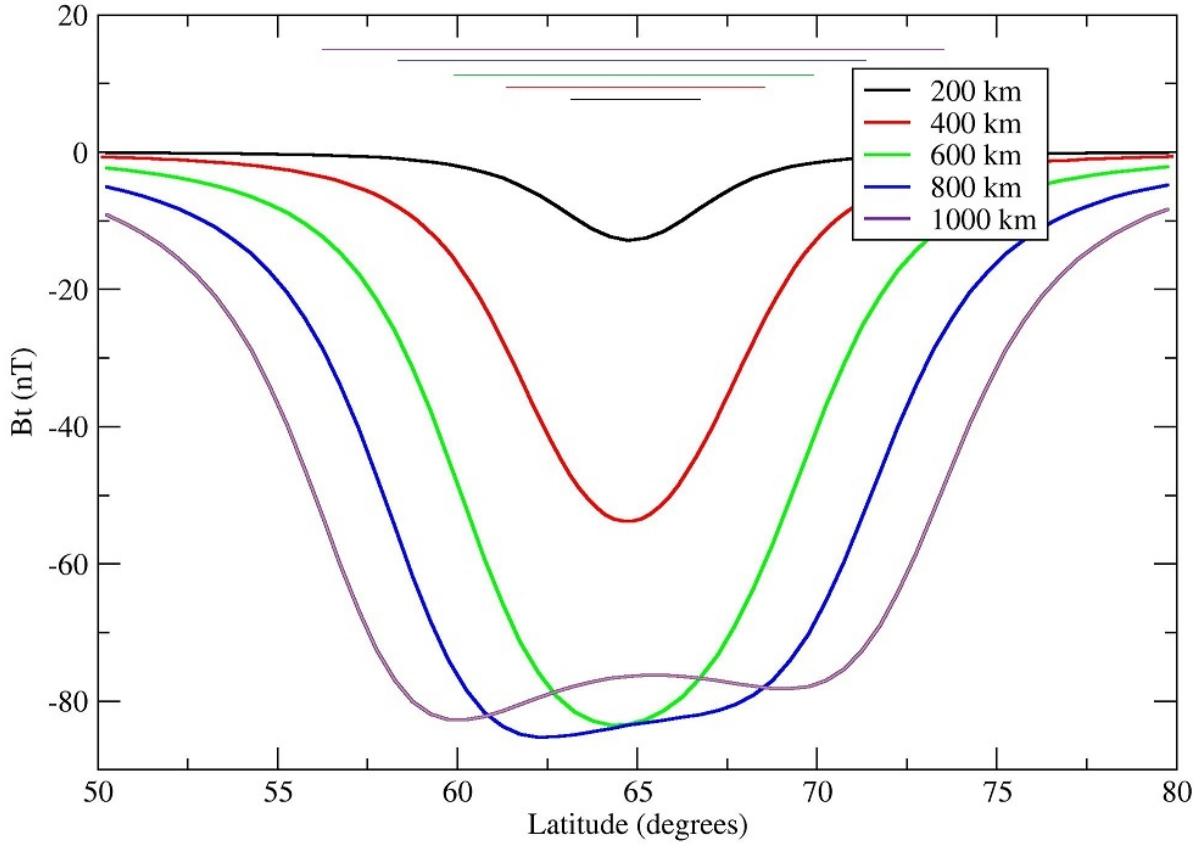

Figure 59: Predicted total magnetic field (deficit) at 185 km altitude over an impact on a 4000 km radius planetary body, along a N-S profiles centered above crater centers with increasing diameters (colored labels) localized in sub-polar areas (vertical magnetization). The extension of 200, 400, 600, 800 and 1000 km diameter craters is shown with straight colored lines.

3.3.4 Comparison between crater anomalies and direct models

Bangui is one of the most impressive magnetic anomalies on Earth (875 km diameter) and by far the largest over Africa, easily seen at satellite altitude. The anomaly might be related to a large impact structure early in the history of the Earth. The basement is early Precambrian and obviously the impact must be of this age. The magnetic anomaly is interpreted as being due to a strong remanent magnetism in the ancient crater floor and surrounds. The anomaly was satisfactorily modeled only by a 4.5 km thick disc, 800 km diameter beneath the ancient basin, and a magnetization of 10 Am^{-1} (Girdler et al., 1992). Here, to model (using ESD method) the amplitude and shape of the anomaly should have an intensity of magnetization of 0.6 Am^{-1}, a transitory diameter of 492 km, with a maximum depth of 40 km. The anomaly is complex, and it is likely to include strong shock remanences acquired at the time of impact and thermal and chemical remanences acquired soon after the impact (with directions significantly different from the present dipole field, as my model parametrized). Besides this, the size of the impact (assuming an impact) contributes to the high and unusual intensity required to explain the anomaly seen in Figure 60.

It is also the case of Chicxulub crater, 170 km diameter, which shows the same complex shape, modeled by shock and termoremanences (Figure 61). Depth-to-diameter ratio was setup 1/10, as for the Mars and the Moon, intensity of the magnetization of 0.6 Am^{-1}, and a transitory crater of 48 km, identical with the central peak diameter.

Preserving the same depth-to-diameter ratio of 1/10 as for the Mars and Moon, the predicted signal for Popigai, 100 km diameter (Figure 62) is associated with the local minimum, but with about 30% lower magnitude. The model take into account an excavated volume approximated with a paraboloid of 80 km diameter (the third inner ring of the crater) and 8 km deep paraboloid of revolution from a pre-magnetized crust of 0.2 Am^{-1}, taking into account that the susceptibility and natural remanent magnetization intensity is two order of magnitude lower inside than outside the Popigai structure (Masaitis et al., 1975). It is noticed the diameter of necessary excavated volume, very different from the transient crater parameters (34 km) and this misfit of the model is especially true for the largest and complex impact craters of the Earth (Isac et al., 2012).

Comparing Popigai with Acraman, 96 km diameter, and preserving the same depth-to-diameter ratio of 1/10 together with an excavated volume approximated by the same third ring of 82 km (going to a depth of 8 km) and a magnetization of the crust of 0.1 Am^{-1}, in this case, the model (Figure 63) fits the central magnetic low of about 200 nT. Here, the shock remanent magnetization due to impact was more effective than thermoremanent magnetization, being associated with a reduction in susceptibility of the 590 My old shattered dacite (Schmidt and Williams, 1996). The magnetic signature of

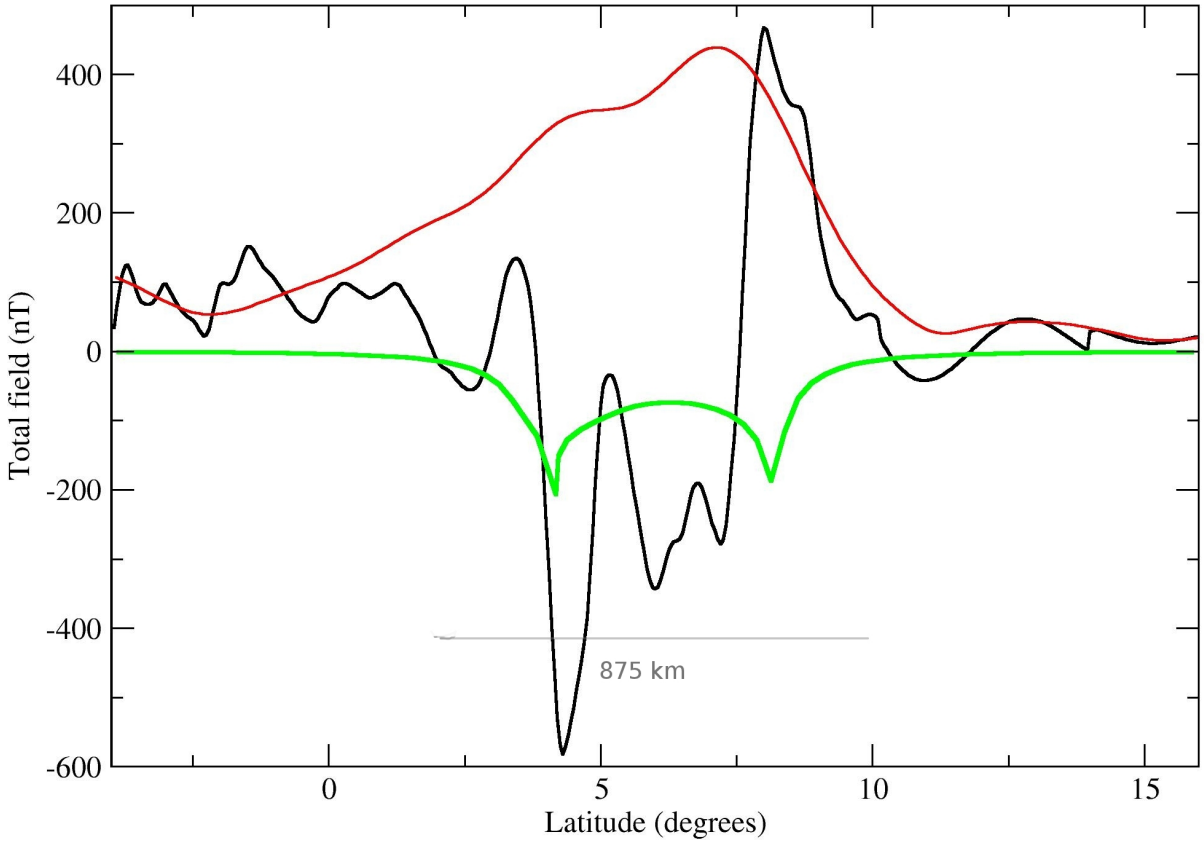

Figure 60: Comparison between the predicted signal, total field (green curve) and ΔT from WDMAM compilation (black curve), at 5 km altitude data over Bangui structure, 875 km diameter, on a N-S profile, near the center of the structure (6°N). The red curve represents predicted total magnetic field from Comprehensive Model (CM4), using only the lithospheric sources (n between 16 and 65) at the same altitude.

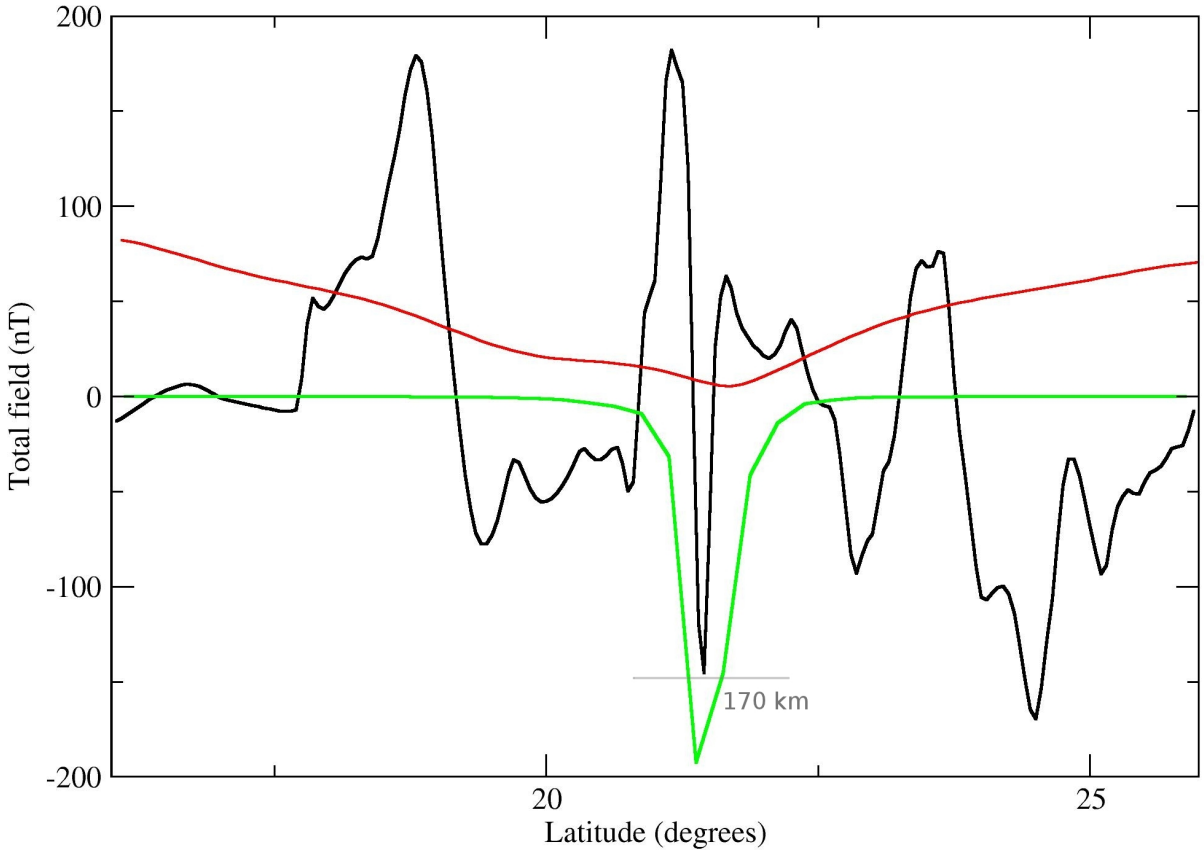

Figure 61: Comparison between the predicted signal, total field (green curve) and ΔT from WDMAM compilation (black curve), at 5 km altitude data over Chicxulub crater, 170 km diameter, on a N-S profile, near the center of the structure (21.3°N). The red curve represents predicted total magnetic field from Comprehensive Model (CM4), using only lithospheric sources (n between 16 and 65) at the same altitude.

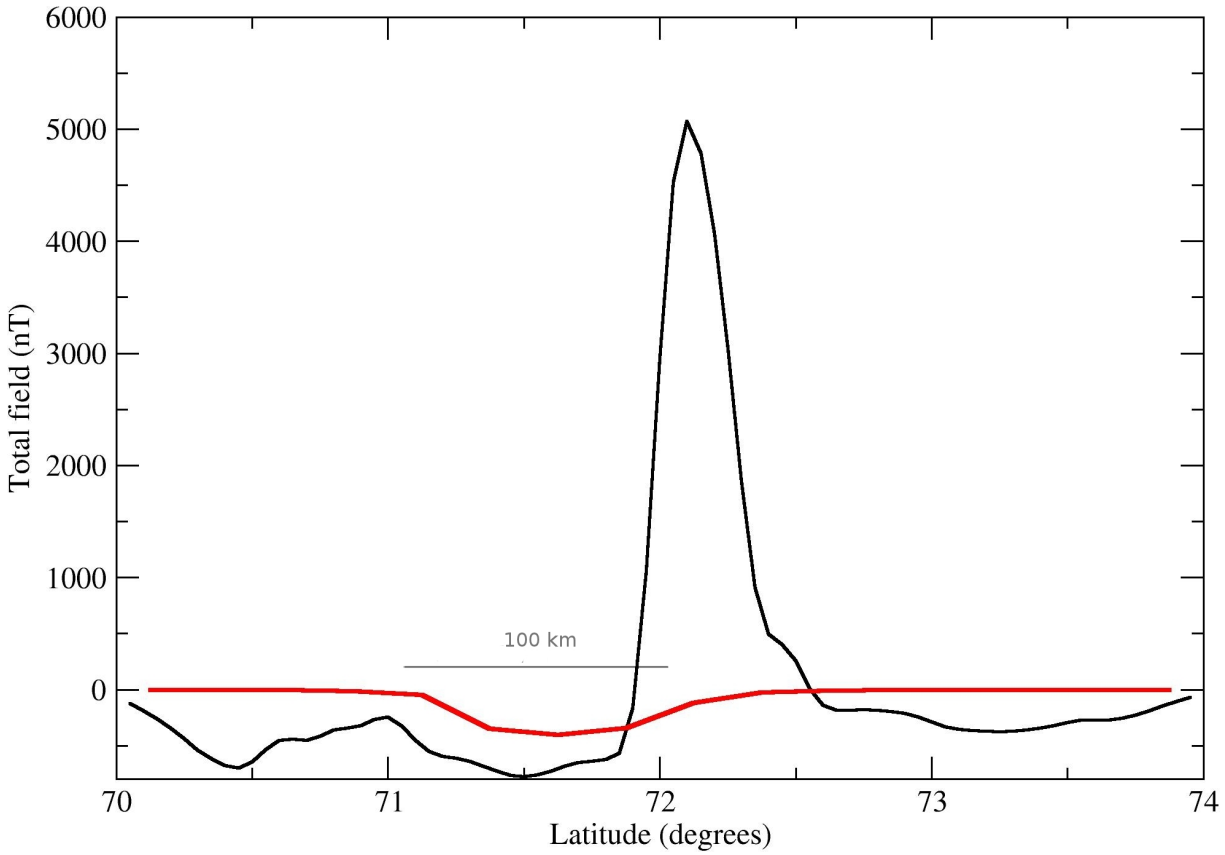

Figure 62: Comparison between the predicted signal, total field (red curve) and ΔT from WDMAM compilation (black curve), a 5 km grid and 5 km altitude data over Popigai crater, 100 km diameter, on a N-S profile, near the center of the structure (71.6°N).

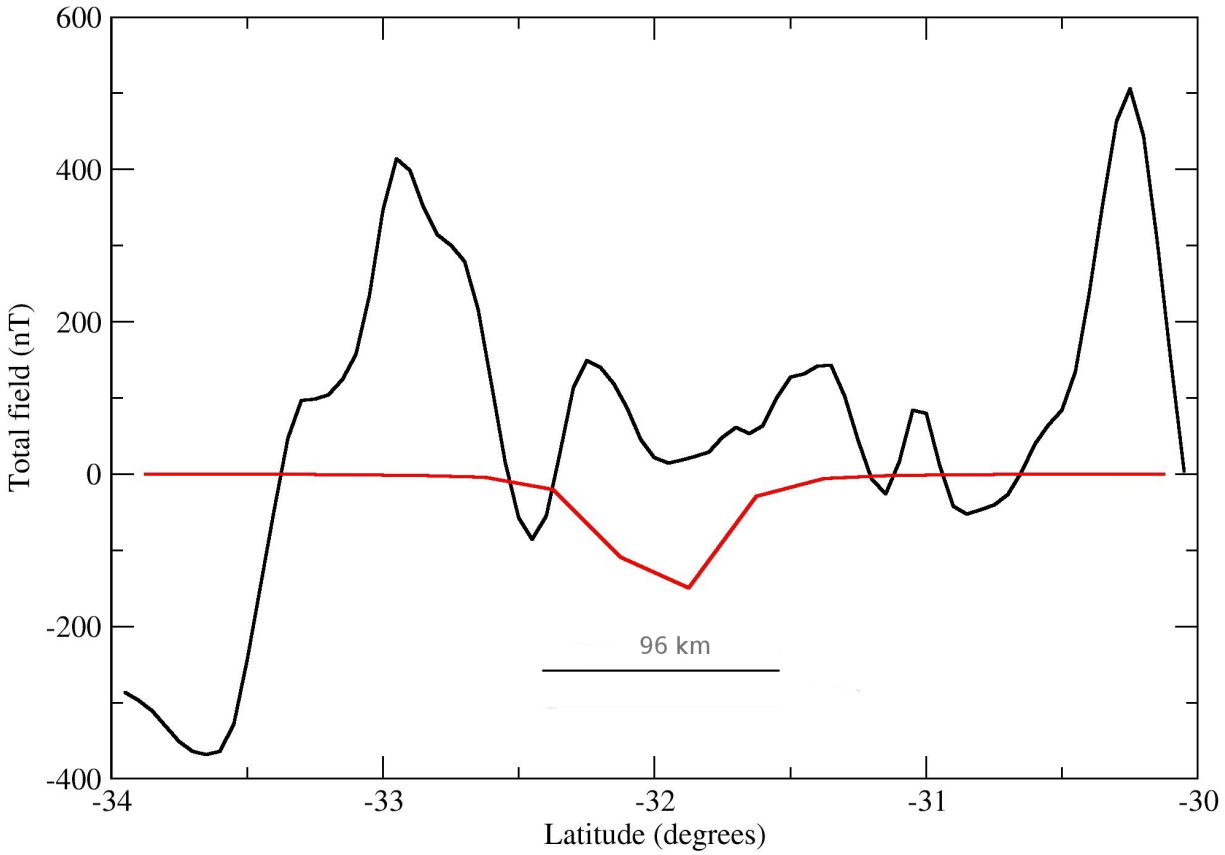

Figure 63: Comparison between the predicted signal, total field (red curve) and ΔT from WDMAM compilation (black curve) at 5 km altitude over Acraman crater, 96 km diameter, on a N-S profile, near the center of the structure ($-32°$N).

Acraman crater is one of the clearest shock magnetized terrestrial impact structure.

Figure 64 illustrates a classic example of a multi-ring basin from Mars, Isidis. Here, from the crater center outward, a peak-ring and two symmetric scarps are observable. The main rim or the inner rings (on the northern side) have probably been eroded and covered or buried with a sedimentary blanket. It is clear that large portions of the martian crust were demagnetized by shock associated with largest impacts. Here, all of the basin radius of Isidis is demagnetized and strongly correlated with the predicted total component of the magnetic field. The synthetic signal was computed using a paraboloid of revolution of 1059 km, equal with the inner ring diameter, 40 km deep, from a pre-magnetization crust of 1 Am^{-1} (see Table 5). The demagnetization process took place in the absence of an active dynamo. Figure 65 shows another typical large martian crater, Hematites, 1006 km diameter, which was modeled by means of a paraboloid of 468 km diameter, identical with its inner ring, going through a depth of 40 km in a pre-magnetized crust of 1 Am^{-1}. Both craters exert in the center of the predicted signal profiles a maximum of

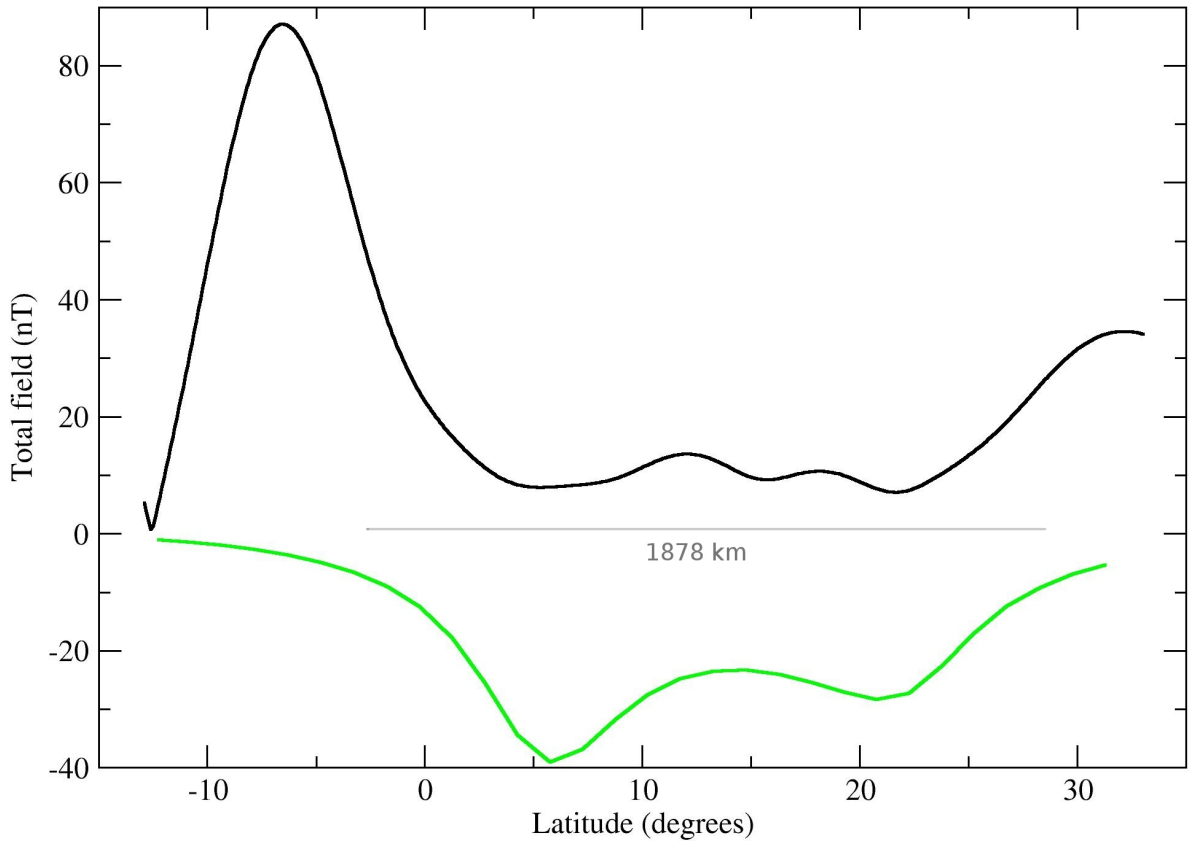

Figure 64: Comparison, on a N-S profile, between the predicted signal, scalar component (green curve) and crustal field magnitude (black curve) due to crustal sources-ER map at 185 km above it (Lillis et al., 2008b), over Isidis crater, 1878 km diameter, centered at 13.5°N.

about $5 - 20$ nT, corresponding to the peaks observed in all plots of craters bigger than 1000 km, positioned near equator, selected from the model by Lillis et al. (2008b), as well as for Isidis and Hematite, presented here. The magnetization deficit is well defined.

The circular features of Serenitatis crater, 677 km diameter, identified from LOLA map was modeled with a paraboloid of revolution of 200 km diameter (less than the inner ring, of 395 km, and associated with the transitory crater), 40 km deep in a pre-magnetized crust of 0.02 Am^{-1} (Figure 66). The magnetic low of about 2 nT is centered over the southern part of the crater due to its sub-equatorial position (26.85 latitude). It was chosen a magnetization value with one order of magnitude smaller than for the Earth, for which it was necessary a thickness of 20 km only (even a depth-to-diameter ratio of 1/10 as for the Earth and Mars was set up).

Crissium crater is representative for some Nectarian craters, which present positive anomalies near the basin center. Here, the anomalies ($4 - 6$ nT amplitude) simulate the inner ring (Figure 67). These, and the lack of the similar anomalies near the crater, might

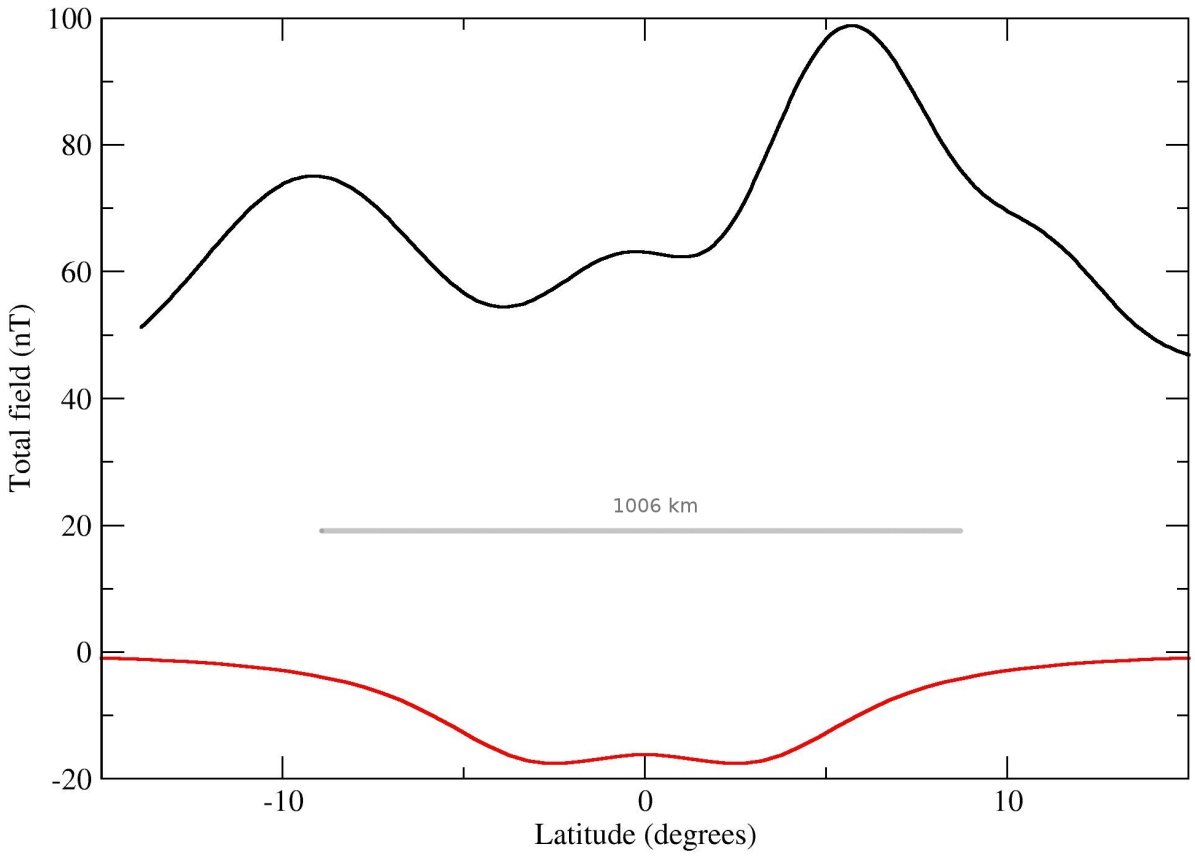

Figure 65: Comparison, on a N-S profile, between the predicted signal, scalar component (red curve) and crustal field magnitude (black curve) due to crustal sources-ER map at 185 km above it (Lillis et al., 2008b), over a younger Noachian crater, Hematite: 1006 km diameter, centered at 1.2°N.

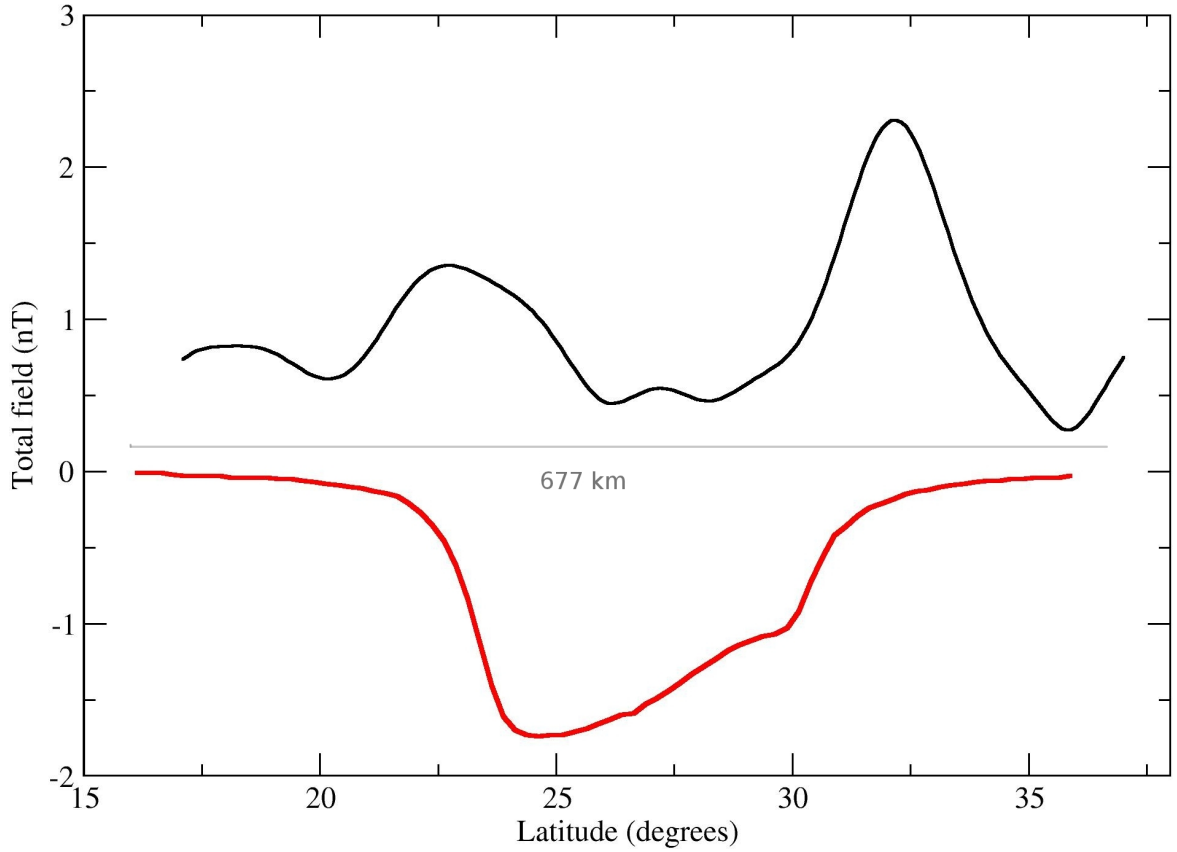

Figure 66: Comparison, on a N-S profile, between the predicted signal, scalar component (red curve) and crustal field magnitude due to global internal magnetic model of the LP observations (64 km wavelength resolution) at 30 km altitude by Purucker and Nicolas (2010), black curve, over Serenitatis crater, 677 km diameter, centered at 27°N.

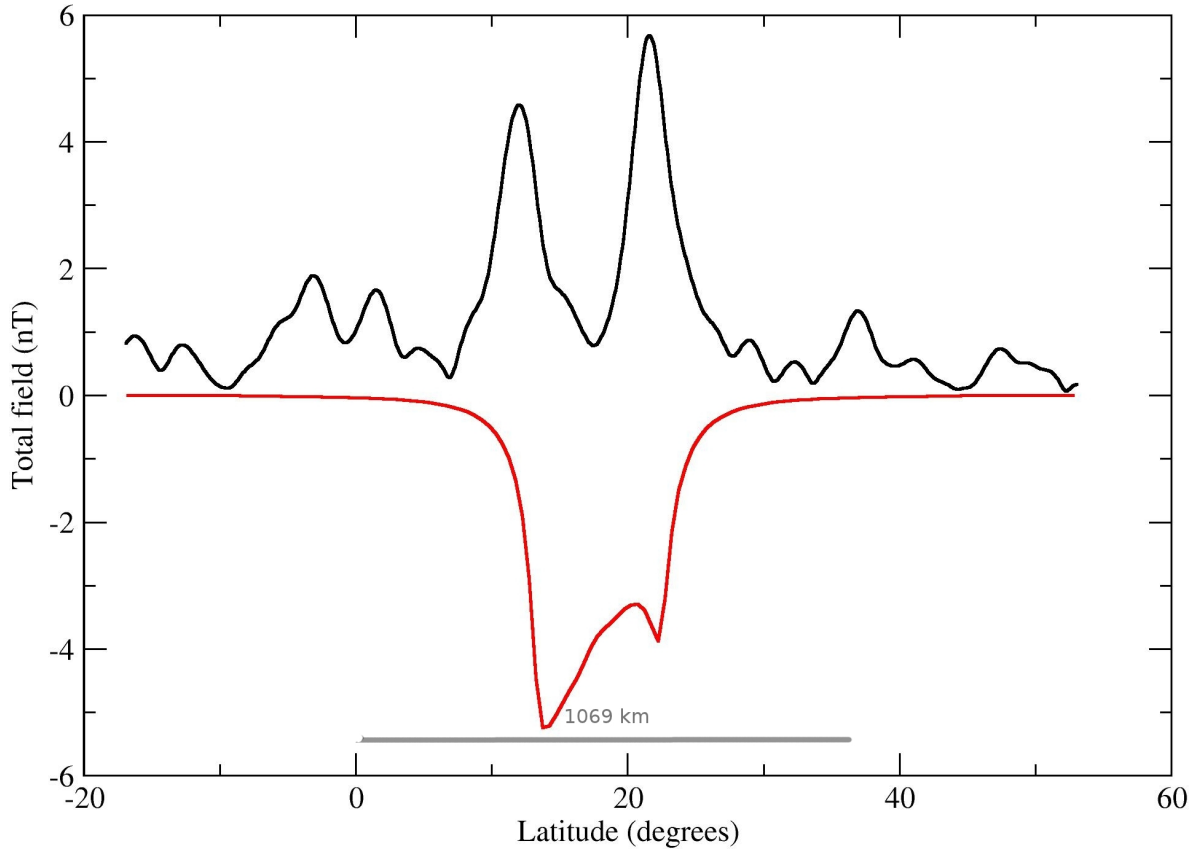

Figure 67: Comparison, on a N-S profile, between the predicted signal, scalar component (red curve) and crustal field magnitude due to global internal magnetic model of the LP observations (64 km wavelength resolution) at 30 km altitude by Purucker and Nicolas (2010), black curve, over late Nectarian Crissium crater, 1069 km diameter, centered at 18°N.

indicate a shock magnetization which erased the magnetization in the center of the crater (simulated by a paraboloid of 370 km, as the crater inner ring) and a thermoremanent magnetization of the impact melt in a magnetizing field (a former dynamo at that time or a strong solar wind plasma). Considering these two assumptions in favor of a past active dynamo, the Crissium, Moscoviense, Humboldtianum craters concur to give a timing cessation scale of the martian former dynamo (Isac et al., 2013). The magnetic characterization by means of labels, see Tables 8 and 7, shows changes from labels as $(2-1-1)$ for Apollo, $(3-2)$ for Ingenii (pre-Nectarian or early Nectarian craters), or $(3-3-2-2-2-2)$ for Crisium, as well as Serenitatis $(3-2-2)$, late Nectarian craters, to labels as $(2-3-3-3)$ for Humorum, late Nectarian, and $(1-1-2)$ for Imbrium or $(1-1-1-2-2)$ for Orientale, younger, of Imbrian ages.

Measurements of the martian magnetic field revealed significantly lower magnetic field intensities over the gigantic impact craters. This is commonly attributed to demagnetization processes related to meteorite impacts in the absence of a global magnetic field (Acuña et al., 1999). As for martian craters, some of the largest lunar craters exert magnetic field which appears lower than that of neighboring terrains. Lower than average magnetic field intensities are also noticed from the satellite observations above some large impact craters on the Earth, like Vredefort. It is easy to conclude that impacts alter the magnetic character of the affected rocks. They also disrupt the pre-existing magnetic fabric and they can be often characterized by broad magnetic lows. In the case of the Earth, the coherence length of the magnetic features as impact craters is not well-matched to the magnetic observations and the models must be adjusted to the Earth's magnetic field complexity. Mars and Moon's global magnetic fields may have already been weak when meteorites struck to form large craters some 4 Gy ago. In their case, shock waves from the largest meteorite impacts could disrupt the field enough to demagnetize rocks in the crater. The topographic data are adequate for this analysis, while the magnetic ones have limitations driven by their limited frequency content. Magnetizations of the crustal rocks within impact basins, if crustal thickness variations are ignored, vary by three orders of magnitude between Mars, Earth, and the Moon. The origin of these differences, still unknown, may reflect differences in magnetic petrology, the magnitude of the core field, or in the crustal thickness. This is an argument for future low altitude missions to better understand internal or surface processes through the history of the terrestrial planets. Swarm mission for Earth, MAVEN and Curiosity for Mars and SELENE for Moon could allow a detailed magnetic signature associated with impact craters. These low-altitude orbital and surface/rover magnetometer measurements will more strongly constrain the depth and/or thicknesses of the sources.

Conclusions

At the beginning of the third millennium, the Solar System planets have been transferred from bright spots in the sky, to real explored planetary bodies. Magnetic measurements represent now one of the most used remote-sensing tool for planetary missions. The existence of crustal magnetic anomalies on Mars and Moon, and the lack of an internally self-generated magnetic field suggest that physical conditions within these bodies have been changed through the geological time-scale, from an earlier active dynamo to a weaker or ceased one. A better understanding of the Earth's magnetic field evolution is only possible by integrated studies, in which information from other geophysical domains or other planetary magnetic fields are considered.

This thesis has been focused on two directions, on one hand the temporal and spatial variations of the geomagnetic field, the more complex among the others, and on the other hand, the main direction, the comparative analysis of the small scale magnetic fields of impact craters for several terrestrial bodies (Earth, Mars and Moon). The best ever survey of the Earth's, Mars' and Moon's magnetic fields from the last decades offered the opportunity to access the newest data and products and to study in a more detailed way short-term variations of geomagnetic field and small-scale magnetic fields of planetary bodies.

* * *

To arrive to a fine interpretation of geomagnetic field features two ingredients are necessary without a doubt: accurate data and powerful data analysis. These issues have been treated in the first part of the thesis. The Surlari National Geomagnetic Observatory, has given the thesis author the opportunity to participate in an international team of the IAGA's Division V - Geomagnetic Observatories, Surveys and Analyses, and to define and detail the measuring techniques on various platforms with a special attention to the accuracy of each kind of data and with the need to estimate their associate errors. This work represents a crucial setting for the current and future activities, and it has been materialized in two reviewed publications in 2011: "Improvements in Geomagnetic Observatory Data Quality" (Reda J., Fouassier D., Isac A., Linthe H.J., Matzka J.,

Turbitt C.)[8] and "Geomagnetic Field, Measurement Techniques" (Mandea M., Isac A.)[9], and in proceedings, extended abstracts or oral presentations at IUGG-IAGA meetings. Among them: "The renewing of Surlari observatory: targets and present status of its data quality" (Isac A., Linthe H.-J., Mandea M., Iancu L.) and "Observatory Data Quality Control – The instrument to ensure the valuable research" (Linthe H.-L., Reda J., Isac A., Maska J., Turbitt C.), in 2012.

Thereafter, the competences acquired in magnetic data acquisition have been used during the next step of the work – data analysis. Indeed, in *Section 2.4*, a special consideration has been given to the temporal variations of the Earth's magnetic field, with its sudden-changes in the secular variation and acceleration, the so-called geomagnetic jerks. To understand these specific characteristics it is crucial to analyze long series of data, provided by geomagnetic observatories or deduced from satellite measurements and models. A novelty is represented by spectral methods applied to long time series recorded by the Surlari National Geomagnetic Observatory.

The main results of the first part of the thesis are presented as follows:

- To better characterize the behavior of the short-term variations of the main field – the jerks – spectral analysis by Short-Time Fourier Transform and Discrete Wavelet Transform has been used for the first time on Romanian long-time series. The presence of noise in the data makes the identification of short-term discontinuities more complicated. For this reason, a de-noising technique using wavelets was applied, for three cases, namely a synthetic signal, the Surlari observatory time series of Y – component and a global scale model – Gufm1 (Jackson et al., 2000). The obtained results for synthetic signals and for Surlari observatory proved that the chosen methods are appropriate to characterize geomagnetic jerks;

- In the more detailed published paper "Geomagnetic jerks characterization via spectral analysis" (Duka B., De Santis A., Mandea M., Isac A., Qamili E.)[10], it was shown that the wavelet analysis applied to monthly series of secular variation generated from the global scale Gufm1 model points out that spectral methods chosen can highlight, both in time and space geomagnetic jerks in secular variation of the magnetic field. The behavior of wavelet decomposition coefficients, for almost every year of the ninetieth century and for each point, gives an interesting view about the spreading and evolution of jerks;

- Most of the well known jerks are confirmed through these methods and new and

[8] http://www.springer.Com/serie/8636
[9] http://www.springer.com/earth+sciences+and+geography/geophysics/book/978-90-481-8701
[10] www.solid-earth.net/3/131/2012/

interesting features have been suggested, such as a longitudinal-like periodicity. Using both national data and global models and maps it was highlighted their regional rather than global behavior, as previously thought;

- On the same line of analysis the temporal variability of the magnetic field, in a recently published paper "Geomagnetic jerks as chaotic fluctuations of the Earth's magnetic field" (Qamili E., De Santis A., Isac A., Mandea M., Duka B., Symonian A.)[11], applying a Nonlinear Forecasting Approach on the Gufm1 values, the well-known jerks detected by different methods have been confirmed with or without a time offset. In addition, few others have been detected, over a period of four centuries.

* * *

The second part of the thesis has been dedicated to the lithospheric small-scale magnetic fields, with a special regard on the magnetic signature of the impact craters on Earth, Mars and Moon, seen in the global topographic and magnetic maps. The work related to magnetic signature of impact craters presented in *Part II* proved that global magnetic maps and models can preserve and highlight the geological processes during the formation of our solar system, such as the Late Heavy Meteoritic Bombardment period. Crater dimensions are considered a unique demonstration of the fact that the maps and global models are capable of detecting magnetic anomalies with local extension, not just regional, to the limit of their resolution.

The most recent compilations, maps and models of crustal magnetic fields, as well as topographic and crustal thickness maps and models have been used. The first compilation *World Digital Magnetic Anomaly Map* (Korhonen et al., 2007) is the most important achievement in describing the Earth's crustal field. For detailed analysis of martian impact craters the electron reflection (ER) map of Lillis et al. (2008b), the low-noise internal magnetic field model of Lillis et al. (2010), the internal dipole model of Langlais et al. (2004) and the model of Mars crustal structure (Neumann et al., 2004), at different altitudes, were used. Recent global models of the internal magnetic field of the Moon used include those of Purucker (2008) and the newest global internal magnetic field model of Purucker and Nicolas (2010). The position of craters and their rings were first established on the morphologic evidence no other than their topographic shape from the most recent topographic maps: the Shuttle Radar Topography Mission (SRTM) (Farr et al., 2007) for Earth, the MOLA map (Zuber et al., 1992; Smith et al., 2001) for Mars, and the Unified Lunar Control Network(ULCN) 2005 (Archinal et al., 2005), the Kaguya-SELENE map (Araki et al., 2009) and LOLA topography (Chin et al., 2007; Smith et al., 2010) for the

[11] http://onlinelibrary.wiley.com/doi/10.1029/2012GC004398/full

Moon. Together with the GRIDVIEW, a NASA's software (Roark et al., 2000; Roark and Frey, 2001) they make it possible for the first time to analyze planetary topographic and magnetic data. The magnetic signature of the largest selected impact structures has been studied then. For the first time, the largest impact craters on Earth, Mars and Moon have been identified not only by their quasi-circular features from the most recent and detailed topographic maps but also from available global magnetic maps. The demagnetization effects by reducing the thickness of the pre-magnetized lithosphere due to the impact shock wave and excavation processes were evaluated by means of a forward modeling approach using Equivalent Source Dipoles (ESD) method. A continuous and homogeneous crust formation (the crust cooled down globally with a slow cooling rate in the presence of a dynamo) has been taken into account for the three bodies (Isac et al., 2012). This scenario allows to consider that only departures from the form of the crust, in this case topographic lows – the craters – are associated with magnetic fields. The "deficit" of the magnetic field signature above a crater has been assumed to be influenced by the transient diameter of the crater, the pre-impact magnetization direction and magnitude, and the thickness of the magnetized layer. The impact has been associated with a a paraboloidal source, the crust being removed and spread away around the crater by the excavation and demagnetized by the high pressures of the shock wave created by the impact. Only the signature of the impact demagnetization effects has been computed. The predicted intensity field of selected craters for Earth, Mars and Moon has been compared with the measured or modeled field at the same altitude, and analyzed. Also, adjustment of calculation algorithms used (the Equivalent Source Dipoles) in the case studies for the three planets, is a new way of processing local anomalies for the objective pursued.

Key findings of the detailed analysis of studied impact craters cover both general comments on data analysis, and quantitative estimates of the features that characterize their magnetic signature. From the first category we mention:

- The resolution of newest magnetic field models of the crustal field of Earth, Mars and Moon is now approaching a level which allows geophysical interpretation of local features. The dimensions of studied craters are considered a unique demonstration of the fact that the latest maps and global models are capable of detecting magnetic anomalies with local extension. Of the 150 craters analyzed at this stage, characteristic magnetic signatures (the quasi-circular shape) could be highlighted for just 101, with significant sizes and magnetic intensities (Isac et al., 2009);

- Impact cratering has shaped the crustal magnetic field of terrestrial planets. It is associated with material excavation, thermal and shock phenomena. Generally, im-

pacts alter the magnetic character of the affected rocks and disrupt the pre-existing magnetic fabric. Impact craters can be often characterized by broad magnetic lows if they were formed in the absence of an active inductive magnetic field. In the presence of an active internal field, the process of (de)magnetization due to the shock impact is associated with post-impact (re)magnetization (mainly thermal) processes, generating a more complex magnetic signature;

- The shock (de)magnetization should be accepted as the prime characteristic of a hypervelocity impact, strongly associated with the mechanics of impact crater formation. The shock pressure area bigger than 1 GPa capable to erase the magnetization, is not restricted to the area of the transient cavity (Scott et al., 1997), but to an area at least double to transient cavity.

In the second category, we include the following:

- For the first time, systematic and precise measurements and studies of topographic and morphometric features of impact craters were done with results that were previously unobtainable. The magnetic signature of 28 craters on Earth, 34 craters on Mars and 37 on the Moon were studied. The resulting characteristics were grouped in tables;

- Earth's impact craters with diameters under 100 km (the largest multiring candidates show more complex signatures) present a low magnetic signature at 5 km altitude (such as the Acraman structure). Here, on Earth, the thermoremanent magnetization in an internal global field is associated with shock demagnetization. In such case, the randomly and strong magnetization vectors effectively cancel out when summed over the whole crater, due to the resulted short-waves anomalies. Thus, the magnetic field appears much lower than that of neighboring areas seen from the altitude of the map or model, like in case of younger impact craters from Mars and Moon. This implies that only magnetic anomalies of meteorite craters cannot be used as evidence for the absence of the planet's internally generated magnetic field at the time of impact;

- All middle and late Noachian large craters from Mars ($< 4\ Gy$) are completely demagnetized, with no significant magnetic anomalies. They have presumably been demagnetized by the impact event that created each large basin, suggesting a ceased dynamo and no global field at that time. This is the case of late largest Nectarian and Imbrian craters ($< 3.85\ Gy$) from the Moon, too. They are characterized by a magnetic disruption signature. Why and how a dynamo stopped is still waiting to be investigated with the new sets of satellite data (Isac et al., 2012);

- The oldest basins from Mars ($> 4.2\ Gy$) or from Moon ($> 3.9\ Gy$) present anomalies with a distribution which might indicate that their sources are genetically associated with the crater-forming events. In these cases, the shock demagnetization of the central uplift is overlapped by the thermoremanent magnetization carried by a higher coercivity component of the impact melt rocks, in a steady magnetizing field of a former dynamo. This is also the case of the three largest multiring craters of the Earth (Vredefort, Sudbury and Chicxulub), that show the same complex magnetic signature (Isac et al., 2011);

- Multiple impacts, the interferences between multiple overlapping basins and low crustal field on Moon have made the interpretation of the shock demagnetization of the crust rather difficult. The same effect had the post-impact structural modifications on Earth, for example erosion and tectonism. The spatial resolution of used magnetic maps and models of the same order as the orbital altitude, only allowed the study of the largest impacts. Craters smaller than 400 km for Mars, 70 km for Moon and 30 km for the Earth could not be included on the study;

- For about 5 large impact craters on each celestial body the Equivalent Source Dipoles modeling technique was applied. Seven of these, representative, were presented in the thesis. The modeling method (ESD) could reveal that in all cases, regardless of the planet, crater size or age, the impact affected the magnetic properties of rocks, primarily due to the shock, disturbing and diminishing previous magnetization. ESD modeling results are especially consistent with the largest and young craters from Mars and Moon ($< 4\ Gy$) and with smaller craters ($< 100\ km$) from Earth;

- $4\ Gy$ is proposed to account for the cessation of martian and lunar dynamos, as a result of a rapid inner core development against a thiner and thiner outer core incapable to longer sustain an active dynamo by means of convection currents. Additionally, largest impacts from Mars and Moon have demagnetized the upper 40 km of the late Noachian and Nectarian crust (the better results were obtained using a rate depth to diameter of 1/10 (Isac et al., 2013). The modeling method is able to demonstrate that largest impacts have affected the entire crust of the planets, especially during the Late Heavy Bombardment, about 4 to 3.8 Gy ago. On Earth, this event was lost due to its constantly renewed surface;

- Generally, impacts undoubtedly alter the initial magnetic properties of rocks, the extreme shock ($5 - 30\ GPa$) demagnetizing the crust to depths of several tens of kilometers (Isac et al., 2010). In most cases the magnetic image is characterized

by a minimum extended at least over the crater, combined also with a magnetic disturbance in the central area, local short-wave anomalies forming a minimum or a maximum depending on the direction and intensity of remagnetization in an active internal field present at the date.

The results of the second part of the thesis are subject of a paper published in 2009 in ESA's Proceedings: "How impacts have shaped the magnetic fields of Earth, Mars and Moon" with M. Mandea and M. Purucker [12] and of a second one, "Magnetic characteristics of impacts on the Moon, Mars and Earth, and hypothetical late-state dynamos", pending to be submitted. Besides these outcomes, the research results were presented at EGU2010: "Impact structures seen by magnetic anomaly maps" (Isac A., Mandea M., Purucker M.), EGU2011: "Magnetic characteristic of the largest impacts on the Moon, Mars and Earth" (Isac A., Purucker M., Mandea M.), EGU2012: "Demagnetization patterns seen in global magnetic models of Earth, Mars and Moon" (Isac A., Langlais B., Mandea M.), EGU2013: "Reading the Magnetic Patterns in Earth complex impact craters to detect similarities and clues from some Nectarian craters of the Moon" by Isac A., Purucker M. and Mandea M.

Despite limitations due to objective reasons, the thesis addresses the first comparative study of crustal magnetism on terrestrial planets which is a novelty. Systematic and comparative analysis of magnetic signatures of impact craters that marked the three celestial bodies revealed another aspect of the scientific possibilities of recent satellite missions. The thesis has used all global investigative opportunities trying to prove scientifically that a planetary geological phenomenon that has shaped the planets of our solar system 4 Gy ago, can be accurately detected by magnetic measurements.

* * *

The work done during this PhD is a part a long-term project which would be continued. It is clear that the nature of the geomagnetic field is complex and there is a continuous need for a better comprehensive separation and understanding of the external and internal sources. Monitoring the magnetic field at higher frequencies, with a very high accuracy, a constant upgrade of the instrumentation, an elaborate data-processing and a close collaboration with space agencies will be the beginning of new directions of research, focused on the characterization of the Earth's magnetic field behavior in space and time, and crustal fields of terrestrial planets. The 2013 Swarm constellation mission will gain new insights into improving the knowledge of the Earth's interior. Scientists already involved in analyzing satellite data and ground-based observations will be able to take full advantage of a new generation of magnetometers enabling high-precision, low-noise and high-resolution measurements of the strength and directions of the magnetic

[12] $http://www.congrex.nl/09c24/S2\_Posters/S2\_P04\_Isac\_paper.pdf$

field. The outgoing surveys on Mars, as 2013 MAVEN satellite which will explore the planet's upper atmosphere, ionosphere and interactions with the Sun and solar wind, will give the chance to solve the controversy whether Mars still has a weak dynamo. For the Moon, the successor of Kaguya, SELENE-2 orbiter, a low-altitude polar-orbiting survey connected with a lander and a rover, in 2017, will be used to constrain possible mechanisms for lunar magnetization.

Bibliography

Acuña, M. H., 2002. Space–based magnetometers. Review of Scientific Instruments 73, Issue 11, 3717–3736.

Acuña, M. H., Connerney, J. E. P., Wasilewski, P., Lin, R. P., Mitchell, D., Anderson, K. A., Carlson, C. W., McFadden, J., Rème, H., Mazelle, C., Vignes, D., Bauer, S. J., Cloutier, P., Ness, N. F., 2001. Magnetic field of Mars: Summary of results from the aerobraking and mapping orbits. J. Geophys. Res. 106, 23403–23418.

Acuña, M. H., Connerney, J. E. P., Ness, N. F., Lin, R. P., Mitchell, D., Carlson, C. W., McFadden, J., Anderson, K. A., Réme, H., Mazelle, C., Vignes, D., Wasilewski, P., Cloutier, P., 1999. Global distribution of crustal magnetization discovered by the Mars Global Surveyor MAG/ER experiment. Science 284, 790–793.

Albee, A. L., Arvidson, R. E., Palluconi, F., Thorpe, T., 2001. Overview of the Mars Global Surveyor mission. J.Geophys.Res. 106, doi:10.1029/2000JE001306.

Alexandrescu, M., Gibert, D., Hulot, G., Mouël, J.-L. L., Saracco, G., 1995. Detection of geomagnetic jerks using wavelet analysis. J. Geophys. Res. 100, 12557–12572.

Alexandrescu, M., Gibert, D., Hulot, G., Mouël, J.-L. L., Saracco, G., 1996. Worldwide wavelet analysis of geomagnetic jerks. J. Geophys. Res. 101, 21975–21994.

Ames, D. E., Gibson, H. L., Watkinson, D. H., 2000. Controls on major impact-induced hydrothermal system, Sudbury structure, Canada. Lunar and Planetary Science Conference XXXI Abstract, 1873.

Anghel, M., Demetrescu, C., 1980. The effect of solar activity on the secular variation of the geomagnetic field in Romania. Phys. Earth. Planet. Inter. 22, 53–59.

Anghel, M., Demetrescu, C., Nestianu, T., 1980. Secular variation studies in Romania. Gerlands Beitr. Geophysik 89, 499–510.

Araki, H., Tazawa, S., et al., 2009. Lunar global shape and polar topography derived from KAGUYA-LALT laser altimetry. Science 323, 897–900, doi:10.1126/science.1164146.

Archinal, B., Rosiek, M., Redding, B., 2005. Unified Lunar Control Network 2005 and Topographic Model. Lunar Planetary Sci. XXXVI, Abstract no.2106, CD-ROM.

Arkani-Hamed, J., 2001. A 50-degree spherical harmonic model of the magnetic field of Mars. Geophys.Res.Lett. 106, 197–208.

Arkani-Hamed, J., 2004. A coherent model of the crustal magnetic field of Mars. Journal of Geophysical Research 109, E03011, doi:10.1029/2004JE002265.

Atanasiu, G., 1968. Variation seculaire des elements geomagnetiques en Transylvanie et au Banat (Roumanie) durant la periode 1848-1968. Rev. Roum. Géol., Géoph. Géogr., serie de Géophysique 12, 87–104.

Atanasiu, G., Nestianu, T., Demetrescu, C., Anghel, M., 1976. Some aspects of the secular variation of the geomagnetic elements H,Z, F, between 1958-1974 in Romania. Phys. Earth. Planet. Inter. 12, 11–17.

Auster, H., Mandea, M., Hemshorn, A., Pulz, E., Korte, M., 2007. Automation of absolute measurements of the geomagnetic field. Earth Plan. Space 59(9), 1007–1014.

Auster, V., Hillenmaier, O., Kroth, R., Weidemann, M., 2006. Proton magnetometer development. In: XIIth IAGA Workshop on Geomagnetic Observatory Instruments, Data Acquisition and Processing, Abstract volume, 21.

Bagenal, F., Dowling, T., McKinnon, W., 2004. Jupiter: The Planet, Satellites and Magnetosphere. Cambridge Planetary Science Cambridge University Press, 719.

Baldwin, R., 1949. The Face of the Moon. The University of Chicago Press, Chicago.

Baldwin, R., 1963. The Measure of the Moon. The University of Chicago Press, Chicago.

Barlow, N., 1988. Constraints on early events in martian history as derived from the cratering record. J. Geophys. Res. 95, 14,191–14,201.

Barraclough, D., 1995. Observations of th Earth's magnetic field in Edinburgh, from 1670 to the present day. Tran. R. Soc. Edinburgh Earth Sci. 85, 239–252.

Beals, C., Innes, M., Rottenberg, J., 1963. Fossil meteorite craters: The Solar System, Vol.IV, The Moon, Meteorites and Comets. Univ. of Chicago Press, Middlehurst B.M. and Kuiper G.P., eds., Chicago.

Becker, J., Sandwell, D., Smith, W., Braud, J., Binder, B., Depner, J., Fabre, D., Factor, J., Ingalls, S., Kim, S.-H., Lander, R., Marks, K., Nelson, S., Pharaoh, A., Trimmer, R.,

Rosenberg, J. V., Wallace, G., Weatherall, P., 2009. Global Bathymetry and Elevation Data at 30 Arc Seconds Resolution: $SRTM30\_Plus$. Marine Geodesy 32, 355–371, doi:10.1029/2004JE002262.

Bhattacharyya, B., 1964. Magnetic anomalies due to prism-shaped bodies with arbitrary polarization. Geophysics 29(4), 517.

Binder, A. B., 1998. Lunar prospector: Overview. Science 281, 1475–1476.

Blakely, R., 1995. Potentiel Theory in gravity and magnetic applications. Cambridge University Press, Cambridge.

Bloxham, J., 2002. Time-independent and time-dependent behaviour of high-latitude flux bundles at the core-mantle boundary. Geophys. Res. Lett. 29, 1854,doi:10.1029/2001GL014543.

Bott, M., 1963. Two methods applicable to computers for evaluating magnetic anomalies due to finite three dimensional bodies. Geophysical Prospecting 11, 292–299.

Boutin, D., Arkani-Hamed, J., 2006. Polar wandering of Mars: Evidence from paleomagnetic poles. Icarus 181, 13–25.

Brockwell, P., Davis, R., 2009. Time series: Theory and methods. 2^{nd} ed., Springer.

Cafarella, L., DeSantis, A., Meloni, A., 1992. Secular variation in Italy from historical geomagnetic field measurements. Phys. Earth. Planet. Inter. 73, 206–221.

Cain, J. C., 2007. POGO (OGO-2, -4 and -6 spacecraft). In: Gubbins, D., Herrero-Bervera, E. (Eds.), Encyclopedia of Geomagnetism and Paleomagnetism. Springer, Heidelberg.

Cain, J. C., Ferguson, B. B., Mozzoni, D., 2003. An n = 90 internal potential function of the Martian crustal magnetic field. Journal of Geophysical Research (Planets) 108, 2–1.

Campbell, H. W., 1997. Introduction to Geomagnetic Fields. Cambridge University Press.

Carporzen, L., Gilder, S., Hart, R., 2005. Palaeomagnetism of the Vredefort meteorite crater and implications for craters on Mars. Nature 435, Issue 7039, doi:10.1038/nature03560, 198–201.

Chambodut, A., Mandea, M., 2005. Evidence for geomagnetic jerks in comprehensive models. Earth Planets Space 57, 139–149.

Chambodut, A., Panet, I., Mandea, M., Diament, M., Holschneider, M., Jamet, O., 2005. Wavelet frames: an alternative to spherical harmonic representation of potential fields. Geophys. J. Int. 163, 875–899.

Chin, G., Brylow, S., et al., 2007. Lunar Reconnaissance Orbiter overview: The instrument suite and mission. Space Sci. Rev. 129, 391–419, doi:10.2007/s11214-007-9153-y.

Cisowski, S., Fuller, M., 1978. The effect of shock on the magnetism of terrestrial rocks. J. Geophys. Res. 83, 3,441–3,458.

Clark, D. A., 1997. Magnetic petrophysics and magnetic petrology: aids to geological interpretation of magnetic surveys. Exploration Geophysics 30, 5–26.

Cohen, B., 2008. Lunar Meteorite Impact Melt Clasts and Lessons Learned for Lunar Surface Sampling. LPSC 39, 2532.

Connerney, J., Acuña, M., N.F.Ness, 2004. Mars crustal magnetism. Space Science Reviews 111, 1–32.

Connerney, J. E. P., Acuña, M. H., Ness, N. F., Kletetschka, G., Mitchell, D. L., Lin, R. P., Reme, H., 2005. Tectonic implications of Mars crustal magnetism. Treatise on Geophysics Planetary Magnetism (Tilman Spohn (ed)).

Constantinescu, L., 1979. Early geomagnetic information concerning the Romanian territory. Memoriile sectiilor stiintifice seria IV II, 146–165.

Courtillot, V., Ducruix, J., Le Mouël, J.-L., 1978. Sur une accélération récente de la variation séculaire du champ magnétique terrestre. C. R. Acad. Sci. Paris. Ser. D 287, 1095–1098.

Cowan, D., Cooper, G., 2005. Enhacement of magnetic signatures of impact structures. Large meteorite impacts III: Geological Society of America Special Paper, 385.

Crawford, D. A., Schultz, P. H., 1999. Electromagnetic properties of impact-generated plasma, vapor and debris. Int. Journal of Impact Engineering 23, 169–180.

Croft, S., Kieffer, S., Ahrens, T., 1979. Low velocity impact craters in ice and icesaturated sand with implications for martian crater count ages. J. Geophys. Res. 84, 8,023–8,032.

Croft, S. K., 1985. The scaling of complex craters. Proc.Lunar Planet. Sci. Conf. 15, 828.

Daubechies, I., 1992. Ten lectures on wavelets. CBMS-NSF Regional Conference Series in Applied Mathematics Society for Industrial and Applied Mathematics, Philadelphia.

de Boor, C., 2001. A Practical Guide to Splines, Applied Mathematical Sciences. Springer-Verlag, New York.

De Michelis, P., Tozzi, R., 2005. A local intermittency measure (lim) approach to the detection of geomagnetic jerks. Earth Planet. Sci. Lett. 235, 261–272.

De Santis, A., Qamili, E., Chianchini, G., 2011. Ergodicity of the recent geomagnetic field. Phys. Earth Plan. Int. 186, 103–110.

Demetrescu, C., Andreescu, M., E.-M., Nestianu, T., 1985. Characteristics of the secular variation of the geomagnetic field between 1964 and 1981 in Romania. Phys. Earth Planet Inter 37, 46–51.

Demetrescu, C., Ene, M., Dobrica, V., 2011. Geomagnetic field change in Romania, 1980-2004. Rom. J. Phys. 56, 790–800.

Dence, M., 1965. The extraterrestrial origin of Canadian craters. Annual New York Academy of Science 123, 941–969.

Dence, M., 1972. The nature and significance of terrestrial impact structures. 24^{th} International Geological Congress, Proceedings Section 15, Montreal, Canada.

Dobrica, V., Demetrescu, C., Stefan, C., 2013. Toward a better representation of the secular variation. Case study: the European network of geomagnetic observatories. Earth, Planets, Space (in print).

Dolginov, S., Zhuzgov, L. N., Pushkov, N. V., Tyurmina, L. O., Fryazinov, I. V., 1962. Some results of measurements of the constant geomagnetic field above the USSR from the third artificial Earth satellite. Geomagnetism and Aeronomy 2, 877–889.

Duka, B., De Santis, A., Mandea, M., **Isac, A.**, Qamili, E., 2012. Geomagnetic jerks characterization via spectral analysis. Solid Earth 3 (http://www.solid-earth.net/3/131/2012/), 131–148.

Duma, G., 2010. European declination map. Central Inst. for Meteorology and Geodynamics, Austria and the MAGNETE team CGMW Resolutions, Paris, February, 16, 9.

Dunlop, D., 2005. Planetary science-Magnetic impact craters. Nature 435(7039), doi: f10.1038/435156a, 156–157.

Dunlop, D. J., Özdemir, O., 1997. Cambridge Studies in magnetism, Rock magnetism: Fundamentals and Frontiers. Cambridge University Press.

Dyment, J., Arkani-Hamed, J., 1998. Contribution of lithospheric remanent magnetization to satellite magnetic anomalies over the world's oceans. J. Geophys. Res. 103, 15423–15442.

Ebbing, J., Janle, P., Koulouris, J., Milkereit, B., 2001. 3D gravity modelling of the Chicxulub impact structure. Planetary and Space Science 49, 599–609.

Farr, T., Rosen, P., Caro, E., Crippen, R., Duren, R., Hensley, S., Kobrick, M., Paller, M., Rodriguez, E., Roth, L., Seal, D., Shaffer, S., Shimada, J., Umland, J., 2007. The Shuttle Radar Topography Mission. Rev. Geophys. 45, RG2004, doi: 10.1029/2005RG000183.

Finlay, C. C., Maus, S., Beggan, C. D., Bondar, T. N., Chambodut, A., Chernova, T. A., Chulliat, A., Golovkov, V. P., Hamilton, B., Hamoudi, M., Holme, R., Hulot, G., Kuang, W., Langlais, B., Lesur, V., Lowes, F. J., Lühr, H., Macmillan, S., Mandea, M., McLean, S., Manoj, C., Menvielle, M., Michaelis, I., Olsen, N., Rauberg, J., Rother, M., Sabaka, T. J., Tangborn, A., Tøffner-Clausen, L., Thébault, E., Thomson, A. W. P., Wardinski, I., Wei, Z., Zvereva, T. I., 2010. International Geomagnetic Reference Field: The Eleventh Generation. Geophys. J. Int. 1, 100.

Fox Maule, C., Purucker, M., Olsen, N., 2009. Inferring magnetic crustal thickness and geothermal heat flux from crustal magnetic Qamilifield models. Danish Climate Centre Report 09-09, 1–33.

French, B., 1998. Traces of a catastrophe: A handbook of shock-metamorphic effects in terrestrial meteorite impact structures. LPI Contribution No. 954, Lunar and Planetary Institute, Houston.

Frey, H., 2006. Impact constraints on the age and origin of the lowlands of Mars. Geophys. Res. Lett. 33, L08S02, 4pp.

Frey, H., 2008. Rapid decrease in Martian crustal magnetization in the Noachian era: implications for the dynamo and climate of early Mars. Geophys. Res. Lett. 35, L13203.

Frey, H., 2010. A minimum crater retention age for the proposed "Borealis Basin" on Mars. Lunar and Planetary Institute, Lunar and Planetary Science Conference XLI, Houston, Texas abstract 1136, CD–ROM.

Friis-Christensen, E., H.Lühr, Hulot, G., 2006. Swarm: A constellation to study the Earth's magnetic field. Earth, Planets and Space 58 (4), 351–358.

Friis-Christensen, E., H.Lühr, Hulot, G., Haagmans, R., Purucker, M., 2009. Geomagnetic research from space. EOS Trans. AGU 90 (25), 213–214.

Gabor, D., 1946. Theory of communications. J. Inst.Elec. Eng. 93, 429–457.

Garrick-Bethell, I., Weiss, B. P., Shuster, D. L., Buz, J., 2009. Early lunar magnetism. Science 9, 323–356.

Gattacceca, J., Berthe, L., Boustie, M., Vadeboin, F., Rochette, P., De Resseguier, T., 2008. On the efficiency of shock magnetization processes. Physics of the Earth and Planetary Interiors 166, 1–10.

Gauss, C. F., 1839. Allgemeine Theorie des Erdmagnetismus. In: Gauss, C. F., Weber, W. (Eds.), Resultate aus den Beobachtungen des Magnetischen Vereins im Jahre 1838. Leipzig, pp. 1–57.

Gilbert, W., 1600. De Magnete, Magneticisque Corporibus, et de Magno Magnete Tellure. Dover Publications, translated by P. F. Mottelay, 1958.

Girdler, R., Taylor, P., Frawley, J., 1992. A possible impact origin for the Bangui magnetic anomaly (Central Africa). Tectonophysics 212, 45–58.

Grajales-Nishimura, J., Cedillo-Pardo, E., Rosales-Dominguez, C., Moran-Zenteno, D., Alvarez, W., Claeys, P., Ruiz-Morales, J., Garcia-Hernandez, J., Padilla-Avila, P., Sanchez-Rios, P., 2000. Chicxulub impact: The origin of reservoir and seal facies in the southeastern Mexico oil fields. Geology 28,no.4, 307–310.

Grieve, R., 1991. Terrestrial impact: The record in the rocks. Meteoritics and Planetary Science 26, 175–194.

Grieve, R., 2004. Economic natural resource deposits at terrestrial impact structures. Geological Society, London, Special Publications 2005 248, 1–29, doi:10.1144/GSL.SP.2005.248.01.01.

Grieve, R., Head, J., 1981. Impact cratering: A geological process on the planets. Episodes, 3–9.

Grieve, R., Masaitis, V., 1994. The economic potential of terrestrial impact craters. International Geological Review 43, 105–151.

Grieve, R., Pilkington, M., 1996. The signature of terrestrial impacts. AGSO Journ. of Australian Geology and Geophysics 16, 399–420.

Halekas, J. S., Mitchell, D. L., Lin, R. P., Hood, L. L., Acuña, M. H., Binder, A. B., 2002. Demagnetization signatures of lunar impact craters. Geophys. Res. Lett. 29 (13), doi:10.1029/2001GL013924.

Hamoudi, M., Cohen, Y., Achache, J., 1998. Can the thermal thickness of the continental lithosphere be estimated from Magsat data? Tectonophysics 284, 19–29.

Hamoudi, M., Quesnell, Y., Dyment, J., Lesur, V., 2011. Aeromagnetic and marine measurements. IAGA Special Sopron Book Series, M. Mandea and M. Korte, Ed. Geomagnetic Observations and Models, 57–104.

Hamoudi, M., Thebault, E., Lesur, V., Mandea, M., 2007. GeoForschungsZentrum Anomaly Magnetic MAp (GAMMA): A candidate model for the World Digital Magnetic Anomaly Map. Geochem., Geophys., Geosys. 8, Q06023, doi:10.1029/2007GC001638.

Hartmann, W., Kuiper, G., 1962. Concentric structures surrounding lunar basins. Comm. Lunar and Planetary Lab. 12,1, 51–66.

Hartmann, W., Neukum, G., 2001. Cratering chronology and the evolution of mars. Space Sci. Rev. 96, 165–194.

Hartmann, W., Wood, C., 1971. Moon: origin and evolution of multi-ring basins. Moon 3, 3–78.

Hawke, P., 2003. A re-evaluation of the size of the acraman impact structure, australia. Meteoritics and Planetary Science, Meteoritical Society Meeting, Munster 38, Abstract 5169.

Hawke, P., 2004. The geophysical signatures and exploration potential of australia's meteorite impact structures. School of Earth and Geographical Sciences, The University of Western Australia Thesis, 1–287.

Heiken, G., Vaniman, D., French, B.M., e., 1991. Lunar Sourcebook: A User's Guide to the Moon. Cambridge University Press.

Hemant, K., Maus, S., 2005. Geological modeling of the new CHAMP magnetic anomaly maps using a Geographical Information System (GIS) technique. J. Geophys. Res. B, 110, B12103, doi:10.1029/2005JB003837.

Henkel, H., Pesonen, L., 1992. Impact craters and craterform structures in Fennoscandia. Tectonophysics 216, 31–40.

Henkel, H., Reimold, W., 1998. Integrated geophysical modeling of a giant, complex impact structure: anatomy of the Vredefort Structure, South Africa. Tectonophysics 287, 1–20.

Henkel, H., Reimold, W., 2002. Magnetic model of the central uplift of the Vredefort impact structure, South Africa. Journal of Applied Geophysics 51, 43–62.

Hildebrand, A. R., Penfield, G. T., Kring, D. A., Pilkington, M., Camargo-Zanoguera, A., Jacobson, S., Boynton, W. V., 1991. Chicxulub crater: A possible Cretaceous/Tertiary boundary impact crater on the Yucatan Peninsula, Mexico. Geology 19, 867–871.

Hildebrand, A. R., Pilkington, M., 2002. Crater-floor exhalative (CRAFEX) sulfide deposits at the Chicxulub Crater, Yucatan, Mexico. Lunar and Planetary Science Conference XXXIII Abstract, 2031.

Holschneider, M., Chambodut, A., Mandea, M., 2003. From global to regional analysis of the magnetic field on the sphere using wavelet frames. Physics of the Earth and Planetary Interiors 135 (2), 107–124.

Hood, L., Richmond, N., Pierazzo, E., Rochette, P., 2003. Distribution of crustal magnetic fields on Mars:Shock effects of basin-forming impacts. Geophysical Res. Lett. 30, 10.1029/2002GL016657.

Hood, L., Young, C., Richmond, N., Harrison, K., 2005. Modeling of major martian magnetic anomalies: Further evidence for polar reorientations during the Noachian. Icarus 177, Issue 1, doi: 10.1016/j.icarus.200502.008, 144–173.

Hood, L., Young, C., Richmond, N., Harrison, K., 2011. Central magnetic anomalies of Nectarian-aged lunar impact basins: Probable evidence for an early core dynamo. Icarus 211, Issue 2, doi: 10.1016/j.icarus.2010.08.012, 1,109–1,128.

Hood, L. L., Zakharian, A., 2001. Mapping and modeling of magnetic anomalies in the northern polar region of Mars. J.Geophys.Res. 106.

Isac, A., Langlais, B., Mandea, M., 2012. Demagnetization patterns seen in global magnetic models of Earth, Mars and Moon. Geophysical Research Abstracts, ISSN:1029-7006 14, EGU2012–7311.

Isac, A., Mandea, M., Purucker, M., 2009. How Impacts Have Shaped the Magnetic Field of Earth, Mars and Moon. Proceedings of ESA's Second Swarm International Science Meeting, GFZ, Potsdam (DE), WPP-303 CD-ROM, 1–7.

Isac, A., Mandea, M., Purucker, M., 2010. Impact structures seen by magnetic anomaly maps. European Geoscience Union General Assembly, Vienna 12, EGU2010–7852.

Isac, A., Mandea, M., Purucker, M., 2013. Reading the Magnetic Patterns in Earth complex impact craters to detect similarities and clues from some Nectarian craters of the Moon. Geophysical Research Abstracts, ISSN:1607-7962 15, EGU2013–9649.

Isac, A., Purucker, M., Mandea, M., Frey, H., 2011. Magnetic characteristics of the largest impacts on the Moon, Mars, and Earth. European Geoscience Union General Assembly, Vienna 13, EGU2011–7455.

Jackson, A., Jonkers, A. R. T., Walker, M. R., 2000. Four centuries of geomagnetic secular variation from historical records. Phil. Trans. R. Soc. Lond. A 358, 957–990.

Jankowski, J., Sucksdorff, C., 1996. IAGA guide for magnetic measurements and observatory practice. IAGA.

Katanforoush, A., Shahshahhani, M., 2003. Distributing points on the sphere. I, Experimental Mathematics 12, Issue 2, 199–209.

Khokhlov, A., Hulot, G., Le Mouël, J., 1999. On the Backus effect - II. Geophys. J. Int. 137, 816–820.

Korepanov, V., Klymovych, Y., Kuznetsov, O., Pristai, A., Marusenkov, A., Rasson, J., 2007. New intermagnet fluxgate magnetometer. Publications of the Institute of Geophysics Pol. Acad. Sc. Monographic Volume C99, 291–298.

Korhonen, J., Fairhead, J., Hamoudi, M., Hemant, K., Lesur, V., Mandea, M., Maus, S., Purucker, M., Ravat, D., Sazonova, T., Thébault, E., 2007. Magnetic Anomaly Map of the World – Carte des anomalies magnétiques du monde, Scale 1:50,000,000. Commission for Geological Map of the World, UNESCO-CGMW,1^{st} Edition.

Korte, M., Mandea, M., Kotzé, P., Nahayo, E., Pretorius, B., 2007. Improved observations at the southern African geomagnetic repeat station network. S. Afr. J. Geol. 110, 175–186.

Korte, M., Mandea, M., Matzka, J., 2009. A historical declination curve for Munich from different data sources. Phys. Earth Planet. Inter. 174, 161–172.

Kumar, P., Georgiu, E., 1994. Wavelet Analysis in Geophysics: An Introduction, in Wavelet Analysis and its Applications. Academic Press, 1–43.

Kuvshinov, A. V., Olsen, N., 2005. Modelling the ocean effect of geomagnetic storms at ground and satellite altitude. In: Reigber, C., Lühr, H., Schwintzer, P., Wickert, J. (Eds.), Earth Observation with CHAMP, Results from Three Years in Orbit. Springer Verlag.

Langel, R. A., 1987. The main field. In: Jacobs, J. A. (Ed.), Geomagnetism. Vol. 1. Academic Press, London, pp. 249–512.

Langel, R. A., Hinze, W. J., 1998. The Magnetic Field of the Earth's Lithosphere – The Satellite Perspective. Cambridge University Press, United Kingdom.

Langel, R. A., Purucker, M., Rajaram, M., 1993. The equatorial electrojet and associated currents as seen in MAGSAT data. J. Atmos. Terr. Phys. 55, 1233–1269.

Langlais, B., Purucker, M., 2007. A polar magnetic paleopole associated with Apollinaris Patera, Mars. Planetary and Space Science 55(3), 270–279.

Langlais, B., Purucker, M., Mandea, M., 2004. Crustal magnetic field of Mars. J. Geophys. Res. 109, doi:10.1029/2033JE002048.

Langlais, B., Quesnel, Y., 2008. New perspectives on Mars' crustal magnetic field. Comptes Rendus Geoscience 340,12.

Langlais, B., Thébault, E., 2011. Predicted and observed magnetic signatures of Martian (de)magnetized impact craters. Icarus 212, 568–578.

Lanzerotti, L. J., Langel, R. A., Chave, A. D., 1993. Geoelectromagnetism. In: Trigg, G. (Ed.), Encyclopedia of Applied Physics, Vol 7. VCH Publishers, New York, pp. 109–123.

Lesur, V., Wardinski, I., Asari, S., Minchev, B., Mandea, M., 2010. Modelling the Earth's core magnetic field under flow constraints. Earth Planets Space 62.

Lesur, V., Wardinski, I., Rother, M., Mandea, M., 2008. GRIMM – The GFZ Reference Internal Magnetic Model based on vector satellite and observatory data. Geophys. J. Int. 173.

Lillis, R., Frey, H., Manga, M., 2008a. Rapid decrease in Martian crustal magnetization in the Noachian era: implications for the dynamo and climate of early Mars. Geophys. Res. Lett. 35, L14203.

Lillis, R., Frey, H., Manga, M., Mitchell, D., Lin, R., Acuña, M., 2007. Basin magnetic signatures and crater retention ages: evidence for rapid shutdown of the Martian dynamo. Lunar and Planetary Science XXXVIII.

Lillis, R., Frey, H., Manga, M., Mitchell, D., Lin, R., Acuña, M., Bougher, S., 2008b. An improved crustal magnetic field map of Mars from electron reflectometry: Highland volcano magmatic history and the end of the martian dynamo. Icarus 194, 575–596.

Lillis, R., Haleskas, J., Stewart, S., Manga, M., 2009. Impact demagnetization at Mars: Using multiple altitude magnetic field data to constrain propreties of crustal magnetization. Lunar and Planetary Science Conference Abstract 2360, Houston, TX.

Lillis, R., Purucker, M., Haleskas, J., Stewart-Mukhopadhyay, K. L. S., Manga, M., Frey, H., 2010. Study of impact demagnetization at Mars using Monte Carlo modeling and multiple altitude data. Journal of Geophysical Research 115, doi:10.1029/2009JE003556.

Linthe, H., Reda, J., **A. Isac**, Matzka, J., Turbitt, C., 2012. Observatory Data Quality Control-the instrument to ensure valuable research. Article in Proceedings of The XV^{th} IAGA Workshop on Geomagnetic Observatory Instruments, Data Acquisition and Processing, San Fernando, Spain ISSN:1131-540, 1–4.

Louzada, K., Stewart, S., Weiss, B.P., a. G.-J., Lillis, R., Haleskas, J., 2011. Impact demagnetization of the Martian crust: Current knoeledge and future directions. Earth and Planetary Science Letters 305, 257–269.

Love, J. J., 2008. Magnetic monitoring of Earth and space. Physics Today 61, 31–37.

Lowes, F. J., 1966. Mean-square values on sphere of spherical harmonic vector fields. J. geophys. Res. 71, 2179.

Luis, J. F., Miranda, M., 2008. Reevaluation of magnetic chrons in the North Atlantic between $35°N$ and $47°N$: Implications for the formation of the Azores Triple Junction and associated plateau. J.Geophys.Res. 113, B10105, doi:10.1029/2007JB005573.

Malin, S. R. C., Bullard, E., 1981. The direction of the Earth's magnetic field at London, 1570-1975. Phil. Trans. R. Soc. Lond. 299, 357–423.

Mandea, M., 2005. Candidate main-field models for producing the IGRF 9^{th} generation. Earth, Planets and Space 57, 1183–1189.

Mandea, M., Bellanger, E., Mouël, J.-L. L., 2000. A geomagnetic jerk for the end of the 20^{th} century? Earth Planet. Sci. Let. 183, 369–373.

Mandea, M., Holme, R., Pais, A., Pinheiro, K., Jackson, A., Verbanac, G., 2010. Geomagnetic jerks: Rapid core field variations and core dynamics. Space Sci. Rev.Doi:10.1007/s11214-010-9675-6.

Mandea, M., **Isac, A.**, 2011. Geomagnetic Fields, Measurement Techniques. In: Gupta, H. K. (Ed.), Encyclopedia of Solid Earth Geophysics. Springer, Berlin, Heidelberg.

Mandea, M., Macmillan, S., 2000. International Geomagnetic Reference Field - the eighth generation. Earth Planets Space 52, 1119–1124.

Mandea, M., Purucker, M., 2005. Observing, Modeling, and Interpreting Magnetic Fields of the Solid Earth. Surveys in Geophysics 26, 415–459.

Mandea, M., Thèbault, E., 2007. The Changing Faces of the Earth's Magnetic Field: A glance at the magnetic lithospheric field, from local and regional scales to a planetary view. Commission for the Geological Map of the World, Paris.

Mandea-Alexandrescu, M., Gibert, D., Le Mouël, J. L., Hulot, G., Saracco, G., 1999. An estimate of average lower mantle conductivity by wavelet analysis of geomagnetic jerks. J. geophys. Res. 104, 17735–17745.

Mark, K., 1987. Meteorite craters. The University of Arizona Press, Tucson.

Masaitis, V., Mihailov, M., Selivanovskaya, T., 1975. The Popigai meteorite crater. NASA TT-F-16900, English Translation 1976, 124pp.

Matsushima, M., Tsunakawa, H., Iijima, Y., Nakazawa, S., Matsuoka, A., Ikegami, S., Ishikawa, T., Shibuya, H., Shimizu, H., Takahashi, F., 2010. Magnetic Cleanliness Program Under Control of Electromagnetic Compatibility for the SELENE (Kaguya) Spacecraft. Space Science Reviews, issue "The Kaguya Mission to the Moon" 154, 253–264.

Mauersberger, P., 1956. Das Mittel der Energiedichte des geomagnetischen Hauptfeldes an der Erdoberfläche und seine säkulare Änderung. Gerlands Beitr. Geophys. 65, 207–215.

Maus, S., Lühr, H., 2005. Signature of the quiet-time magnetospheric magnetic field and its electromagnetic induction in the rotating Earth. Geophys. J. Int. 162, doi:10.1111/j.1365–246X.2005.02691.x.

Maus, S., Lühr, H., Balasis, G., Rother, M., Mandea, M., 2005a. Introducing POMME, the Potsdam Magnetic Model of the Earth. In: Reigber, C., Lühr, H., Schwintzer, P., Wickert, J. (Eds.), Earth Observation with CHAMP, Results from Three Years in Orbit. Springer Verlag, Berlin - Heidelberg, pp. 293–298.

Maus, S., Lühr, H., Hemant, K., Balasis, G., Ritter, P., Stolle, C., 2007. Fifth generation lithospheric magnetic field model from CHAMP satellite measurements. Geochem. Geophys. Geosys. 8, Q05013, doi:10.1029/2006GC001521.

Maus, S., McLean, S., Dater, D., Lühr, H., Rother, M., Mai, W., Choi, S., 2005b. NGDC/GFZ candidate models for the 10^{th} generation International Geomagnetic Reference Field. Earth, Planets, and Space 57, 1151–1156.

Maus, S., Rother, M., Stolle, C., Mai, W., Choi, S.-C., Lühr, H., Cooke, D., Roth, C., 2006. Third generation of the Potsdam Magnetic Model of the Earth (POMME). Geochem. Geophys. Geosyst. 7, Q07008, doi:10.1029GC001269.

Maus, S., Weidelt, P., 2004. Separating the magnetospheric disturbance magnetic field into external and transient internal contributions using a 1D conductivity model of the Earth. Geophys. Res. Lett. 31, L12614, doi: 10.1029/2004GL020232.

Maus, S., Yin, F., Lühr, H., Manoj, C., Rother, M., Rauberg, J., Michaelis, I., Stolle, C., Müller, R., 2008. Resolution of direction of oceanic magnetic lineations by the sixth-generation lithospheric magnetic field model from CHAMP satellite magnetic measurements. Geochem. Geophys. Geosyst. 9 (7), Q07021.

Mayhew, M., Estes, R., 1983. Equivalent source modeling of the core magnetic field using Magsat data. J. Geomagn. Geoelectr. 35, 119–130.

Mc Pherron, R. L., Baker, D. N., Crooker, N. U., 2009. Role of the Russell–Mc Pherron effect in the acceleration of relativistic electrons. Journal of Atmospheric and Solar-Terrestrial Physics 10–11, 1032–1044.

McPherron, R. L., 1991. Physical processes producing magnetospheric substorms and magnetic storms. In: Jacobs, J. A. (Ed.), Geomagnetism. Vol. 4. Academic Press, London, pp. 593–739.

Melosh, H., 1989. Impact cratering: a geologic process. Oxford University Press New York, 245p.

Melosh, H., Ivanov, B., 1999. Impact crater collapse. Annu. Rev. Earth Planet. Sci. 27, 385–415.

Merrill, R. T., McElhinny, M. W., McFadden, P. L., 1996. The Magnetic Field of the Earth. Academic Press, London.

Mitchell, D., Lillis, R., Lin, R., Connerney, J., Acuña, M., 2007. A global map of Mars' crustal magnetic field based on electron reflectometry. Journal of Geophysical Research 112, doi:10.1029/2005JE002564.

Mitchell, D. L., Halekas, J. S., Lin, R. P., Frey, S., Hood, L. L., Acuña, M. H., Binder, A., 2008. Global mapping of lunar crustal magnetic fields by Lunar Prospector. Icarus 194.

Morgan, J., Christenson, G., Zelt, C., 2002. Testing the resolution of a 3D velocity tomogram across the Chicxulub crater. Tectonophysics 355, 217–228.

Nagao, H., Iyemori, T., Higuchi, T., Araki, T., 2003. Lower mantle conductivity anomalies estimated from geomagnetic jerks. J. geophys. Res. 108.

Ness, N. F., 1979. The Magnetic Fields of Mercury, Mars, and Moon. Annual Review of Earth and Planetary Sciences 7, 249–288, doi: 10.1146/annurev.ea.07.050179.001341.

Neubert, T., Mandea, M., Hulot, G., von Freese, R., Primdahl, F., Jørgensen, J., Friis-Christensen, E., Stauning, P., Olsen, N., Risbo, T., 2001. Ørsted satellite captures high-precision geomagnetic field data. EOS, Trans., AGU 82 (7), 81–88.

Neukum, G., Ivanov, B., Hartmann, W., 2001. Cratering records in the inner solar system. Chronology and Evolution of Mars Kluwer, 55–86.

Neumann, G., Zuber, M., Wieczorek, M., McGovern, P., Lemoine, F., Smith, D., 2004. Crustal structure of Mars from gravity and topography. Journal of Geophysical Research 109, E08002, doi:10.1029/2004JE002262.

Newitt, L., Chulliat, A., Orgeval, J.-J., 2009. Location of the North Magnetic Pole in April 2007. Earth Planets Space 61, 703–710.

Newitt, L. R., Barton, C. E., Bitterly, J., 1996. Guide for magnetic repeat station surveys. International Association of Geomagnetism and Aeronomy.

O'Keefe, J., Ahrens, T., 1993. Planetary cratering mechanics. J. Geophys. Res. 98:17011-28.

Olsen, N., 1999. Induction studies with satellite data. Surveys in Geophysics 20, 309–340.

Olsen, N., 2007. Encyclopedia of Geomagnetism and Paleomagnetism. Springer, Heidelberg, Ch. Örsted, pp. 743–746.

Olsen, N., Haagmans, R., Sabaka, T. J., Kuvshinov, A., Maus, S., Purucker, M. E., Rother, M., Lesur, V., Mandea, M., 2006a. The Swarm End-to-End mission simulator study: Separation of the various contributions to the Earth's magnetic field using synthetic data. Earth, Planets and Space 58, 359–370.

Olsen, N., Lühr, H., Sabaka, T., Mandea, M., Rother, M., Toffner-Clausen, L., Choi, S., 2006b. CHAOS – A model of the Earth's magnetic field derived from CHAMP, Ørsted, and SAC-C magnetic satellite data. Geophys. J. Int. 166(1), 67–75.

Olsen, N., Mandea, M., 2008. Rapidly changing flows in the Earth's core. Nature Geosciences 1, 390–394.

Olsen, N., Mandea, M., Sabak, T. J., Tøffner-Clausen, L., 2009. CHAOS-2 – A Geomagnetic Field Model Derived from one Decade of Continuous Satellite Data. Geophys. J. Int. 179, 1477–1487.

Olsen, N., Mandea, M., Sabaka, T. J., Toffner-Clausen, L., 2010. The CHAOS-3 geomagnetic field model and candidates for the 11^{th} generation IGRF. Earth, Planets and Space.

Olsen, N., Sabaka, T., Lowes, F., 2005. New parameterisation of external and induced fields in geomagnetic field modelling, and a candidate model for IGRF 2005. Earth Planet Space 57, 1141–1149.

Oppenheim, A., Schafer, R., 1989. Discrete-time signal processing. Prentice Hall, Englewood 22, NJ.

Ortiz-Aleman, C., Urrutia-Fucugauchi, J., Pilkington, M., 2001. Three-dimensional modeling of aeromagnetic anomalies over the Chicxulub crater. Lunar Planet. Sci. Conf., XXXII, Houston, Texas, Conference CD Files.

Parker, R., 1991. A theory of ideal bodies for seamount magnetism. Journal of Geophysical Research-Solid Earth 96(B10).

Parker, R., 2003. Ideal bodies for Mars magnetics. Journal of Geophysical Research-Planets 2108(E1), doi: f10.1029/2001JE001760.

Parker, R. L., Shure, L., Aug. 1982. Efficient modeling of the Earth's magnetic field with harmonic splines. Geophys. Res. Lett. 9, 812–815.

Parker, T., Rosenberg, S., 1987. Invariants of Conformal Laplacians. J. Differential Geometry 25, 199–222.

Pike, J., 1974. Depth / diameter relations of fresh lunar craters: revision from spacecraft data. Geophysical Research Letters 1, 291–294.

Pike, J., 1985. Some morphologic systematics of complex impact structures. Meteoritics 20, 49–68.

Pilkington, M., Grieve, R., 1992. The geophysical signature of terrestrial impact craters. Reviews of Geophysics 30, 161–181.

Pilkington, M., Hildebrand, A., 2003. Transient and disruption cavity dimensions of complex terrestrial impact structures derived from magnetic data. Geophysical Research Letters 30, 2087, 4pp.

Pilkington, M., Hildebrand, A., Ortiz-Aleman, C., 1994. Gravity and magnetic field modeling and structure of the Chicxulub Crater, Mexico. Journ. of Geophysical Research 99 (E6), 13,147–13,162.

Pilkington, M., Jansa, L. F., Grieve, R., 1995. Geophysical studies of the Montagnais impact crater, Canada. Meteoritics 30, 446–450.

Plescia, J., 2003. Application of gravity data to understanding impact mechanics. In Impact Cratering: Bridging the Gap Between Modeling and Observations LPI Contribution No.1155, Lunar and Planetary Institute, Houston, Abstract 8051.

Purucker, M., 2008. A global model of the internal magnetic field of the Moon based on Lunar Prospector magnetometer observations. Icarus 197 (1), 19–23.

Purucker, M., Head, J., Wilson, L., 2012. Magnetic signature of the lunar South Pole-Aitken Basin: Character, origin, and age. Journ. of Geophysical Research-Planets 117, E05001, doi:10.1029/2011JE003922.

Purucker, M., Langlais, B., Olsen, N., Hulot, G., Mandea, M., 2002. The southern edge of cratonic North America: Evidence from new stallite magnetometer observations. Geophys. Res. Lett. 29, (15), 8000.

Purucker, M., Nicolas, J., 2010. Global spherical harmonic models of the internal magnetic field of the Moon based on sequential and coestimation approaches. Journal of Geophysical Research 115, EI2007, doi: 10.1029/2010JE003650.

Purucker, M., Sabaka, T., Solomon, S., Anderson, B., Korth, H., Zuber, M., Neumann, G., 2008. Mercury's internal magnetic field: Constraints on large-and small-scale fields of crustal origin. Earth and Planetary Science Letters 285(3-4, Sp. Iss. SI), doi: f10.1016/j.epsl.2008.12.017, 340–346.

Purucker, M., Whaler, K., 2007. Crustal magnetism. Geomagnetism, M. Kono(ed.), Elsevier, Treatise on Geophysics 5, 195–237.

Purucker, M. E., 2007. Magsat. In: Gubbins, D., Herrero-Bervera, E. (Eds.), Encyclopedia of Geomagnetism and Paleomagnetism. Springer, Heidelberg.

Purucker, M. E., Dyment, J., 2000. Satellite magnetic anomalies related to seafloor spreading in the South Atlantic Ocean. Geophys. Res. Lett. 27, 2765–2768, doi:10.1029/1999GL008437, provided by the NASA Astrophysics Data System.

Purucker, M. E., Langel, R. A., Rajaram, M., Raymond, C., 1998. Global magnetization models with a priori information. J. geophys. Res. 103, 2563–2584.

Purucker, M. E., Sabaka, T., Langel, R. A., 1996. Conjugate gradient analysis: a new tool for studying satellite magnetic data sets. Geophys. Res. LETT. 23, 507–510.

Purucker, M. E., Sabaka, T., Langel, R. A., 2006. The lunar magnetic field environment: interpretation od new maps of internal and external fields. Lunar and Planetary Science XXXVII, Abstract, 1933.

Qamili, E., De Santis, A., **Isac, A.**, Mandea, M., Duka, B., Simonyan, A., 2013. Geomagnetic jerks as chaotic fluctuations of the earth's magnetic field. Geochemistry, Geophysics, Geosystems 14 (4), DOI: 10.1029/2012GC004398.

Quesnel, Y., Langlais, B., Sotin, C., 2007. Local inversion of magnetic anomalies: Implication for Mars' crustal evolution 55 (3), 258–269.

Rasson, J., van Loo, S., Berrami, N., 2009. Automatic DIflux measurements with AUTODIF. In:Love J.J. (ed), Proceedings of the $XIII^{th}$ IAGA Workshop on Geomagnetic Observatory Instruments, Data Acquisition and Processing, Boulder, Colorado. U.S. Geological Survey Open File Report 2009-1226, 220–224.

Raymond, C. A., Labreque, J. L., 1987. Magnetization of the oceanic crust: thermoremanent magnetization or chemical remanent magetization. J. Geophys. Res. 92, 8077–8088.

Reda, J., Fouassier, D., **Isac, A.**, Linthe, H. J., Matzka, J., Turbitt, C. W., 2011. Improvements in geomagnetic observatory data quality. Geomagnetic Observations and Models, IAGA Special Sopron Book Series 5, 127–148.

Richmond, N. C., Hood, L. L., 2008. A preliminary global map of the vector lunar crustal magnetic field based on Lunar Prospector magnetometer data. Journal of Geophysical Research 113, doi:10.1029/2007JE002933.

Roark, J., Frey, H., 2001. Gridview: Recent improvements in research and education software for exploring mars topography. LPSC XXXIII, Houston, TX Abstract 1618.

Roark, J., Frey, H., Sakimoto, S., 2000. Interactive graphics tools for analysis of mola and other data. LPSC XXXI, Houston, TX Abstract 2026.

Roberts, P. H., Glatzmaier, G. A., 2000. Geodynamo theory and simulations. Rev. of Modern Physics 72, 1081–1123.

Rondot, J., 1994. Recognition of eroded astroblemes. Earth-Science Reviews 35, 331–365.

Runcorn, S. K., 1975. On the interpretation of lunar magnetism. Phys. Earth and Planet. Int. 10, 327–335.

Russell, C. T., 1993. Magnetic fields of the Terrestrial Planets. J. Geophys. Res. 98, 18,681–18,695.

Sabaka, T. J., Olsen, N., Purucker, M. E., 2004. Extending comprehensive models of the Earth's magnetic field with Ørsted and CHAMP data. Geophys. J. Int. 159, 521–547.

Schmidt, P. W., Williams, G. E., 1995. Definition of shallow subsurface structure around the Chicxulub impact crater using ground penetrating radar. LPSC XXVI, 495–496.

Schmidt, P. W., Williams, G. E., 1996. Paleomagnetism of the ejecta-bearing Bunyeroo Formation, late Neoproterozoic, Adelaide fold belt, and the age of the Acraman impact. Earth and Planetary Science Letters 144, 347–357.

Schumaker, L. L., 1981. Spline functions: Basic theory. John Wiley & Sons, New York.

Scott, R. G., Pilkington, M., Tanczyk, E. I., 1997. Magnetic investigations of West Hawk, Deep Bay and Clearwater impact structures, Canada. Meteoritics and Planetary Science 32, 293–308.

Sharpton, V., Dalrymple, G., Marin, L., Ryder, G., Schuraytz, B., Urrutia-Fucugauchi, J., 1992. New links between the Chicxulub impact structure and the Cretaceous/Tertiary boundary. Annual New York Academy of Science 123, 941–969.

Shoemaker, E., 1963. Impact Mechanics at Meteor Crater, Arizona: The Solar System. Univ. of Chicago Press, Middlehurst B.M. and Kuiper G.P., eds. IV, The Moon, Meteorites and Comets, 301–336.

Shoemaker, E., 1998. Impact cratering through geologic time. Journal of the Royal Astronomical Society of Canada 92, 297–309.

Shure, L., Parker, R., Backus, G., jun 1982. Harmonic splines for geomagnetic modelling. Physics of the Earth and Planetary Interiors 28, 215–229.

Shure, L., Parker, R. L., Langel, R. A., 1985. A preliminary harmonic spline model from Magsat data. jgr 90, 11505+.

Smith, D., Zuber, M., et 18 colleagues, 2010. Initial observations from Lunar Orbiter Laser Altimeter (LOLA). Geophysical Research Letters 37, L18204, doi:10.1029/2010GL043751.

Smith, D., Zuber, M., et 23 colleagues, 2001. Mars Orbiter Laser Altimeter: Experiment summary after the first year of global mapping on Mars. Journal of Geophysical Research 106, 23,689–23,722, doi:10.1029/2000JE001364.

Smith, E. J., Davis, L. J., Coleman, P. J., Jones, D. E., 1965. Magnetic field measurements near Mars. Science 149, 1241.

Smith, J. A., 1992. Precursors to Peregrinus: the early history of magnetism and the Mariner's compass in Europe. Journ. of Medieval History 18, 21–74.

Soare, A., Cucu, G., Mandea-Alexandrescu, M., 1998. Historical geomagnetic measurements in Romania. Annali di Geofisica 41, 539–554.

Spray, J., Butler, H., Thompson, L., 2004. Tectonic influences on the morphometry of the Sudbury impact structure: implications for terrestrial cratering and modeling. Meteoritics and Planetary Science 39, 287–301.

St-Louis, B., 2008. INTERMAGNET Technical Reference Manual. Available at wwww.intermagnet.org, Version 4.4.

Stacey, F. D., 1992. Physics of the Earth. Brookfield Press, Australia.

Stanley, S., Bloxam, J., 2004. Convective-region geometry as the cause of Uranus' and Neptune's unusual magnetic fields. Nature 428, 151–153.

Stevenson, D., 2001. Mars' core and magnetism. Reports on Progress in Physics 46, 555–620.

Stevenson, D., 2003. Planetary magnetic fields. Earth and Planetary Science Letters 208, 1–11.

Stöffler, D., Ivanov, B., Hecht, L., Kenkmann, T., Schmidtt, R., Salge, T., Schönian, F., Tagle, R., Weseler, S., Wittmann, A., 2003. Origin and emplacement of the impact

formations at Chicxulub, Mexico, with special emphasis on the Yax-1 deep drilling. Third International Conference on Large Meteorite Impacts, LPI Contribution No. 1167, Lunar and Planetary Institute Houston, Abstract 4092.

Stöffler, D., Ryder, G., 2001. Stratigraphy and isotope ages of lunar geologic units: Chronological standard for the inner solar system. Chronology and Evolution of Mars Kluwer, 9–54.

Takahashi, F., Shimizu, H., Matsushima, M., Shibuya, H., Matsuoka, A., Nakazawa, S., Iijima, Y., Otake, H., Tsunakawa, H., 2009. In-orbit calibration of the lunar magnetometer onboard SELENE (KAGUYA). Earth, Planets and Space 61, 1269–1274.

Thébault, E., 2006. Global lithospheric magnetic field modelling by successive regional analysis. Earth, Planets and Space 58, 485–495.

Therriault, J., Grieve, R., Reimold, W., 1997. Original size of the Vredefort Structure: Implications for the geological evolution of the Witswatersrand Basin. Meteoritics and Planetary Science 32, 71–78.

Tsikalas, F., Gudlaugsson, S., Eldholm, O., Faleide, J., 1998. Integrated geophysical analysis supporting the impact origin of the Mjølnir Structure, Barents Sea. Tectonophysics 289, 257–280.

Tsikalas, F., Steinar, T., Gudlaugsson, S., Faleide, J., Eldholm, O., 1999. Mjølnir Structure, Barents Sea: A marine impact crater laboratory. Large Meteorite Impacts and Planetary Evolution II, Geological Society of America Special Paper 339, 193–204.

Turner, G., Rasson, J., Reeves, C., 2007. Observation and measurement techniques. In: Kono, M. (Ed.), Treatise on Geophysics. Vol. 5. Elsevier Ltd., Amsterdam.

Ugalde, H., Artemieva, N., Milkereit, B., 2005. Magnetization on impact structures-constraints from numerical modeling and petrophysics. GSA Special Papers 384, 25–42, doi:10.1130/0-8137-2384-1.25.

Unsworth, M., Enriquez, O. C., Belmonte, S.and Arzate, J., Bedrosian, P., 2002. Crustal structure of the Chicxulub impact crater imaged with magnetotelluric exploration. Geophysical Research Letters 29, 16–35.

Van Loo, S., Rasson, J., 2006. Presentation of the prototype of an automatic DI-Flux. In: XII^{th} IAGA Workshop on Geomagnetic Observatory Instruments, Data Acquisition and Processing, Abstract volume, 21.

Voorhies, C., Sabaka, T., Purucker, M., 2002. On magnetic spectra of Earth and Mars. Journal of Geophysical Research-Planets 107(E6), 5034, doi: 10.1029/2001JE001534.

Weiss, B., Vali, H., Baudenbacher, F., J.L.Kirschvink, Stewart, S., Shuster, D., 2002. Records of an ancient Martian magnetic field in ALH84001. Earth and Planetary Science Letters 201, 449–463.

Weiss, B. P., Gattacceca, J., Stanley, S., Rochette, P., R., C. U., 2009. Paleomagnetic records of meteorites and early planetesimal differentiation. Space Science Reviews 152, 341–390.

Wessel, P., Smith, W. H. F., 1991. Free software helps map and display data. EOS trans. AGU 72, 441 & 445–446.

Whaler, K. A., Purucker, M. E., 2005. A spatially continuous magnetization model for Mars. Journal of Geophysical Research 110, doi:10.1029/2004JE002393.

Wilhelms, D., 1984. The Geologic History of the Moon. United States Geological Survey Professional Paper 1348.

Wood, C. A., Head, J. W., 1976. Comparison of impact basins on Mercury, Mars and the Moon. Proc. 7^{th} Lunar Sci. Conf., 3629–3651.

Zuber, M., 2001. The crust and mantle of Mars. Nature 412, 220–227.

Zuber, M., Smith, D., Solomon, S., Muhlemann, D., Head, J., Garvin, J., Abshire, J., Bufton, J., 1992. The Mars Observer laser altimeter investigation. Journal of Geo. Rev. 97, 7,781–7,797.

APPENDIX

List of figures and tables

List of Figures

List of Tables

List and copies of related peer-reviewed publications

- Qamili, E., De Santis, A., **Isac, A.**, Mandea, M., Duka, B., Simonyan, A., 2013, Geomagnetic jerks as chaotic fluctuations of the Earth's magnetic field, *Geochemistry, Geophysics, Geosystems (G^3)*, 14, 4, DOI: 10.1029/2012GC004398[13], AIS 2, 499, ISI Impact Factor: 3.021;

- Duka, B., De Santis, A., Mandea, M., **Isac, A.**, Qamili, E., 2012, Geomagnetic jerks characterization via spectral analysis, *Solid Earth*, Interactive Open Access Journal of the European Geoscience Union[14], 3, 131-148, DOI:10.5194/se-3-131-2012[15];

- Mandea, M., **Isac, A.**, 2011, Geomagnetic Field, Measurement Techniques, *Encyclopedia of Solid Earth Geophysics*, 381-385, Harsh K. Gupta (Ed.), Springer Science and Business Media B.V.,(overview paper), DOI: 10.1007/978-90-481-8702-7[16];

- Reda, J., Fouassier, D., **Isac, A.**, Linthe, H.-J., Matzka, J., Turbitt, C., 2011, Improvements in Geomagnetic Observatory Data Quality, *Geomagnetic Observations and Models*, IAGA Special Sopron Book Series 5, 6, 127-148, M.Mandea and M.Korte (Eds.), Springer Science and Business Media B.V., (overview paper), DOI: 10.1007/978-90-481-9858-0[17];

- Isac, A., Mandea, M., Purucker, M., 2009, How impacts have shaped the magnetic field of Earth, Mars and Moon, European Space Agency, *WPP-303 Proceedings of ESA's Second Swarm International Science Meeting* (CD-ROM)[18].

[13] $http://onlinelibrary.wiley.com/doi/10.1029/2012GC004398/full$
[14] $http://www.solid-earth.net/se\_indexed\_in\_the\_science\_citation\_index\_expanded.pdf$
[15] $http://www.solid-earth.net/3/131/2012/$
[16] $http://www.springer.com/earth+sciences+and+geography/geophysics/book/978-90-481-8701$
[17] $http://www.springer.com/serie/8636$
[18] $http://www.congrex.nl/09c24/S2\_Posters/S2\_P04\_Isac\_paper.pdf$